

# Implementation of AASHTOWare Pavement ME Design Software for pavement rehabilitation

by

Shuvo Islam

BS, Bangladesh University of Engineering and Technology, 2009  
MCE, North Carolina State University, 2013

AN ABSTRACT OF A DISSERTATION

Submitted in partial fulfillment of the requirements for the degree

DOCTOR OF PHILOSOPHY

Department of Civil Engineering  
College of Engineering

KANSAS STATE UNIVERSITY  
Manhattan, Kansas

2019

## **Abstract**

The 1993 version of the American Association of State Highway Transportation Officials (AASHTO) design guide has been the primary pavement design tool for state highway agencies in the United States. Recently, a mechanistic-empirical pavement design guide (MEPDG) has been developed for new and rehabilitated pavement design. MEPDG approaches have been incorporated into a proprietary design software (commonly known as AASHTOWare Pavement ME Design (PMED)) for new and rehabilitated pavement designs. The main objective of this study was to facilitate implementation of this AASHTOWare PMED software for rehabilitated pavement design in Kansas. As part of this implementation, transfer functions for translating mechanistic pavement responses into visible distresses embedded in the AASHTOWare PMED software were locally calibrated to eliminate bias and reduce standard error for rehabilitated pavements in Kansas. Rehabilitated pavement sections included asphalt concrete (AC) over AC and jointed plain concrete pavement (JPCP) sections. The PMED software requires periodic recalibration of the prediction models to account for improvements in the PMED models, changes in agency design and construction strategies, and updates in performance data. Thus, another objective of this study was to develop an automated technique for calibrating the AASHTOWare PMED software performance models. The automated methodology developed in this study incorporated robust sampling techniques to verify calibrated PMED models. In addition, a statistical equivalence testing approach was incorporated to ensure PMED-predicted performance results tend to agree with the in-situ data.

# Implementation of AASHTOWare Pavement ME Design Software for pavement rehabilitation

by

Shuvo Islam

BS, Bangladesh University of Engineering and Technology, 2009  
MCE, North Carolina State University, 2013

A DISSERTATION

Submitted in partial fulfillment of the requirements for the degree

DOCTOR OF PHILOSOPHY

Department of Civil Engineering  
College of Engineering

KANSAS STATE UNIVERSITY  
Manhattan, Kansas

2019

Approved by:

---

Major Professor  
Dr. Mustaque Hossain

# **Copyright**

© Shuvo Islam 2019.

## **Abstract**

The 1993 version of the American Association of State Highway Transportation Officials (AASHTO) design guide has been the primary pavement design tool for state highway agencies in the United States. Recently, a mechanistic-empirical pavement design guide (MEPDG) has been developed for new and rehabilitated pavement design. MEPDG approaches have been incorporated into a proprietary design software (commonly known as AASHTOWare Pavement ME Design (PMED)) for new and rehabilitated pavement designs. The main objective of this study was to facilitate implementation of this AASHTOWare PMED software for rehabilitated pavement design in Kansas. As part of this implementation, transfer functions for translating mechanistic pavement responses into visible distresses embedded in the AASHTOWare PMED software were locally calibrated to eliminate bias and reduce standard error for rehabilitated pavements in Kansas. Rehabilitated pavement sections included asphalt concrete (AC) over AC and jointed plain concrete pavement (JPCP) sections. The PMED software requires periodic recalibration of the prediction models to account for improvements in the PMED models, changes in agency design and construction strategies, and updates in performance data. Thus, another objective of this study was to develop an automated technique for calibrating the AASHTOWare PMED software performance models. The automated methodology developed in this study incorporated robust sampling techniques to verify calibrated PMED models. In addition, a statistical equivalence testing approach was incorporated to ensure PMED-predicted performance results tend to agree with the in-situ data.

# Table of Contents

List of Figures .....	xii
List of Tables .....	xviii
Acknowledgements .....	xxiii
Dedication .....	xxv
Chapter 1 - Introduction .....	1
1.1 Background .....	1
1.2 Problem Statement .....	5
1.3 Research Objectives .....	6
1.4 Automated Calibration of PMED .....	6
1.5 Research Contribution .....	7
Chapter 2 - Literature Review .....	10
2.1 Mechanistic-Empirical Design Philosophy .....	10
2.2 KDOT Rehabilitation Options and Design .....	13
2.3 AASHTOWare PMED Performance Models for AC Overlay .....	14
2.3.1 Rut depth .....	14
2.3.2 Load-related cracking .....	15
2.3.3 Transverse reflection cracking model .....	16
2.3.4 Smoothness model .....	17
2.4 Local Calibration Efforts of AASHTOWare PMED Software .....	18
2.4.1 Local calibration of MEPDG performance models in Missouri .....	19
2.4.2 Local calibration of MEPDG performance models in Iowa .....	20
2.4.3 Calibration and implementation of MEPDG in Colorado .....	22

2.4.4 Calibration and implementation of MEPDG in Arizona .....	23
2.4.5 Local calibration of MEPDG for flexible pavements in North Carolina .....	24
2.4.6 MEPDG calibration for pavement rehabilitation in Oregon.....	25
2.4.7 MEPDG local calibration effort in Louisiana .....	26
2.4.8 Local calibration and implementation of MEPDG in Michigan .....	26
2.4.9 Local calibration of MEPDG for northeastern United States .....	27
Chapter 3 - Methodology .....	28
3.1 NCHRP 1-40B Calibration Steps .....	28
3.2 Application of NCHRP 1-40B Calibration Procedures to Kansas Conditions.....	35
3.3 Hierarchical Input Level .....	40
3.4 Traffic Input .....	41
3.4.1 Vehicle class factors .....	44
3.4.2 Monthly adjustment factors.....	46
3.4.3 Hourly distribution factors .....	47
3.4.4 Axle load spectra.....	48
3.4.5 Axle group per vehicle .....	49
3.5 Pavement Cross-Section Inputs .....	50
3.5.1 PMED modeling of AC over AC sections .....	51
3.5.2 PMED modeling of AC over JPCP sections .....	59
3.6 Material Inputs .....	63
3.6.1 AC layer properties .....	64
3.6.2 JPCP layer properties.....	66
3.6.2.1 JPCP mix inputs.....	66
3.6.2.2 JPCP design inputs .....	70
3.6.3 Base layer inputs .....	71
3.6.4 Subgrade soil inputs.....	72
3.7 Climatic Inputs.....	72

3.8 Evaluation of KDOT Distress Data .....	73
3.8.1 Laser crack measurement system.....	73
3.8.2 Interpretation of LCMS data.....	75
3.8.3 Manual distress data collection method .....	76
3.8.4 Comparison of pavement distresses to trigger values .....	77
3.8.5 Evaluation of distress/IRI data .....	80
3.9 Characterizing Existing Pavement Layers .....	84
3.9.1 AC pavement rehabilitation .....	84
3.9.1.1 Volumetric properties .....	85
3.9.1.2 Mechanical properties .....	86
3.9.1.3 Pre-overlay condition data .....	92
3.9.2 JPCP rehabilitation .....	94
Chapter 4 - Local Calibration and Validation.....	97
4.1 Local Calibration and Validation of AC over AC sections .....	97
4.1.1 AC rutting model calibration for AC over AC sections .....	97
4.1.1.1 Bias assessment of the AC rutting model.....	98
4.1.1.2 Elimination of bias of the rutting model .....	99
4.1.2 Transverse cracking model calibration for AC over AC sections .....	100
4.1.2.1 Bias assessment of transverse cracking model .....	102
4.1.2.2 Elimination of bias of the transverse cracking model .....	103
4.1.3 Load-related cracking model calibration for AC over AC sections .....	104
4.1.3.1 Bias assessment of the top-down cracking model.....	105
4.1.3.2 Elimination of bias of the top-down cracking model .....	106
4.1.4 IRI model calibration for AC over AC sections .....	108
4.1.4.1 Bias assessment of the IRI model.....	109
4.1.4.2 Elimination of bias of the IRI model .....	110
4.2 Local Calibration and Validation of AC over JPCP sections .....	111
4.2.1.1 Bias assessment of the AC rutting model.....	112
4.2.1.2 Elimination of bias of the AC rutting model .....	113
4.2.2 Transverse cracking model calibration for AC over JPCP sections .....	115



4.2.2.1	<i>Bias assessment of the transverse cracking model</i>	115
4.2.2.2	<i>Elimination of bias of the transverse cracking model</i>	116
4.2.3	<i>Load-related cracking model calibration for AC over JPCP sections</i>	117
4.2.3.1	<i>Bias assessment of the top-down cracking model</i>	118
4.2.3.2	<i>Elimination of bias of the top-down cracking model</i>	119
4.2.4	<i>IRI model calibration for AC over JPCP sections</i>	120
4.2.4.1	<i>Bias assessment of the IRI model</i>	121
4.2.4.2	<i>Elimination of bias of the IRI model</i>	122
Chapter 5	<b>Automated Calibration</b>	124
5.1	<b>Automated Calibration Technique</b>	124
5.1.1	<i>Objective function</i>	125
5.1.2	<i>Optimization technique</i>	125
5.2	<b>Resampling Techniques</b>	126
5.2.1	<i>Traditional split sampling approach</i>	127
5.2.2	<i>Jackknifing approach</i>	127
5.2.3	<i>Bootstrapping approach</i>	128
5.3	<b>Equivalence Testing</b>	129
5.3.1	<i>Traditional equivalence testing</i>	129
5.3.2	<i>Two one-sided t-test</i>	130
5.4	<b>Automated Calibration Methodology</b>	131
5.4.1	<i>Programming routine for the automated technique</i>	132
5.4.2	<i>Incorporating sampling methods into the automated technique</i>	134
5.4.2.1	<i>Traditional split sampling approach</i>	134
5.4.2.2	<i>Jackknifing sampling approach</i>	134
5.4.2.3	<i>Bootstrapping approach</i>	136
5.5	<b>Local Calibration of AC over AC sections</b>	138
5.5.1	<i>Permanent deformation model</i>	138
5.5.1.1	<i>Traditional split sampling approach</i>	139
5.5.1.2	<i>Jackknifing approach</i>	142

5.5.1.3	<i>Bootstrapping approach</i>	144
5.5.2	<i>Transverse cracking model</i>	146
5.5.2.1	<i>Traditional split sampling approach</i>	147
5.5.2.2	<i>Jackknifing approach</i>	151
5.5.2.3	<i>Bootstrapping approach</i>	154
5.5.3	<i>Top-down cracking model</i>	156
5.5.3.1	<i>Traditional split sampling approach</i>	158
5.5.3.2	<i>Jackknifing approach</i>	161
5.5.3.3	<i>Bootstrapping approach</i>	164
5.5.4	<i>IRI model</i>	166
5.5.4.1	<i>IRI model constraints</i>	168
5.5.4.2	<i>Split sampling approach</i>	169
5.5.4.3	<i>Jackknifing approach</i>	172
5.5.4.4	<i>Bootstrapping approach</i>	175
5.6	<i>Local Calibration of AC over JPCP sections</i>	178
5.6.1	<i>Permanent deformation model</i>	178
5.6.1.1	<i>Traditional split sampling approach</i>	180
5.6.1.2	<i>Jackknifing approach</i>	183
5.6.1.3	<i>Bootstrapping approach</i>	185
5.6.2	<i>Transverse cracking model</i>	187
5.6.2.1	<i>Traditional split sampling approach</i>	188
5.6.2.2	<i>Jackknifing approach</i>	191
5.6.2.3	<i>Bootstrapping approach</i>	194
5.6.3	<i>Top-down cracking model</i>	196
5.6.3.1	<i>Traditional split sampling approach</i>	197
5.6.3.2	<i>Jackknifing approach</i>	200
5.6.3.3	<i>Bootstrapping approach</i>	203
5.6.4	<i>IRI model</i>	205
5.6.4.1	<i>Split sampling approach</i>	207
5.6.4.2	<i>Jackknifing approach</i>	210
5.6.4.3	<i>Bootstrapping approach</i>	213

5.7 Limitation of the Automated Calibration Technique.....	216
Chapter 6 - Conclusion .....	217
6.1 Local Calibration Results.....	218
6.1.1 <i>Permanent deformation model</i> .....	218
6.1.2 <i>Transverse cracking model</i> .....	218
6.1.3 <i>Load-related cracking model</i> .....	219
6.1.4 <i>IRI model</i> .....	220
6.2 Automated Calibration Technique.....	221
6.2.1 <i>Sampling technique</i> .....	221
6.2.2 <i>Equivalence testing</i> .....	222
6.3 Recommendations and Needs for Future Research .....	223
References.....	227
Appendix A - AASHTOWare Traffic Inputs.....	238
Appendix B - Site Specific Material Properties.....	248
Appendix C - Backcalculated Modulus .....	258

## List of Figures

Figure 1-1 Schematic of bias and $S_e$ (precision) for model calibrations (Haider et al., 2014) .....	4
Figure 2-1 Flowchart of the AASHTOWare pavement ME design process .....	12
Figure 3-1 Locations of selected AC over AC projects across Kansas .....	37
Figure 3-2 Locations of selected AC over JPCP projects across Kansas .....	39
Figure 3-3 FHWA vehicle classification (Traffic monitoring guide, FHWA, 2016) .....	45
Figure 3-4 Average VCFs for urban (left) and rural (right) principal arterials .....	46
Figure 3-5 MAFs for rural and urban principal arterials in Kansas.....	47
Figure 3-6 HDFs for rural and urban principal arterials in Kansas .....	48
Figure 3-7 Single (left) and tandem (right) axle loads for class 9 trucks in Kansas.....	49
Figure 3-8 Schematic of rehabilitated pavement structures in Kansas .....	51
Figure 3-9 AC unit weight distribution of HMA mixes .....	65
Figure 3-10 Effective binder content distribution AC mixes of existing pavement.....	65
Figure 3-11 Strength gains over time for the selected JPCP projects.....	69
Figure 3-12 KDOT Laser crack measurement system.....	74
Figure 3-13 Cross section of survey lane with wheel paths and survey area between wheel paths (AASHTO PP 67-16).....	76
Figure 3-14 Rut depth on selected AC over JPCP (left) and AC over AC (right) sections.....	79
Figure 3-15 Top-down cracking in selected AC over AC (left) and AC over JPCP (right) sections .....	79
Figure 3-16 Transverse cracking in AC over AC (left) and AC over JPCP (right) sections.....	80
Figure 3-17 Measured IRI in selected AC over AC (left) and AC over JPCP (right) sections ....	80
Figure 3-18 Rutting measurements for AC over AC (left) and AC over JPCP (right) sections...	81

Figure 3-19 Top-down crack measurements for AC over AC (left) and AC over JPCP (right) sections.....	81
Figure 3-20 Transverse cracking measurements for AC over AC (left) and AC over JPCP (right) sections.....	82
Figure 3-21 Transverse cracking measurements for AC over AC (left) and AC over JPCP (right) sections.....	82
Figure 3-22 Time-series plot of measured transverse cracking for project KA-2836-01 .....	83
Figure 3-23 Time-series plot of measured longitudinal cracking for project KA-1951-01.....	84
Figure 3-24 AC unit weight distribution of overlay AC mixes .....	85
Figure 3-25 Effective binder content distribution in overlay HMA mixes.....	86
Figure 3-26 AC layer damage computation for level 1 inputs (NCHRP 1-37A, 2004) .....	87
Figure 3-27 Backcalculated moduli for pavement section KA-1436-01 .....	90
Figure 3-28 Boxplot of backcalculated AC moduli for pavement section KA-1436-01 .....	91
Figure 3-29 Pre-overlay top-down fatigue cracking for the AC over AC sections .....	93
Figure 3-30 Pre-overlay transverse cracking for AC over AC sections .....	93
Figure 3-31 Pre-overlay permanent deformation for AC over AC sections.....	94
Figure 3-32 Pre-overlay IRI for AC over AC sections .....	94
Figure 3-33 Transverse joint faulting of the JPCP rehabilitated project prior to overlay.....	96
Figure 4-1 Predicted vs measured AC rutting with globally calibrated factors.....	98
Figure 4-2 Predicted vs measured AC rutting with locally calibrated factors.....	100
Figure 4-3 Predicted vs measured transverse cracking with globally calibrated factors .....	102
Figure 4-4 Predicted vs measured transverse cracking with locally calibrated factors .....	104
Figure 4-5 Predicted vs measured longitudinal cracking with globally calibrated factors.....	106

Figure 4-6 Predicted vs measured longitudinal cracking with locally calibrated factors .....	108
Figure 4-7 Predicted vs measured AC IRI with globally calibrated factors .....	109
Figure 4-8 Predicted vs measured AC IRI with locally calibrated factors .....	111
Figure 4-9 Predicted vs measured AC rutting with globally calibrated factors.....	113
Figure 4-10 Predicted vs measured AC rutting with locally calibrated factors .....	114
Figure 4-11 Predicted vs measured transverse cracking with globally calibrated factors .....	116
Figure 4-12 Predicted vs measured transverse cracking with locally calibrated factors .....	117
Figure 4-13 Predicted vs measured longitudinal cracking with globally calibrated factors.....	119
Figure 4-14 Predicted vs measured longitudinal cracking with locally calibrated factors .....	120
Figure 4-15 Predicted vs measured IRI with globally calibrated factors.....	121
Figure 4-16 Predicted vs measured AC IRI with locally calibrated factors .....	123
Figure 5-1 Analysis process for automated calibration technique.....	133
Figure 5-2 Working method of jackknife sampling approach .....	135
Figure 5-3 Working method of bootstrap sampling approach .....	137
Figure 5-4 Predicted vs measured total rutting with globally calibrated factors .....	139
Figure 5-5 Predicted vs measured total rutting with local coefficients for AC over AC sections .....	141
Figure 5-6 Predicted versus measured rutting for the validation dataset for AC over AC sections .....	142
Figure 5-7 Distribution of the $\beta_{1r}$ parameter using jackknife sampling .....	143
Figure 5-8 Rutting model equivalence margin with respect to $\beta_{1r}$ parameter .....	144
Figure 5-9 Distribution of the $\beta_{1r}$ parameter using bootstrap resampling approach .....	145
Figure 5-10 Rutting model equivalence margin with respect to $\beta_{1r}$ parameter .....	146

Figure 5-11 Predicted vs measured transverse cracking with globally calibrated factors .....	147
Figure 5-12 Predicted vs measured total rutting with local coefficients for AC over AC sections .....	150
Figure 5-13 Predicted versus measured transverse cracking for the validation dataset .....	151
Figure 5-14 Distribution of the $C_4$ coefficient using jackknife sampling technique .....	152
Figure 5-15 Distribution of the $C_5$ coefficient using jackknife sampling technique .....	153
Figure 5-16 Distribution of the $C_4$ coefficient using bootstrap sampling technique .....	155
Figure 5-17 Distribution of the $C_5$ coefficient using bootstrap sampling technique .....	155
Figure 5-18 Predicted vs measured top-down cracking with globally calibrated factors.....	157
Figure 5-19 Predicted vs measured top-down with local coefficients for AC over AC sections	160
Figure 5-20 Predicted versus measured top-down cracking for the validation dataset .....	161
Figure 5-21 Distribution of the $C_1$ coefficient using jackknife sampling technique .....	162
Figure 5-22 Distribution of the $C_2$ coefficient using jackknife sampling technique .....	163
Figure 5-23 Distribution of the $C_1$ coefficient using bootstrap technique .....	164
Figure 5-24 Distribution of the $C_2$ coefficient using bootstrap sampling technique .....	165
Figure 5-25 Predicted vs measured top-down cracking with globally calibrated factors.....	167
Figure 5-26 Predicted vs measured top-down with local coefficients for AC over AC sections	171
Figure 5-27 Predicted versus measured top-down cracking for the validation dataset .....	172
Figure 5-28 Distribution of the $C_1$ coefficient of IRI model using jackknife technique .....	173
Figure 5-29 Distribution of the $C_2$ coefficient of IRI model using jackknife technique .....	174
Figure 5-30 Distribution of the $C_3$ coefficient of IRI model using jackknife technique .....	174
Figure 5-31 Distribution of the $C_4$ coefficient of IRI model using jackknife technique .....	175
Figure 5-32 Distribution of the $C_1$ coefficient of IRI model using bootstrap technique .....	176

Figure 5-33 Distribution of the $C_2$ coefficient of IRI model using bootstrap technique .....	177
Figure 5-34 Distribution of the $C_3$ coefficient of IRI model using bootstrap technique .....	177
Figure 5-35 Distribution of the $C_4$ coefficient of IRI model using bootstrap technique .....	178
Figure 5-36 Predicted vs measured rutting with global factors for AC over JPCP sections .....	180
Figure 5-37 Predicted vs measured total rutting with local coefficients for AC over JPCP sections .....	182
Figure 5-38 Predicted versus measured rutting for validation dataset for AC over JPCP sections .....	183
Figure 5-39 Distribution of the $\beta_{1r}$ parameter using jackknife sampling .....	184
Figure 5-40 Rutting model equivalence margin with respect to $\beta_{1r}$ parameter .....	185
Figure 5-41 Distribution of the $\beta_{1r}$ parameter using bootstrap resampling approach .....	186
Figure 5-42 Rutting model equivalence margin with respect to $\beta_{1r}$ parameter .....	186
Figure 5-43 Predicted vs measured transverse cracking for AC over JPCP sections (global factors) .....	188
Figure 5-44 Predicted vs measured transverse cracking for AC over JPCP sections (local factors) .....	190
Figure 5-45 Predicted versus measured transverse cracking for the validation dataset .....	191
Figure 5-46 Distribution of the $C_4$ coefficient using jackknife sampling technique .....	192
Figure 5-47 Distribution of the $C_5$ coefficient using jackknife sampling technique .....	193
Figure 5-48 Distribution of the $C_4$ coefficient using bootstrap sampling technique .....	194
Figure 5-49 Distribution of the $C_5$ coefficient using bootstrap sampling technique .....	195
Figure 5-50 Predicted vs measured top-down cracking with globally calibrated factors.....	197



Figure 5-51 Predicted vs measured top-down with local coefficients for AC over JPCP sections .....	199
Figure 5-52 Predicted versus measured top-down cracking for the validation dataset .....	200
Figure 5-53 Distribution of the $C_1$ coefficient using jackknife sampling technique .....	201
Figure 5-54 Distribution of the $C_2$ coefficient using jackknife sampling technique .....	202
Figure 5-55 Distribution of the $C_1$ coefficient using bootstrap technique .....	203
Figure 5-56 Distribution of the $C_2$ coefficient using bootstrap technique .....	204
Figure 5-57 Predicted vs measured IRI with global factors for AC over JPCP sections.....	206
Figure 5-58 Predicted vs measured IRI with local coefficients for AC over JPCP sections .....	208
Figure 5-59 Predicted versus measured IRI for the validation dataset with local factors .....	210
Figure 5-60 Distribution of the $C_1$ coefficient of IRI model using jackknife technique .....	211
Figure 5-61 Distribution of the $C_2$ coefficient of IRI model using jackknife technique .....	212
Figure 5-62 Distribution of the $C_3$ coefficient of IRI model using jackknife technique .....	212
Figure 5-63 Distribution of the $C_4$ coefficient of IRI model using jackknife technique .....	213
Figure 5-64 Distribution of the $C_1$ coefficient of IRI model using bootstrap technique .....	214
Figure 5-65 Distribution of the $C_2$ coefficient of IRI model using bootstrap technique .....	215
Figure 5-66 Distribution of the $C_3$ coefficient of IRI model using bootstrap technique .....	215
Figure 5-67 Distribution of the $C_4$ coefficient of IRI model using bootstrap technique .....	216

## List of Tables

Table 2-1 Criteria for determining global model adequacy for Colorado conditions.....	23
Table 3-1 Adjusted flexible pavement transfer function calibration parameters to eliminate bias and reduce standard error (AASHTO, 2010) .....	34
Table 3-2 Minimum sample size guidelines for local calibration of distress models (Haider et al., 2014) .....	36
Table 3-3 General descriptions of selected AC over AC projects in Kansas .....	38
Table 3-4 General descriptions of selected AC over JPCP projects in Kansas .....	40
Table 3-5 WIM stations used in this study .....	43
Table 3-6 AVC stations used in this study.....	43
Table 3-7 AGPV for rural and urban roadways in Kansas .....	50
Table 3-8 Strength properties of mixes for the selected JPCP sections.....	67
Table 3-9 Site-specific JPCP design input parameters .....	71
Table 3-10 Input parameters of base layer.....	72
Table 3-11 KDOT-specified failure criteria for pavement distresses .....	77
Table 3-12 FWD testing data available for the AC over AC section .....	89
Table 3-13 KDOT guidelines for estimating LTE.....	95
Table 4-1 Statistical analysis summary results for nationally calibrated factors.....	99
Table 4-2 Statistical analysis results for locally calibrated factors for AC rutting model.....	99
Table 4-3 Summary statistics for validation set of AC rutting model with local factors .....	100
Table 4-4 Statistical analysis summary results for nationally calibrated factors.....	102
Table 4-5 Summary statistics for locally calibrated total transverse cracking model .....	103

Table 4-6 Summary statistics for validation set of transverse cracking model with local factors .....	104
Table 4-7 Summary statistics for top-down cracking model with nationally calibrated factors	106
Table 4-8 Summary statistics for top-down cracking model with locally calibrated factors .....	107
Table 4-9 Summary statistics for validation set of top-down cracking model with local factors .....	108
Table 4-10 Statistical analysis summary results for nationally calibrated factors.....	109
Table 4-11 Statistical analysis results for locally calibrated factors for AC rutting model.....	110
Table 4-12 Summary statistics for validation set of AC rutting model with local factors .....	111
Table 4-13 Statistical analysis summary results for nationally calibrated factors.....	112
Table 4-14 Statistical analysis results for locally calibrated factors for AC rutting model.....	113
Table 4-15 Summary statistics for validation set of AC rutting model with local factors .....	114
Table 4-16 Statistical analysis summary results for nationally calibrated factors.....	115
Table 4-17 Summary statistics for locally calibrated total transverse cracking model .....	116
Table 4-18 Summary statistics for validation set of transverse cracking model with local factors .....	117
Table 4-19 Summary statistics for top-down cracking model with nationally calibrated factors .....	118
Table 4-20 Summary statistics for top-down cracking model with locally calibrated factors ...	119
Table 4-21 Summary statistics for validation set of top-down cracking model with local factors .....	120
Table 4-22 Statistical analysis summary results for nationally calibrated factors.....	121
Table 4-23 Statistical analysis results for locally calibrated factors for AC rutting model.....	122

Table 4-24 Summary statistics for validation set of AC rutting model with local factors .....	123
Table 5-1 Initial value of $\delta$ for verification of PMED models .....	131
Table 5-2 Summary statistics for the nationally calibrated rutting model for AC over AC sections .....	138
Table 5-3 Summary statistics for the locally calibrated rutting model for AC over AC sections .....	140
Table 5-4 Calibrated model equivalence margin between measured and predicted rutting .....	140
Table 5-5 Validation results for the calibrated rutting model for AC over AC sections .....	142
Table 5-6 Summary statistics for the globally calibrated transverse cracking model .....	146
Table 5-7 Summary statistics for the locally calibrated transverse cracking model.....	148
Table 5-8 Calibrated model equivalence margin between measured and predicted transverse cracking.....	149
Table 5-9 Validation results of the calibrated rutting model for AC over AC sections .....	151
Table 5-10 Combination of $C_4$ and $C_5$ considered for repeated TOST.....	154
Table 5-11 Combination of $C_4$ and $C_5$ considered for repeated TOST.....	156
Table 5-12 Summary statistics for the globally calibrated top-down cracking model .....	157
Table 5-13 Summary statistics for the locally calibrated top-down cracking model .....	158
Table 5-14 Calibrated model equivalence margin between measured and predicted rutting .....	159
Table 5-15 Validation results for the calibrated rutting model for AC over AC sections .....	161
Table 5-16 Combination of $C_1$ and $C_2$ considered for repeated TOST for the jackknife technique .....	164
Table 5-17 Combination of $C_1$ and $C_2$ considered for repeated TOST for the bootstrap technique .....	165

Table 5-18 Results for the globally calibrated IRI model for AC over AC sections.....	166
Table 5-19 IRI model coefficients bounds considered for this study .....	169
Table 5-20 Summary statistics for the locally calibrated IRI model .....	169
Table 5-21 Calibrated model equivalence margin between measured and predicted rutting .....	170
Table 5-22 Validation results for the calibrated IRI model for AC over AC sections .....	172
Table 5-23 Results for the nationally calibrated rutting model for AC over JPCP sections .....	179
Table 5-24 Summary statistics for the locally calibrated rutting model for AC over JPCP sections .....	180
Table 5-25 Calibrated model equivalence margin between measured and predicted rutting .....	181
Table 5-26 Validation results for the calibrated rutting model for AC over JPCP sections.....	183
Table 5-27 Results for globally calibrated transverse cracking model for AC over JPCP sections .....	187
Table 5-28 Summary statistics for the locally calibrated transverse cracking model.....	189
Table 5-29 Calibrated model equivalence margin for measured and predicted transverse cracking .....	189
Table 5-30 Validation results for the calibrated rutting model for AC over JPCP sections.....	191
Table 5-31 Combination of $C_4$ and $C_5$ considered for repeated TOST.....	193
Table 5-32 Combination of $C_4$ and $C_5$ considered for repeated TOST.....	195
Table 5-33 Results for the globally calibrated top-down cracking model for AC over JPCP sections.....	196
Table 5-34 Summary statistics for the locally calibrated top-down cracking model .....	198
Table 5-35 Calibrated model equivalence margin between measured and predicted rutting .....	198

Table 5-36 Validation results for the calibrated top-down cracking model for AC over JPCP sections.....	200
Table 5-37 Combination of $C_1$ and $C_2$ considered for repeated TOST for the jackknife technique .....	203
Table 5-38 Combination of $C_1$ and $C_2$ considered for repeated TOST for the bootstrap technique .....	204
Table 5-39 Results for the globally calibrated IRI model for AC over JPCP sections.....	205
Table 5-40 Summary statistics for the locally calibrated IRI model .....	207
Table 5-41 Calibrated model equivalence margin between measured and predicted rutting .....	208
Table 5-42 Validation results for the calibrated IRI model for AC over JPCP sections .....	209

## Acknowledgements

First, I would like to pay my earnest gratitude and utmost respect to Almighty Allah for allowing me to complete my dissertation research.

I would like to express my earnest gratitude to my major professor Dr. Mustaque Hossain for his invaluable guidance and encouragement throughout my graduate study. I am grateful for his continuous support and inspiration to understand the very rudiments in pavement engineering and venture new ideas and conduct original research. His motivation and encouragement has been instrumental in publishing journal papers and presenting in technical conferences.

I would also like to thank Dr. Cristopher A. Jones for agreeing to be in my doctoral committee and providing guidance and advice for my dissertation research. I would like to thank Dr. Stacy Kulesza for being my committee member and providing valuable inputs to improve this dissertation. I am grateful to Dr. Christopher Vahl for his helpful suggestions and feedback. I also want to acknowledge Dr. Steve Warren for agreeing to be the committee chairperson for my doctoral program.

I express my gratitude to Mr. Ryan Barrett (Kansas Department of Transportation) and Mr. Nat Velasquez, Jr. (Kansas Department of Transportation) for the consistence support and guidance throughout the duration of my research. Without their encouragement, valuable input, and effort, this research work could not be completed. I also appreciate Mr. Rick Miller (Kansas Department of Transportation) for his contribution to the various aspects of this research.

I am grateful to Mr. Avishek Bose (Computer Science Department, Kansas State University) for his continuous support and assistance for the completion of this research. I sincerely thank Dr. Wouter Brink (Applied Research Associates, Inc.) for his advice to conduct

this research work. I want to acknowledge my graduate colleagues Dr. Nassim Sabahfar, Dr. Masoumeh Tavakol, Abu Sufian, Humaira Zahir, Xingdong Wu, and Ya Gao.

I would like to thank my dear wife Tazrin Jannat Khan for her constant support and motivation for the entire duration of my graduate study. I want to express my deepest respect and affection to my parents, and my sister. Finally, I want to acknowledge the people of Bangladesh whose contribution allowed me to pursue my undergraduate study at Bangladesh University of Engineering and Technology (BUET).



## **Dedication**

This dissertation is dedicated to my wife, Tazrin Jannat Khan, my son, Zahran Abdullah, my parents, Dilara Islam and Md. Qumrul Islam, my sister, Dr. Farzana Islam, my brother-in-law, Dr. Moklasur Rahman, my nephews, Rafid Aiman, and Raid Ayan.

# Chapter 1 - Introduction

State highway agencies in the United States have predominantly used the *American Association of State Highway Transportation Officials (AASHTO) Guide for Design of Pavement Structures* (AASHTO, 1993) and the associated DARWin software to design new and rehabilitated highway pavements. These design methodologies, which are empirical in nature, were developed based on field performance data obtained from the AASHO Road Test (Huang, 1993). Although the 1993 AASHTO design guide contains state-of-the-practice refinements in material input parameters and design procedures, an update was warranted to incorporate the principles of engineering mechanics in pavement design (Khanum, 2005). To implement an improved design guide for new and rehabilitated pavements, a new mechanistic-empirical pavement design guide (MEPDG) and corresponding software were developed through the National Cooperative Highway Research Program (NCHRP) 1-37A project. The MEPDG considers relevant input parameters, such as traffic, climate, and pavement structure material properties, and utilizes the theories of mechanics to assess pavement performance (Li et al., 2011).

The mechanistic portion of the MEPDG design guide refers to application of the theory of engineering mechanics to estimate pavement stress and strain responses based on design inputs and then use those responses to compute incremental damage over time (Robbins et al., 2017). Cumulative damage is then converted to typical pavement distresses via transfer functions embedded in the software. These transfer functions are empirically calibrated with pavement distress measurements of in-service sections (Michigan DOT, 2017).

## 1.1 Background

The National Academy of Science utilized the NCHRP to develop a user-friendly procedure for executing mechanistic-empirical (M-E) design while accounting for local

environmental conditions, local highway materials, and actual highway traffic distribution using axle load spectra (NCHRP 1-37A, 2004). The first edition of the MEPDG (software version 0.7) was released in 2004. Following this release, another NCHRP study was conducted under project 1-40 to investigate the design guide's underlying assumption, evaluate engineering reasonableness, and implement the M-E approach for designing highway pavements (Ceylan, 2015). The outcomes of this effort were included in the introduction of the MEPDG software version 1.1 and a performance prediction model calibration guide. Since its inception, the MEPDG software underwent several improvements (versions) and was later adopted by AASHTO and incorporated into the AASHTOWare Pavement ME Design (PMED) software. AASHTOWare Pavement ME version 2.5 is the latest version of the AASHTOWare series (Islam et al., 2019).

Transfer functions in the PMED software were calibrated using the Long-Term Pavement Program (LTPP) sections as a representative database of in-service pavement sections throughout North America (Robbins, 2017). Even though the nationally calibrated prediction models of the software are reflective of national-level design practices, these models may not be accurate enough for routine pavement design for a particular state or region. Since design and construction practices, pavement materials, and climatic conditions vary throughout the country, prediction models in the PMED software must be calibrated for a specific state or region. Without this calibration the new guide will be of limited use for design purposes.

Calibration refers to the process through which the bias or residual error and the standard error are minimized between the observed and predicted pavement distress values (Kim et al., 2011). This process includes verification of nationally calibrated factors, calibration of prediction model coefficients, and validation of the performance models. Bias refers to the average over or under prediction of the performance models compared to the observed distress, or International

Roughness Index (IRI), values. A biased model in the AASHTOWare PMED software will produce over-designed or under-designed pavements (NCHRP 1-40B, 2010). Another objective of model calibration is to increase prediction accuracy since lack of precision in the model leads to ineffective design of pavement sections and premature failures.

The local calibration guide for AASHTOWare PMED defines the standard error of estimate ( $S_e$ ) as the standard deviation of residual errors for pavement sections included in the calibration dataset for each prediction model. The standard error is usually obtained by taking the positive square root of the variance of the statistic. The local calibration guide for the AASHTOWare ME lists four components of the  $S_e$ . The first component pertains to measurement errors associated with distress or smoothness measurements in the field. The second component is an input error, which is the underestimation or overestimation of certain input parameters required by the method. The third component is deficiencies in the transfer functions within the AASHTOWare PMED software, while the fourth component is pure error. Pure error is dependent on the input level, distress type, and prediction equation. Figure 1-1 presents various scenarios of bias and standard error (Haider et al., 2014).

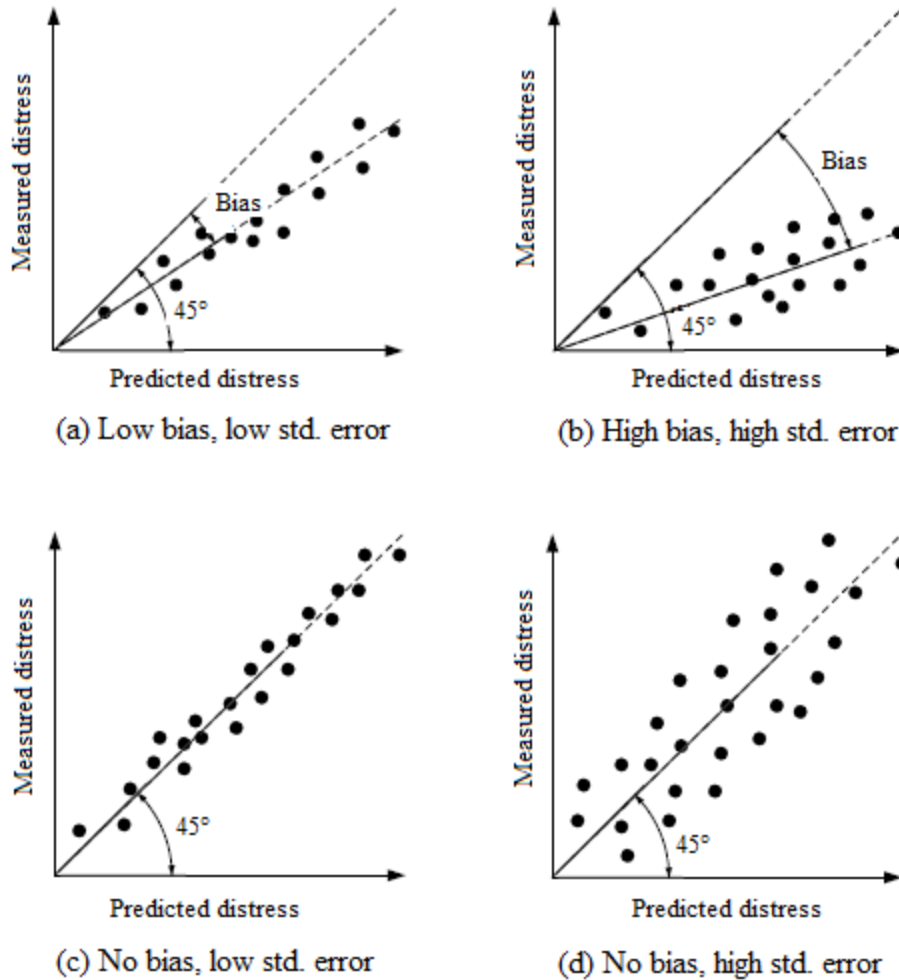


Figure 1-1 Schematic of bias and  $S_e$  (precision) for model calibrations (Haider et al., 2014)

Since the release of this methodology, several states have attempted local calibration and software implementation for day-to-day pavement design. In 2014, NCHRP synthesis 457 study surveyed 57 highway transportation agencies across North America. Survey results showed that three agencies had implemented MEDPG and 46 agencies were in the process of evaluating MEDPG models. In addition, 12 agencies confirmed that relevant MEDPG prediction models were being calibrated to local conditions. In 2017, the National Center for Asphalt Technology (NCAT) conducted a detailed review of highway agencies' local calibration studies for flexible pavements

and listed the methodologies and results of those efforts. Previous researchers listed several PMED software implementation challenges, including the complex nature of PMED software, data needs, field investigation and laboratory testing to characterize input parameters, local calibration of performance models, and resource constraints (Buch et al., 2013).

## **1.2 Problem Statement**

The Kansas Department of Transportation (KDOT) is transitioning from the 1993 AASHTO pavement design guide to AASHTOWare PMED. Kansas State University completed the evaluation and local calibration of performance models in the PMED software for new/reconstructed pavements for Kansas (Islam et al., 2019). Because a major portion of KDOT pavement work involves rehabilitation of existing pavements, implementation of AASHTOWare PMED software is imperative for effective rehabilitation design.

Jointed plain concrete pavement (JPCP) and asphalt concrete (AC) pavements are the prevalent pavement types in Kansas, and AC overlays are the primary rehabilitation options for flexible and rigid pavements throughout the state. KDOT has been using Chapter 5 of the 1993 *AASHTO Design Guide* to design AC overlays over existing flexible or rigid pavements. In order to implement PMED software for rehabilitation design, however, the prediction models (i.e., alligator and longitudinal cracking, permanent deformation or rutting, transverse cracking, and IRI models) must be calibrated to local conditions to accurately predict pavement performance. In this study, calibration and verification of PMED performance models were conducted for both AC over JPCP and AC over AC sections.

One of the concerns with implementing PMED software is the need to recalibrate the performance models after updating the distress models or as more performance data become

available. A unique contribution of this study is to present a framework to automate the calibration process of PMED performance models.

### **1.3 Research Objectives**

The primary objective of this research was to calibrate and validate pavement performance models embedded in the AASHTOWare PMED software for AC overlays in Kansas. The first task assessed nationally calibrated performance models in the software, the second task calibrated the performance models to reduce bias and  $S_e$ , and the third task validated the locally calibrated performance models. Completion of these tasks involved selecting pavement projects across Kansas that were reflective of current and future KDOT design standards and construction practices, accumulating as-constructed input parameters required to analyze selected projects in the PMED software platform, evaluating time-series distress data of these projects, and calibrating the PMED performance models in terms of goodness-of-fit criteria to estimate best values of the model coefficients.

The second objective of this study was to develop an automated calibration technique to help highway agencies conduct periodic in-house calibration of the PMED software. The necessary steps to accomplish this objective included forming a programming routine to extract required information from the software, defining a clear objective function and optimization technique for parameter adjustments, incorporating several sampling techniques to verify the calibrated PMED models, and conducting suitable statistical testing so that the predicted performance data are in agreement with the measured data.

### **1.4 Automated Calibration of PMED**

Following the release of MEPDG in 2004, several states attempted implementation of the PMED software for routine pavement design. In 2017, a technical report of the AASHTO

Pavement ME national user group found that 9 of the 21 responding highway agencies had successfully implemented PMED software for asphalt pavements (AASHTO Pavement ME National User Group Meeting, 2017). The report also listed software implementation challenges such as local calibration and verification of PMED performance models, availability of performance data, characterizing bound and unbound layer material properties, compatibility of performance measures, and threshold criteria.

From its inception, the software underwent several improvements that necessitated frequent software recalibration (Tran et al., 2017). Changes in agency construction and design policy may also require recalibration of the performance models. Many highway agencies also reported long-term concerns regarding continuing resource allocation for the PMED model recalibration. Therefore, this study developed a programming routine to automate the computational process of the PMED model calibration system. In addition to the traditional split sampling approach, the jackknifing and the bootstrapping techniques were incorporated into the automated technique to verify PMED models. Furthermore, an equivalence testing approach was studied to ensure PMED predicted performance data comply with field performance data within a certain error margin.

### **1.5 Research Contribution**

According to the Transportation Works for Kansas (T-WORKS) website, KDOT budgeted over \$1 billion for pavement rehabilitation with AC overlays for the years 2010–2020 (tworks.ksdot.org, 2011). Approximately \$96 million was spent on constructing AC overlay in Kansas in fiscal year 2012–2013. Efficient design of AC overlay will ensure optimal cost of materials and construction and beneficially extend the fatigue life of the existing pavement. Even though the PMED software has become state-of-the-practice for designing new pavements for



many highway agencies in the United States, substantial effort is needed to implement this approach for designing rehabilitated pavements.

Calibration of PMED software requires development of a database for input parameters. The AASHTOWare software requires a wide range of design inputs to analyze a pavement section. This study analyzed traffic data from Kansas weigh-in-motion (WIM) and automated vehicle classification (AVC) facilities to generate statewide level 2 traffic inputs for Kansas. Characterization of Kansas traffic characteristics will be beneficial for future KDOT pavement design, and material inputs used in this study will help KDOT identify sensitive material properties for designing pavements.

This study also introduced a framework to automate the calibration and validation processes of the PMED performance models. Prior to this study, there was no evidence of using an automated technique to calibrate the prediction models in the PMED software. The automated calibration technique developed in this study will be extremely beneficial to highway agencies to conduct periodic in-house PMED performance model calibration. This study also implemented several statistical sampling techniques for calibrating and validating performance models. Since performance models in PMED software are continuously updated, the recommended sampling option can be used in future calibration studies.

Previous local calibration studies of AASHTOWare PMED software primarily used a traditional equivalence testing approach (paired  $t$ -test) to determine bias. The local calibration guide of the PMED software recommends use of the paired  $t$ -test to evaluate significant differences between measured and predicted data. Although differences in datasets can be confirmed using this approach, their equality cannot be supported. Furthermore, a margin of equivalence cannot be established between the predicted and measured data in a paired  $t$ -test

setting. This study is the first to use an equivalence testing approach (i.e., two one-sided test (TOST)) to investigate measured and predicted data for a margin of equivalence. Use of the TOST approach can help establish an equivalence margin for the PMED predicted and field-measured distresses.

## Chapter 2 - Literature Review

Many state highway agencies have adopted the MEPDG approach and accompanying PMED software to supplement or replace empirical pavement design procedures from the 1993 *AASHTO Design Guide*. A prerequisite for implementing the PMED software for routine design is to verify and calibrate the performance models to local conditions. This chapter contains a detailed literature review of the MEPDG design and its performance prediction models for AC rehabilitation, KDOT rehabilitation options and design, and efforts undertaken by state highway agencies to locally calibrate PMED models.

### 2.1 Mechanistic-Empirical Design Philosophy

M-E design aims to characterize the physical, or mechanistic, causes of stresses in pavement structures and calibrate them with observed, or empirical, pavement performance (pavementinteractive.org, 2012). M-E design applies engineering mechanics to compute pavement responses (i.e., deflection, stress, and strain), and these response values are used to predict pavement distresses (i.e., fatigue cracking and pavement deformation) from field-performance data (Huang, 2003).

Figure 2-1 shows the iterative design and analysis procedure of the M-E approach used in the AASHTOWare PMED software. The software requires users to select a trial design strategy and input site conditions such as traffic, climate, and layer material properties. Critical responses such as deflection, stress, and strain are computed using structural analysis models in the software. These models include Jacob Uzan Layered Elastic Analysis (JULEA) for flexible pavements and the ISLAB2000 program for rigid pavements. In addition, the climatic effects tool Integrated Climatic Model (ICM) models temperature and moisture within each pavement layer and foundation (AASHTO, 2015). Transfer functions then predict field performance based on the

critical responses. If the trial design satisfies agency-approved performance criteria at the specific design reliability, it becomes a candidate design structure and undergoes life cycle cost analysis (LCCA) for constructability (Kim et al., 2011). The Federal Highway Administration has listed the following advantages of the M-E design approach over traditional empirical approaches (Sufian, 2016):

- Provision of agency-established performance criteria for design;
- Ability to characterize material parameters to reflect pavement performance;
- Capability to evaluate pavement damage caused by unique loading configurations or increased axle loads;
- Inclusion of seasonal variation effects; and
- Capability to consider alternate design strategies and additional design features.

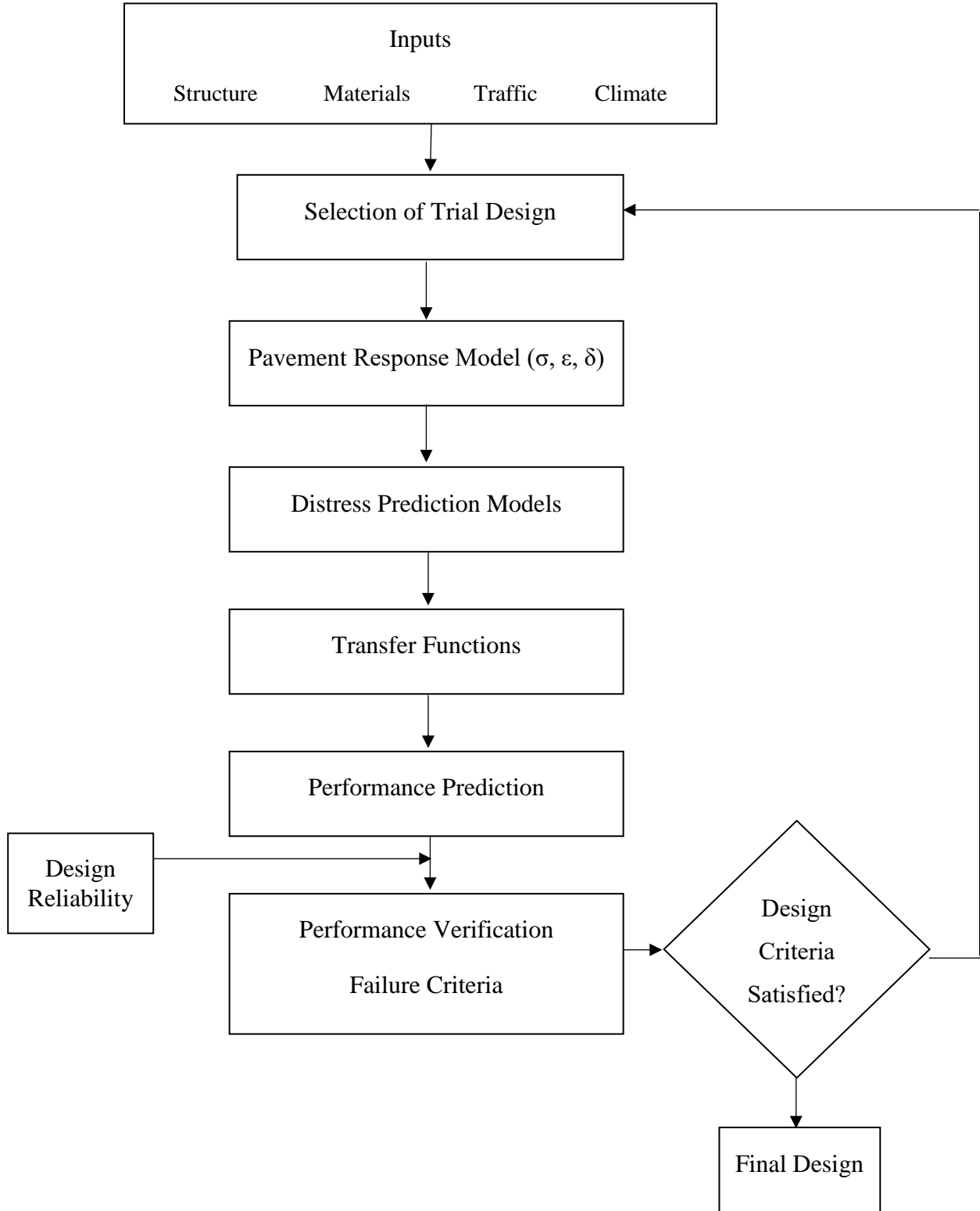


Figure 2-1 Flowchart of the AASHTOWare pavement ME design process

## **2.2 KDOT Rehabilitation Options and Design**

The most common maintenance technique for pavements exposed to moderate and heavy traffic is to place an overlay on top of existing pavement (Huang, 1993). AC overlays have commonly been placed on top of existing asphalt or concrete pavements throughout the United States because they provide a new wearing surface while advantageously utilizing the remaining fatigue life and load-carrying capacity of the existing pavement (Wargo et al., 2014). A significant amount of KDOT's rehabilitation work involves overlaying existing JPCP and AC pavements with an AC overlay.

Maintenance and rehabilitation strategies for flexible and concrete pavements are commonly categorized into three groups: routine maintenance, preventive maintenance, and pavement rehabilitation. For concrete pavement, routine maintenance includes joint and crack sealing, and preventative maintenance includes full and partial depth repair, load transfer restoration, sub-sealing and under-sealing. Rehabilitation techniques include grinding and milling, AC overlays, and Portland cement concrete (PCC) overlays. For flexible pavements, routine maintenance activities include crack sealing and patching (localized repair), and preventative maintenance activities include thin surface applications such as chip seal and ultra-thin bonded asphalt surface (UBAS). Rehabilitation techniques include hot-mix asphalt (HMA) overlays with or without cold milling, hot or cold recycling with reclaimed asphalt pavement (RAP), and PCC overlays.

Rehabilitation options in Kansas that can be designed using the AASHTOWare Pavement ME software are AC overlay on top of JPCP pavement, AC overlay on top of HMA pavement, bonded and unbonded concrete overlays over JPCP, and PCC overlay over AC pavements. The most prevalent rehabilitation techniques in Kansas are AC overlay on top of JPCP pavements and

AC overlay on top of existing AC pavements. Design considerations for AC overlay include pre-overlay repair to achieve uniform strength condition, reflection crack control, future traffic loading, milling of existing AC surfaces, and drainage improvements.

### 2.3 AASHTOWare PMED Performance Models for AC Overlay

AASHTOWare software predicts AC rutting, top-down and bottom-up fatigue cracking, thermal cracking, reflective cracking and smoothness degradation for AC-overlaid pavement sections. These performance models are briefly described in this section; more detailed description is available in the *AASHTO MEPDG Manual of Practice* (AASHTO, 2015).

#### 2.3.1 Rut depth

AASHTOWare PMED software defines rut depth as the highest difference in elevation between the transverse profile of the AC/AC surface and wire-line across the lane width (AASHTO 2015). The incremental damage approach is used to predict total rutting. For HMA mixtures, the permanent deformation model is shown in Equation 2.1.

$$\Delta_{p(HMA)} = \epsilon_{p(HMA)} h_{(HMA)} = \beta_{1r} k_z \epsilon_{r(HMA)} 10^{k_{1r}} n^{k_{2r}} \beta_{2r} T^{k_{3r}} \beta_{3r} \quad (2.1)$$

Where:

$\Delta_{p(HMA)}$  = Accumulated permanent or plastic vertical deformation in the AC (HMA) layer, in.;

$\epsilon_{p(HMA)}$  = Accumulated permanent or plastic axial strain in the AC (HMA) layer/sublayer (in./in.);

$h_{(HMA)}$  = Thickness of the AC (HMA) layer/sublayer (in.);

$\epsilon_{r(HMA)}$  = Resilient or elastic strain calculated by the structural response model at the mid-depth of each AC (HMA) layer, in;

$n$  = Number of axle-load repetitions;

$T$  = Mix or pavement temperature, °F;

$k_z$  = Depth confinement factor;

$k_{1r}, k_{2r}, k_{3r}$  = Global calibration factors (material-specific coefficients determined from repeated load tri-axial tests for permanent deformation); and

$\beta_{1r}, \beta_{2r}, \beta_{3r}$  = Local calibration coefficients.

### 2.3.2 Load-related cracking

AASHTOWare PMED software predicts two types of fatigue or load-related cracking: bottom-up alligator cracking and top-down longitudinal cracking. Fatigue damage prediction is based on the incremental damage approach, and the allowable number of axle-load applications ( $N_{f-HMA}$ ) is required to calculate the damage indices. AASHTOWare software uses the Asphalt Institute (MS-1) model to determine  $N_{f-HMA}$ , as shown in Equation 2.2.

$$N_{f-HMA} = k_{f1} (C) (C_H) \beta_{f1} (\varepsilon_t)^{k_{f2} \beta_{f2}} (E_{HMA})^{k_{f3} \beta_{f3}} \quad (2.2)$$

Where:

$\varepsilon_t$  = Tensile strain at critical locations;

$E_{HMA}$  = Dynamic modulus of HMA measured in compression, psi;

$k_{f1}, k_{f2}$ , and  $k_{f3}$  = Global field calibration coefficients (material-specific coefficients);

$\beta_{f1}, \beta_{f2}$  and  $\beta_{f3}$  = Local calibration coefficients;

$C = 10^M$ ;

$$M = 4.84 * \left( \frac{V_{be}}{V_a + V_{be}} - 0.69 \right); \quad (2.3)$$

$V_{be}$  = Effective asphalt content by volume, %;

$V_a$  = Percent air voids in HMA mixture; and

$C_H$  = Thickness correction factor.

AASHTOWare calculates the cumulative damage ( $DI$ ) by summing the incremental damage indices over time, as

$$DI = \sum (\Delta DI)_{j,m,l,p,t} = \sum \left( \frac{n}{N_{f-HMA}} \right)_{j,m,l,p,t} \quad (2.4)$$



Fatigue damage transfer functions for top-down ( $FC_{Top-Down}$ ) and bottom-up ( $FC_{Bottom-up}$ ) cracking are

$$FC_{Top-Down} = 10.56 * \left( \frac{1000}{1 + e^{C_1 - C_2 * \log DI_{top}}} \right) \quad (2.5)$$

Where:

$C_1, C_2$  = Local calibration coefficients;

And

$$FC_{Bottom-up} = \left( \frac{6000}{1 + e^{(C_1 C'_1 + C_2 C'_2 \log(DI * 100))}} \right) \quad (2.6)$$

Where:

$$C'_1 = 2 * C'_2;$$

$$C'_2 = -2.40874 - 39.748(1 + H_{HMA})^{-2.856}; \quad (2.7)$$

$H_{HMA}$  = AC layer thickness; and

$C_1, C_2$  = Local calibration coefficients.

### **2.3.3 Transverse reflection cracking model**

The transverse reflection cracking model, which was developed under the NCHRP 1-41 project, has recently been integrated into the PMED software (Titus-Glover et al., 2016). The newly developed reflection cracking model replaces the empirically derived reflection cracking model and follows a combination of finite element and fracture mechanics approaches based on the Paris Law (Lytton et al., 2010). The newly developed reflection cracking model also considers incremental crack growth due to flexure, shear, and thermal stress in the overlaid AC layer. The transverse reflective crack model is show in Equations 2.8–2.14.

$$\Delta C = k_1 * \Delta_{Bending} + k_2 * \Delta_{Shearing} + k_3 * \Delta_{Thermal} \quad (2.8)$$

$$\Delta_{Bending} = A(SIF)_B^n \quad (2.9)$$

$$\Delta_{Shearing} = A(SIF)_S^n \quad (2.10)$$

$$\Delta_{Thermal} = A(SIF)_T^n \quad (2.11)$$

$$\Delta D = \frac{c_1 k_1 1 * bending + c_2 k_2 * shearing + c_3 k_3 * thermal}{h_{OL}} \quad (2.12)$$

$$D = \sum_{i=1}^N \Delta D \quad (2.13)$$

$$RCR = \left( \frac{100}{c_4 + e^{c_5 \log D}} \right) * EX_{CRK} \quad (2.14)$$

Where:

$\Delta C$  = Crack length increment, in.;

$\Delta D$  = Incremental damage ratio;

$\Delta_{Bending}, \Delta_{Shearing}, \Delta_{Thermal}$  = Crack length increments due to bending, shearing, and thermal loading;

$k_1, k_2, k_3, c_1, c_2, c_3$  = Calibration factors;

$A, n$  = AC (HMA) material fracture properties;

$N$  = Total number of days;

$(SIF)_B, (SIF)_S, (SIF)_T$  = Stress intensity factors due to bending, shearing, and thermal loading;

$D$  = Damage ratio;

$h_{OL}$  = Overlay thickness, in.;

$RCR$  = Cracks in underlying layers, reflected, %; and

$EX_{CRK}$  = Transverse cracking in underlying pavement layers, ft/mile (transverse cracking)

= Alligator cracking in underlying layers, % lane area (alligator cracking),

### 2.3.4 Smoothness model

AASHTOWare PMED software predicts IRI based on the following equation:

$$IRI = IRI_o + C_1 * (RD) + C_2 * (FC_{total}) + C_3 * (TC) + C_4 (SF) \quad (2.15)$$

Where:

$IRI$  = Predicted IRI, in./mile;

$IRIo$  = Initial IRI after construction, in./mile;

$RD$  = Average rut depth, in.;

$FC_{total}$  = Area of fatigue cracking (combined alligator, longitudinal, and reflection cracking in the wheel path), percent total lane area. All load-related cracks are combined on an area basis; length of cracks is multiplied by 1 ft to convert length into area;

$TC$  = Length of transverse cracking, ft/mile; and

$C_1, C_2, C_3, C_4$  = Calibration factors

Site factor (SF) is based on Equation 2.16:

$$SF = AGE^{1.5} * \{ [\ln (Precip + 1) (FI+1) P_4] \} + \{ [\ln (Precip + 1) (PI+1) P_{200}] \} \quad (2.16)$$

Where:

$AGE$  = Pavement age, year;

$PI$  = Percent plasticity index of the soil;

$Precip$  = Average annual precipitation, in.;

$FI$  = Average annual freezing index, °F-days;

$P_4$  = Percent passing the 0.02 mm sieve; and

$P_{200}$  = Percent passing the 0.075 mm sieve.

## 2.4 Local Calibration Efforts of AASHTOWare PMED Software

Following the release of the MEPDG, numerous studies have been conducted at national and state levels to implement PMED software for pavement design. These studies have focused on sensitivity analysis to identify key design inputs, database development for traffic and material, verification of nationally calibrated AASHTOWare PMED models, calibration of these models,

and implementation of PMED software for routine pavement design. A brief description of these studies is provided in the following sections.

#### ***2.4.1 Local calibration of MEPDG performance models in Missouri***

The Missouri Department of Transportation (MoDOT) attempted to verify and locally calibrate MEPDG version 1.0 in 2009 (Mallela et al., 2009). The study included new and reconstructed AC and JPCP, AC over AC, and AC over JPCP sections. Materials were characterized at different hierarchical levels based on available information. For example, level 1 inputs were used for HMA unit weight and volumetric properties, level 2 inputs were used for HMA dynamic modulus, and level 3 inputs were used for HMA creep compliance and indirect tensile strength tests. An MEPDG database, modeled after the LTPP database, was developed to support the calibration effort. Traffic data from 12 permanent WIM sites, including nine LTPP WIM sites were analyzed to produce traffic inputs required by the MEPDG software. The analyzed data were compared to national default values in the software. MoDOT also performed laboratory tests to determine dynamic modulus and repeated-load permanent deformation characteristics of HMA mixes taken from the field. Results showed that the MEPDG equation for estimating level 2 dynamic modulus input works reasonably well for MoDOT HMA mixtures with modified and unmodified binders. Sensitivity analysis was also performed to study the effect of changing design input parameters on MEPDG distress and IRI models. This verification and calibration study revealed the following:

- The MEPDG software overpredicted total rutting, and a poor correlation was observed ( $R^2 = 0.32$  and  $S_e = 0.11$ ) between predicted and measured data. A fair correlation ( $R^2 = 0.52$  and  $S_e = 0.05$ ) was reported after local calibration.

- Approximately 99% of all measured alligator cracking was less than 5% of the total lane area). The researcher suggested that the nationally calibrated MEPDG model be used at the time of the study, and the model should be reevaluated when data indicated higher magnitudes of alligator cracking.
- Significant bias and standard error were found between predicted transverse cracking with global MEPDG coefficients and measured values. The local calibration coefficient  $\beta_t$  was adjusted to 0.625 from 1.5 to reduce bias. The researchers suggested use of level 1 creep compliance and tensile strength values to obtain reasonable prediction of HMA transverse cracking for routine design.
- The researchers concluded that, following local calibration, predictions were reasonable for new pavements in relatively good condition, but they suggested use of higher reliability for pavement sections older than 15 years.

#### ***2.4.2 Local calibration of MEPDG performance models in Iowa***

Several studies have been conducted to calibrate AASHTOWare prediction models and implement the software in Iowa (Ceylon et al., 2009; Ceylon et al., 2013). An initial verification study, conducted in 2009, evaluated HMA pavement rutting and IRI models with nationally calibrated coefficients and bias reported for rutting and IRI models. In 2013, MEPDG version 1.1 was used to perform local calibration in Iowa (Ceylan et al., 2013). A total of 35 HMA sections, 35 JPCP sections, and 60 HMA over JPCP sections were selected. Software inputs were collected from the Iowa DOT pavement management information system (PMIS) database, material test records, design database, and previous reports relevant to MEPDG implementation in Iowa. Linear and nonlinear optimization techniques were used to improve accuracy of the prediction models.

Traditional split sampling method was used for calibration and validation; 70% of the total sections were used for calibration, and the remaining 30% of the sections were used for validation.

The study found that the accuracy of rutting and top-down fatigue cracking predictions improved for new HMA pavement sections after local calibration. Although little or no thermal cracking was predicted when proper binder grade was used for regional climate conditions, significant thermal cracking was observed for new HMA pavement sections. The nationally calibrated bottom-up cracking model was found to be acceptable for predictions for new HMA pavements. For HMA over JPCP sections, the study reported that both rutting and alligator cracking models with globally calibrated coefficients provided good/acceptable predictions, while the locally calibrated top-down cracking model provided better predictions with lower bias and standard error. Transverse cracking model was not calibrated for HMA overlays over JPCP pavements.

In 2015, a recalibration study was conducted with the same pavement sections using the AASHTOWare PMED version 2.1.24 (Ceylan, 2015). The objectives of this study were to evaluate the accuracy of nationally calibrated and previously calibrated MEPDG performance models and to recalibrate performance models, if necessary. Researchers reported that the AASHTOWare PMED software significantly increased the accuracy of rutting and IRI models with locally calibrated coefficients compared to the nationally calibrated and previously calibrated MEPDG models for AC over JPCP pavements. The subsequent calibration effort also reported improved accuracy of the top-down fatigue cracking model. Because the Iowa DOT PMIS database distinguishes between thermal and reflective cracking for AC overlaid sections, this study considered measured transverse cracking data for such sections to be thermal cracking and thereby only calibrated the thermal cracking model.

### ***2.4.3 Calibration and implementation of MEPDG in Colorado***

MEPDG version 1 was used for a calibration and implementation study for the Colorado Department of Transportation (CDOT) in 2013 (Mallela et al., 2013). The principal objective of the study was to incorporate the MEPDG guide and the accompanying software into routine pavement design, management, and forensic analysis practices. A total of 127 new and rehabilitated pavement projects were selected from the LTPP and CDOT pavement management system database. MEPDG input parameter characterization involved reviewing traffic, climate, and other relevant data records; laboratory testing materials to determine strength and modulus; and conducting field surveys, destructive, and nondestructive testing of in-service pavements to assess condition. Alligator cracking, rutting, transverse cracking, and IRI models were verified and recalibrated for Colorado conditions for new and rehabilitated flexible pavements. Nonlinear optimization technique was used to calibrate MEPDG prediction models and reasonable goodness of fit was determined using diagnostic statistics  $R^2$  and  $S_e$ . The criteria to determine model accuracy for Colorado conditions are presented in Table 2-1. In addition, design comparisons and sensitivity studies were conducted to establish confidence in pavement design results using the MEPDG. Researchers recommended establishing an enterprise-level database of CDOT default inputs to cover performance criteria, reliability, traffic, climate, materials, and soils.

Table 2-1 Criteria for determining global model adequacy for Colorado conditions

Criterion of Interest	Test Statistic	Range of $R^2$ and Model $S_e$	Rating
Goodness of fit	$R^2$ , percent (all models)	81 to 100	Very good (strong relationship)
		64 to 81	Good
		49 to 64	Fair
		< 49	Poor (weak or no relationship)
	Global HMA transverse cracking model $S_e$ , percent	< 5	Good
		5 to 10	Fair
		> 10	Poor
	Global HMA transverse cracking model $S_e$	-	N/A
	Global HMA total rutting model $S_e$ , in	< 0.1	Good
		0.1 to 0.2	Fair
		> 0.2	Poor
	Global HMA IRI model $S_e$ , in/mil	< 19	Good
		19 to 38	Fair
> 38		Poor	
Bias	Hypothesis testing of slope ( $b_1$ ) of the linear measured vs predicted distress/IRI model; $H_o : b_1 = 0$	$p$ -value	Reject if $p$ -value is < 0.05 (i.e., 5% significant level)
	Paired $t$ -test between measured and predicted distress/IRI	$p$ -value	Reject if $p$ -value is < 0.05 (i.e., 5% significant level)

#### 2.4.4 Calibration and implementation of MEPDG in Arizona

Local calibration of MEPDG software was conducted for Arizona conditions in a study sponsored by the Arizona Department of Transportation (ADOT) (Darter et al., 2014). A total of 180 pavement sections, including 119 LTPP test sections, were selected for this study. The selected pavement types were new HMA pavement, AC overlay over existing AC pavement, new JPCP, new composite (AC overlaid JPCP), and AC overlay (old, intact JPCP and fractured JPCP).



Software input parameters were obtained from the LTPP database, ADOT files and videos, and field surveys conducted by the research team. Material properties were characterized at different hierarchical levels based on available information. For example, level 1 inputs were used for HMA creep compliance, while level 3 inputs were used for effective binder content. Traditional split sampling method was used for calibration and validation; 10% of the sections were used for validation. Statistical software SAS was used to determine local calibration coefficients. The researchers reported notable improvement of goodness of fit and bias reduction in prediction models after local calibration.

#### ***2.4.5 Local calibration of MEPDG for flexible pavements in North Carolina***

MEPDG version 1 was used to calibrate and validate rutting and alligator cracking models in North Carolina in 2008 (Muthadi et al., 2008). Fifty-three flexible pavement sections were selected from the LTPP and North Carolina Department of Transportation (NCDOT) databases. Another study was conducted in 2011 to calibrate rutting and alligator cracking models using MEPDG software version 1.1 (Kim et al., 2011). A total of 46 pavement sections were chosen for this study, including 22 LTPP sites used for calibration. Material-specific global field calibration coefficients in the rutting model and fatigue model coefficients were determined for 12 most commonly used asphalt mixtures in North Carolina. Repeated load tri-axial permanent deformation and viscoelastic continuum damage fatigue tests were conducted in the laboratory to develop material-specific coefficients for the rutting and fatigue cracking models, respectively. For subgrade soil characterization, a GIS-based methodology was developed to accurately identify road sections of interest on NCHRP 9-23 soil maps and extract related soil information. Two optimization techniques were used for calibration: the generalized reduced gradient (GRG) method and the genetic algorithm (GA) method. The latter yielded statistically better rutting and alligator

cracking predictions. Model adequacies of the prediction models were evaluated using  $R^2$ ,  $S_e$ ,  $S_e/S_y$ , and the  $p$ -value for the null hypothesis (average bias is zero) at 95% confidence level. Although the bias and  $S_e$  were less than the global counterparts after local calibration, this improvement was not significant enough to accept (fail to reject) the null hypothesis at 95% confidence level. For future calibration efforts, researchers recommended checking reasonableness of MEPDG assumptions when assigning observed surface pavement deformations to each layer and to differentiate between bottom-up and top-down fatigue cracks.

#### ***2.4.6 MEPDG calibration for pavement rehabilitation in Oregon***

A study for local calibration of MEPDG was done for the Oregon Department of Transportation (Oregon DOT) in 2013 (Williams et al., 2013). Since a majority of pavement work conducted by the Oregon DOT involves rehabilitation, the main focus of the study was to verify and calibrate prediction models in MEPDG for rehabilitated pavements. Forty-four pavement sections were selected to account for geographical diversity in Oregon (i.e., coastal, valley, and eastern), and the pavement types included HMA over aggregate base, HMA inlay or overlay over aggregate base, HMA inlay or overlay over cement-treated base (CTB), and HMA over CRCP. The principal objective of this research was to provide Oregon DOT with performance models embedded in the MEPDG software that can predict alligator cracking, longitudinal cracking, rutting, and thermal cracking calibrated to Oregon conditions. Verification results showed significant bias between the measured and predicted distresses using nationally calibrated coefficients. Local calibration was conducted for rutting, alligator cracking, longitudinal cracking, and thermal cracking models; the IRI model was not calibrated in this study. After local calibration, the rutting and alligator cracking prediction models showed improved predictions with lower bias and standard error than the nationally calibrated models. A high degree of variability between

measured and predicted data was reported for the longitudinal and thermal cracking models even after local calibration.

#### ***2.4.7 MEPDG local calibration effort in Louisiana***

Several studies have evaluated MEPDG performance models for Louisiana. The first research project, conducted in 2012, investigated only new and full-depth rehabilitated (with a reconstructed base) flexible pavements (Wu et al., 2012). A follow-up project was conducted in 2016 to locally calibrate and validate the AASHTOWare PMED software in Louisiana (Wu et al., 2016). Eighty-four pavement sections were selected from the Louisiana Department of Transportation and Development (LADOTD) highway network. The pavements types were flexible pavements with HMA base, rubblized PCC base, crushed stone or recycled PCC base, soil cement base, and stabilized base with stone interlayer; rigid pavements with unbound granular base and asphalt mixture blanket base; and HMA overlay on top of existing flexible pavements. Software input parameters were obtained from network-level data sources at LADOTD, and a default input strategy reflecting LaDOTD's pavement design practices and conditions was developed for the software based on an extensive sensitive analysis of key parameters. Verification analysis indicated that the PMED software generally under-predicted alligator cracking but over-predicted rutting for flexible pavements with nationally calibrated coefficients. Local calibration was carried out to reduce bias and standard error, and implementation guidelines were developed for routine design and analysis for new and rehabilitated pavement structures in Louisiana.

#### ***2.4.8 Local calibration and implementation of MEPDG in Michigan***

Several studies have been conducted to evaluate, calibrate, and validate MEPDG performance models in Michigan. In 2008, the first research project conducted a sensitivity analysis to investigate key input parameters and validate the performance models in MEPDG

(Buch et al., 2008). In addition, extensive research was conducted to characterize traffic and pavement materials in Michigan, including quantifying concrete mix coefficient of thermal expansion (Buch et al., 2008), evaluating rehabilitation measures in Michigan (Buch et al., 2013), characterizing truck traffic in Michigan (Buch et al., 2009), and characterizing HMA mixtures (Kutay et al., 2013). A local calibration study, conducted in 2015, considered 20 JPCP and 108 HMA reconstruction projects and 41 rehabilitation projects (Brink, 2015). Five types of sampling techniques were used to improve accuracy of the calibrated performance models: no sampling, traditional split sampling, repeated split sampling, jackknifing, and bootstrapping. Calibrated models derived from the bootstrapping sampling technique consistently showed lower standard error and bias. Top-down longitudinal cracking, bottom-up alligator cracking, thermal cracking, rutting, and IRI models were calibrated for flexible pavements, and the calibrated performance models were shown to significantly improve predictions for Michigan conditions. Researchers recommended that local calibration of the prediction models be conducted every six years.

#### ***2.4.9 Local calibration of MEPDG for northeastern United States***

A verification and calibration study of the MEPDG was conducted for northeastern states of the United States in 2011 (Momin, 2011). The study was sponsored by the New York State Department of Transportation and carried out at the University of Texas at Arlington. Seventeen LTPP pavement sections were selected from Connecticut, Maine, Massachusetts, New Jersey, Pennsylvania, Vermont, New Hampshire, and New York. Design input parameters were obtained from the LTPP database, and predicted distress data were compared to LTPP measured data from the selected sites. MEPDG version 1.1 was used in the study. Significant differences were observed between measured and predicted distresses (with nationally calibrated models), and local calibration was performed to minimize the differences. Simple linear regression with no intercept

was performed for each pavement layer to calibrate the rutting model, and a new set of model coefficients was proposed for AC, granular base, and subgrade soil layer. Coefficients of top-down and bottom-up fatigue cracking models were derived from fatigue damage output generated from the software. A simple linear regression was used to calibrate the IRI model by computing model coefficients based on relevant distresses.

## **Chapter 3 - Methodology**

Processes for verification, calibration, and validation of performance prediction models in the AASHTOWare PMED software are described in this chapter. Furthermore, Kansas truck traffic characterization, pavement materials, and climatic input parameters are discussed in detail, and analysis of KDOT automated distress survey data is presented.

### **3.1 NCHRP 1-40B Calibration Steps**

The local calibration guide for AASHTOWare PMED software, developed under NCHRP project 1-40B, outlined an 11-step procedure for local calibration (AASHTO, 2010).

*Step 1: Select hierarchical input level for each input parameter*

The AASHTOWare Pavement ME software allows users to input layer material properties and traffic input parameters at three hierarchical levels. The hierarchical approach offers substantial flexibility for obtaining design inputs based on available resources. Level 1 inputs, which represent the highest level of accuracy and the lowest level of input errors, are project-specific with extensive laboratory test results and precisely counted traffic volume, distribution, and axle load spectra. Dynamic modulus testing of HMA or site-specific average annual daily truck traffic (AADTT) is an example of level 1 input (Williams et al., 2013). Such extensive testing and data collection, however, require significant resource allocation. Level 2

input represents an intermediate level of accuracy and can be estimated from correlations or regression equations, such as estimating PCC elastic moduli from the compressive strength test or calculating soil resilient moduli from the Dynamic cone penetration (DCP) or California bearing ratio (CBR) tests. Level 3 inputs are based on global default values in the software. These inputs are user-selected, typical average values or best-estimated values, such as default soil resilient modulus values for a particular soil type, or Poisson's ratio for a particular material type. Level 3 input has the least accuracy but requires least resource allocation for material testing and data collection.

Input level selection is a policy decision dependent on an agency's construction practices and specifications. This selection is extremely important for local calibration since errors associated with each input parameter contribute to the final standard error of the distress models and reflect upon material quality requirements and construction costs (AASHTO, 2010).

*Step 2: Develop local experimental plan and sampling template*

The second step in the local calibration and validation process develops a detailed sampling template based on an agency's construction practice and design specification. The experimental design should consider typical pavement type and thickness, traffic level, and climatic condition for the region. The sampling template could be a full factorial or fractional factorial design depending on the number of roadway segments for each combination.

*Step 3: Estimate sample size for specific distress prediction models*

The third step involves estimating the minimum number of roadway projects required to conduct local calibration and validation of distress models in the PMED software. AASHTO suggests the following equations for estimating the number of roadway segments ( $N$ ) for calibration and validation:

$$N \geq \left( \frac{t^* S_y}{e_t} \right)^2 \quad (3.1)$$

$$N = \left( \frac{Z_{\alpha^*} \sigma}{e_t} \right)^2 \quad (3.2)$$

$$\frac{S_e}{S_y} \geq \left[ \frac{\chi_{\alpha^2}}{N-1} \right]^{0.5} \quad (3.3)$$

Where:

$S_y$  = standard deviation of the measured distress;

$S_e$  = standard deviation of bias between measured and predicted distress;

$\alpha$  = performance indicator threshold value or level of significance at typical agency design reliability level;

$\chi^2$  = chi-square value based on degree of freedom and  $\alpha$  level of significance;

$Z$  = standard normal deviate based on degree of freedom and  $\alpha$  level of significance;

$t$  =  $t$  distribution value based on the degree of freedom and level of significance; and

$e_t$  = tolerable bias between measured and predicted distresses.

Equations 3.1 and 3.2 estimate the sample size based on the mean or bias between measured and predicted distresses, while Equation 3.3 estimates sample size based on variance or precision (Abdullah et al., 2015). AASHTO suggests the level of significance to be 90% as the practical level for determining the sample size for calibration.

#### *Step 4: Select roadway segments*

Step 4 populates the sampling template developed in step 3. The selected projects should be representative of an agency's design and construction practices and should be spread throughout the agency's administrative region (Darter et al., 2014). Roadway segments should consist of the least number of structural layers and materials to reduce the amount of testing and input required for material characterization (AASHTO, 2010). The selected projects also should

have similar time intervals between distress measurements, and at least three condition surveys should be available for each roadway segment (AASHTO, 2010).

*Step 5: Extract and evaluate distress and project data*

Input data for each project are collected and verified in step 5. In addition, distress data are extracted, preferably from the agency's pavement management system database, and the compatibility of distress data with PMED software requirements are ensured. The local calibration guide developed under NCHRP 1-40 B categorizes step 5 into four activities (AASHTO, 2010):

- I. Extract distress data and review the measured data to determine whether the distress data are consistent with values predicted by the software.
- II. Compare the performance data to trigger values or design criteria used by the agency.
- III. Evaluate the distress data for anomalies and outliers.
- IV. Determine input parameters for the software. The local calibration guide lists possible data sources that could be used in the calibration process. These sources are construction records, quality control and quality assurance database, and as-built construction plans.

*Step 6: Conduct field and forensic investigations*

Step 6 involves field sampling and material testing to obtain missing data and verify key inputs for the selected projects. Field and forensic investigations include extracting cores from asphalt pavements to determine initiation of crack propagation (top-down versus bottom-up) and measuring rutting in individual layers. Resource constraints require an agency to decide what, if any, forensic investigations are required. Field and forensic investigations are not necessary if the agency accepts the assumptions embedded in the software.



*Step 7: Assess local bias by applying globally calibrated values to local conditions, policies, and materials*

The principal goal of distress and IRI model calibration is to reduce or eliminate the bias between software-predicted and measured distress data since a biased model in the AASHTOWare PMED software will produce oversized or under-designed pavements (AASHTO 2010). Step 7 compares predicted and measured distresses to determine the bias and validate each distress prediction model for local conditions, policies, specifications, and materials (AASHTO, 2010).

The null hypothesis for the sampling template should be evaluated to determine bias. A paired *t*-test is often used to determine the presence of significant bias at a specified confidence level (AASHTO, 2010). The null hypothesis is

$$H_0 : \sum_{i=1}^n (y_{measured} - x_{predicted}) = 0 \quad (3.4)$$

Where:

$y_{measured}$  = measured value, and

$x_{predicted}$  = predicted value by AASHTOWare PMED software.

The local calibration guide suggests the use of two other model parameters to fully evaluate model bias, the intercept ( $b_o$ ) and slope ( $m$ ), from the following fitted linear regression model between  $y_{measured}$  and  $x_{predicted}$  values.

$$\hat{y}_i = b_o + m(x_i) \quad (3.5)$$

The intercept ( $b_o$ ) and slope ( $m$ ) are used in hypothesis testing as follows:

$$H_0 : b_o = 0 \quad (3.6)$$

$$H_0 : m = 1.0 \quad (3.7)$$

*Step 8: Eliminate local bias of distress prediction models*

If significant bias exists between predicted and measured distresses, the cause of bias must be determined and eliminated via local calibration (Haider et al., 2014). The processes for eliminating or reducing bias depend on the bias sources and desired accuracy. NCHRP 1-40 B project lists three scenarios of bias manifestation (AASHTO, 2010):

- I. If residual errors from measured and predicted distresses are consistently positive or negative with low  $S_e$  compared to the agency-specified trigger value and the slope of residual errors versus predicted values is relatively constant and close to zero, then the precision of the prediction model is reasonable, but the accuracy is poor. This condition generally requires the least amount of effort and the least number of AASHTOWare software runs to reduce bias. In this situation, coefficients of the transfer function must be adjusted to eliminate bias.
- II. If the bias is low and relatively constant with the time or number of loading cycles and the residual errors have a wide dispersion varying from positive to negative values, then model accuracy is reasonable, but precision is poor. In this scenario, coefficients of the transfer functions must be modified. However, these coefficients could be dependent on site features, material properties, or design features in the sampling template. This situation requires more AASHTOWare runs and increased effort to reduce dispersion of residual errors.
- III. If residual errors versus predicted values exhibit a significant and variable slope and the slope seems to be dependent on the predicted value, then the precision of the predictive model is poor, the accuracy is time dependent, and the correlation between measured and predicted distresses is very poor. This is the most complex scenario for calibrating the

prediction model since this condition requires the highest level of effort and the greatest number of software runs.

The NCHRP 1-40B study recommended calibration parameters for a transfer function that should be adjusted to eliminate bias between the measured and predicted data (AASHTO, 2010). Table 3-1 lists these suggested coefficients. However, additional calibration parameters in a transfer function may need adjustments since these parameters are dependent on site factors, layer properties, and agency policies.

Table 3-1 Adjusted flexible pavement transfer function calibration parameters to eliminate bias and reduce standard error (AASHTO, 2010)

Distress		Eliminate bias	Reduce standard error
Total rutting	Unbound materials and HMA layers	$K_{r1}, \beta_{s1}, \text{ or } \beta_{r1}$	$K_{r2}, K_{r3}, \text{ and } \beta_{r2}, \beta_{r3}$
Load-related cracking	Alligator cracking	$C_2 \text{ or } k_{f1}$	$k_{f2}, k_{f3}, \text{ and } C_1$
	Longitudinal cracking	$C_2 \text{ or } k_{f1}$	$k_{f2}, k_{f3}, \text{ and } C_1$
	Semi-rigid pavements	$C_2 \text{ or } \beta_{c1}$	$C_1, C_2, C_4$
Non-load-related cracking	Transverse cracking	$\beta_{t3}$	$\beta_{t3}$
IRI		$C_4$	$C_1, C_2, C_3$

*Step 9: Assess the standard error of the estimate*

Step 9 determines the  $S_e$  from the locally calibrated dataset; this  $S_e$  must then be compared to the  $S_e$  computed from the globally calibrated dataset. Models with local  $S_e$  values higher than global  $S_e$  values should be recalibrated to lower the standard error (Robbins et al., 2017). However, an agency can decide to accept the higher standard error from the locally calibrated model if it is within the agency's acceptable limit. The NCHRP 1-40B report listed reasonable values of standard error for each distress transfer function (AASHTO, 2010). These values are also provided in Table 3-1.

*Step 10: Reduce standard error of the estimate*

High standard error of the prediction models can lead to overly conservative design at higher reliability. In such cases, the agency can decide to revise the locally calibrated parameters in the transfer function. Of the four components of standard error, calibration can reduce only the lack-of-fit or model error.

*Step 11: Interpret results and determine adequacy of calibration parameters*

Step 11 evaluates the locally calibrated distress and IRI models at different reliability levels. Pavement sections analyzed with locally calibrated AASHTOWare PMED software should be reviewed if the expected design life is reasonable for agency performance criteria and reliability levels (Robbins et al., 2017). The agency also must decide whether the predicted design thicknesses make sense given historical performance of in-service pavement sections.

### **3.2 Application of NCHRP 1-40B Calibration Procedures to Kansas Conditions**

Despite the detailed recommendations listed in the NCHRP 1-40B report, local calibration efforts conducted by state highway agencies do not always follow the suggested guidelines (Robbins et al., 2017). For example, the local calibration guide recommends determining the minimum number of projects to verify and calibrate PMED performance models, assuming that, for local calibration, state highway agencies should use level 1 and level 2 inputs to reflect local materials, conditions, and practices. However, such detailed input may not be available for the required number of projects. Table 3-2 presents AASHTO-suggested required number of pavement section for validation and calibration of PMED performance models for various distress types.

Table 3-2 Minimum sample size guidelines for local calibration of distress models (Haider et al., 2014)

Distress type	Number of pavement sections
Distortion-rutting and faulting	20
Load-related cracking	30
Non-load-related cracking	26
Reflective cracking (HMA surfaces only)	26

As shown in Table 3-2, at least 26 pavement sections are required for verification and calibration of the reflective cracking model of the AASHTOWare software. In addition, the calibration guide suggests that each considered section should have at least three condition surveys. Since maintenance activities are more frequent for rehabilitated pavements than new pavements, finding HMA-overlaid pavement sections with three or more condition surveys is difficult. This study selected 25 AC over AC sections based on the following project selection criteria and in consultation with KDOT:

- Projects in which existing highway segment construction occurred in 1995 or later to ensure that required Pavement ME input information was available in the KDOT construction management system (CMS)
- Projects in which less than five overlays occurred during the life of the existing pavement structure
- Projects that contain a minimum 1-in. HMA overlay on top of the existing HMA pavement and a minimum 1.5-in. overlay on top of the existing AC section
- Projects that encompass all six districts of KDOT

The selected project locations are shown in Figure 3-1, and general features of these projects are listed in Table 3-3.

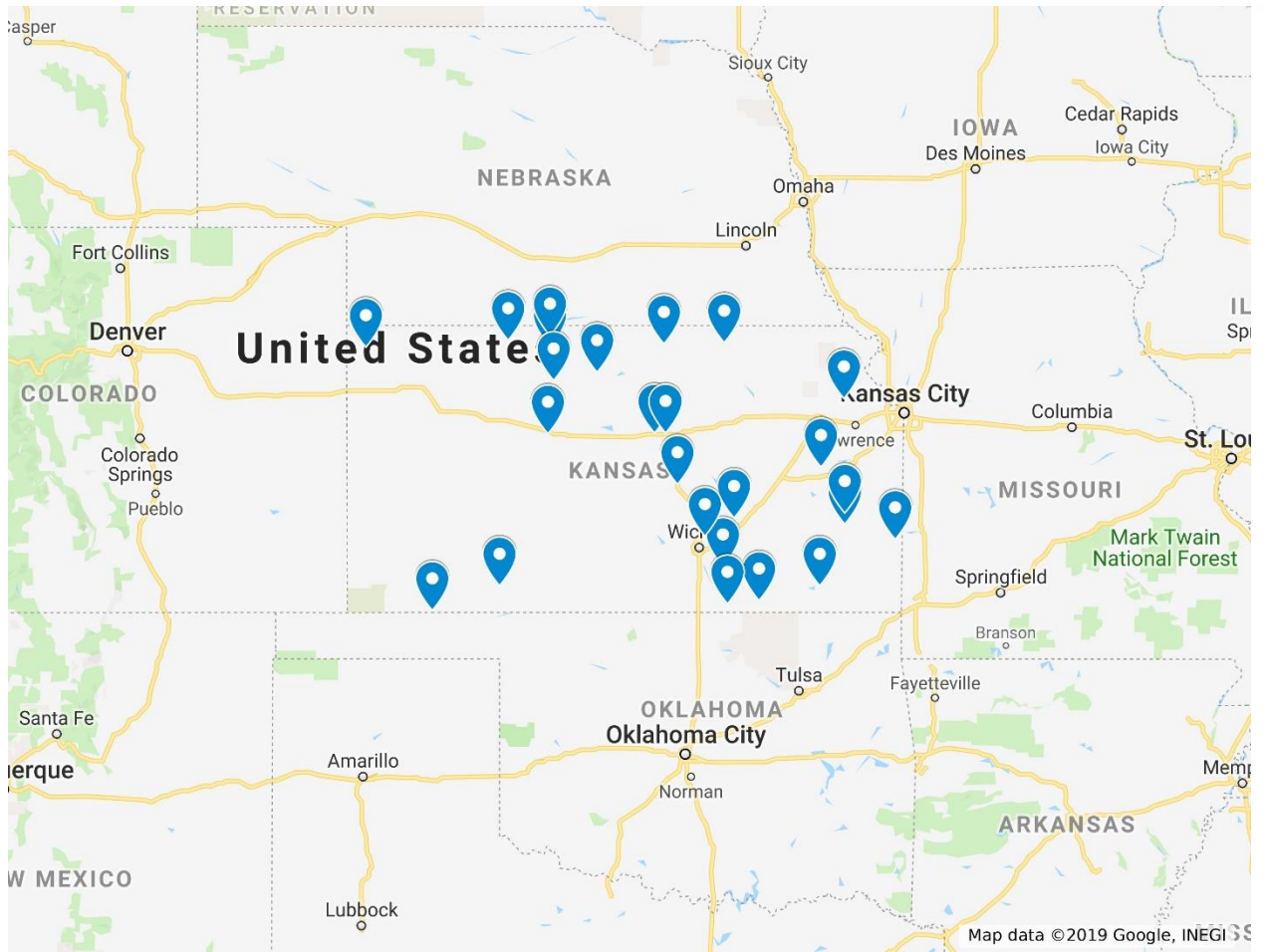


Figure 3-1 Locations of selected AC over AC projects across Kansas

Table 3-3 General descriptions of selected AC over AC projects in Kansas

No.	Project Name	Route	County	Begin milepost	End milepost	Length (mile)
1	KA-2628-01	I-70	Saline	0.000	8.000	8.00
2	KA-9466-01	I-70	Saline	8.000	15.000	7.00
3	KA-4013-01	US-24	Osborne	23.000	30.000	7.00
4	KA-1436-01	US-36	Cheyenne	14.029	19.000	4.97
5	KA-2188-01	US-36	Republic	7.000	8.101	1.101
6	KA-0813-01	US-36	Washington	17.269	26.445	9.176
7	K-0657-01	US-69	Bourbon	6.009	9.603	3.6
8	KA-0811-01	US-75	Montgomery	27.000	31.000	4.00
9	KA-0310-01	US-75	Osage	7.000	12.738	5.738
10	KA-4192-01	US-77	Butler	0.000	12.000	12.00
11	KA-2941-01	US-77	Butler	43.558	50.671	7.11
12	KA-2923-01	US-81	McPherson	0.000	2.562	2.56
13	K-8431-01	US-83	Seward	1.000	6.000	5.00
14	KA-1480-01	US-160	Clark	6.000	1.000	5.00
15	K-7756-01	US-166	Chautauqua	0.000	5.000	5.00
16	KA-1460-01	US-166	Cowley	13.145	19.145	6.00
17	KA-2200-01	US-169	Allen	14.897	22.941	8.044
18	KA-2204-01	US-169	Anderson	0.000	4.153	4.15
19	KA-2966-01	US-183	Ellis	0.000	3.000	3.00
20	KA-2505-01	US-183	Rooks	20.315	22.332	2.02
21	KA-1444-01(1)	US-183	Phillips	15.050	22.000	6.95
22	KA-1444-01(2)	US-183	Phillips	23.000	32.753	9.75
23	KA-3674-01	US-283	Norton	20.790	32.049	11.26
24	K-9364-01	K-92	Jefferson	8.000	12.738	4.738
25	KA-3496-01	K-254	Sedgwick	5.000	10.319	5.32

This study selected 18 AC over JPCP sections based on the following project selection

criteria:

- Projects that were overlaid after 2000
- Projects in which the existing JPCP surface did not experience diamond grinding
- Projects with less than five overlays during the life of the existing pavement structure
- Projects that contain an HMA overlay on top of existing concrete pavement
- Projects should encompass all six districts of KDOT

Selected project locations are shown in Figure 3-2, and general project features are listed in

Table 3-4.

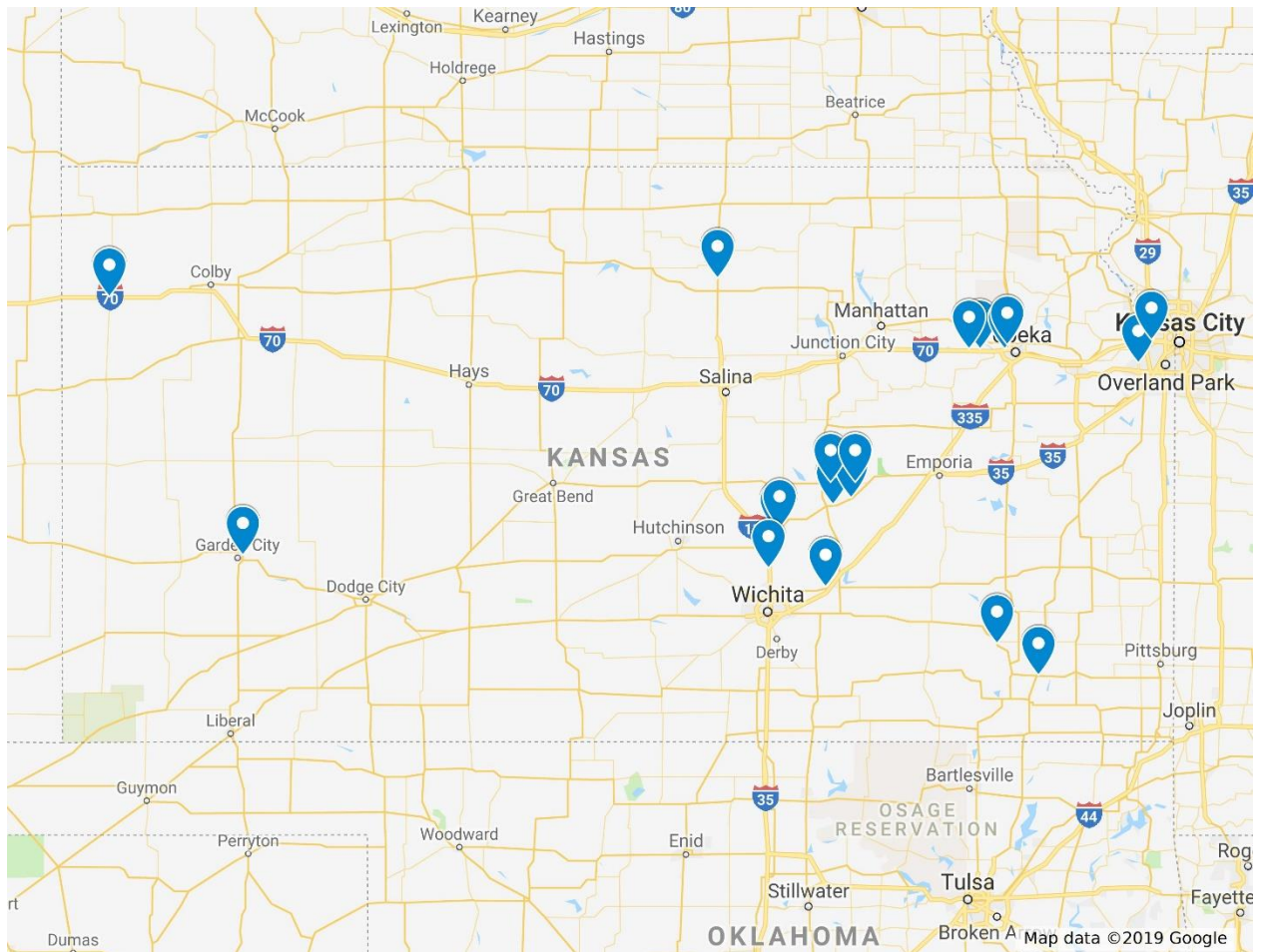


Figure 3-2 Locations of selected AC over JPCP projects across Kansas



Table 3-4 General descriptions of selected AC over JPCP projects in Kansas

No.	Project Name	Route	County	Begin milepost	End milepost	Length (mile)
1	KA-2836-01	I-70	Shawnee	0.000	4.000	4.00
2	KA-4136-01	I-70	Shawnee	11.000	15.657	4.66
3	KA-4036-01	I-70	Sherman	17.142	27.000	9.86
4	KA-2835-01	I-70	Wabaunsee	20.000	24.009	4.00
5	KA-3282-01	I-70	Wyandotte	8.000	12.000	4.00
6	KA-4236-01	I-135	Harvey	0.000	7.015	7.02
7	KA-1950-01	US-50	Marion	16.126	20.995	4.87
8	KA-1951-01	US-50	Chase	0.000	9.000	9.00
9	KA-0378-01(1)	US-50	Harvey	28.641	35.560	6.92
10	KA-0378-01(2)	US-50	Harvey	27.000	28.641	1.64
11	KA-2669-01	US-54	Shawnee	17.841	20.326	2.49
12	KA-1931-01	US-81	Cloud	0.000	16.000	16.00
13	KA-3848-01	US-400	Labette	0.000	8.807	8.81
14	K-7823-01	K-7	Johnson	18.687	20.955	2.27
15	KA-2681-01	K-57	Marion	0.000	8.008	8.01
16	KA-2682-01	K-150	Chase	0.000	8.637	8.64
17	KA-3006-01	K-156	Finney	1.936	3	1.06
18	KA-2001-01	K-254	Butler	11.882	14.309	2.43

### 3.3 Hierarchical Input Level

Hierarchical level of inputs must be selected to characterize as-constructed pavements in the PMED software because performance model predictions directly rely on input parameter selection (Haider et al., 2014). Many studies have attempted to identify sensitive input parameters that affect pavement performances. Pavement cross sections and layer moduli have been shown to be sensitive in predicting performances for all pavement types (NCHRP 1-37A,

2004), as have truck traffic volume and loading (Li et al., 2009). A sensitivity study conducted in Michigan for AC pavement rehabilitation with AC overlay observed that existing pavement condition rating prior to overlay and thickness of overlay are critical for all performance measures (Buch et al., 2013). In addition, percent air void in the AC overlay and the interaction between existing pavement condition and overlay effective binder content were found to be sensitive in determining fatigue cracking. Accuracy of the calibrated PMED models significantly rely on the available pavement cross section, material, traffic, and pavement performance data (Haider et al., 2014).

Selection of the hierarchical level of input parameters is essential since software calibration with inaccurate input parameters would yield overdesigned or under-designed pavements. Best available input level has been used in this study for the selected pavement sections. The input selection procedure for traffic, layer materials, climate, and pavement cross sections is discussed in the following sections.

### **3.4 Traffic Input**

Traffic data is one of the primary inputs for design and analysis of pavement structures. AASHTOWare PMED software, which requires axle load spectra to represent loads from mixed traffic, are derived from traffic data collected at WIM stations (Islam et al, 2017). These spectra represent the percentage of total axle load applications within designated load intervals for single, tandem, tridem, and quad axles. In addition, seasonal and hourly traffic variations are also required and represented as monthly adjustment factor (MAF) and hourly distribution factor (HDF), respectively. These factors are computed by continuous vehicle count and AVC data recorded by vehicle classification stations. However, Kansas collects WIM data for shorter durations at specific sites in Kansas.

In addition to traffic volume adjustment factors (MAFs and HDFs), the following vehicle class factors (VCFs), axle load distribution factors, and several other traffic inputs are also required for the AASHTOWare PMED software (NCHRP 1-37A, 2004):

- Initial two-way AADTT
- Percentage of trucks in the design direction and design lane
- Traffic growth factors
- Vehicle operation speed
- Axle and wheelbase configurations

Traffic inputs embedded in the AASHTOWare PMED software estimate loads applied throughout the design life of the pavement. Since site-specific level 1 traffic inputs are difficult to generate for every design project throughout the state, statewide level 2 inputs based on similar characteristics for the traffic stream must be developed. Haider et al. (2011) analyzed data collected from 44 WIM stations and 51 AVC stations and developed level 2 inputs for Michigan using the Ward's method of cluster analysis. Romanoschi et al. (2011) collected WIM and AVC data for New York state from 2004 to 2009 and found that HDF and MAF values vary significantly from AASHTOWare default values. They also discovered significant differences between state average axle load spectra and nationally recommended values. Ahn et al. (2008) developed axle load spectra for Arizona and concluded that Arizona default distribution factors perform better than national default distribution factors.

The current study developed traffic volume adjustment factors from 11 AVC stations and axle load spectra and axle group per vehicle (AGPV) from 10 WIM stations to use as input parameters for design analysis of pavement structures in Kansas. Tables 3-5 and 3-6 list brief descriptions of WIM and AVC sites, respectively, used in this study.

Table 3-5 WIM stations used in this study

WIM Station	County	Route	Functional Classification
2WOA86	Seward	US-54	Rural principal arterial
3MXC22	Meade	US-54	Rural principal arterial
2OPUF5	Logan	US-83	Rural principal arterial
4LGSU3	Thomas	I-70	Rural interstate
9M4PS3	Saline	I-70	Rural interstate
9ORQP1	Sedgwick	I-135	Urban interstate
9Q9OK1	Sedgwick	I-135	Urban interstate
BWGAA6	Lyon	I-35	Urban interstate
DVMSP3	Douglas	I-70	Urban interstate
F07WC7	Wyandotte	I-70	Urban interstate

Table 3-6 AVC stations used in this study

AVC Station	County	Route	Functional Classification
7XRME7	Kingman	US-54	Rural principal arterial
61ILJ3	Kiowa	US-54	Rural principal arterial
91TFY5	Republic	US-81	Rural principal arterial
AW9N83	Butler	US-400	Rural principal arterial
CTQ1D1	Brown	US-36	Rural principal arterial
CV64B3	Montgomery	I-166	Rural principal arterial
F10VD5	Bourbon	US-61	Rural principal arterial
0DT453	Sherman	I-70	Rural principal arterial
7HOM63	Russel	I-70	Urban principal arterial
9LON61	Sedgwick	I-235	Urban principal arterial
9Q9OK1	Sedgwick	I-135	Urban principal arterial

This study developed HDF and MAF values and level 2 traffic inputs from data collected from the 11 AVC sites. AGPV and axle load spectra were also developed for rural and urban roadways in Kansas.

### ***3.4.1 Vehicle class factors***

VCFs refer to the frequency of trucks in each class from class 4 to class 13 (NCHRP 1-37A, 2004). Federal Highway Administration (FHWA) vehicle classes are shown in Figure 3-3. This study developed VCFs for rural and urban roadways from data generated by the AVC stations listed in Table 3-6. Figure 3-4 shows that, although average VCF values of rural roadways are close to default values in the PMED software, average VCF values for urban roadways in Kansas vary from AASHTOware PMED default values, with a higher frequency of vehicle classes 4 and 9 on Kansas urban principal arterials.

































<b>Class 1</b> Motorcycles		<b>Class 7</b> Four or more axle, single unit	
<b>Class 2</b> Passenger cars		<b>Class 8</b> Four or less axle, single trailer	
			
			
			
<b>Class 3</b> Four tire, single unit		<b>Class 9</b> 5-Axle tractor semitrailer	
			
			
<b>Class 4</b> Buses		<b>Class 10</b> Six or more axle, single trailer	
			
			<b>Class 11</b> Five or less axle, multi trailer
<b>Class 5</b> Two axle, six tire, single unit		<b>Class 12</b> Six axle, multi-trailer	
			
			<b>Class 13</b> Seven or more axle, multi-trailer
<b>Class 6</b> Three axle, single unit			
			
			

Figure 3-3 FHWA vehicle classification (Traffic monitoring guide, FHWA, 2016)

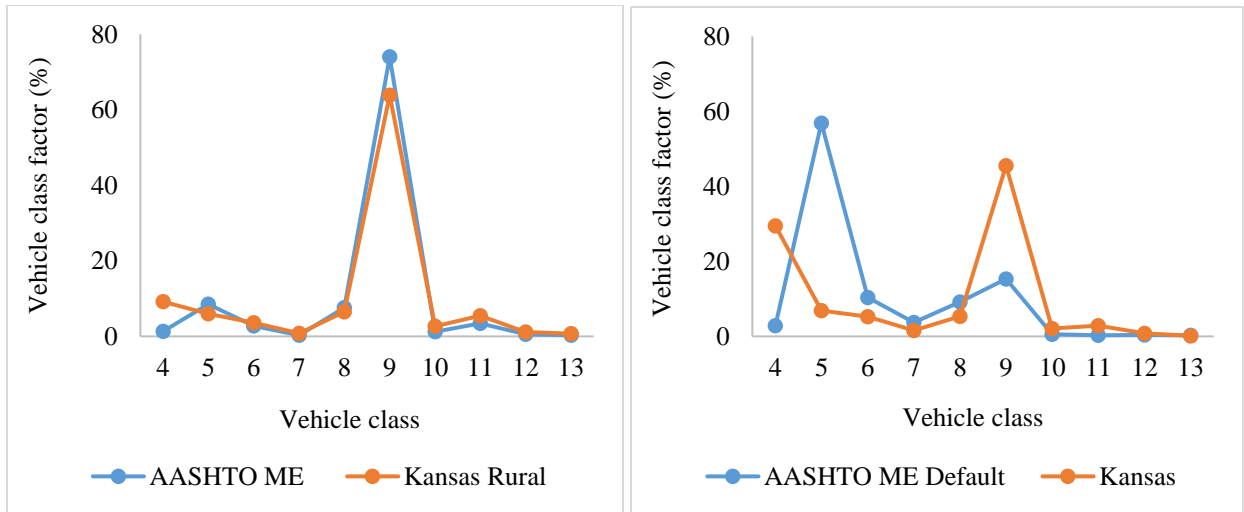


Figure 3-4 Average VCFs for urban (left) and rural (right) principal arterials

### 3.4.2 Monthly adjustment factors

MAFs are defined as the fraction of yearly truck traffic in each month for a particular truck class. These factors include the distribution of truck volumes each month in a typical year (NCHRP, 2004). MAFs are influenced by factors such as adjacent land use, industry locations, and roadway locations (Khanum et al., 2005).

Because class 9 is the prevalent vehicle class in Kansas, this study utilized two-dimensional clustering analysis with class 9 MAF values derived from AVC stations listed in Table 3-6. Cluster analysis showed two distinctive patterns for rural and urban principal arterials. Average MAF values of vehicle class 9 for rural and urban AVC stations are shown in Figure 3-5. As shown in the figure, both rural and urban sites demonstrated higher MAF values in spring and summer seasons than in the winter. However, MAF values were shown to be higher for AVC stations on urban principal arterials than on rural principal arterials.

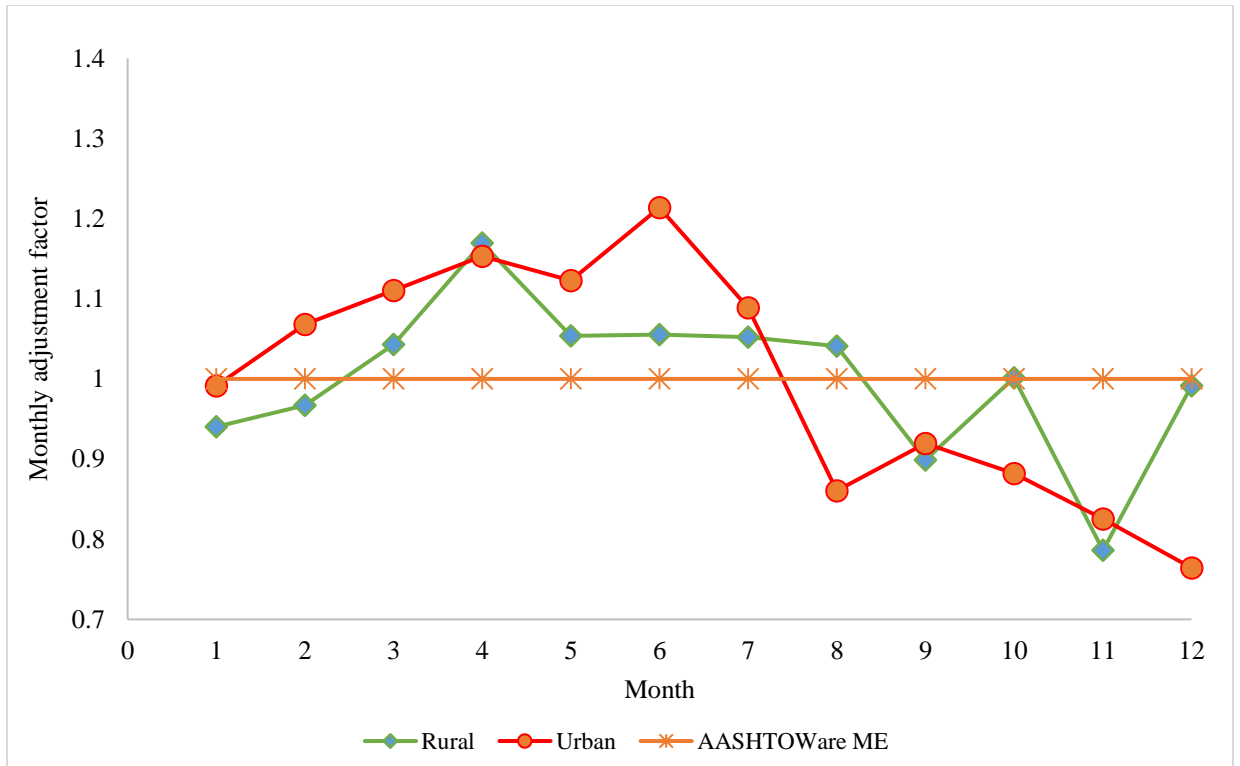


Figure 3-5 MAFs for rural and urban principal arterials in Kansas

### 3.4.3 Hourly distribution factors

HDFs are derived from AADTT at each hour of the day (NCHRP 1-37A, 2004). Hourly distribution factors of truck traffic help compute incremental damage of PCC pavements at different thermal gradients over a 24-hour period (Khanum et al., 2005).

This study generated HDF values for 11 AVC stations located on urban and rural principal arterials in Kansas and then categorized these values based on the functional class of the roadways. Average HDF values for rural and urban principal arterials are provided in Figure 3-6. Both rural and urban principal arterials showed HDF values that were higher during afternoon, evening, and night periods than AASHTOWare PMED software recommended.



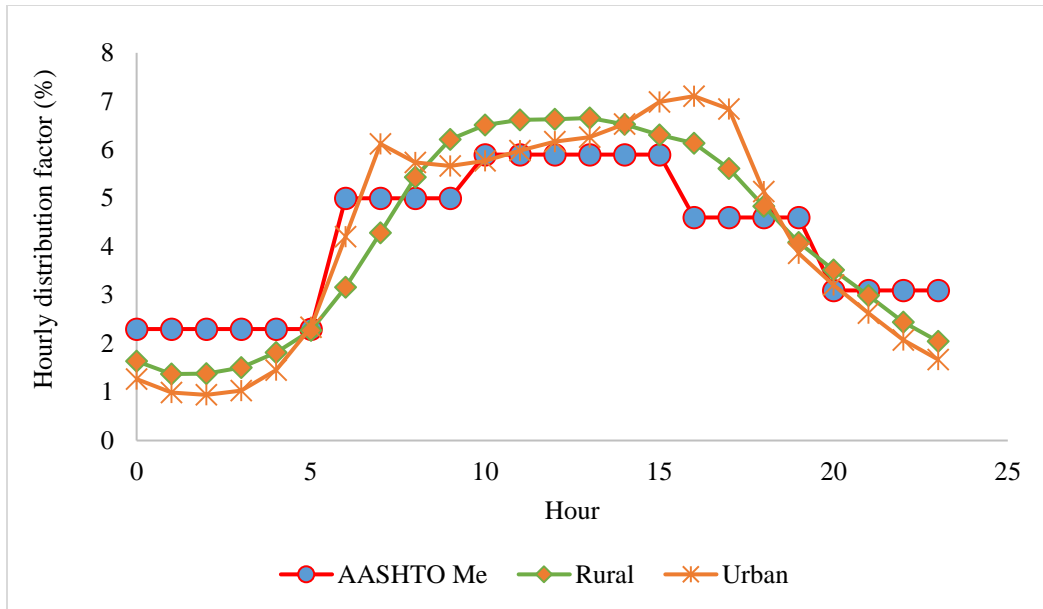


Figure 3-6 HDFs for rural and urban principal arterials in Kansas

### 3.4.4 Axle load spectra

AASHTOWare PMED software requires the frequency of load applications at specific load intervals for each axle type (single, tandem, tridem, and quad) and vehicle class for every month of the year. Load distribution is 3,000–40,000 lbs at 1,000-lb intervals for single axles, 6,000–80,000 lbs at 2,000-lb intervals for tandem axles, and 2,000–102,000 lbs at 3,000-lb intervals for tridem and quad axles.

This study generated axle load spectra by processing “W” card data from the WIM stations listed in Table 3-5. In Kansas, WIM data is typically collected for short (48 hr) durations. The MEPDG recommends deriving axle load distribution for each month of the year, but previous research of traffic inputs for MEPDG using data from the GPS-5 section in Marion County, Indiana, indicated that variations in load spectra across the months within a year and along the years are insignificant (Tam and Von Quintus, 2004). Thus, this study assumed that load spectra derived from portable sites are representative throughout the year. Figure 3-7 shows

the distribution of single and tandem axle loads for class 9 trucks on rural and urban roadways in Kansas compared to default AASHTOWare PMED software.

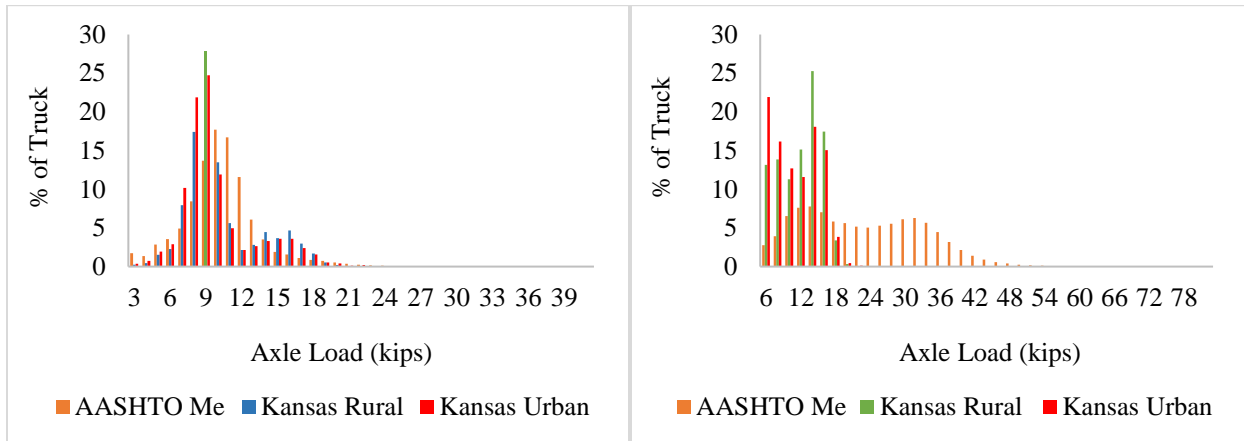


Figure 3-7 Single (left) and tandem (right) axle loads for class 9 trucks in Kansas

Single axle load distribution in Kansas rural traffic showed greater frequency between 7,000 lbs and 16,000 lbs, whereas Kansas urban traffic showed greater frequency between 7,000 lbs and 14,000 lbs. Overall traffic showed very low frequency above 20,000 lbs compared to AASHTOWare default values.

For single axle load distribution, Kansas rural traffic indicated higher frequency from 6,000 lbs to 18,000 lbs, whereas Kansas urban traffic showed greater frequency between 6,000 lbs and 16,000 lbs. Both urban and rural traffic showed very low frequency above 20,000 lbs compared to AASHTOWare PMED default values.

### 3.4.5 Axle group per vehicle

The AASHTOWare PMED software requires AGPV and axle load spectra to compute average damage induced to pavement structures by truck traffic in each vehicle class (Romanoschi et al., 2011). In this study, average AGPV values for rural and urban roadways in Kansas were computed from the WIM data listed in Table 3-5. Table 3-7 shows level 2 AGPV

developed for Kansas. Traffic parameters developed for individual AVC and WIM stations are provided in the appendix A.

Table 3-7 AGPV for rural and urban roadways in Kansas

Vehicle Class	Kansas Rural				Kansas Urban				AASHTO ME Default			
	Single	Tandem	Tridem	Quad	Single	Tandem	Tridem	Quad	Single	Tandem	Tridem	Quad
4	1.90	0.28	-	-	2.21	0.57	0.00	-	1.62	0.39	-	-
5	2.16	0.68	0.08	-	2.08	0.50	0.06	-	2.00	-	-	-
6	1.32	1.70	-	-	1.35	1.65	-	-	1.02	0.99	-	-
7	2.20	0.80	0.10	0.13	1.87	0.96	0.92	0.45	1.00	0.26	0.83	-
8	2.19	1.52	-	-	2.30	1.49	-	-	2.38	0.67	-	-
9	1.54	3.45	0.01	0.00	1.53	3.46	0.02	-	1.13	1.93	-	-
10	2.64	2.00	1.23	0.01	2.21	2.06	1.59	0.29	1.19	1.09	0.89	-
11	4.00	0.00	-	-	5.00	0.00	-	-	4.29	0.26	0.06	-
12	3.84	1.75	-	-	3.99	2.01	-	-	3.52	1.14	0.06	-
13	2.53	0.82	0.55	-	3.70	1.07	-	-	2.15	2.13	0.35	-

### 3.5 Pavement Cross-Section Inputs

Pavement cross-section inputs including each bound and unbound layer except the semi-infinite, bottommost subgrade layer are required for modeling in the PMED software (NCHRP 1-37A, 2004). This study collected layer thicknesses from the PMIS database for each layer.

Kansas generally constructs AC overlay in one, two, or three layers on top of existing pavement sections. Depending on the project, the AC overlay can include a reflective crack interlayer (RCI) with a maximum thickness of 1 in. and an ultra-thin bonded asphalt surface (UBAS) layer with thickness varying from 0.5 in. to 0.75 in. AC over JPCP sections typically have a treated base beneath the PCC layer. Due to high plasticity, the top 6 in. of the subgrade layer is generally treated with lime or fly ash (Islam et al., 2017). AC over AC sections can be full depth or have

an aggregate base depending on the AADTT of the pavement segment. Schematics of typical AC-overlaid pavement sections are shown in Figure 3-8.

1.5" to 4.0" AC overlay	0.5" to 0.75" UBAS	1.5" to 4.0" overlay	Chip seal/slurry seal
Existing JPCP	1.5" to 4.0" AC overlay	Existing AC	1.5" to 4.0" overlay
Treated base layer	1.0" RCI	Existing AC	Existing AC
Treated subgrade	Existing JPCP	Treated subgrade	Treated subgrade
Semi-infinite soil subgrade	Treated base layer	Semi-infinite soil subgrade	Semi-infinite soil subgrade
	Treated subgrade		
	Semi-infinite soil subgrade		

Figure 3-8 Schematic of rehabilitated pavement structures in Kansas

Site-specific structural information of selected rehabilitated AC sections are presented in Appendix C.

### 3.5.1 PMED modeling of AC over AC sections

The maximum number of AC overlay that can be modeled in the PMED software is four (AASHTO, 2010). Pavement repairs and milling of the existing surface layer can also be incorporated into PMED. This study modeled 25 AC over AC sections using the AASHTOWare PMED software. A detailed description of how the AC over AC sections were modeled is provided below. AC mixture properties are provided in Appendix C.

- Project KA-0310-01 is a full-depth AC pavement on route US-75 in Osage County. The existing HMA layer, constructed in October 1998, consisted of a 1-in. surface course (0.375 in. nominal maximum aggregate size (NMAS)), 4-in. binder course (0.75 in. NMAS) and 6-in. bituminous-treated base (BTB) course (0.75 in. NMAS). A 2-in.

overlay (0.5 in. NMAS) was placed in September 2006. The section was modeled with three existing HMA layers and a 2-in. overlay.

- Project K-9364-01 on K-92 in Jefferson County was constructed in June 1999. This project consisted of a 1.5-in. AC surface course and a 3.5-in. base course on top of a 4-in. aggregate base layer. In April 2004, a 2-in. overlay was placed with two AC courses: a 1-in. course with 0.75 in. NMAS and another 1-in. course with 0.375 in. NMAS. AC mixture properties are provided in Appendix B. In 2009, chip seal was placed on this section as a maintenance activity. The project was modeled with a 4-in. aggregate base, two existing HMA layers, and two separate 1-in. layers as overlays. The section was analyzed for a 5-year design period, and the chip seal action was not considered in PMED calibration.
- Project KA-2188-01, a full-depth HMA pavement constructed in April 2002, consisted of a 2.5-in. surface course and an 11.5-in. base course. In 2014, a 6-in. overlay was placed after a 2-in. profile mill. The 6-in. overlay was placed in two courses: PG 58-28 binder in the bottom 2 in. and PG 64-28 in the top 4 in. To model this section, the milled thickness had to be deducted from the existing AC thickness. The section was then modeled with an existing AC thickness of 12 in. with two separate AC overlay courses.
- Project KA-0813-01 in US-36 in Washington County was constructed in July 2000. This section consisted of a 1.5-in. surface course and a 7.1-in. base course on top of a 12.6-in. aggregate base course. Modified slurry seal was placed in 2004. In 2007, a 1.5-in. overlay was placed after a 0.5-in. profile mill. In 2007, chip seal was placed on this section as a maintenance activity. The chip seal action was not considered for this study, so analysis was conducted until year 2007. However, PMED modeling had to account for slurry seal

thickness, so the slurry seal was assumed to be a 0.4-in. layer per KDOT recommendation. This section was designed with two existing AC layers: a 1.4-in. surface layer of existing AC and a 7-in. base layer of existing AC followed by a 1.5-in. AC overlay.

- Project KA-9466-01 on route I-70 in Saline County was reconstructed in October 2007. This project consisted of a 1-in. surface course, 7-in. intermediate course, and 9-in. base course on top of a 6-in. fly ash modified bituminous subbase. In November 2004, the 1-in. surface course was milled off, and a 3-in. overlay was placed in two courses: a 1.5-in. overlay surface course (0.375 in. NMAS) and a 1.5-in. overlay base course (0.75 in. NMAS). In 2012, a UBAS layer was placed as a maintenance action. This layer was not modeled in this study, and analysis was conducted up to 2012. The section was then modeled with two existing AC layers and with two separate AC overlay layers.
- Project KA-2628-01 on I-70 in Saline County was reconstructed in June 1996. The eastbound section had a 2-in. surface course and an 8.2-in. base course. The westbound section had a 2-in. surface course, 2-in. intermediate course, and 10.4-in. base. Only the eastbound section was analyzed in this study. In November 2004, the surface course was milled off, and a 3-in. overlay and 0.625-in. UBAS layer were placed. Since AASHTOWare PMED software does not define pavement layer thinner than 1.0 in., UBAS surfaces could not be considered as individual layers. Instead, the thickness of the UBAS layer was added to the AC overlay layer per KDOT suggestion, so that the total thickness of the overlay layer remained constant. Even though the aggregate gradation and binder content in the UBAS layer differed from the underlying AC layer, it was assumed that differences of material properties of such a thin layer would not

significantly alter performance prediction. In 2012, the highway segments were again rehabilitated with 2-in. milling and a 3-in. overlay. The second overlay was not modeled in this study, and the analysis was conducted up to 2012. Thus, the section was modeled with two existing AC layers and a 3.625-in. AC overlay.

- Project KA-2923-01 was constructed in 1999 and consisted of a 2-in. surface course and a 5.5-in. base course on top of a 6-in. bound drainable course and a 9.5-in. AB-3 aggregate base course. In 2013, the top 1 in. of the surface course was milled off, and a 1.5-in. overlay was placed. The section was modeled with two existing AC layers and a 1.5-in. overlay.
- Project KA-4013-01 on US-24 in Osbourne County was reconstructed in April 2004. This project consisted of a 1.5-in. surface course, 2.5-in. intermediate course, and 8-in. base course on top of a 5.5-in. aggregate base. Chip seal was placed in 2007 as a rehabilitation action. In May 2015, the chip seal was milled off and a 1.5-in. overlay (0.5 in. NMAS) was placed. The section was modeled with three layers of existing HMA and a 1.5-in. overlay.
- Project KA-1436-01, is a full-depth AC pavement on US-36 in Cheyenne County, was constructed in September 1996. This project consisted of a 1.5-in. surface course and an 8.5-in. base course. Modified slurry seal was placed in 2004, and a 1.5-in. overlay was placed in August 2009. The section was then modeled with two existing AC layers: a 1.9-in. surface layer of existing AC and an 8.5-in. base layer of existing AC followed by a 1.5-in. AC overlay.
- KA-1444-01 pavement section on route US-183 is in Phillips County (mileposts 15.00–32.00). The segment of highway from mileposts 15.00 to 22.75 was reconstructed in

1995, and the segment from milepost 22.75 to milepost 32.00 was reconstructed in 1994. Because initial construction of the two highway segments was one year apart, they were analyzed as separate sections: KA-1444-01(1) and KA-1444-01(2). The existing AC layer of the entire segment consisted of a surface course of 1.5 in. and a base course of 5 in. In 2002, the surface course was milled 0.5 in. and a 1.5-in. overlay was placed in 2002, while a 1-in. milling was done, followed by a 1.5-in. overlay, in 2009. In October 2017, a 1-in. milling was done, and a 2-in. overlay was placed. The third overlay action was not considered for analysis in this study because there was insufficient measured distress data for calibration. The second rehabilitated action was considered the overlay layer; everything beneath was considered the existing AC layer.

- Project KA-2505-01 on US-183 in Rooks County was reconstructed in August 2002. This project consisted of a 1-in. surface course and a 6.3-in. base course. Chip seal was placed in 2008 as a rehabilitation action. In June 2012, 1.5 in. of the top surface was milled off, and a 2-in. overlay (0.5 in. NMAS) was placed. The section was modeled with three layers of existing HMA and a 1.5-in. overlay. The chip seal thickness was assumed to be 0.5-in. per KDOT recommendation. The section was then modeled with a 6.3-in. existing AC layer followed by a 2-in. AC overlay.
- Project KA-2966-01 on US-183 in Ellis County was reconstructed in 1997. This project consisted of a 1-in. surface course and a 9-in. base course. Bituminous seal was placed in 2004 as a rehabilitation action. A 1.5-in. overlay was placed in November 2013 (0.5 in. NMAS). The section was then modeled with two existing AC layers: a 1.4-in. surface layer of existing AC and a 9-in. base layer of existing AC followed by a 1.5-in. AC overlay.



- Project KA-3674-01 on route US-283 in Norton County was reconstructed in May 2003. This project consisted of 1.5-in. surface course, 2.5-in. intermediate course, and 8-in. base course. Chip seal was placed in 2007 as a rehabilitation action. In May 2015, the chip seal was milled off, and a 1.5-in. overlay (0.5 in. NMAAS) was placed. The section was modeled with three layers of existing HMA and a 1.5-in. overlay.
- Project K-0657-01 on US-69 in Bourbon County was reconstructed in 1995. This project consisted of a 1-in. surface course and a 10.5-in. base course. Modified slurry seal was placed in 2004 as a preventive action. The seal was then milled off, and a 1.5-in. overlay was placed in October 2007 (0.5 in. NMAAS). The section was modeled with two existing AC layers: a 1-in. surface layer of existing AC and a 9-in. base layer of existing AC followed by a 1.5-in. AC overlay.
- Project KA-0811-01 on US-75 in Montgomery County was reconstructed in July 1998. This project consisted of a 1-in. surface course, 2.5-in. intermediate course, and 3-in. base course on top of a 6-in. bound drainable course and an 11-in. aggregate base course. This project was overlaid in August 2007 with a 1-in. AC layer. The project was modeled with three existing AC layers followed by a 1-in. overlay.
- Project K-7756-01 on US-166 in Chautauqua County was reconstructed in March 1997. This project consisted of a 1-in. surface course and a 7-in. base course on top of a 6-in. bound drainable course and an 11-in. aggregate base course. This project was overlaid in March 2000 with a 2-in. AC layer. The project was modeled with the two existing AC layers followed by the 2-in. overlay.
- Project KA-2200-01 on US-169 in Allen County was constructed in May 2000 and consisted of a 2-in. surface course, 3-in. intermediate course, and 6-in. base course. In

2003, modified slurry seal was placed. In 2008, a 0.625-in. UBAS was placed as a preventive action. In 2015, a 4-in. cold mill was conducted, and a 7-in. overlay was placed in two courses: a 3-in. overlay surface course (0.5 in. NMAS) and a 4-in. overlay base course (0.75 in. NMAS). The section was modeled with two existing AC layers of a 2-in. intermediate layer of existing AC and a 6-in. base layer of existing AC, as well as two separate AC overlay layers: a 3-in. AC surface layer and a 4-in. AC base layer.

- Project KA-2204-01 on US-169 in Anderson County was constructed in April 2000 and consisted of a 1.5-in. surface course, 2-in. intermediate course, and 4-in. base course. In 2003, a modified slurry seal was placed. In 2015, 4-in. deep cold milling was done, and a 7-in. overlay was placed. The section was modeled with an existing AC layer of 4 in. followed by the 7-in. AC overlay layer.
- Project KA-2941-01 on US-77 in Butler County was constructed in August 2004 and consisted of a 1.5-in. surface course, 2.5-in. intermediate course, and 8-in. base course. In 2013, a 1.5-in. overlay was placed. The project was modeled with the three existing AC layers and a 1.5-in. overlay.
- Project KA-4192-01 on US-77 in Butler County was reconstructed in June 2004 and consisted of a 1.5-in. surface course, 2.5-in. intermediate course, and 4-in. base course on top of an 11-in. aggregate base layer. In 2009, a 0.5-in. UBAS layer was placed as a maintenance action, and a 1.5-in. overlay was placed in 2013. The project was modeled with three existing AC layers and a 1.5-in. overlay. The UBAS layer was not modeled separately and added to the 1.5-in. surface course of the existing AC layer.
- Project KA-1460-01 on US-166 in Cowley County was constructed in August 1996 and consisted of a 1.5-in. surface course and a 7-in. base course on top of a 6-in. bound

drainable course and a 7-in. aggregate base course. In 1999, 0.5-in. of the surface course was milled off and a 2-in. overlay (0.5 in. NMAS) was placed. In 2009, a 0.5-in. deep milling was done, and a 1.5-in. (0.5 in. NMAS) overlay was placed. The first overlay action was considered an existing layer; thus, the section was modeled with three existing AC layers: a 1.5-in. AC layer overlaid in 1999, a 1-in. remaining AC surface layer from 1996, and a 7-in. base layer from 1996 followed by the 1.5-in. overlay placed in 2009.

- Project KA-3496-01 on K-254 in Sedgwick County was constructed in August 1998. This project had a 1-in. surface course (0.375 in. NMAS), a 1-in. intermediate course (0.75 in. NMAS), and a 5.5-in. base course (0.75 in. NMAS) on top of a 6-in. bound drainable course and a 7-in. aggregate base course. In 2004, the section was treated with modified slurry seal, the seal was milled off, and a 1.5-in. (0.5 in. NMAS) overlay was placed. The project was modeled with three existing layers followed by the AC overlay.
- Project KA-1480-01 on US-160 in Clark County was constructed in October 1998. This project consisted of a 1.5-in. surface course and an 8.5-in. base course. In May 2009, 1-in. deep cold milling was conducted, and a 1.5-in. overlay (0.5 in. NMAS) was placed. The remaining 0.5-in. thickness of the existing AC surface course could not be modeled separately, so the existing AC was modeled as one layer with a 9-in. thickness.
- Project KA-8431-01 on US-83 in Seward County was constructed in August 1995 and consisted of a 1-in. surface course and a 13-in. base course. The project was overlaid in October 2001 with 1-in. AC layer. The project was modeled with the two AC existing layers followed by the overlay.

### ***3.5.2 PMED modeling of AC over JPCP sections***

This study modeled 18 AC over JPCP sections using the AASHTOWare PMED software. PMED allows a maximum of three HMA layers for modeling the overlay on JPCP sections (AASHTO, 2010). Mixture information required for HMA must be specified for each layer. Required AC mixture properties are provided in Appendix B. A detailed description of how the AC over JPCP sections were modeled is provided below.

- Project K-7823-01 on route K-7 in Johnson County was constructed in June 1986. This section consisted of a 9-in. PCC layer on top of a 4-in. Portland cement-treated base (PCTB). In June 2000, a 4-in. overlay was placed in two courses: a 1.5-in. overlay surface course (0.375 in. NMAAS) and a 2.5-in. overlay base course (0.75 in. NMAAS). In 2013, a 0.625-in. UBAS layer was placed as a maintenance action. The UBAS layer was not modeled in this study, and analysis was conducted up to 2012. The section was modeled with 9-in. PCCP and 4-in. PCTB with two layers of HMA on top.
- Project KA-2836-01 on I-70 in Shawnee County was constructed in 2003 and consisted of a 12-in. PCCP on top of a 4-in. PCTB. In June 2013, a 4-in. overlay was placed in two courses: a 1.5-in. overlay surface course (0.375 in. NMAAS) and a 2.5-in. overlay base course (0.5 in. NMAAS). The section was modeled with 9-in. PCC and 4-in. PCTB with two layers of HMA on top.
- Project KA-4136-01 on I-70 in Shawnee County was constructed in July 1993 and consisted of a 10.5-in. PCC on top of a 4-in. CTB. PCC patching and joint repair actions were performed in 2011. In 2015, a 3-in. overlay was placed (0.5 in. NMAAS) followed by a 0.625-in. UBAS layer. UBAS surfaces could not be considered as individual layers. The thickness of the UBAS layer was added to the AC overlay layer, so a total 3.625-in.

AC overlay was modeled on top of a 9-in. PCCP and 4-in. PCTB. Even though the aggregate gradation and binder content in the UBAS layer differed from the underlying AC layer, it was assumed that differences of material properties in the UBAS layer would not significantly alter performance prediction.

- Project KA-2669-01 on US-54 in Shawnee County was constructed in June 2003 and consisted of an 11-in. PCC on top of a 4-in. BTB. In 2012, a 3-in. overlay was placed (0.5 in. NMAS). The section was modeled with 11-in. PCCP and 4-in. PCTB with a 3-in. HMA layer on top.
- Project KA-2835-01 on I-70 in Wabaunsee County was constructed in June 2004. This section had 12-in. PCC on top of a 4-in. bound drainable base (BDB). In June 2013, a 4-in. overlay was placed in two courses: a 1.5-in. overlay surface course (0.375 in. NMAS) and a 2.5-in. overlay base course (0.5 in. NMAS). The section was modeled with 12-in. PCC and 4-in. BDB with two layers of HMA on top.
- Project KA-3282-01 on I-70 in Wyandotte County was constructed in May 1989. This project consisted of a 10-in. PCC on top of a 4-in. BTB. PCC patching was performed in 2002 and 2006. In 2014, a 3-in. overlay was placed (0.5 in. NMAS), followed by a 0.625-in. UBAS layer. The thickness of the UBAS layer was added to the AC overlay layer, meaning that a 3.625-in. AC overlay was modeled on top of a 9-in. PCCP and a 4-in. BTB.
- Project KA-1951-01 on US-50 in Chase County was constructed in 1997. This project consisted of a 10-in. PCC on top of a 4-in. PCCB. In August 2011, a 3-in. overlay was placed (0.5 in. NMAS). The section was modeled with 10-in. PCCP and 4-in. PCTB with a 3-in. HMA layer on top.

- Project KA-2682-01 on K-150 in Chase County was constructed in August 2003. This project consisted of a 9.5-in. PCC on top of a 4-in. CTB. In December 2012, a 3-in. overlay was placed (0.5 in. NMAS). The section was modeled with 10-in. PCCP and 4-in. CTB with a 3-in. HMA layer on top.
- Project KA-1931-01 on US-81 in Cloud County was constructed in November 1998. This project consisted of a 9-in. PCC on top of a 4-in. BDB. Crack sealing on PCC was done in 2004. In December 2012, a 3-in. overlay was placed (0.5 in. NMAS), followed by a saw-and-seal operation. The section was modeled with 10-in. PCCP and 4-in. BDB with a 3-in. HMA layer on top.
- Project KA-1950-01 on US-50 in Marion County was constructed in November 2011. This project consisted of a 9-in. PCC on top of a 4-in. BDB. In August 2011, a 3-in. overlay was placed (0.5 in. NMAS). The section was modeled with 9-in. PCC and 4-in. BDB with a 3-in. HMA layer on top.
- Project KA-2681-01 on K-57 in Marion County was constructed in August 2003. This project consisted of a 9.5-in. PCC on top of a 4-in. PCTB. In December 2012, a 3-in. overlay was placed (0.5 in. NMAS), followed by a saw-and-seal operation. The section was modeled with 9.5-in. PCC and 4-in. PCTB with a 3-in. HMA layer on top.
- Project KA-4036-01 is in the eastbound direction of I-70 in Sherman County. This project consisted of a 10-in. PCC on top of a 4-in. PCTB. In December 2015, a 3-in. overlay was placed in two courses: a 1.5-in. overlay surface course (0.5 in. NMAS, PG 70-28) and a 1.5-in. overlay base course (0.5 in. NMAS, PG 70-28). The section was modeled with 10-in. PCC and 4-in. PCTB with two layers of HMA on top.

- Project KA-3848-01 on US-400 in Labette County was constructed in May 1997. This project consisted of a 9-in. PCC on top of a 4-in. BDB. In September 2015, a 0.625-in. UBAS layer and a 2.5-in. AC overlay (0.5 in. NMAS) were placed on top of a 1-in. RCI. The thickness of the UBAS layer was added to the 2.5-in. AC layer; thus, the AC overlay was modeled in two layers: a 3.125-in. AC layer on top of a 1-in. RCI.
- Project KA-2001-01 on K-254 in Butler County was constructed in September 1995. This project consisted of a 9-in. PCC on top of a 4-in. treated base. In October 2011, a 0.625-in. UBAS layer and a 2-in. AC overlay (0.5 in. NMAS) was placed on top of a 1-in. RCI. The thickness of the UBAS layer was added to the 2-in. AC layer; thus, the pavement section was modeled with two AC layers: a 2.625-in. AC layer on top of the 1-in. RCI followed by the 9-in. PCC and the 4-in. PCTB.
- Project KA-4236-01 on I-135 in Harvey County was constructed in March 2000. This section consisted of an 11-in. PCC on top of a 4-in. BDB. In May 2011, significant PCC repair activities were performed, including polyurethane concrete raising, tie-bar insertion, and partial depth PCC patching. In October 2011, a 3.5-in. AC overlay (0.5 in. NMAS) was placed on top of a 1-in. RCI. The pavement section was modeled with two AC layers: a 3.5-in. AC layer on top of the 1-in. RCI, followed by the 11-in. PCC and the 4-in. BDB.
- KA-0378-01 pavement section on route US-50 is also located in Harvey County, beginning from milepost 27.00 to milepost 35.56. Highway segment from milepost 28.64 to milepost 35.56 was constructed in February 1995, and mile post 27.00 to milepost 28.64 was constructed in August 1997. PCC thickness from milepost 27.00 to 28.64 is 10 in., while PCC thickness from milepost 28.64 to 35.56 is 9 in. Both segments had a 4-in.

PCTB beneath the PCC layer. These two segments were analyzed as separate sections. Highway segment from milepost 28.64 to milepost 35.56 was named KA-0378-01(1), and highway segment from milepost 27.00 to milepost 28.64 was named KA-0378-01(2). Segment KA-0378-01(1) underwent significant PCC crack repair in 2001 and 2005. In May 2006, a 0.5625-in. UBAS layer and a 2-in. AC overlay (0.5 in. NMAS) was placed on top of a 1-in. RCI in both segments. Section KA-0378-01(1) was modeled with two AC layers: a 2.57-in. AC layer on top of the 1-in. RCI, followed by the 9-in. PCC. Section KA-0378-01(2) was modeled with two AC layers: a 2.57-in. AC layer on top of the 1-in. RCI, followed by the 10-in. PCC.

- Project KA-3006-01 on K-156 in Finney County was constructed in May 1986. This section consisted of a 9-in. PCC on top of a 4-in. BTB. In 2008, a 1.5-in. AC overlay was placed. In March 2013, the 1.5-in. HMA was milled off, and a 2-in. overlay (0.5 in. NMAS) was placed. The section was modeled with 9-in. PCC and 4-in. BTB with a 2-in. HMA layer on top.

### **3.6 Material Inputs**

AASHTOWare software requires layer material properties that represent conditions right after construction for new pavement layers (NCHRP 1-37A, 2004). Whenever available, this study collected as-constructed material properties for the new layers at the time of construction. The pavement design team at KDOT amassed the in-situ material properties after reviewing the CMS database for the selected AC over JPCP sections. In addition, quality control-quality assurances spreadsheets were available for eight projects.



### ***3.6.1 AC layer properties***

AASHTOWare PMED software requires mixture volumetrics and HMA mechanical and thermal properties to characterize the AC overlay. Mixture volumetrics include percent air void, effective binder content, Poisson's ratio, and unit weight of the HMA mix. AASHTOWare software requires the air void percentage of the HMA mix to be representative of as-constructed pavement. The target air void at  $N_{design}$  level was recorded in the CMS for all HMA mixes for the projects listed in Tables 3-3 and 3-4. However, the target air void does not represent the in-situ air void at the time of construction. In this study, percent air void was 7% for all HMA mixes since KDOT aims for  $93\% \pm 1\%$  compaction at the time of construction. The HMA unit weight for all projects was recorded in the CMS. The range of unit weight for the AC overlay of selected JPCP rehabilitation projects was 125–155 lb/ft<sup>3</sup>. Figure 3-9 shows the variation of AC unit weight in the HMA mixes for the selected JPCP rehabilitated sections. The effective binder content (by volume) was computed by subtracting the AC target air void from AC void in mineral aggregate (VMA). The distribution of effective binder content for all HMA mixes for the selected pavement sections is presented in Figure 3-10. The Poisson's ratio for all HMA mixes was assumed to be 0.35.

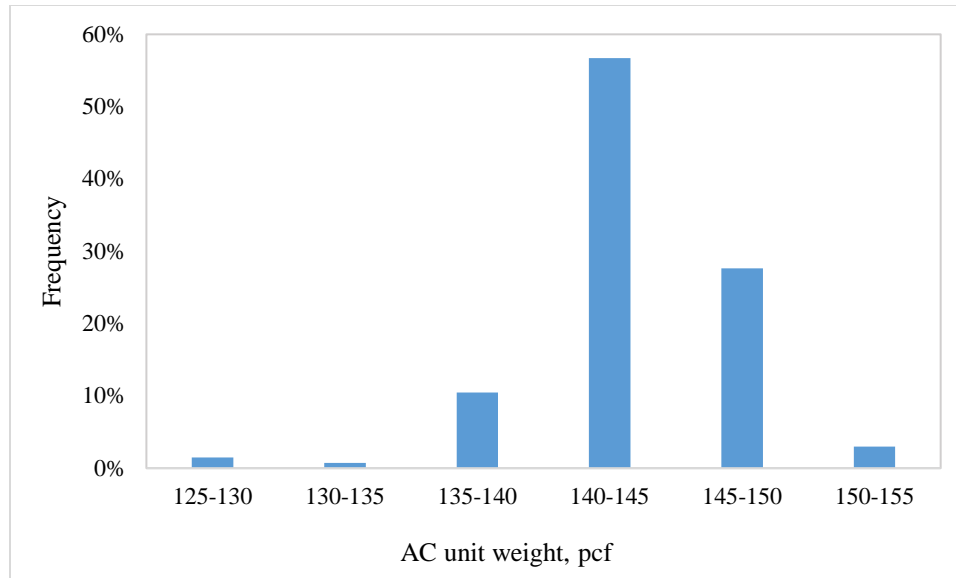


Figure 3-9 AC unit weight distribution of HMA mixes

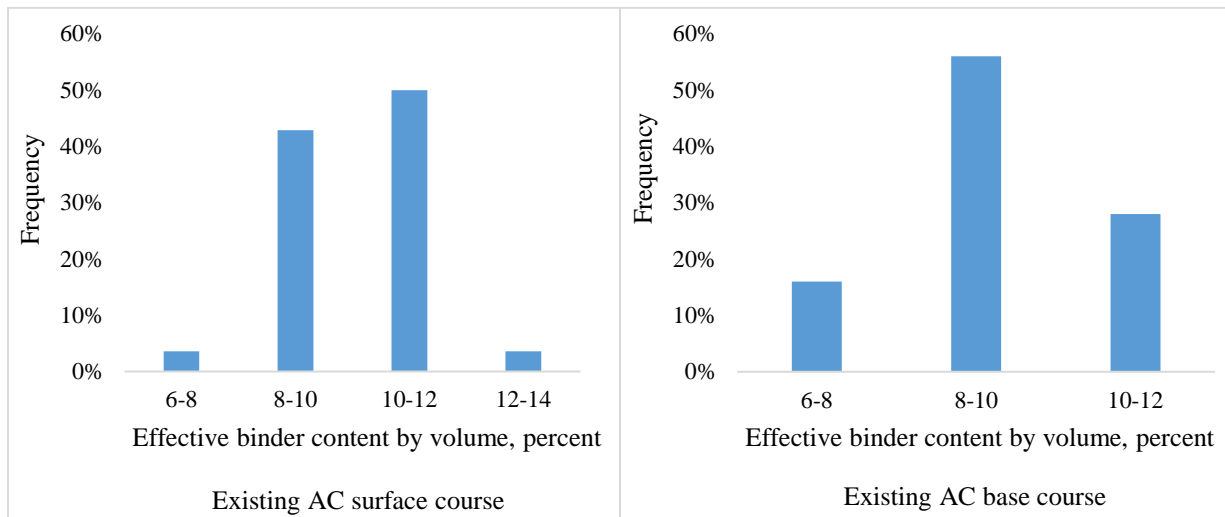


Figure 3-10 Effective binder content distribution AC mixes of existing pavement

AASHTOWare PMED software requires information about asphalt binder, creep compliance, dynamic modulus, and indirect tensile strength of the asphalt mix to characterize mechanical properties. For level 1 analysis, the software requires dynamic modulus  $|E^*|$  of the AC mix at a minimum of three temperatures and three frequency levels. In addition, binder complex modulus ( $G^*$ ) and phase angle ( $\delta$ ) values are required at a minimum of two

temperatures (Kim et al., 2011). For level 2 analysis, the software requires mixture aggregate gradations, binder  $G^*$  and  $\delta$  values. For level 3 analysis, mixture aggregate gradation and asphalt binder performance grade (PG) information is required. This study used site-specific aggregate gradations and PG binder grade values to generate HMA mechanical properties. Site-specific AC layer properties of the pavement sections are provided in Appendix C.

### ***3.6.2 JPCP layer properties***

Input parameters required to characterize JPCP layers include thickness, Poisson's ratio, unit weight, coefficients of thermal expansion (CTE), PCC heat capacity, and PCC thermal conductivity. Aggregate type, cement content, and water-cement ratio (w/c ratio) are required inputs for the concrete mix. Furthermore, JPCP design parameters such as dowel diameter and spacing, PCC joint spacing, and PCC erodibility index are also required (Haider et al., 2014).

#### ***3.6.2.1 JPCP mix inputs***

In this study, the CTE value for limestone and non-limestone aggregates was chosen to be  $5.5 \times 10^{-6}$  in/in/°F per KDOT suggestion. PCC 28-day compressive strength and flexural strength values were extracted from the CMS database. Table 3-8 lists the compressive strength,  $f'_c$  and modulus of rupture (MOR) values for the selected JPCP projects.

Table 3-8 Strength properties of mixes for the selected JPCP sections

Project	Route	County	PCC thickness (inch)	Cement content (lb./yd <sup>3</sup> )	w/c ratio	$f'_c$ @28 days (psi)	MOR age (days)	MOR (psi)
KA-2836-01	I-70	Shawnee	12.0	521	0.43	4,590	2	597
KA-4136-01	I-70	Shawnee	10.5	620	0.49	-	-	-
KA-4036-01	I-70	Sherman	10.0	565	0.45	5,064	4	566
KA-2835-01	I-70	Wabaunsee	12.0	521	0.44	4,598	4	695
KA-3282-01	I-70	Wyandotte	10.0	620	0.49	-	-	-
KA-4236-01	I-135	Harvey	11.0	545	0.44	-	7	535
KA-1950-01	US-50	Marion	10.0	620	0.43	-	7	521
KA-1951-01	US-50	Chase	10.0	620	0.42	5,385	7	474
KA-0378-01(1)	US-50	Harvey	9.0	639	0.44	-	5	455
KA-0378-01(2)	US-50	Harvey	10.0	620	0.43	-	4	478
KA-2669-01	US-54	Shawnee	11.0	521	0.44	4,890	3	537
KA-1931-01	US-81	Cloud	9.0	620	0.46	4,781	3	563
KA-3848-01	US-400	Labette	9.0	592	0.46	4950	-	-
K-7823-01	K-7	Johnson	9.0	623	0.46	-	-	-
KA-2681-01	K-57	Marion	12.0	545	0.45	-	7	541
KA-2682-01	K-150	Chase	9.5	545	0.45	-	6	542
KA-3006-01	K-156	Finney	9.0	620	0.49	-	-	-
KA-2001-01	K-254	Butler	9.0	620	0.44	-	4	497

PMED software requires 7-, 14-, 28-, and 90-day PCC elastic modulus and MOR values for level 1 input. In addition, ratio of 20-yr to 28-day elastic modulus and MOR values are also

required. For level 2 input, 7-, 14-, 28-, and 90-day PCC compressive strength and the ratio of 20-yr to 28-day compressive strength are needed (AASHTO 2015).

Laboratory-tested 7-, 14-, 28-, and 90-day PCC elastic modulus and MOR values were not available for this study. A predictive model (Equation 3.8), developed under an FHWA (2012) project, was used to determine 7-, 14-, 28-, and 90-day PCC compressive strength. This model was developed using SPS sections to predict concrete cylinder strength up to 1 year. Figure 3-11 presents compressive strength gain using the FHWA short-term predicting model over time.

$$f_{ct} = 6358.60655 + 3.53012 * CMC - 34.24312 * \frac{w}{c} * uw + 633.3489 * \ln(t) \quad (3.8)$$

Where:

$f_{ct}$  = Compressive strength at age  $t$  years, psi;

$CMC$  = Cementitious materials content, lb/yd<sup>3</sup>;

$w/c$  = Water to cement ratio;

$uw$  = Unit weight, lb/yd<sup>3</sup>; and

$t$  = Short-term age up to 1 year.

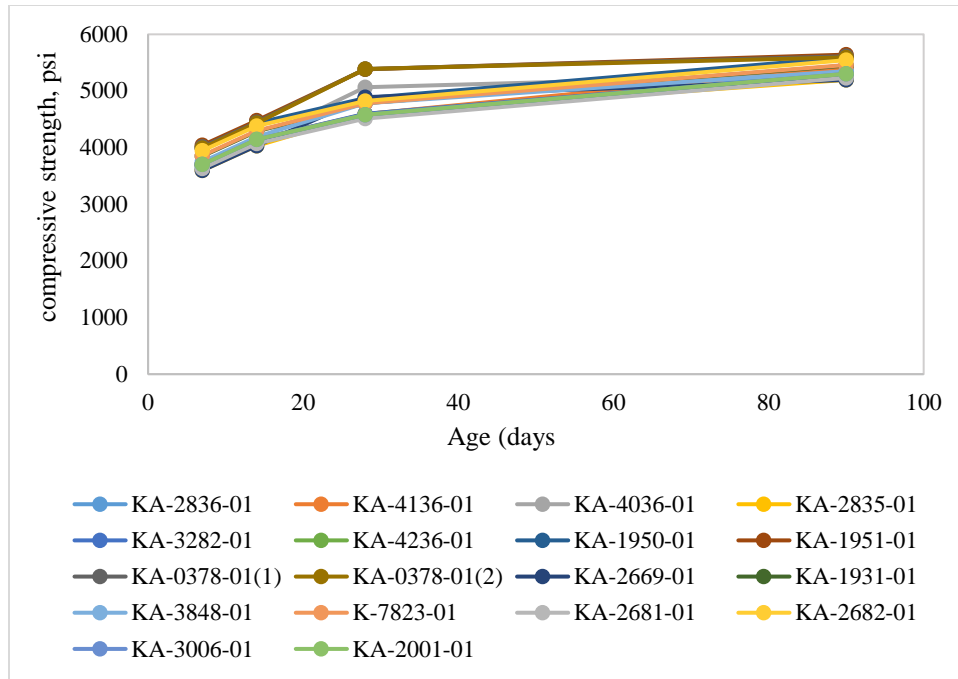


Figure 3-11 Strength gains over time for the selected JPCP projects

The long-term concrete strength model developed under the FHWA (2012) project was used to determine the 20-year compressive strength. Equation 3.9 lists the long-term compressive strength model.

$$f_{c,LT} = -3467.3508 + 3.63452 * CMC + 0.42362 * uw^2 \quad (3.9)$$

Where:

$f_{c,LT}$  = Compressive strength at age  $t$  years, psi;

$CMC$  = Cementitious materials content, lb/yd<sup>3</sup>; and

$uw$  = Unit weight, lb/yd<sup>3</sup>.

For level 3 analysis, the software requires the following combination of 28-day compressive strength, 28-day elastic modulus, and 28-day MOR (Islam et al., 2019):

- 28-day compressive strength only
- 28-day MOR only

- 28-day compressive strength and 28-day elastic modulus
- 28-day MOR and 28-day elastic modulus

All four options were used in this study to analyze the selected JPCP sections with the PMED software. The 28-day MOR, however, was not available for any of the projects, and the 28-day MOR and  $E_c$  were estimated using the standard empirical equations 3.10 and 3.11 (AASHTO, 2015).

$$E_c = 57000\sqrt{f'_c} \quad (3.10)$$

$$MOR = 9.5\sqrt{f'_c} \quad (3.11)$$

### 3.6.2.2 JPCP design inputs

In this study, project-specific PCC thickness and joint spacing, cement content, w/c ratio, and aggregate type information were extracted from the CMS database. Dowel diameters and dowel spacing information were also available in the CMS database. Dowel spacing was 12 in. for each of the selected JPCP sections. Site-specific JPCP design input parameters are listed in Table 3-9.

Table 3-9 Site-specific JPCP design input parameters

Project	Route	County	Slab width	Dowel diameter (in.)	PCC joint spacing (in.)	Tied shoulder
KA-2836-01	I-70	Shawnee	12	1.5	15	Yes
KA-4136-01	I-70	Shawnee	12	1.375	30	Yes
KA-4036-01	I-70	Sherman	12	1.25	15	Yes
KA-2835-01	I-70	Wabaunsee	12	1.5	15	Yes
KA-3282-01	I-70	Wyandotte	12	1.25	20	Yes
KA-4236-01	I-135	Harvey	12	1.375	15	Yes
KA-1950-01	US-50	Marion	12	1.25	15	Yes
KA-1951-01	US-50	Chase	12	1.25	15	Yes
KA-0378-01(1)	US-50	Harvey	12	1.125	15	Yes
KA-0378-01(2)	US-50	Harvey	12	1.125	15	Yes
KA-2669-01	US-54	Shawnee	12	1.375	15	Yes
KA-1931-01	US-81	Cloud	12	1.25	15	Yes
KA-3848-01	US-400	Labette	12	1.125	15	Yes
K-7823-01	K-7	Johnson	12	1.5	15	No
KA-2681-01	K-57	Marion	15	1.25	15	No
KA-2682-01	K-150	Chase	15	1.25	15	No
KA-3006-01	K-156	Finney	12	1.125	15	Yes
KA-2001-01	K-254	Butler	1.125	12	15	Yes

### 3.6.3 Base layer inputs

All selected AC over JPCP sections have a treated base layer beneath the PCC layer.

PCTB and BDB were used in the selected sections. Required inputs of the base layers for the



PMED software are presented in Table 3-10. Values of these input parameters were suggested by KDOT.

Table 3-10 Input parameters of base layer

Base layer type	Thickness	Elastic/Resilient Modulus	Poisson's ratio
PCTB	Project-specific	1,000,000 psi	0.2
BDB	Project-specific	650,000 psi	0.35

### 3.6.4 Subgrade soil inputs

The subgrade soil of the selected AC over JPCP sections were A-6 and A-7-6. The top 6 in. layer of all selected projects was treated with lime or fly ash or mechanically stabilized. The top 18 in. of the subgrade was compacted to 95% of the maximum dry density on all projects. County-wise resilient modulus ( $M_R$ ) data were provided by KDOT. Subgrade soil gradation and Atterberg limits values were extracted from the soil survey reports of the Soil Conservation Service for each county. The resilient modulus of the lime or fly ash-treated subgrade layer was computed using equation 3.12 (Sun et al., 2014). The county-wise subgrade soil properties are presented in Appendix B.

$$\text{Treated subgrade } M_R = (2.03 \times \text{untreated subgrade } M_R) + 225 \quad (3.12)$$

### 3.7 Climatic Inputs

Environmental conditions, specifically moisture and temperature, significantly affect rigid and flexible pavement performance (NCHRP 1-37A). Unbound layer material performance generally is affected by moisture change, and bound layer material performance is affected by the temperature gradient (Kim et al., 2011). The Enhanced Integrated Climatic Model (EICM) incorporated in the AASHTOWare PMED software considers moisture and temperature effects

on pavement response (AASHTO, 2015). The EICM is a heat and moisture flow program that simulates changes in material properties over time by considering climatic data of the closest weather station. These climatic data include air temperature, relative humidity, precipitation, wind speed, sunshine percentage, and rainfall.

The AASHTOWare PMED version 2.5 incorporates modern-era retrospective analysis for research and application (MERRA) climatic data developed by the National Aeronautics and Space Administration (NASA). The MERRA database includes uniformly gridded meteorological data at an hourly temporal resolution and 0.5 degrees latitude by 0.67 degrees longitude (approximately 31 miles by 37 miles at mid-latitudes) spatial resolution over the entire globe (Ziedan, 2017). This study used project coordinates for all selected rehabilitated sections as site-specific values, or level 1 inputs.

### **3.8 Evaluation of KDOT Distress Data**

In 2013, KDOT began using the laser crack measurement system (LCMS) to collect automated pavement distress data on the entire road network. Since then, KDOT has conducted windshield surveys to manually collect distress data. LCMS-generated automated distress data were primarily used in this study. However, for pavement sections overlaid prior to 2013, manually collected distress data were used.

#### ***3.8.1 Laser crack measurement system***

The LCMS consists of two high-performance three-dimensional (3-D) laser profilers that measure complete transverse road profiles with 1-mm resolution at highway speed. Figure 3-12 shows the KDOT LCMS system used in this study. The  $z$ -axis resolution is 0.1 mm in the figure. The 3-D laser profilers use high-power laser line projectors, custom filters, and a camera as the detector. The light strip is projected onto the pavement, and the camera captures its image. The

shape of the pavement is acquired as the inspection vehicle travels along the road using a signal from an odometer to synchronize the sensor acquisition. All images coming from the camera are sent to the frame grabber to be digitized and processed by the central processing unit. Saving the raw images would require storing nearly 30 GB per kilometer at 100 km/h, but the use of lossless data compression algorithms for the 3-D data and fast jpeg compression on the intensity data brings the data rate down to a manageable 20Mb/s or 720Mb/km (Laurent et al., 2017). The high resolution 3-D data acquired by LCMS is then processed using proprietary algorithms that were developed to automatically extract crack data, including crack type and severity, rutting, potholes, and raveling. Cracks are generally categorized as longitudinal or transverse. The severity level of a crack is determined by the width of the crack and usually classified into low, medium, and high severity levels. LCMS can be operated under various types of lighting conditions and on various pavement types (Laurent and Hebert, 2002).



Figure 3-12 KDOT Laser crack measurement system

### ***3.8.2 Interpretation of LCMS data***

The LCMS-generated cracking data were interpreted and quantified following the AASHTO Standard PP 67-16 and AASHTO Standard 68-14. According to the AASHTO PP 67-16 standard, cracking measurements were based on the five measurement zones of the pavement section created by the wheel paths and the areas between and outside the wheel paths.

Three types of cracking are defined in AASHTO PP 67-16: transverse cracking, longitudinal cracking, and pattern cracking. Figure 3-13 shows the cross section of a survey lane with wheel paths and survey area between wheel paths.

#### *Longitudinal Crack*

According to AASHTO, a longitudinal crack is at least 12 in. long with a crack orientation between  $\pm 20$  degrees relative to the lane centerline. Longitudinal cracks are reported as the sum of longitudinal cracks across the five measurement zones. However, in this study, longitudinal cracks were computed considering only zone 2, zone 3, and zone 4, since these three zones typically reflect the impact of traffic loading (AASHTO PP 67-16).

#### *Pattern Crack*

AASHTO defines pattern crack as a network of cracks that form an identifiable area or grouping of cracks. These crack groups are determined by interconnecting cracks with lengths less than 12 in. In this study, pattern cracks were also computed considering cracks in zone 2, zone 3, and zone 4.

#### *Transverse Crack*

According to AASHTO PP 67-16 standard, a transverse crack is at least 12 in. long with a crack orientation between 70 and 110 degrees relative to the lane centerline.

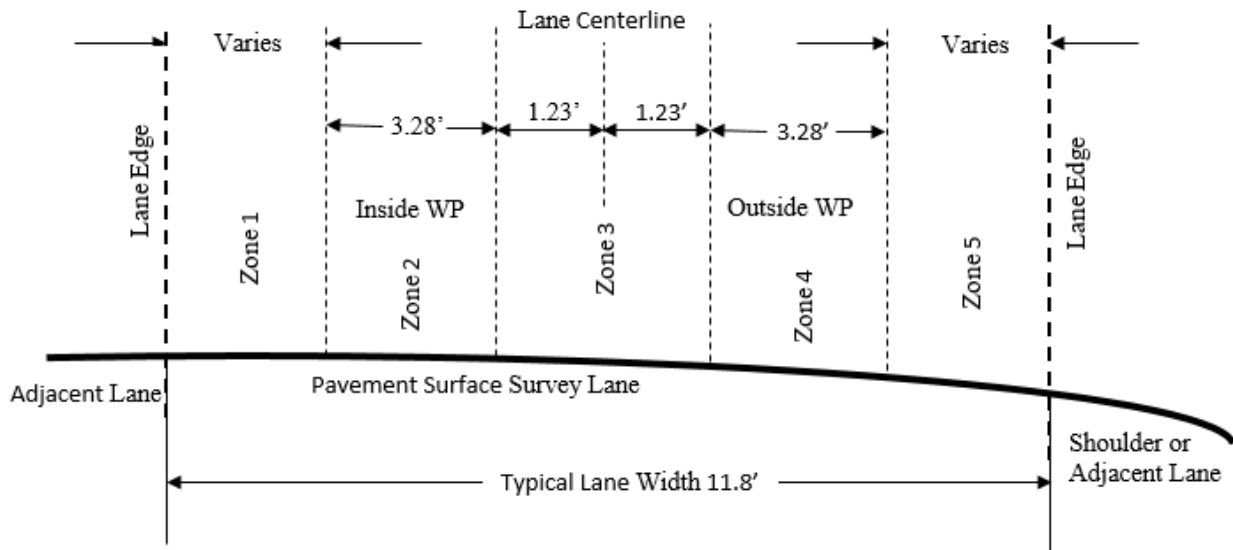


Figure 3-13 Cross section of survey lane with wheel paths and survey area between wheel paths (AASHTO PP 67-16)

Cracking values are reported in linear feet, and the LCMS reported distress/IRI values every 0.1 mile. In this study, cracking values at every 0.1-mile segment were added for the total length of the project and normalized every mile. However, because there were bridges at some of the 0.1-mile segments, distress values of those segments were not included in the analysis. Longitudinal and pattern cracking were considered top-down fatigue cracking, since KDOT recognizes all load-related cracking to be top-down cracking.

### 3.8.3 Manual distress data collection method

KDOT used to collect pavement distresses by conducting windshield surveys in which three 100-foot samples were surveyed per 1-mile segment. These distresses were then extrapolated for a 1-mile segment and reported in the PMIS database. Only distress types predicted by the AASHTOWare PMED have been considered in this study. All load-related cracking was considered top-down. Rutting and IRI values were reported for every mile in the PMIS database.

### 3.8.4 Comparison of pavement distresses to trigger values

According to the NCHRP 1-40 B local calibration guide, the magnitudes of time-series distress and IRI values should be compared with the design threshold values for each distress type and IRI to investigate whether extracted distresses/IRI from the selected projects are typical for the locale (AASHTO, 2010). In addition, the average maximum measured distress values should exceed 50% of the design criteria. If distress/IRI values from the selected projects are significantly lower than the agency's design criteria for a distress type, the accuracy and bias of the transfer function may not be well defined at the values that trigger major rehabilitation. Table 3-11 lists KDOT-specified failure criteria/trigger values for the considered pavement distress types for the AC overlays.

Table 3-11 KDOT-specified failure criteria for pavement distresses

Distress Type	KDOT Trigger Value
Terminal IRI (in./mile)	164
Permanent deformation – AC only (in.)	0.25
AC top-down fatigue cracking (ft/mile)	500
AC total transverse cracking: thermal + reflective (ft/mile)	1200

The distribution of each distress type for the selected pavement sections is shown in Figures 3-14 through 3-17. The following results were observed while analyzing measured data from the selected pavement sections:

- Approximately 50% of the measured AC rut depth ranged from 0.05 to 0.1 for AC over AC and AC over JPCP sections. No measurements exceeded the trigger value of 0.25 in. for the rehabilitated JPCP sections. Only 3% of the measured rut depth exceeded the trigger value for AC over AC sections. Average rut depths across all AC over AC and

AC over JPCP projects were 0.1 and 0.09 in., respectively, which are close to 50% of the design criteria (0.125 in.)

- Approximately 55% of the measured top-down cracking data for AC over AC sections exceeded the agency-specified trigger value of 500 ft/mile. Average measured top-down cracking across all the rehabilitated AC projects was 1,180 ft/mile, and 24% of the measured longitudinal data exceeded the trigger value for the AC over JPCP sections. The average top-down cracking data across all AC over JPCP projects was 1,050 ft/mile. In addition, the standard deviations of measured top-down cracking across the AC over AC projects and AC over JPCP projects were 2,000 ft/mile and 1,850 ft/mile, respectively, which suggests that longitudinal cracking varies significantly from project to project in Kansas.
- Approximately 85% of the measured transverse cracking was less than 200 ft/mile for AC over AC sections. None of the measured transverse data exceeded the agency-specific trigger value of 1,200 ft/mile for AC over AC sections. On the other hand, 20% of the measured transverse cracking data exceeded the trigger value for the AC over JPCP sections. Average measured transverse cracking across all AC over AC projects and AC over JPCP projects were 103 ft/mile and 365 ft/mile, respectively. In addition, the standard deviation of measured transverse cracking across all AC rehabilitation sections was 200 ft/mile; for JPCP rehabilitation projects, the standard deviation was 530 ft/mile. The variation in transverse cracking was higher in JPCP rehabilitation sections than AC rehabilitation sections.
- All measured IRI values were well within the agency-specific limiting value. The average measured IRI for both selected AC rehabilitation and JPCP rehabilitation sections was 57

in./mile, which is below the 50% agency-specific trigger value, suggesting that the predictive IRI model may not be accurate enough for projects with high IRI values.

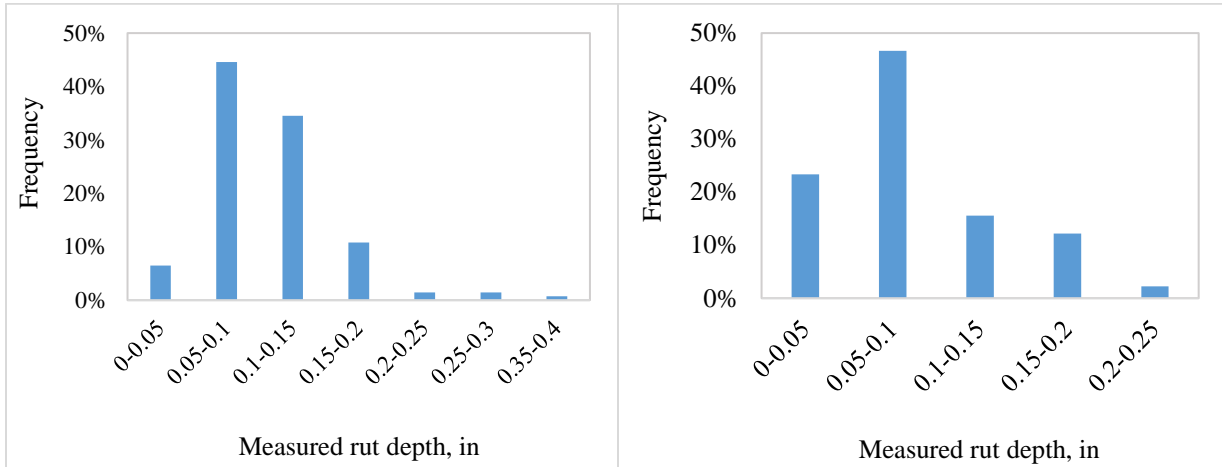


Figure 3-14 Rut depth on selected AC over JPCP (left) and AC over AC (right) sections

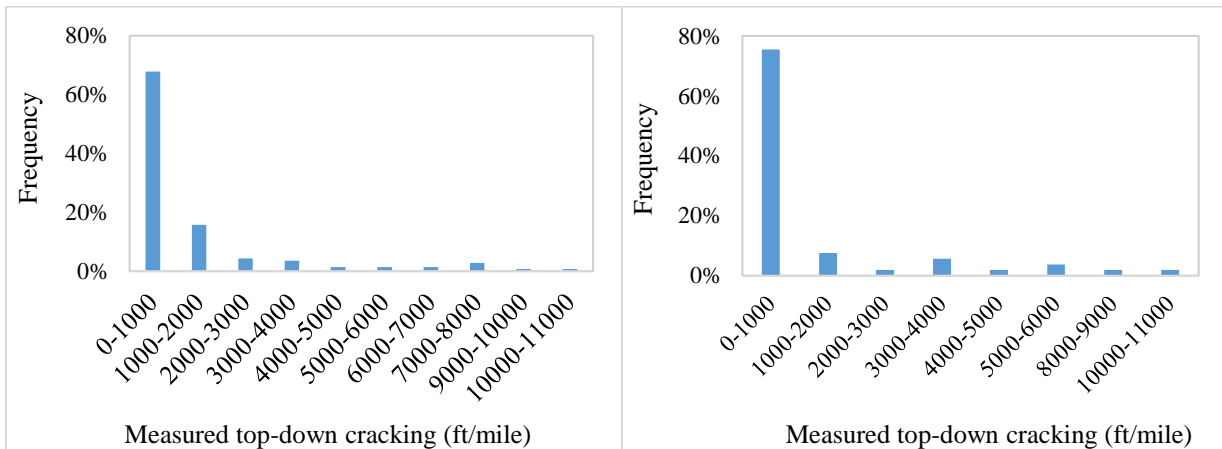


Figure 3-15 Top-down cracking in selected AC over AC (left) and AC over JPCP (right) sections



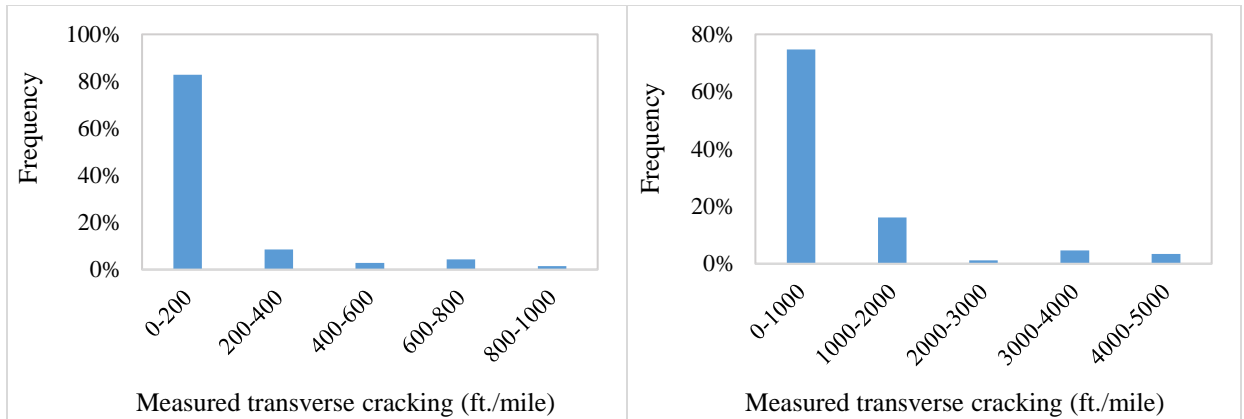


Figure 3-16 Transverse cracking in AC over AC (left) and AC over JPCP (right) sections

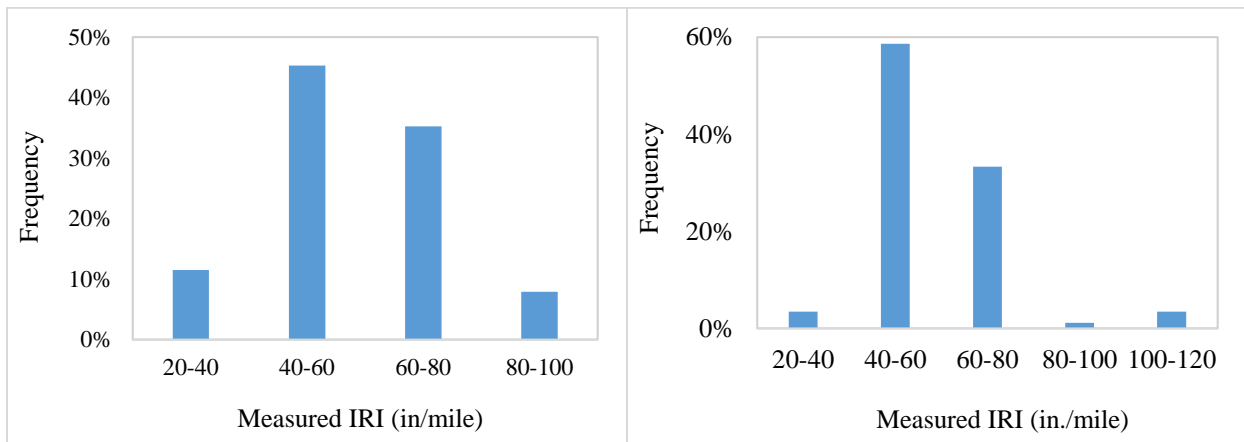


Figure 3-17 Measured IRI in selected AC over AC (left) and AC over JPCP (right) sections

### 3.8.5 Evaluation of distress/IRI data

This study evaluated measured distress/IRI data to identify potential outliers. In addition, time-series plots for each distress type were inspected for all selected projects to ensure that the observed trends in distress/IRI were reasonable.

#### *Investigation of potential outlier*

To identify outlier and influential points, first quartile ( $Q1$ ), third quartile ( $Q3$ ), and interquartile range ( $IQR$ ) of each distress type were computed. The upper bound and lower bound were calculated following Equations 3.13 and 3.14:

$$\text{Upper bound} = Q3 + 1.5 * IQR \quad (3.13)$$

$$\text{Lower bound} = Q1 - 1.5 * IQR \quad (3.14)$$

Any values outside the upper and lower bounds were considered outliers. Boxplots with outliers for each distress type are shown in Figures 3-18 through 3-21.

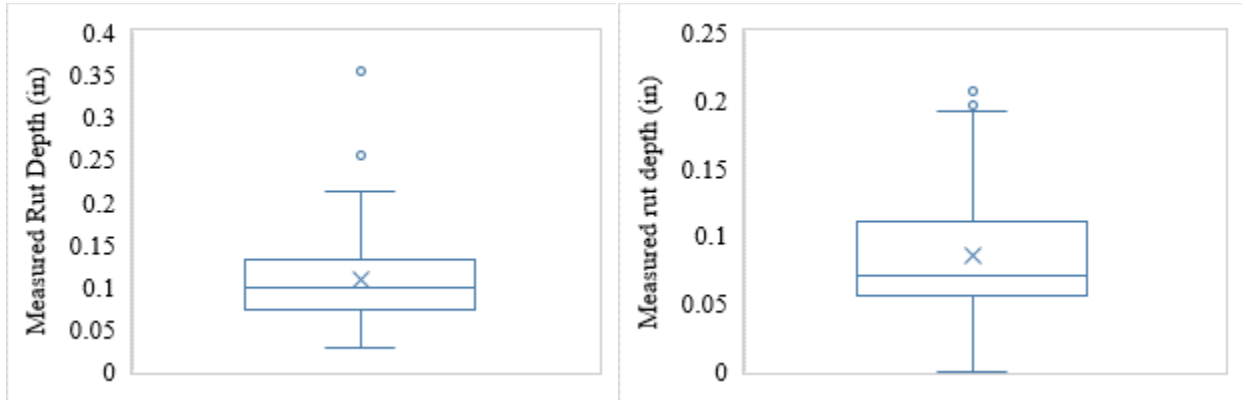


Figure 3-18 Rutting measurements for AC over AC (left) and AC over JPCP (right) sections

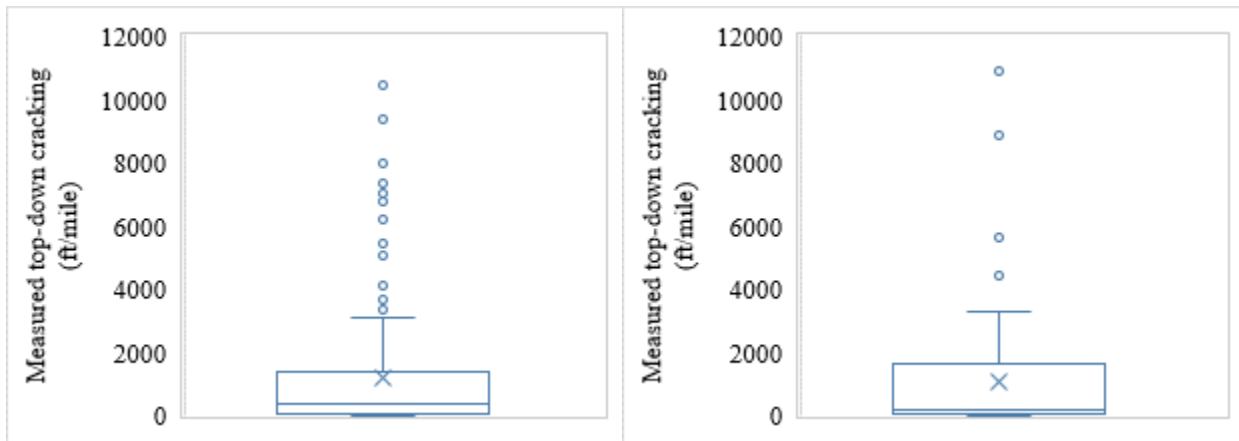


Figure 3-19 Top-down crack measurements for AC over AC (left) and AC over JPCP (right) sections

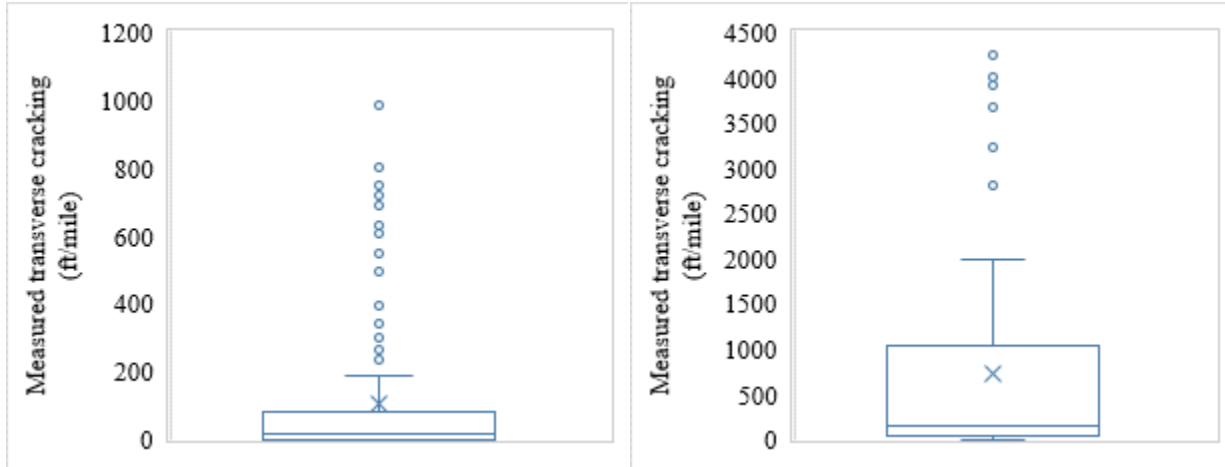


Figure 3-20 Transverse cracking measurements for AC over AC (left) and AC over JPCP (right) sections

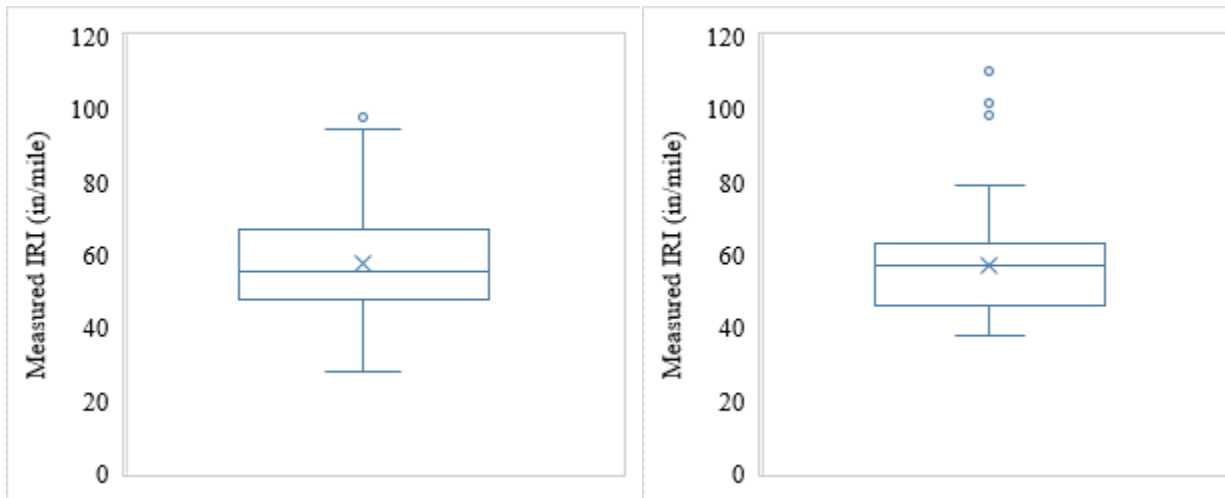


Figure 3-21 Transverse cracking measurements for AC over AC (left) and AC over JPCP (right) sections

*Inspection of time-series plot*

Time-series plots of distress/IRI were visually inspected for each project to identify unexpected trend among measurements. Distress measurements for a project were expected to increase with time if no maintenance or treatment actions were performed. However, for some projects, distress measurements on a survey date were lower than the previous year. For instance,

the time-series plot of transverse cracking for project KA-2836-01 (Figure 3-22) shows a reduction in transverse cracking in 2017 compared to the previous two years. No maintenance or treatment action was recorded in the KDOT PMIS database for this project in 2017. In addition, a time-series plot of longitudinal cracking for project KA-1951-01 (Figure 3-23) shows an unusual pattern in longitudinal cracking for this project. KDOT does not keep record of in-house maintenance activities, and thus it is impossible to explain such an unusual trend in distress observation, even with LCMS measurements.

This study normalized the distress data for a particular project and a particular year for a 1-mile segment. For projects in which an unusual time-series pattern was observed, distress data for the entire project was scrutinized, and segments with unusual distress trends were discarded. Additionally, some observations were removed and not considered for analysis. For example, the transverse cracking measurement for project KA-2836-01 in 2017 was not considered when analyzing the transverse cracking model. Each distress type was considered individually.

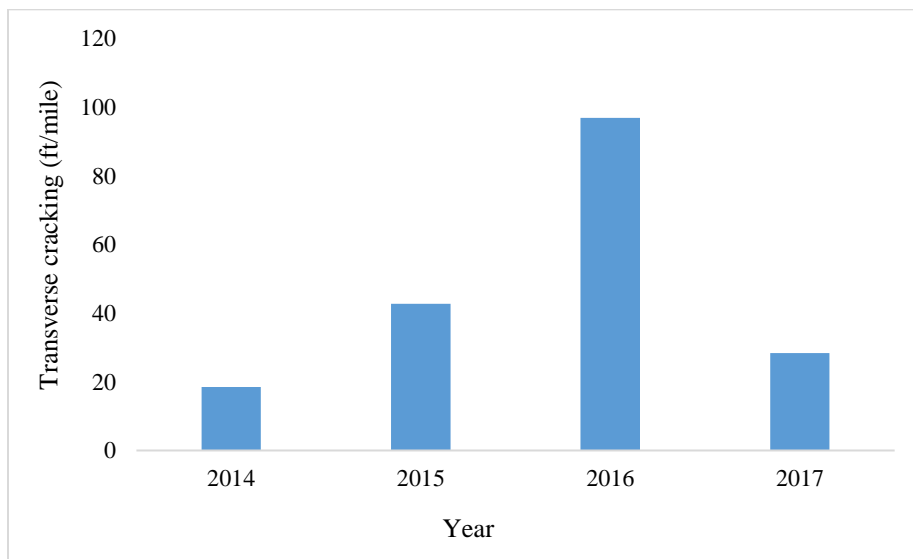


Figure 3-22 Time-series plot of measured transverse cracking for project KA-2836-01

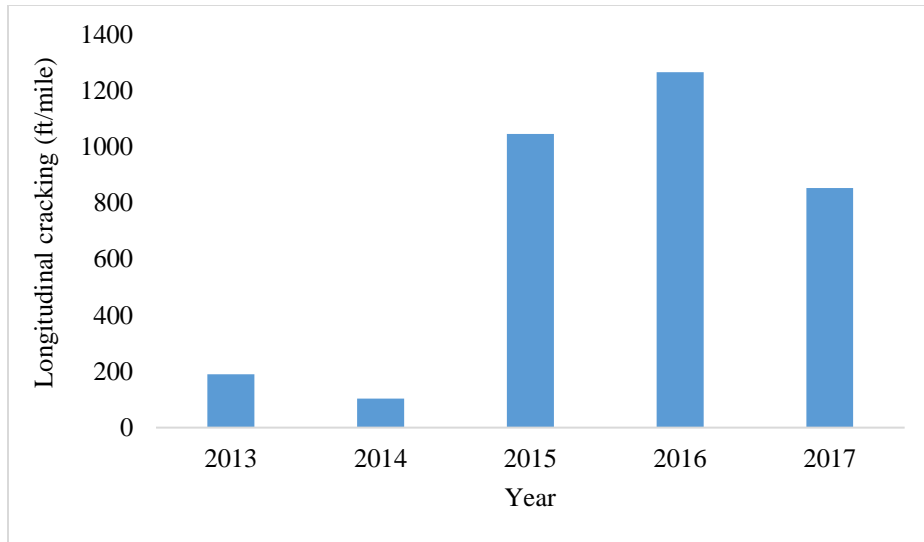


Figure 3-23 Time-series plot of measured longitudinal cracking for project KA-1951-01

### 3.9 Characterizing Existing Pavement Layers

Characterizing existing pavement structure damage is one of the primary requirements for rehabilitated pavement design in the AASHTOWare PMED software. The software considers development of distresses on AC overlay and the continuation of damage in the existing JPCP or AC layer (AASHTO, 2015).

#### 3.9.1 AC pavement rehabilitation

The PMED software assumes pre-overlay damage as the starting point for future performance prediction with necessary adjustments for pre-overlay repairs (AASHTO, 2010). The PMED manual of practice (AASHTO, 2015) lists eight categories for assessing existing pavement condition: structural adequacy, functional adequacy, subsurface drainage accuracy, material durability, shoulder structural profile and condition, extent of maintenance activities performed in the past, variation of pavement condition, and miscellaneous constraints, such as bridge and lateral clearance. The manual of practice (AASHTO, 2015) also states that

determination of the extent of damage and in-situ material properties is the most critical challenge for existing pavement evaluation.

### 3.9.1.1 Volumetric properties

AASHTOWare PMED software requires mixture volumetric properties to characterize the existing AC layer. Mixture volumetrics include percent air void, effective binder content, Poisson's ratio, and unit weight of the HMA mix. The existing AC layer unit weight and the percent air void information were extracted from KDOT CMS for this study. The range of unit weight for the AC overlay of the selected rehabilitation projects varied from 128 lb/ft<sup>3</sup> to 150 lb/ft<sup>3</sup>. Figure 3-24 shows the distribution of unit weight in the HMA mixes for all the overlay mixes. The Poisson's ratio for all HMA mixtures was assumed to be 0.35.

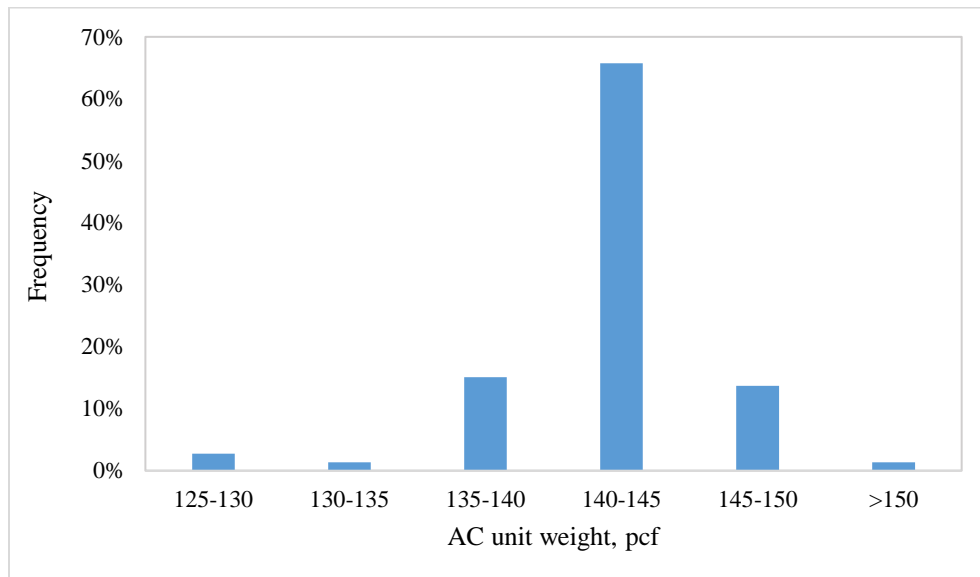


Figure 3-24 AC unit weight distribution of overlay AC mixes

The void filled with asphalt (VFA) and VMA of the existing layer of HMA mixes were available in the CMS, while the effective binder content (by volume) was computed by

subtracting the AC target air void from the VMA. Frequency distribution of effective binder content of AC mixes for the selected JPCP rehabilitated sections is presented in Figure 3-25. The existing AC mix gradation and binder grade information were also available in the CMS database. Appendix B presents the layer mixture properties of the AC over AC sections considered for this study.

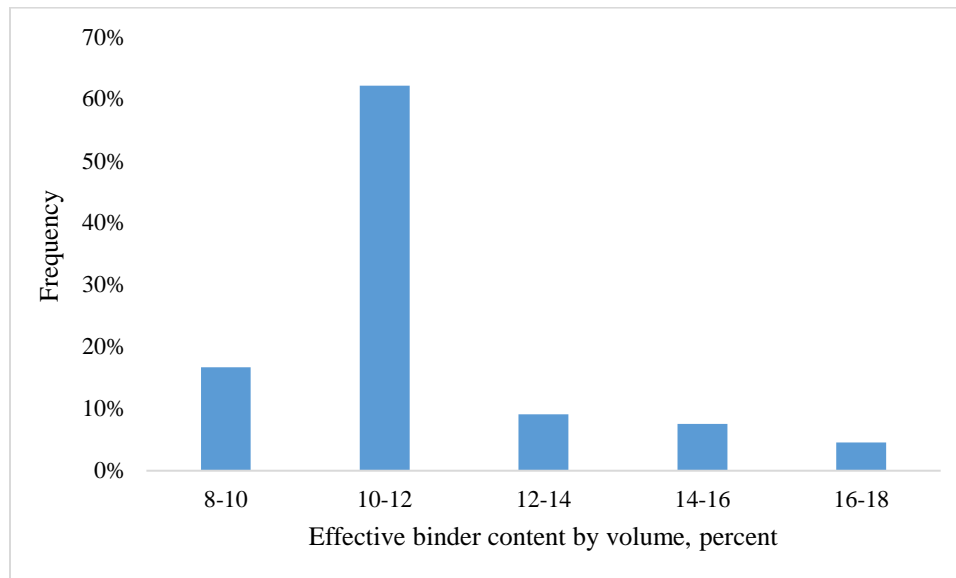


Figure 3-25 Effective binder content distribution in overlay HMA mixes

### 3.9.1.2 Mechanical properties

AASHTOWare PMED software allows three hierarchical levels of inputs to characterize existing AC pavement. For level 1 rehabilitation input, the PMED software requires backcalculated moduli from the falling weight deflectometer (FWD) testing. The corresponding pavement temperature and FWD load frequency information are also required to develop damaged modulus master curves. The software uses undamaged and damaged AC dynamic modulus master curves to compute existing AC pavement damage. Ayala et al. (2017) explained

the PMED damage characterization process for existing pavements. At undamaged state, the AC dynamic modulus,  $|E^*|$  is obtained using equation 3.15.

$$|\log E^*| = \delta + \frac{\alpha}{1 + e^{\beta + \delta \log t_r}} \quad (3.15)$$

Where:

$\delta$ ,  $\alpha$ ,  $\beta$ , and  $\delta$  = dynamic modulus mastercurve parameters; and

$t_r$  = reduced time, which is a function of loading time  $t$  and time temperature shift factor,  $a_t$ .

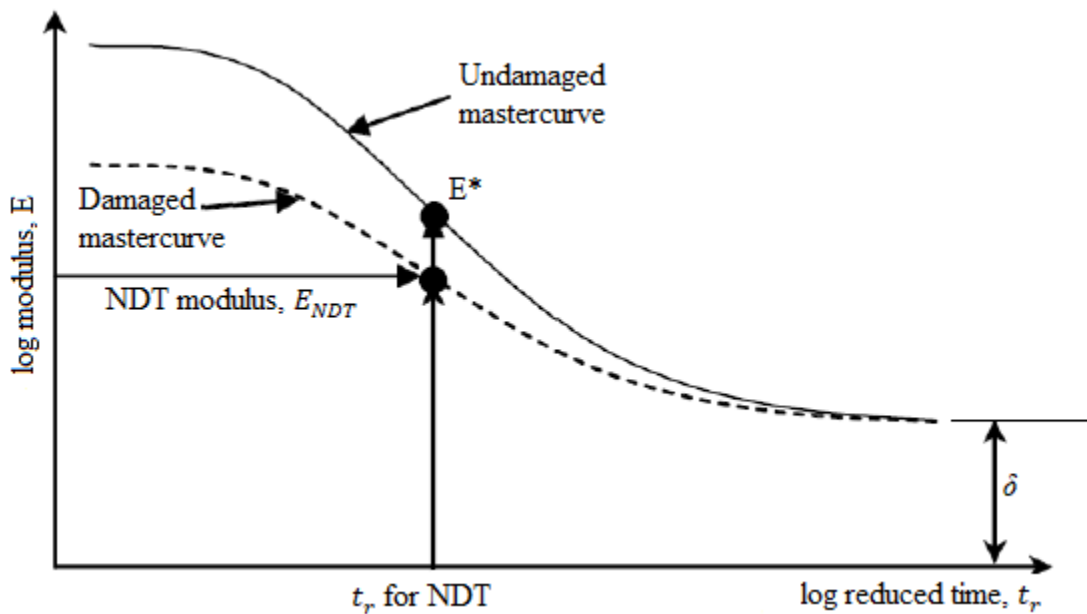


Figure 3-26 AC layer damage computation for level 1 inputs (NCHRP 1-37A, 2004)

The PMED software computes the accumulative damage in the existing AC by reducing the undamaged modulus. Figure 3-26 shows the PMED software damage computation process of existing AC pavements (NCHRP 1-37A, 2004) for level 1 inputs, including damaged and undamaged master curves. The damaged master curve is obtained by vertically shifting the undamaged master curve downward so that the latter curve passes through the  $E_{NDT}$  point.  $E_{NDT}$  is



the existing AC in-situ modulus backcalculated from FWD tests. Damage in the existing AC pavement,  $d_{AC}$ , is then computed using equation 3.16.

$$E_{NDT} = 10^\delta + \frac{E_{PRED} - 10^\delta}{1 + e^{-0.3 + 0.5 \log d_{AC}}} \quad (3.16)$$

Where:

$E_{pred}$  = Undamaged modulus; and

$E_{NDT}$  = Existing AC in-situ modulus backcalculated from FWD testing.

Pre-overlay FWD deflection data were available for 16 AC over AC projects of the 25 sections selected for this study. For a few cases, however, the duration between FWD testing and overlay placement was more than 1 year, so FWD test information would not exactly represent pre-overlay damage of the existing pavement. However, the PMED software uses pre-overlay condition data for both level 1 and level 2 inputs, including percent fatigue cracking, transverse cracking, and layer-wise permanent deformation information. In this study, the latest pavement condition data available for each AC rehabilitation project were less than 1 year old from the time of overlay construction.

Table 3-12 lists the available FWD testing information for the AC over AC projects. The LTPP seven sensors configuration was for FWD testing for each of these projects.

Table 3-12 FWD testing data available for the AC over AC section

Project	Route	County	FWD test date	Overlay construction date
KA-4013-01	US-24	Osborne	October 2013	May 2015
KA-1436-01	US-36	Cheyenne	July 2003	August 2009
KA-0813-01	US-36	Washington	June 2003	December 2007
KA-0811-01	US-75	Montgomery	July 2002	August 2007
KA-0310-01	US-75	Osage	July 2003	September 2006
KA-4192-01	US-77	Butler	September 2015	December 2015
KA-2941-01	US-77	Butler	June 2012	August 2013
KA-1480-01	US-160	Clark	July 2005	May 2009
KA-1460-01	US-166	Cowley	October 2008	December 2009
KA-2200-01	US-169	Allen	July 2013	January 2015
KA-2204-01	US-169	Anderson	August 2011	January 2015
KA-1444-01(1)	US-183	Phillips	August 2005	September 2009
KA-1444-01(2)	US-183	Phillips	August 2005	September 2009
KA-3674-01	US-283	Norton	June 2014	May 2015
K-9364-01	K-92	Jefferson	June 2001	April 2004
KA-3496-01	K-254	Sedgwick	November 2003	November 2004

The AASHTOWare PMED software requires backcalculated AC moduli of existing pavement and corresponding pavement temperature and loading frequency at the time of FWD testing (Bech, 2015). KDOT operates one Dynatest 8000 and one Jils FWD. The typical load pulse duration of a Dynatest FWD is 15-35 ms, and the resulting load frequency is 29–67 Hz

(Ayala et al., 2016). Gedafa et al. (2010) previously studied existing AC pavement stiffness from FWD testing and laboratory dynamic modulus testing collected from field cores. They assumed a loading frequency of 25 Hz to compare the backcalculated modulus with the laboratory-tested dynamic modulus. Rao and Von Quintus (2015) recommended using a FWD loading frequency of 30 Hz for PMED software input.

This study used EVERCALC version 5.0 software to backcalculate the existing AC pavement moduli for the projects listed in Table 3-12. Backcalculation results were obtained for each FWD drop at a 9,000-lb (9-kip) load level. Any resulting backcalculated modulus yielding a root mean square error more than 5% was eliminated from the analysis. Figure 3-27 shows the backcalculated moduli for the pavement section KA-1436-01, and Appendix D presents the backcalculated moduli for pavement sections listed in Table 3-12. The pavement temperature at the time of the FWD testing was 126–133 °F.

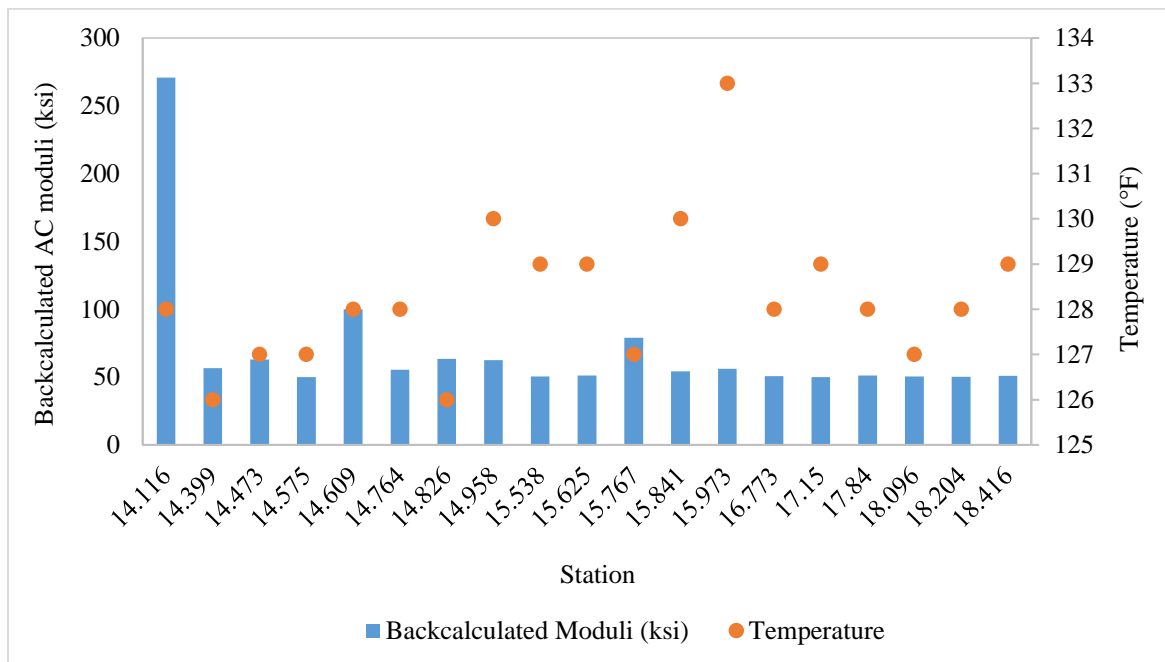


Figure 3-27 Backcalculated moduli for pavement section KA-1436-01

Figure 3-27 shows that the backcalculated AC moduli varied significantly along the length of pavement section KA-1436-01. Variation in backcalculated moduli along the pavement section was observed for other projects as well. These backcalculated AC moduli were then evaluated to identify potential outliers. First quartile ( $Q1$ ), third quartile ( $Q3$ ), and interquartile range ( $IQR$ ) values were computed, and boxplots were drawn to identify outlier and influential points. The boxplot for backcalculated AC moduli of the KA-1436-01 section is shown in Figure 3-28. The figure shows two distinct outliers that were removed from the analysis of damage characterization of existing AC layers of section KA-1436-01. The same inspection procedure was followed for backcalculated AC moduli for every project listed in Table 3-12.



Figure 3-28 Boxplot of backcalculated AC moduli for pavement section KA-1436-01

Backcalculated moduli are not required for level 2 AC rehabilitation input. PMED software predicts damage from existing pavement fatigue cracking quantity and severity using an empirical transfer function presented in Equation 3.17 (NCHRP, 2004).

$$FC = \left(\frac{1}{60}\right) \frac{C_4}{1 + e^{c_1 c_1' + c_2 c_2' \log(d_{AC} * 100)}} \quad (3.17)$$

where  $C_1$ ,  $C_2$ , and  $C_4$  are transfer function coefficients. For the globally calibrated AASHTOWare PMED model,  $C_1 = 1$ ,  $C_2 = 1$  and,  $C_4 = 6.0$ .

The  $C_1'$  and  $C_2'$  parameters are computed from equation 3.18 and equation 3.19.

$$C_1' = -2 * C_2' \quad (3.18)$$

$$C_2' = -2.40874 - 39.748(1 + H_{AC})^{-2.856} \quad (3.19)$$

where  $H_{AC}$  is the total thickness of the AC layer.

FWD testing information was not available for nine projects of the 25 AC over AC sections considered in this study, so level 2 inputs were used for those projects.

### 3.9.1.3 Pre-overlay condition data

For both level 1 and level 2 AC rehabilitation inputs, PMED software requires pre-overlay condition data. For level 1 inputs, severity of fatigue cracking, severity and quantity of transverse cracking, and layer-wise rutting information are required. For level 2 inputs, both severity and quantity of the percent fatigue cracking information are required. This study considered all load-related fatigue cracking to be top-down and expressed in ft/mile because of the predominant construction of thick full-depth HMA pavements throughout Kansas and because the KDOT PMIS database does not differentiate between bottom-up or top-down cracks. For level 2 AC rehabilitation inputs, however, total longitudinal cracking values were multiplied by a lane width of 12 ft and subsequently converted to a percentage value.

Figures 3-29 through 3-32 present pre-overlay condition data for AC over AC sections considered for this study. The pre-overlay top-down cracking and transverse cracking varied significantly for the sections, potentially due to the change of pavement condition data collection

system in 2013 when KDOT began collecting automated pavement distress data on the entire road network using LCMS. Until 2013, KDOT conducted manual surveys to collect distress data. Additionally, an overlay rehabilitation decision triggered by ride comfort and no fatigue cracking can contribute to variation in the pre-overlay cracking pattern.

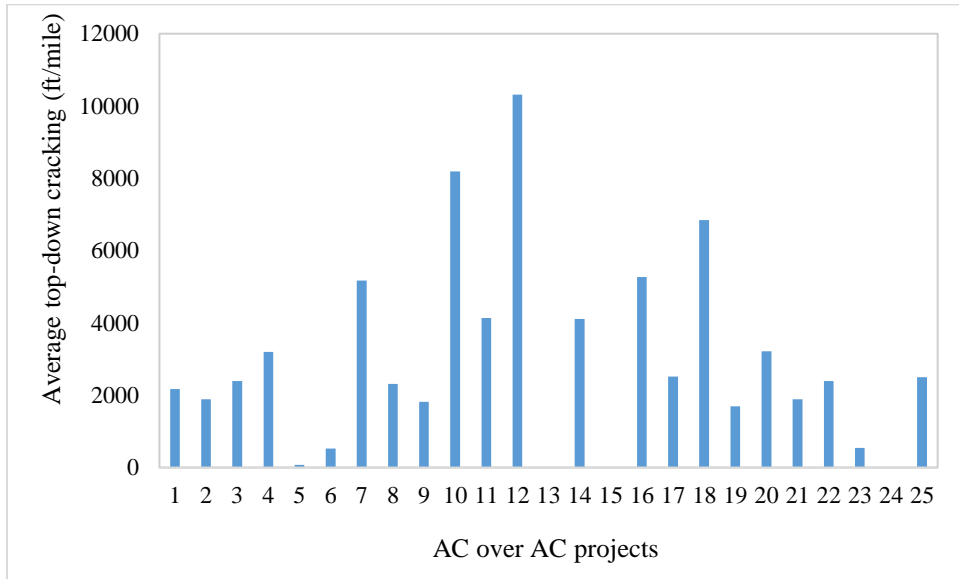


Figure 3-29 Pre-overlay top-down fatigue cracking for the AC over AC sections

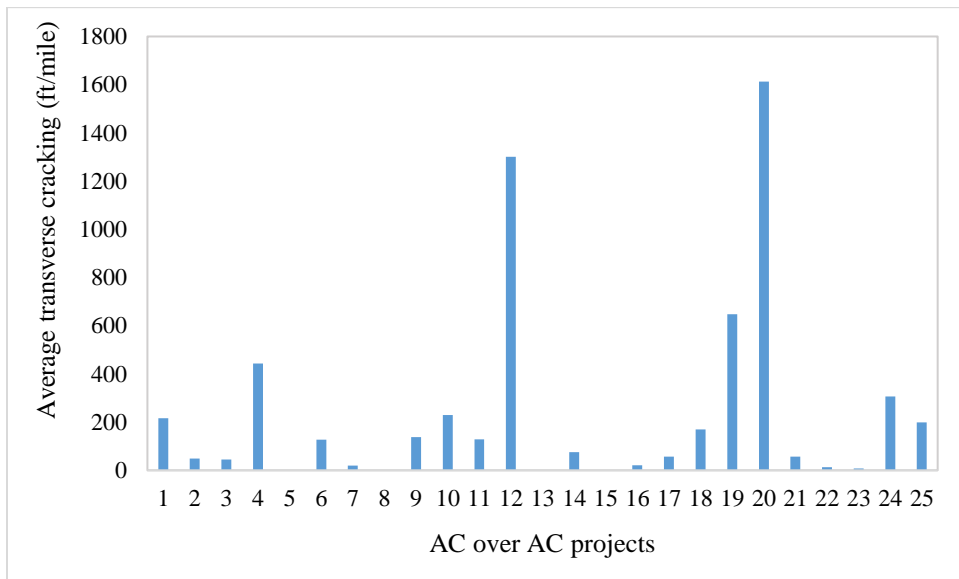


Figure 3-30 Pre-overlay transverse cracking for AC over AC sections

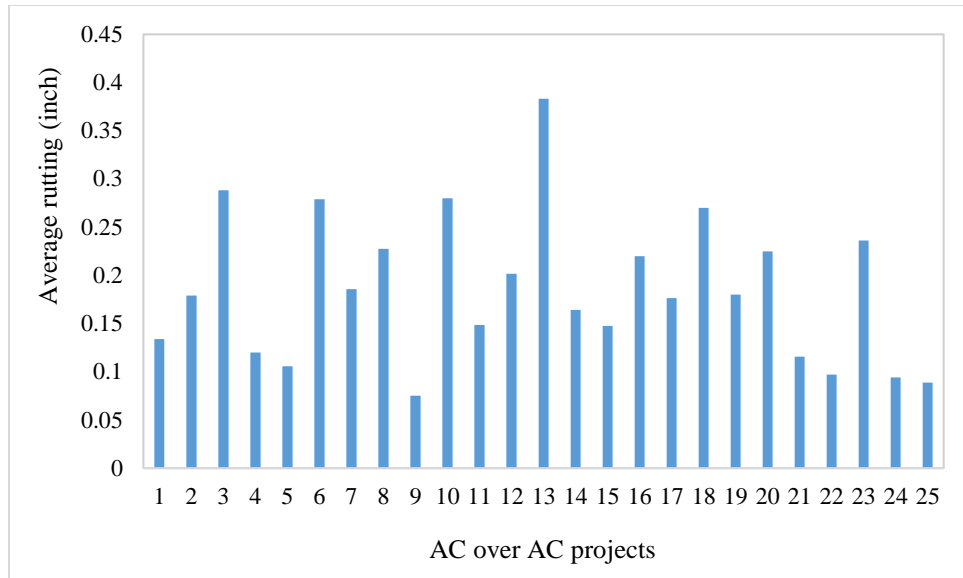


Figure 3-31 Pre-overlay permanent deformation for AC over AC sections

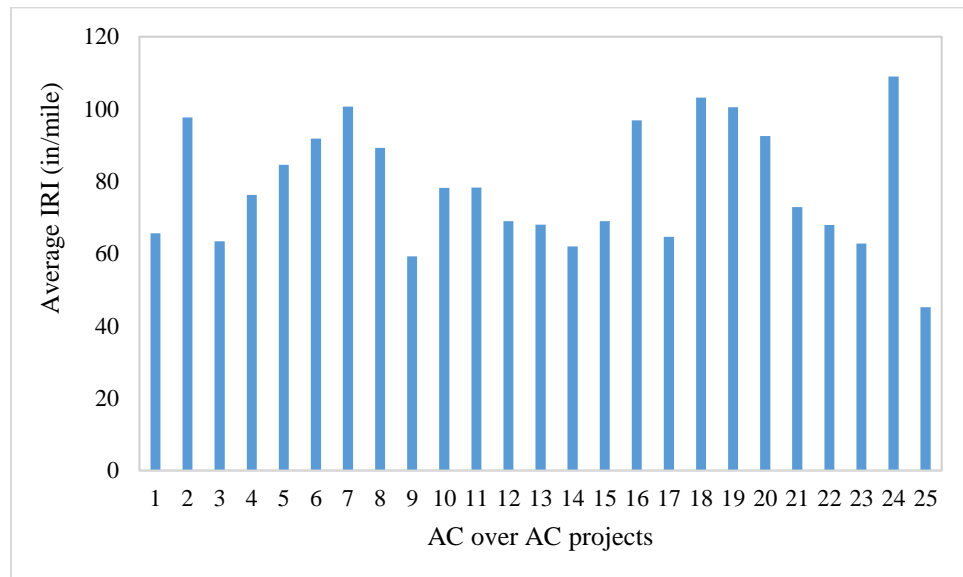


Figure 3-32 Pre-overlay IRI for AC over AC sections

### 3.9.2 JPCP rehabilitation

For JPCP rehabilitated sections, damage is computed from the total percent of slabs with transverse cracking and the percentage of replaced slabs (NCHRP, 2004). In addition, transverse joint load transfer efficiency (LTE) value is required to assess reflection cracking potential for JPCP sections with AC overlay.

KDOT does not collect transverse cracking data for JPCP sections since this slab cracking is not prevalent on its concrete pavement network. Thus, project-specific percent slab cracking data was not available. Furthermore, percent slab replacement information also was not available. In this study, 3% slab cracking was assumed to be the trigger value for rehabilitation of JPCP sections in Kansas. KDOT does not conduct FWD testing on concrete pavements prior to overlay, so site-specific LTE values were not available. However, project-specific joint faulting data were available. LTE is one of the contributory factors to transverse joint faulting in concrete pavements (Khazanovich and Gotlif, 2003). This study followed a KDOT-provided guideline to determine LTE values for the selected rehabilitated JPCP projects. This guideline is based on the assumptions that JPCP sections with high faulting values would have poor LTE values and JPCP sections with low faulting values would have good LTE values. Table 3-13 lists the guidelines for estimating LTE, and Figure 3-33 shows the mean joint faulting of the selected JPCP rehabilitated projects prior to overlay.

Table 3-13 KDOT guidelines for estimating LTE

Functional class of the roadway	Faulting criteria (in.)	Recommended LTE (%)
Interstate	< 0.1 in.	80%
	0.1–0.15 in.	65%
	> 0.15 in.	50%
Principal arterials	< 0.125 in.	80%
	0.125–0.20 in.	65%
	> 0.20 in.	50%
Local roads	< 0.15 in.	80%
	0.15–0.30 in.	65%
	> 0.30 in.	50%



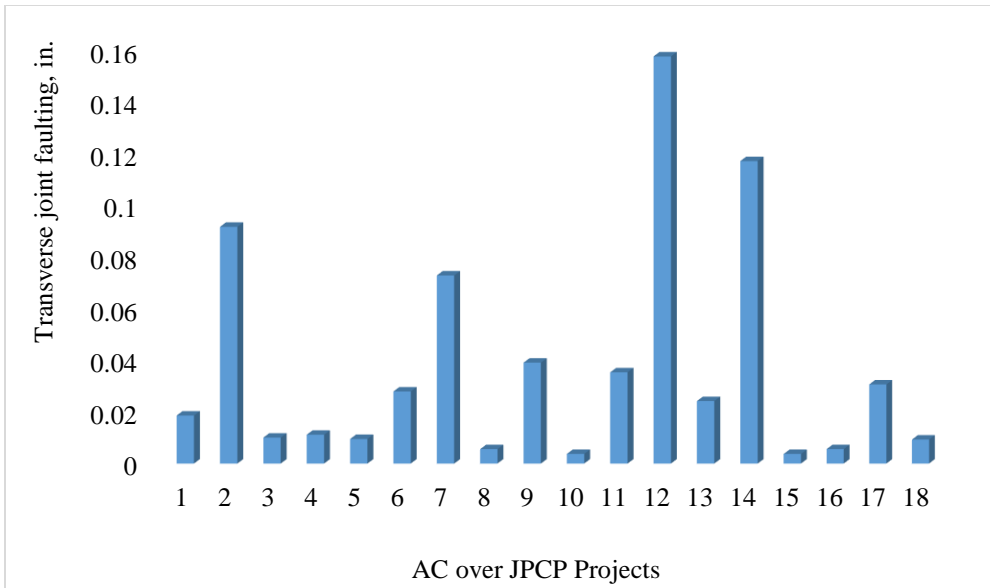


Figure 3-33 Transverse joint faulting of the JPCP rehabilitated project prior to overlay

## Chapter 4 - Local Calibration and Validation

The calibration procedure included assessing the bias with nationally calibrated coefficients, calibrating the performance models, and validating the performance models. Two types of models are embedded in the PMED software: structural response model and transfer functions. Calibration of the structural response models involves detailed laboratory testing, while later models empirically relate the structural models to pavement distresses. This study calibrated transfer functions of the performance models to Kansas conditions. This chapter describes local calibration of PMED performance models for AC over AC and AC over JPCP sections.

### 4.1 Local Calibration and Validation of AC over AC sections

During local calibration, null hypothesis for the sampling template was evaluated to determine the bias between measured and predicted distresses. Paired  $t$ -test was conducted to determine initial bias between the actual distresses and AASHTOWare-predicted results with globally calibrated coefficients at 95% confidence level. In addition, the ratio of standard error of estimate ( $S_e$ ) and standard deviation of the measured data ( $S_y$ ) was calculated for each distress model calibration to understand variability in the predicted performance and measured performance.  $S_e/S_y$  ratio greater than 1 indicated that variability in residual error between predicted and measured performances was larger than variability in the measured data;  $S_e/S_y$  ratio less than 1 indicated that variability in residual error was smaller than in the measured data. The second scenario is preferred for each distress model calibration (Kim et al., 2011).

#### 4.1.1 AC rutting model calibration for AC over AC sections

The AASHTOWare PMED software computes rutting on overlay and in existing AC layers. Computed rutting in existing layers accumulate at a decreased rate during the overlay

period due to the hardening effect of traffic prior to overlay (NCHRP, 2004). Permanent deformation in each layer of existing pavement at the time of overlay is used to predict future rutting in existing layers (AASHTO, 2015). A prior study calibrated the PMED rutting model for new flexible pavements in Kansas (Islam et al., 2019). The current study calibrated the total pavement rutting model for AC over AC sections.

#### 4.1.1.1 Bias assessment of the AC rutting model

Bias between measured and predicted rutting was computed to verify the total pavement permanent deformation model in PMED for AC rehabilitation sections. The globally calibrated rutting model showed significant bias in the paired  $t$ -test, and the null hypothesis was rejected at 95% confidence interval. The  $p$ -value from the paired  $t$ -test was less than 0.05, indicating that predicted and measured rutting differ. Measured versus predicted total rutting for globally calibrated coefficients are shown in Figure 4-1, and summary statistics of the fit are shown in Table 4-1.

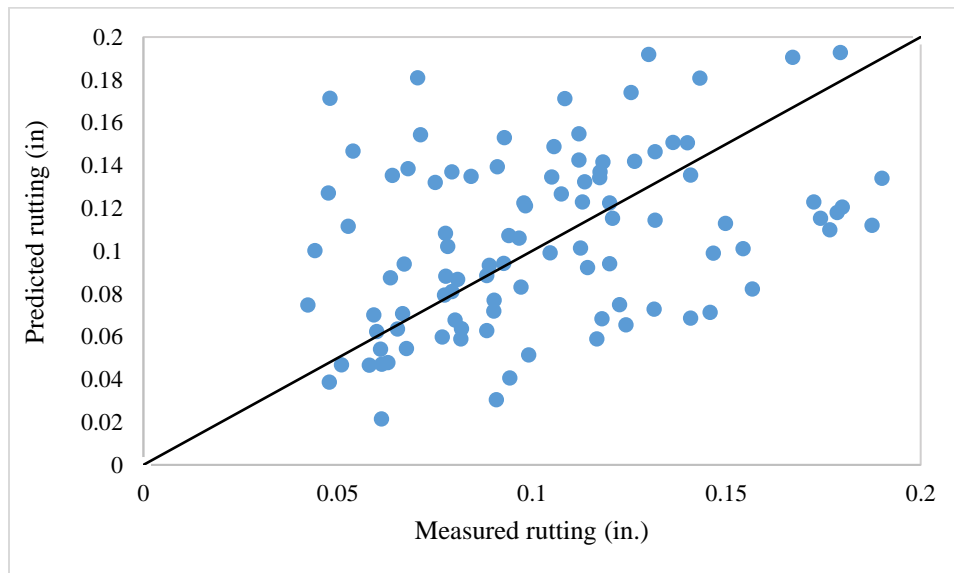


Figure 4-1 Predicted vs measured AC rutting with globally calibrated factors

Table 4-1 Statistical analysis summary results for nationally calibrated factors

Bias	SSE	$S_e$	$S_e/S_y$	$p$ -value	Hypothesis, $H_0: \sum(Meas.-Pred.) = 0$
1.29	0.33	0.055	1.36	<0.001	Rejected

4.1.1.2 Elimination of bias of the rutting model

Equation 2.1 shows that rutting model calibration parameters  $\beta_{1r}$  can be optimized outside of the AASHTOWare software to reduce bias and standard error. The generalized reduced gradient (GRG) nonlinear optimization technique was applied using Microsoft Excel Solver to optimize  $\beta_{1r}$ . In addition, a paired  $t$ -test was conducted between measured and predicted data. The  $p$ -value from the paired  $t$ -test was higher than 0.05, indicating that predicted rutting and measured rutting differ. Results of the statistical analysis after local calibration are presented in Table 4-2.

Table 4-2 Statistical analysis results for locally calibrated factors for AC rutting model

Bias	SSE	$S_e$	$S_e/S_y$	$p$ -value	Hypothesis, $H_0: \sum(Meas.-Pred.) = 0$
0.59	0.29	0.053	1.31	0.28	Failed to reject

A comparison of Table 4-1 and Table 4-2 showed minimal improvement of goodness-of-fit statistics after optimizing the  $\beta_{1r}$  parameter. The NCHRP 1-40B local calibration guide recommends adjusting coefficients  $\beta_{2r}$  and  $\beta_{3r}$  to further reduce  $S_e$  of the AC permanent deformation model. Coefficients  $\beta_{2r}$  and  $\beta_{3r}$  are power function parameters for temperature effect and number loading cycles, respectively, for computing accumulated AC permanent deformation. Therefore, coefficients  $\beta_{2r}$  and  $\beta_{3r}$  cannot be optimized outside of the AASHTOWare PMED software. The PMED software must run numerous times considering a large factorial of  $\beta_{2r}$  and  $\beta_{3r}$  coefficients to yield a combination that produces the least  $S_e$ . The

local calibration guide recommends that  $S_e$  be within 0.1 in. for the AC rutting model. Measured versus predicted total rutting with locally calibrated coefficients is shown in Figure 4-2.

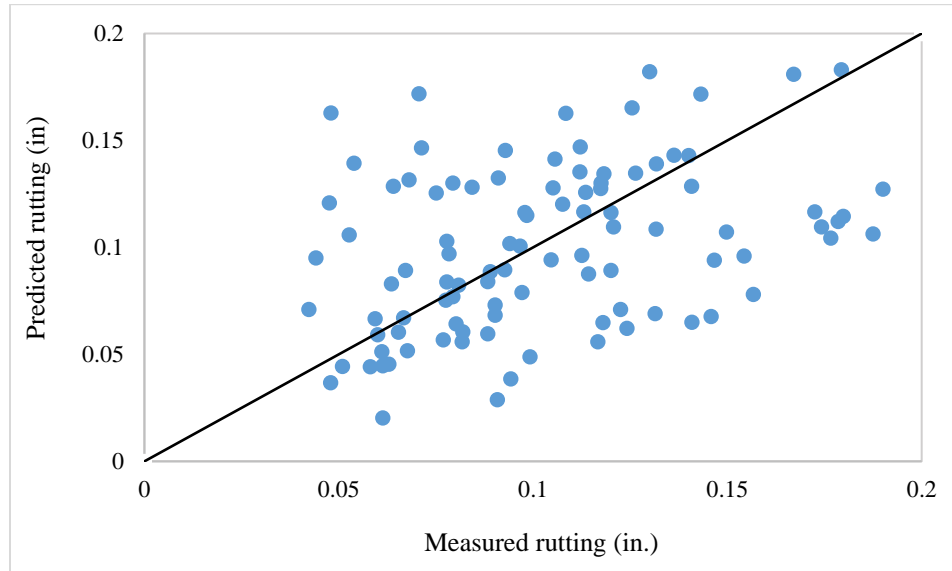


Figure 4-2 Predicted vs measured AC rutting with locally calibrated factors

Statistical analysis results for the rutting model and the validation dataset are shown in Table 4-3. Goodness-of-fit statistics showed minimal variation for the validation dataset with locally adjusted coefficients.

Table 4-3 Summary statistics for validation set of AC rutting model with local factors

Bias	SSE	$S_e$	$S_e/S_y$	$p$ -value	Hypothesis, $H_0: \sum(Meas.-Pred.) = 0$
0.2	0.19	0.08	1.31	0.65	Failed to reject

#### 4.1.2 Transverse cracking model calibration for AC over AC sections

For AC over AC sections, transverse cracking is generated as the sum of AC thermal cracking and reflection cracking. Calibration of the total transverse cracking model with the newly developed reflection cracking model was described at a webinar organized by the Transportation Research Board standing committee on pavement rehabilitation (Von Quintus,

2016). Since reflection cracking could not be distinguished from thermal cracking for AC overlay during a distress survey of the LTPP sections, AC overlays and new AC pavements had the same thermal cracking transfer function coefficient. The transverse cracking model was calibrated by adjusting the reflection cracking model calibration coefficients.

Section 3.8.5 describes how KDOT collects full lane-width transverse cracking data for AC pavements but does not distinguish between thermal and reflection cracks. Furthermore, AC thermal cracking model coefficients were not adjusted in the previous PMED calibration study for new/reconstructed AC/HMA pavements for Kansas (Islam et al., 2019). For that study, automated distress survey data were not available, and the manual distress survey yielded no thermal cracking for 13 of the 27 new AC pavement projects. In addition, no material-specific level 1 input data in terms of creep compliance and indirect tensile strength were available for calibrating the AC thermal cracking model, and the PMED software did not predict any thermal cracking for any projects selected for new AC pavement calibration.

A zone-wise AC thermal cracking model was recommended for calibration for new HMA pavement sections with prevalent thermal cracking. In this study, however, the selected AC over AC projects exhibited significant transverse cracking and the PMED transverse cracking model needed to be calibrated. Therefore, the transverse cracking model was calibrated by adjusting the reflection cracking model coefficients only. Global factors were used for the AC thermal cracking model. However, AASHTOWare PMED software did not predict any AC thermal cracking for the selected JPCP rehabilitated sections with nationally calibrated coefficients; thus, all transverse cracking may be regarded as reflection cracking. The traditional split sampling method was implemented to calibrate the total transverse cracking model. An 80-20 split of the dataset was considered for calibration and validation.

4.1.2.1 Bias assessment of transverse cracking model

Bias between measured and predicted data was computed to verify the PMED total transverse cracking model for AC over AC sections. The globally calibrated transverse cracking model showed significant bias in the paired *t*-test, and the null hypothesis was rejected at 95% confidence interval. The *p*-value from the paired *t*-test was less than 0.05, indicating that predicted and measured transverse cracking differ. Measured versus predicted total transverse cracking with globally calibrated coefficients is shown in Figure 4-3, and summary statistics are shown in Table 4-4. The measured versus predicted transverse cracking plot in the figure shows an unsymmetrical trend to the line of equality.

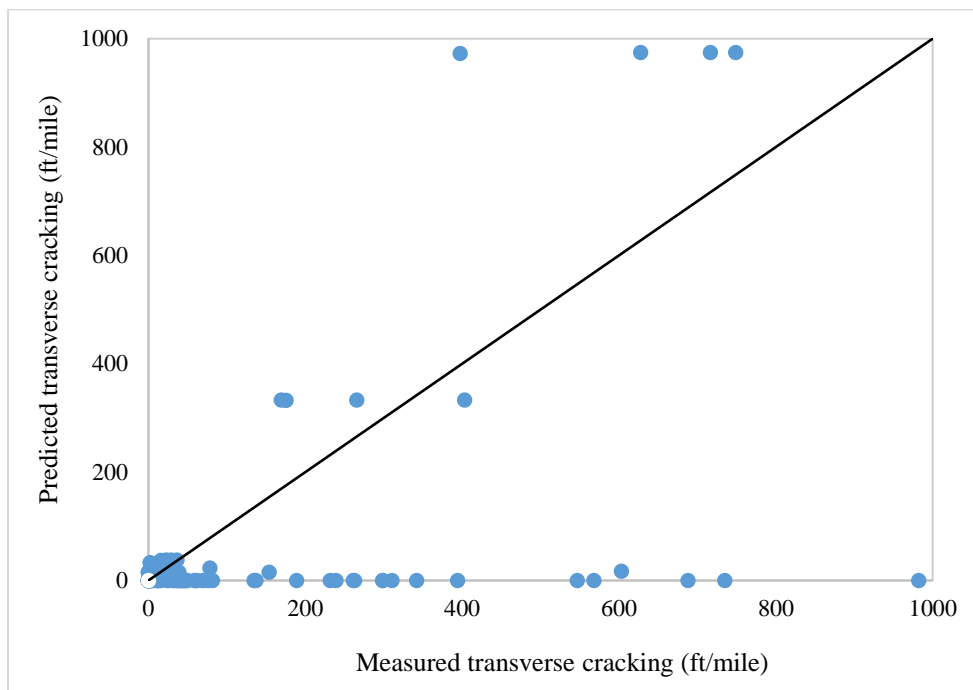


Figure 4-3 Predicted vs measured transverse cracking with globally calibrated factors

Table 4-4 Statistical analysis summary results for nationally calibrated factors

Bias	SSE	$S_e$	$S_e/S_y$	<i>p</i> -value	Hypothesis, $H_0: \sum(Meas.-Pred.) = 0$
6712	4,525,304	195	0.96	0.0013	Rejected

#### 4.1.2.2 Elimination of bias of the transverse cracking model

Equations 2.8–2.13 show that calibration parameters  $C_4$  and  $C_5$  of the transverse cracking model can be optimized outside of the AASHTOWare software if damage ratio ( $D$ ) and percent reflective cracking rate (RCR) values are available. PMED software generates a text file “transverseReflectiveCracking.log,” that contains time-series results from Equations 2.8–2.13. In this study, time-series  $D$  and RCR values were extracted for selected AC over JPCP projects, and the total transverse cracking model calibration coefficients were computed outside the AASHTOWare software. GRG nonlinear optimization technique was applied to determine a combination of  $C_4$  and  $C_5$  parameters that yielded the least SSE between measured and predicted total transverse cracking.

Adjusted  $C_4$  and  $C_5$  coefficients were used as locally calibrated coefficients in the total transverse cracking model of the AASHTOWare PMED software, and a paired  $t$ -test was conducted between the measured and predicted data. Summary statistics of the transverse cracking model after local calibration are shown in Table 4-5, indicating that the bias significantly decreased after local calibration. The  $S_e$  of the calibrated model decreased to 112 ft/mile, which is within the AASHTO-suggested  $S_e$  range of transverse cracking model (250 ft/mile). The  $p$ -value from the paired  $t$ -test was higher than 0.05, which suggests that no evidence is present to conclude the predicted and measured transverse cracking differ.

Table 4-5 Summary statistics for locally calibrated total transverse cracking model

Bias	SSE	$S_e$	$S_e/S_y$	$p$ -value	Hypothesis, $H_0: \sum(Meas.-Pred.) = 0$
1,244	1,279,336	109	0.53	0.27	Failed to reject



Measured versus predicted transverse cracking with locally calibrated coefficients is shown in Figure 4-4. A significant improvement in data location with respect to the line of equality was noticed after local calibration.

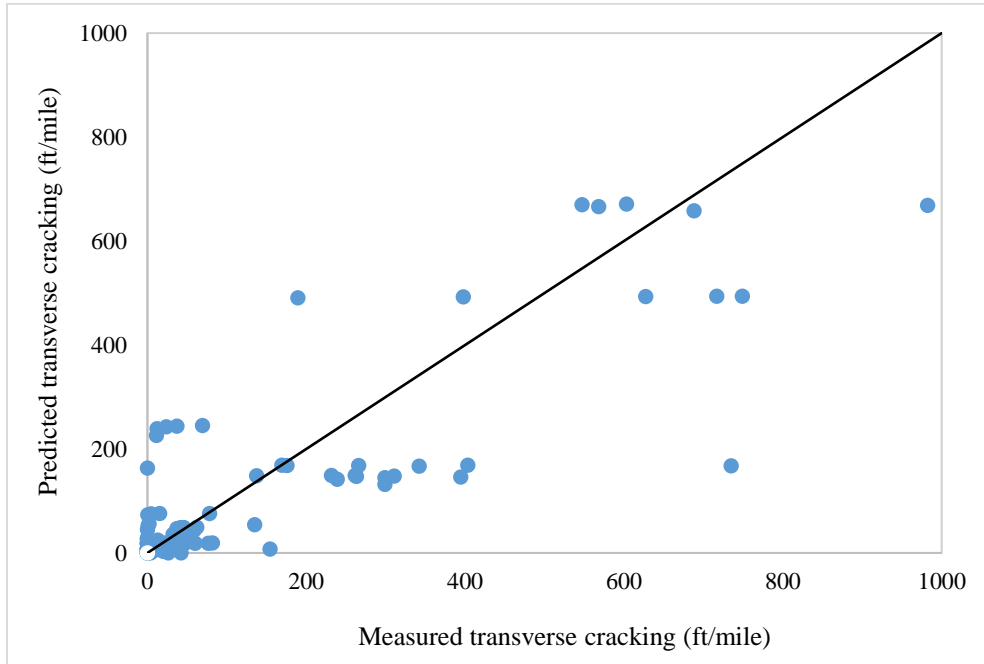


Figure 4-4 Predicted vs measured transverse cracking with locally calibrated factors

Statistical analysis results for the total transverse cracking model with the validation dataset are shown in Table 4-6. Goodness-of-fit statistics results showed increased bias and  $S_e$  for the validation dataset compared to the calibration dataset.

Table 4-6 Summary statistics for validation set of transverse cracking model with local factors

Bias	SSE	$S_e$	$S_e/S_y$	$p$ -value	Hypothesis, $H_0: \sum(Meas.-Pred.) = 0$
895	703,562	147	0.88	0.29	Failed to reject

#### 4.1.3 Load-related cracking model calibration for AC over AC sections

AASHTOWare PMED software predicts two types of load-related cracking: bottom-up and top-down fatigue cracking. Bottom-up fatigue cracks, or alligator cracks, initiate at the

bottom of the HMA layers and propagate to the surface (NCHRP, 2004). Bottom-up fatigue cracks, which are caused by tensile strain at the bottom of the HMA layers, propagate at the surface as multiple, short, longitudinal, or transverse cracks in the wheel path and become interconnected with continued loading (Kim et al., 2011). Top-down fatigue cracks are load-related longitudinal cracks in the wheel paths (Haider et al., 2014) that initiate at the pavement surface and propagate downwards with continued traffic loading (NCHRP, 2004). Three primary reasons account for longitudinal cracking. The first reason is development of tension, torsion, and shear stresses at the pavement surface due to truck traffic loading. The second reason for longitudinal cracking is the development of tensile stress at the pavement surface due to daily and seasonal temperature variation, and the third reason is longitudinal crack growth due to aging (Kim et al., 2011).

The NCHRP 1-40B project recommended extracting 6-in. diameter cores on top of load-related cracks to determine crack origin. However, KDOT considers all load-related cracking to be top-down due to the prevalence of thick HMA pavements throughout the state. KDOT assumes that use of full-depth thick HMA pavements or overlay on top of thick HMA pavements keeps tensile strain at the bottom of the AC layer below the fatigue endurance limit, thereby restricting the growth of bottom-up fatigue cracking. This study assumed that all load-related cracks initiate at the pavement surface.

#### *4.1.3.1 Bias assessment of the top-down cracking model*

Bias between measured and predicted data was computed to verify the PMED top-down cracking model for AC overlays on AC sections. The globally calibrated total top-down cracking model showed significant bias in the paired  $t$ -test, and the null hypothesis was rejected at 95% confidence interval. The  $p$ -value from the paired  $t$ -test was less than 0.05, indicating that

predicted rutting and measured top-down cracking differ. Summary statistics are shown in Table 4-7.

Table 4-7 Summary statistics for top-down cracking model with nationally calibrated factors

Bias	SSE	$S_e$	$S_e/S_y$	$p$ -value	Hypothesis, $H_0: \sum(Meas.-Pred.) = 0$
95069	803,584,612	2594	1.34	<0.001	Rejected

Measured versus predicted top-down cracking with globally calibrated coefficients is shown in Figure 4-5. The measured versus predicted top-down cracking plot shows an unsymmetrical trend to the line of equality.

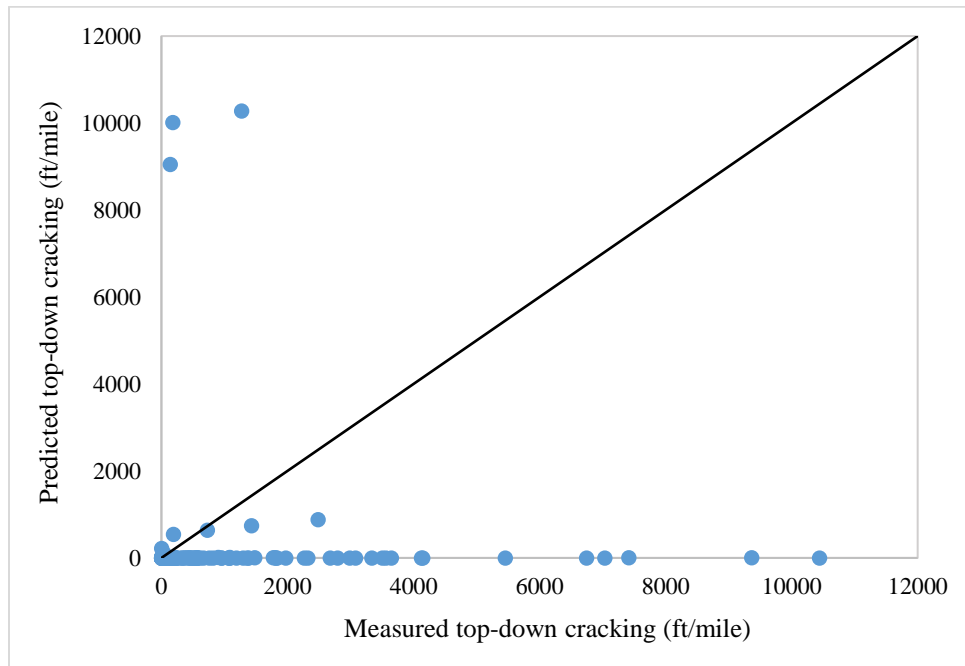


Figure 4-5 Predicted vs measured longitudinal cracking with globally calibrated factors

#### 4.1.3.2 Elimination of bias of the top-down cracking model

Equation 2.5 shows that the calibration parameters  $C_1$  and  $C_2$  of the top-down cracking model can be optimized outside of the AASHTOWare software if the time-series cumulative damage index at the top of the surface ( $DI_{top}$ ) values are available. These values were extracted

for the selected AC over AC projects from the Excel output, and top-down cracking values were computed outside the AASHTOWare software. GRG nonlinear optimization technique was applied to determine a combination of  $C_1$  and  $C_2$  parameters that yielded the least SSE between measured and predicted top-down cracking.

Adjusted  $C_1$  and  $C_2$  coefficients were used as locally calibrated coefficients in the top-down cracking model of the AASHTOWare PMED software, and a paired  $t$ -test was conducted between measured and predicted data. Results of the paired  $t$ -test after local calibration are shown in Table 4-8, which confirms that the bias decreased significantly after local calibration: the  $S_e$  of the calibrated model decreased to 1,900 ft/mile from 2,594 ft/mile. However, the local calibration guide (AASHTO, 2010) recommends that the  $S_e$  of the longitudinal cracking model should be within 600 ft/mile. The  $p$ -value from the paired  $t$ -test was higher than 0.05, which suggests no evidence that predicted rutting and measured top-down cracking differ.

Table 4-8 Summary statistics for top-down cracking model with locally calibrated factors

Bias	SSE	$S_e$	$S_e/S_y$	$p$ -value	Hypothesis, $H_0: \sum(Meas.-Pred.) = 0$
18626	389,144,470	1900	0.98	0.34	Failed to reject

Measured versus predicted top-down cracking with local coefficients is shown in Figure 4-6. No significant improvement was noticed in data location with respect to the line of equality after local calibration.

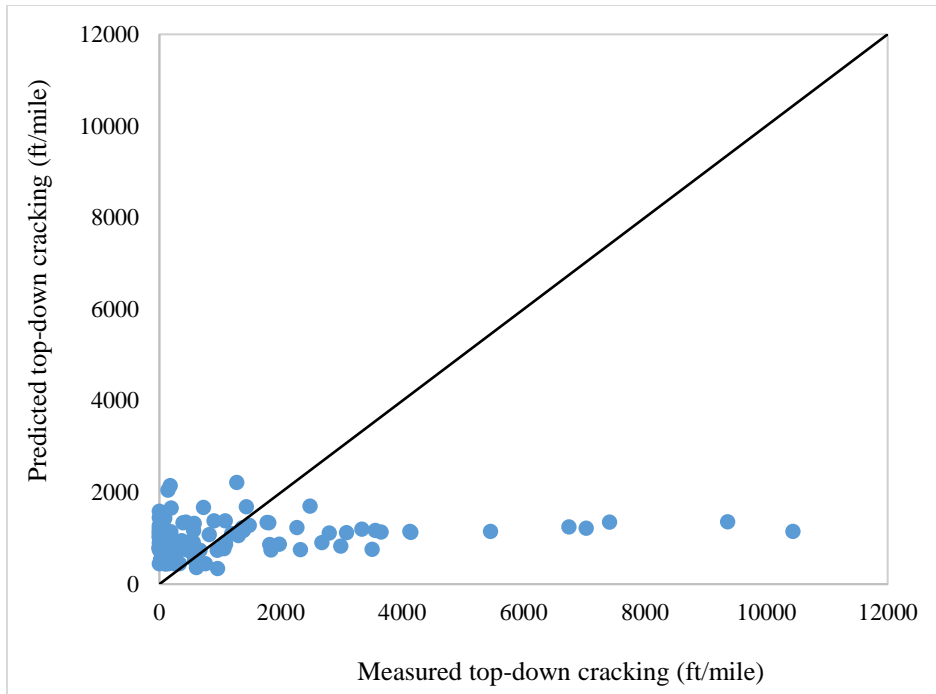


Figure 4-6 Predicted vs measured longitudinal cracking with locally calibrated factors

Statistical analysis results for the top-down cracking model after validation are shown in Table 4-9. Goodness-of-fit statistics results showed high bias and  $S_e$  for the validation dataset.

Table 4-9 Summary statistics for validation set of top-down cracking model with local factors

Bias	SSE	$S_e$	$S_e/S_y$	$p$ -value	Hypothesis, $H_0: \sum(Meas.-Pred.) = 0$
7169	159,792,367	2259	0.86	0.58	Failed to reject

#### 4.1.4 IRI model calibration for AC over AC sections

IRI is a measurement of the functional adequacy of pavement smoothness (Haas et al., 2015). PMED software predicts IRI empirically as a function of the initial IRI at the time of construction and pavement distresses (i.e., fatigue cracking, transverse cracking, permanent deformation, and site factors representing subgrade soil shrink/swell and frost-heave potential).

#### 4.1.4.1 Bias assessment of the IRI model

Bias between measured and predicted IRI was computed to verify the nationally calibrated model for AC rehabilitated sections. The globally calibrated model showed significant bias in the paired  $t$ -test, and the null hypothesis was rejected at 95% confidence interval. The  $p$ -value from the paired  $t$ -test was less than 0.05, indicating that predicted rutting and measured IRI differ. Summary statistics are shown in Table 4-10, and measured versus predicted total IRI for globally calibrated coefficients is shown in Figure 4-7. The measured versus predicted IRI plot shows an unsymmetrical trend to the line of equality.

Table 4-10 Statistical analysis summary results for nationally calibrated factors

Bias	SSE	$S_e$	$S_e/S_y$	$p$ -value	Hypothesis, $H_0: \sum(Meas.-Pred.) = 0$
1436	38,580	14	0.98	<0.001	Rejected

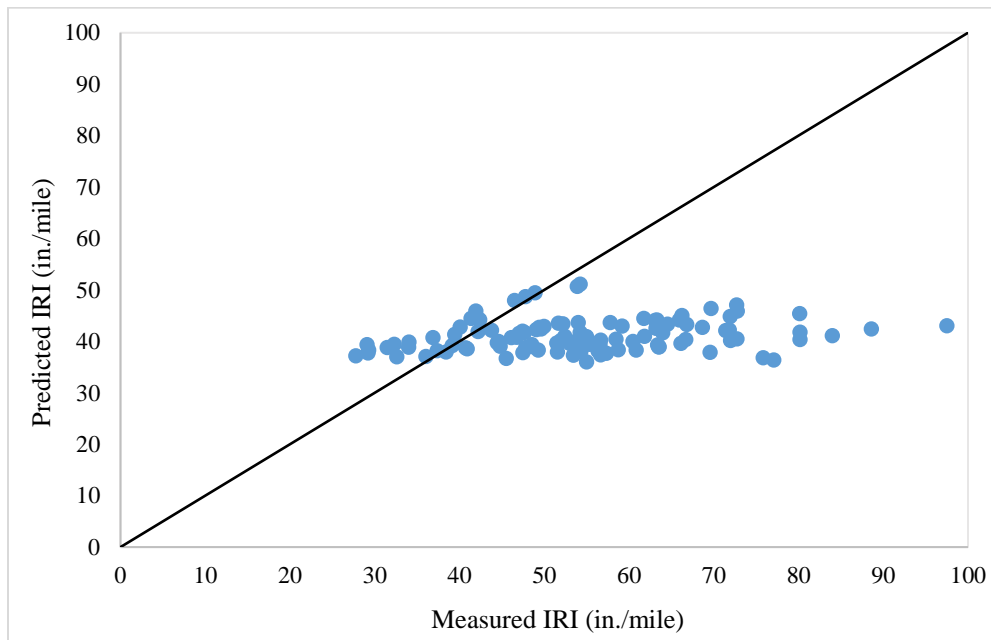


Figure 4-7 Predicted vs measured AC IRI with globally calibrated factors

#### 4.1.4.2 Elimination of bias of the IRI model

Equation 2.15 shows that IRI model calibration parameters  $C_1$ ,  $C_2$ ,  $C_3$ , and  $C_4$  can be optimized outside of the AASHTOWare PMED environment if the initial IRI, pavement distresses, and site factor information are available for each project at the corresponding dates of measured IRI. In addition, site-wise annual rainfall, freezing index, soil plasticity index, and subgrade soil percent passing through a US No. 4 sieve and US No. 200 sieve are required to calculate site-factor information. This study extracted the required input parameters from PMED output files, and the IRI model was calibrated outside the AASHTOWare PMED environment. A paired  $t$ -test was then conducted between measured and predicted IRI with local coefficients. The  $p$ -value from the paired  $t$ -test was higher than 0.05, which suggests no evidence that predicted and measured IRI differ. Results of the statistical analysis after local calibration are presented in Table 4-11.

Table 4-11 Statistical analysis results for locally calibrated factors for AC rutting model

Bias	SSE	$S_e$	$S_e/S_y$	$p$ -value	Hypothesis, $H_0: \sum(Meas.-Pred.) = 0$
66	27,528	16	1.16	0.69	Failed to reject

Measured versus predicted IRI with locally calibrated coefficients are shown in Figure 4-8. A significant improvement in data location with respect to the line of equality was observed after local calibration.

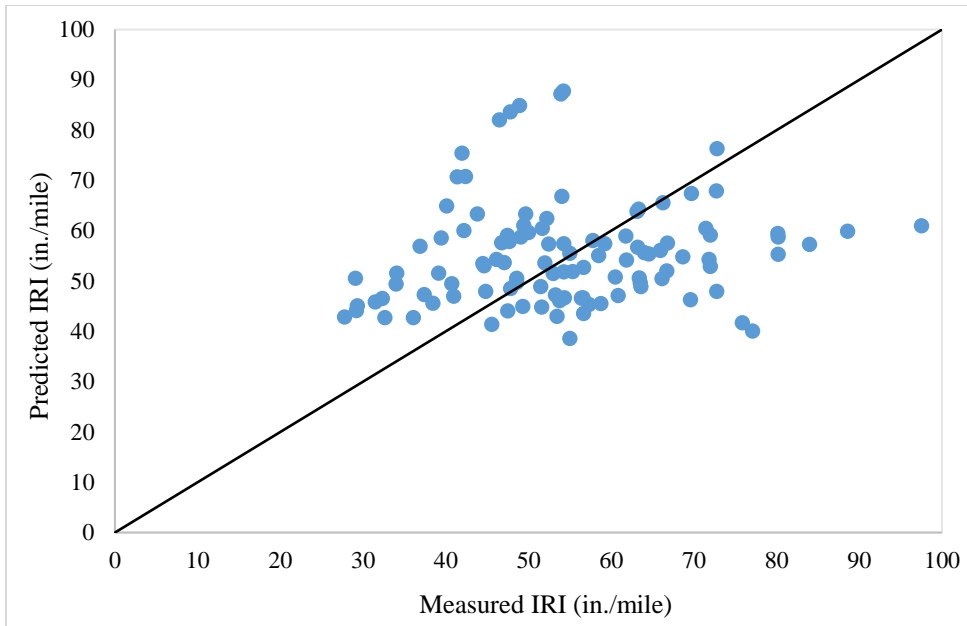


Figure 4-8 Predicted vs measured AC IRI with locally calibrated factors

Statistical analysis results for the rutting model with the validation dataset are shown in Table 4-12. The  $p$ -value from the paired  $t$ -test was less than 0.05, indicating that predicted and measured IRI differ for the validation dataset.

Table 4-12 Summary statistics for validation set of AC rutting model with local factors

Bias	SSE	$S_e$	$S_e/S_y$	$p$ -value	Hypothesis, $H_0: \sum(Meas.-Pred.) = 0$
380	11,830	15	1.16	<0.001	Rejected

## 4.2 Local Calibration and Validation of AC over JPCP sections

This study calibrated PMED transfer function parameters for AC over JPCP sections. The rutting model, transverse cracking, top-down cracking, and IRI models were also calibrated.

### 4.2.1 AC rutting model calibration for AC over JPCP sections



For AC over JPCP sections, rutting occurs in the overlay on top of the PCC layer. At the first step, traditional split sampling method was used to calibrate the AC rutting model. An 80-20 split of the dataset was considered for calibration and validation.

*4.2.1.1 Bias assessment of the AC rutting model*

Bias between measured and predicted rutting was computed to verify the PMED AC rutting model for AC over JPCP sections. The globally calibrated rutting model showed significant bias in the paired *t*-test for the AC rutting model, and the null hypothesis was rejected at 95% confidence interval. The *p*-value from the paired *t*-test was less than 0.05, indicating that predicted rutting and measured rutting differ. Summary statistics are shown in Table 4-13.

Table 4-13 Statistical analysis summary results for nationally calibrated factors

Bias	SSE	$S_e$	$S_e/S_y$	<i>p</i> -value	Hypothesis, $H_0 : \sum(Meas.-Pred.) = 0$
2.73	0.24	0.042	0.9	<0.0001	Rejected

Measured versus predicted total rutting for globally calibrated coefficients is shown in Figure 4-9. The measured versus predicted rutting plot shows an unsymmetrical trend to the line of equality.

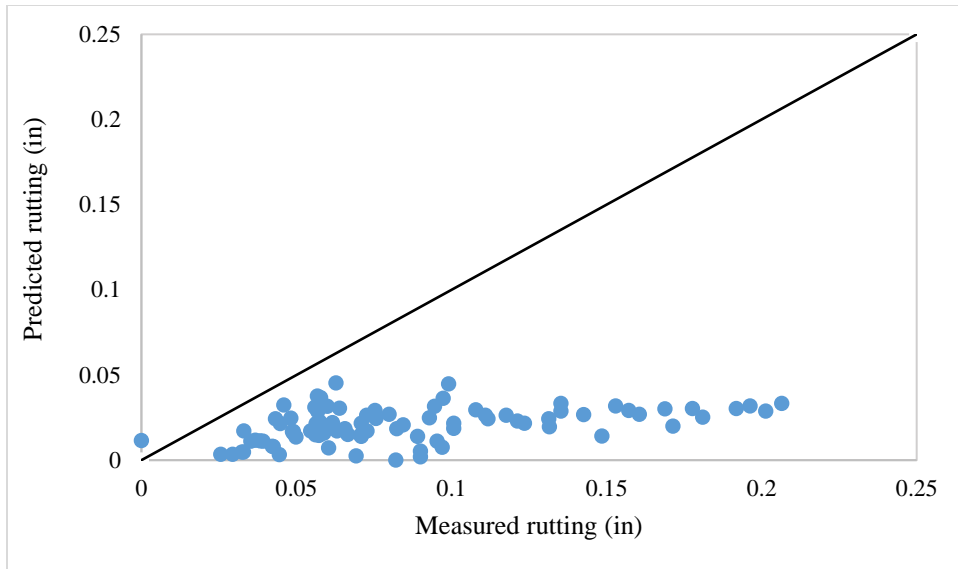


Figure 4-9 Predicted vs measured AC rutting with globally calibrated factors

4.2.1.2 Elimination of bias of the AC rutting model

Equation 2.1 shows that calibration parameters  $\beta_{1r}$  can be optimized outside of the AASHTOWare software to reduce bias and standard error. The GRG nonlinear optimization technique was applied using Microsoft Excel Solver to optimize  $\beta_{1r}$ , and a paired  $t$ -test was conducted between the measured and predicted data. Results of the paired  $t$ -test after local calibration are shown in Table 4-14, which confirm a significantly reduced bias.

Table 4-14 Statistical analysis results for locally calibrated factors for AC rutting model

Bias	SSE	$S_e$	$S_e/S_y$	$p$ -value	Hypothesis, $H_0: \sum(Meas.-Pred.) = 0$
0.68	0.17	0.046	0.98	0.08	Failed to reject

A comparison of Table 4-13 and Table 4-14 show that  $S_e$  slightly increased after reducing bias between measured and predicted rutting. The NCHRP 1-40B local calibration guide recommends adjusting coefficients  $\beta_{2r}$  and  $\beta_{3r}$  to reduce  $S_e$  of the AC permanent deformation model. Coefficients  $\beta_{2r}$  and  $\beta_{3r}$  are power function parameters for temperature effect and number

loading cycles, respectively, for computing accumulated AC permanent deformation. Therefore, coefficients  $\beta_{2r}$  and  $\beta_{3r}$  cannot be optimized outside of the AASHTOWare PMED software.

PMED software must run numerous times considering a large factorial of  $\beta_{2r}$  and  $\beta_{3r}$  coefficients to yield a combination that produces the least  $S_e$ . However, the local calibration guide recommends the  $S_e$  be within 0.1 in. for the AC rutting model.

Measured versus predicted total rutting with locally calibrated coefficients is shown in Figure 4-10. A significant improvement in data location with respect to the line of equality was noticed after local calibration.

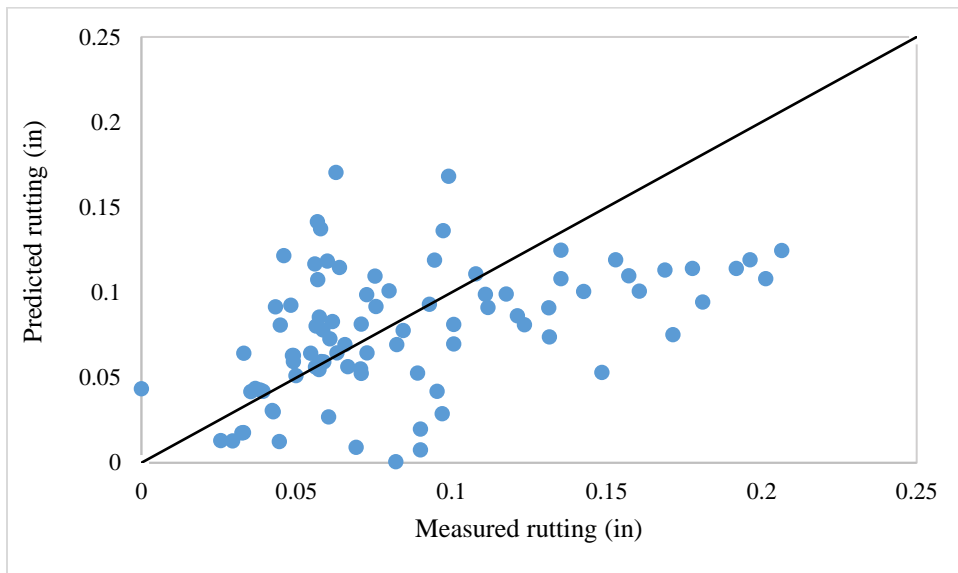


Figure 4-10 Predicted vs measured AC rutting with locally calibrated factors

Statistical analysis results for the rutting model with the validation dataset are shown in Table 4-15. Goodness-of-fit statistics did not vary significantly for the validation dataset with locally adjusted coefficients.

Table 4-15 Summary statistics for validation set of AC rutting model with local factors

Bias	SSE	$S_e$	$S_e/S_y$	$p$ -value	Hypothesis, $H_0 : \sum(Meas. - Pred.) = 0$
0.44	0.05	0.045	1.09	0.06	Failed to reject

#### 4.2.2 Transverse cracking model calibration for AC over JPCP sections

PMED software computes transverse cracking as the sum of AC thermal cracking and reflection cracking for AC over JPCP sections. In this study, reflection cracking and thermal cracking measured data could not be distinguished. AC thermal cracking model coefficients were not adjusted in the previous PMED calibration study for new/reconstructed HMA pavements for Kansas, so thermal cracking model coefficients and the national default stayed the same, and the transverse cracking model was calibrated by adjusting the reflection cracking model coefficients only. The PMED software did not predict any thermal cracking for any JPCP rehabilitated sections considered for this study. The traditional split sampling method was implemented to calibrate the transverse cracking model. An 80-20 split of the dataset was considered for calibration and validation.

##### 4.2.2.1 Bias assessment of the transverse cracking model

Bias between measured and predicted data was computed to verify the PMED transverse cracking model for AC over JPCP sections. The globally calibrated transverse cracking model showed significant bias in the paired  $t$ -test, and the null hypothesis was rejected at 95% confidence interval. The  $p$ -value from the paired  $t$ -test was less than 0.05, indicating that predicted and measured transverse cracking differ. Summary statistics are shown in Table 4-16.

Table 4-16 Statistical analysis summary results for nationally calibrated factors

Bias	SSE	$S_e$	$S_e/S_y$	$p$ -value	Hypothesis, $H_0: \sum(Meas.-Pred.) = 0$
5459	18,574,025	594	1.26	<0.0001	Rejected

Measured versus predicted total transverse cracking with globally calibrated coefficients is shown in Figure 4-11. The measured versus predicted transverse cracking plot shows an unsymmetrical trend to the line of equality.

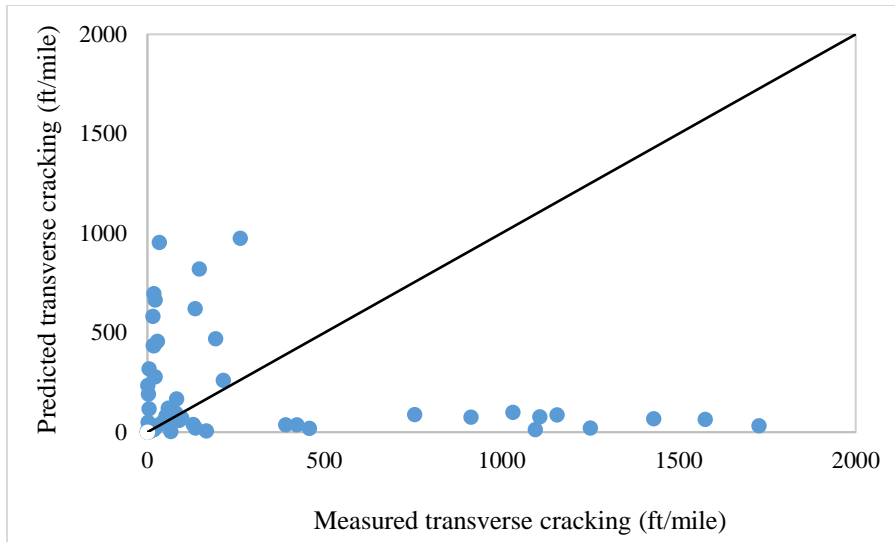


Figure 4-11 Predicted vs measured transverse cracking with globally calibrated factors

#### 4.2.2.2 Elimination of bias of the transverse cracking model

This study calibrated the transverse cracking model outside the PMED software environment. The time-series  $D$  and RCR values were extracted for the selected AC over JPCP projects, and the  $C_4$  and  $C_5$  parameters were optimized. Adjusted  $C_4$  and  $C_5$  coefficients were then used as locally calibrated coefficients in the total transverse cracking model of the AASHTOWare PMED software, and a paired  $t$ -test was conducted between the measured and predicted data. Results of the paired  $t$ -test after local calibration are shown in Table 4-17, which confirm that the model goodness-of-fit statistics improved slightly after local calibration. The  $S_e$  of the calibrated model decreased to 570 ft/mile from 594 ft/mile; however, the local calibration guide (AASHTO, 2010) recommends that the  $S_e$  of the transverse cracking model be within 250 ft/mile.

Table 4-17 Summary statistics for locally calibrated total transverse cracking model

Bias	SSE	$S_e$	$S_e/S_y$	$p$ -value	Hypothesis, $H_0 : \sum(Meas.-Pred.) = 0$
5188	17,072,580	570	1.20	0.21	Failed to reject

Measured versus predicted total transverse cracking with locally calibrated coefficients is shown in Figure 4-12. Minimal improvement was observed in data location relative to the line of equality after local calibration.

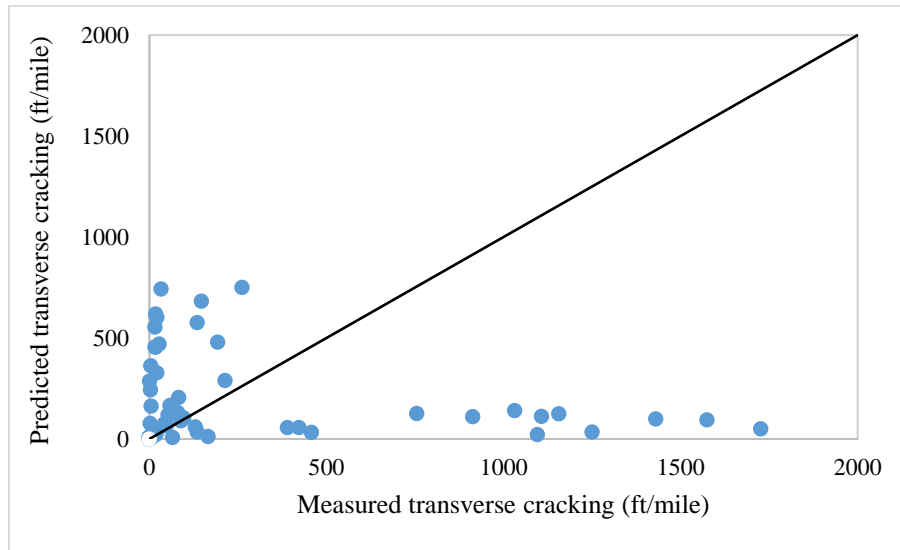


Figure 4-12 Predicted vs measured transverse cracking with locally calibrated factors

Statistical analysis results for the total transverse cracking model with the validation set are shown in Table 4-18. Goodness-of-fit statistics results showed high bias and  $S_e$  for the validation dataset.

Table 4-18 Summary statistics for validation set of transverse cracking model with local factors

Bias	SSE	$S_e$	$S_e/S_y$	$p$ -value	Hypothesis, $H_0: \sum(Meas.-Pred.) = 0$
5859	17,238,328	946	1.33	0.16	Failed to reject

#### 4.2.3 Load-related cracking model calibration for AC over JPCP sections

KDOT considers all load-related cracking to be top-down because HMA overlays on top of thick PCC sections keep tensile strain at the bottom of the asphalt layer below the fatigue

endurance limit, thereby restricting the growth of bottom-up fatigue cracking. Therefore, this study assumed that all load-related cracks originate at the surface of the AC overlay.

4.2.3.1 Bias assessment of the top-down cracking model

Bias between measured and predicted data was computed to verify the PMED top-down cracking model for AC overlays on JPCP sections. The globally calibrated total top-down cracking model showed significant bias, and the null hypothesis was rejected at 95% confidence interval. The *p*-value from the paired *t*-test was less than 0.05, indicating that the predicted and measured top-down cracking differ. Summary statistics are shown in Table 4-19.

Table 4-19 Summary statistics for top-down cracking model with nationally calibrated factors

Bias	SSE	$S_e$	$S_e/S_y$	<i>p</i> -value	Hypothesis, $H_0: \sum(Meas.-Pred.) = 0$
87502	58,388,750	814	1.0	<0.001	Rejected

Measured versus predicted top-down cracking with globally calibrated coefficients is shown in Figure 4-13. The measured versus predicted top-down cracking plot shows an unsymmetrical trend to the line of equality.

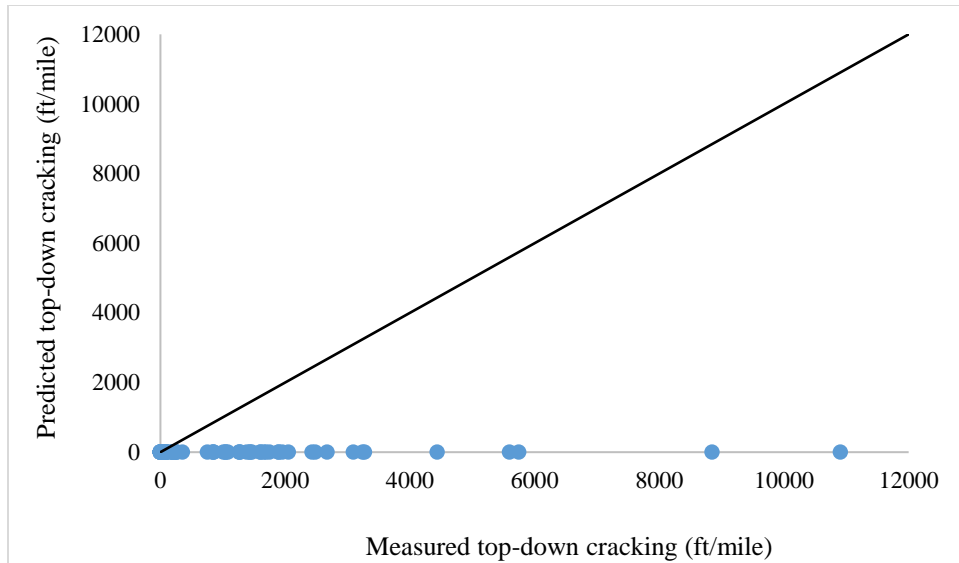


Figure 4-13 Predicted vs measured longitudinal cracking with globally calibrated factors

#### 4.2.3.2 Elimination of bias of the top-down cracking model

This study calibrated the top-down cracking model outside the PMED software environment. Time-series cumulative damage index ( $DI_{top}$ , at the top of the surface) values were extracted for the selected AC over JPCP projects, and the  $C_1$  and  $C_2$  parameters were optimized. Adjusted  $C_1$  and  $C_2$  coefficients were then used as locally calibrated coefficients in the top-down cracking model of the AASHTOWare PMED software, and a paired  $t$ -test was conducted between measured and predicted data. Summary statistics after local calibration are shown in Table 4-20. The  $p$ -value from the paired  $t$ -test was higher than 0.05, which suggests that there is no evidence that predicted rutting and measured top-down cracking differ. Although the bias and SSE decreased slightly after local calibration, the  $S_e$  increased after optimizing the  $C_1$  and  $C_2$  coefficients of the transfer function.

Table 4-20 Summary statistics for top-down cracking model with locally calibrated factors

Bias	SSE	$S_e$	$S_e/S_y$	$p$ -value	Hypothesis, $H_0: \sum(Meas.-Pred.) = 0$
11220	45,029,936	840	1.0	0.09	Failed to reject



Measured versus predicted top-down cracking with globally calibrated coefficients is shown in Figure 4-14. Minimal improvement was observed in data location relative to the line of equality after local calibration.

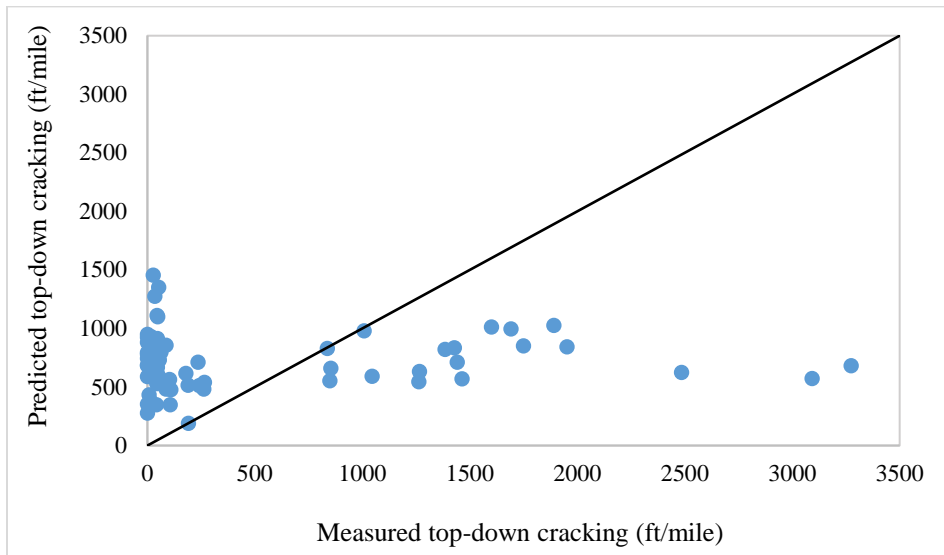


Figure 4-14 Predicted vs measured longitudinal cracking with locally calibrated factors

Statistical analysis results for the top-down cracking model with the validation set are shown in Table 4-21. Goodness-of-fit statistics results showed high bias and  $S_e$  for the validation dataset.

Table 4-21 Summary statistics for validation set of top-down cracking model with local factors

Bias	SSE	$S_e$	$S_e/S_y$	$p$ -value	Hypothesis, $H_0: \sum(Meas.-Pred.) = 0$
7479	16,844,936	873	0.87	0.08	Failed to reject

#### 4.2.4 IRI model calibration for AC over JPCP sections

PMED software for the AC over JPCP sections predicts IRI empirically and considers IRI at the time of construction. Pavement distresses (i.e., fatigue cracking, transverse cracking,

permanent deformation, and site factors such as subgrade soil shrink/swell and frost-heave potential).

4.2.4.1 Bias assessment of the IRI model

Bias between measured and predicted IRI was computed to verify the nationally calibrated model for JPCP rehabilitated sections. Summary statistics are shown in Table 4-22. The globally calibrated model showed significant bias in the paired *t*-test, and the null hypothesis was rejected at 95% confidence interval. The *p*-value from the paired *t*-test was less than 0.05, indicating that predicted rutting and measured IRI differ for AC over JPCP sections.

Table 4-22 Statistical analysis summary results for nationally calibrated factors

Bias	SSE	$S_e$	$S_e/S_y$	<i>p</i> -value	Hypothesis, $H_0: \sum(Meas.-Pred.) = 0$
1,364	33,445	10	0.89	<0.001	Rejected

Measured versus predicted total IRI for globally calibrated coefficients is shown in Figure 4-15. The measured versus predicted IRI plot shows an unsymmetrical trend to the line of equality.

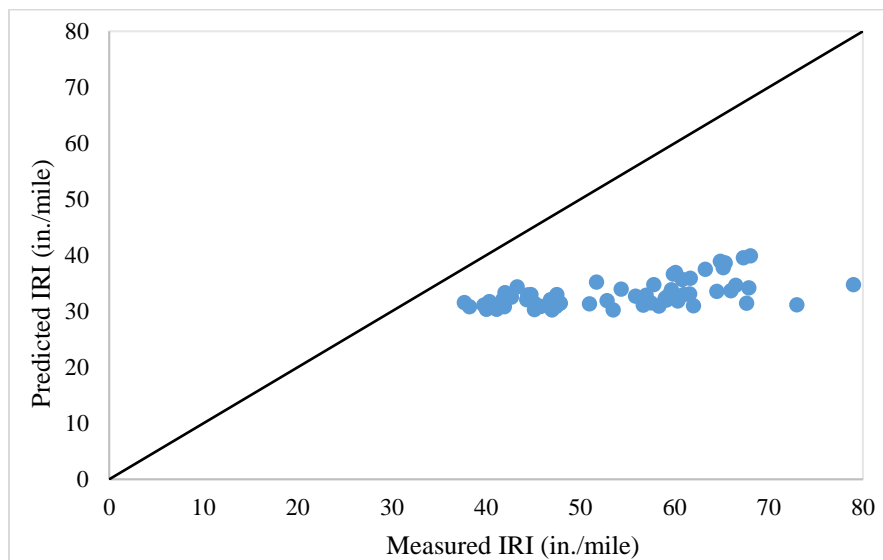


Figure 4-15 Predicted vs measured IRI with globally calibrated factors

#### 4.2.4.2 Elimination of bias of the IRI model

IRI model calibration parameters  $C_1$ ,  $C_2$ ,  $C_3$ , and  $C_4$  for AC over JPCP sections were optimized outside of the AASHTOWare PMED environment. Project-wise soil plasticity index and subgrade soil percent passing through a US No. 4 sieve and US No. 200 sieve were extracted from PMED software output for each project. In addition, project-specific rut depth, fatigue cracking, and transverse cracking values were extracted for the corresponding IRI data collection date. Optimized IRI model coefficients were used for prediction, and a paired  $t$ -test was then conducted between measured and predicted IRI. Results of the statistical analysis after local calibration are presented in Table 4-23, which shows significant improvement in the goodness-of-fit statistics. The  $p$ -value from the paired  $t$ -test was higher than 0.05, which suggests that there is no evidence that the predicted and measured IRI differ.

Table 4-23 Statistical analysis results for locally calibrated factors for AC rutting model

Bias	SSE	$S_e$	$S_e/S_y$	$p$ -value	Hypothesis, $H_0: \sum(\text{Meas.} - \text{Pred.}) = 0$
59	4,711	8	0.8	0.39	Failed to reject

Measured versus predicted IRI with locally calibrated coefficients is shown in Figure 4-16. A significant improvement in data location with respect to the line of equality was observed after local calibration.

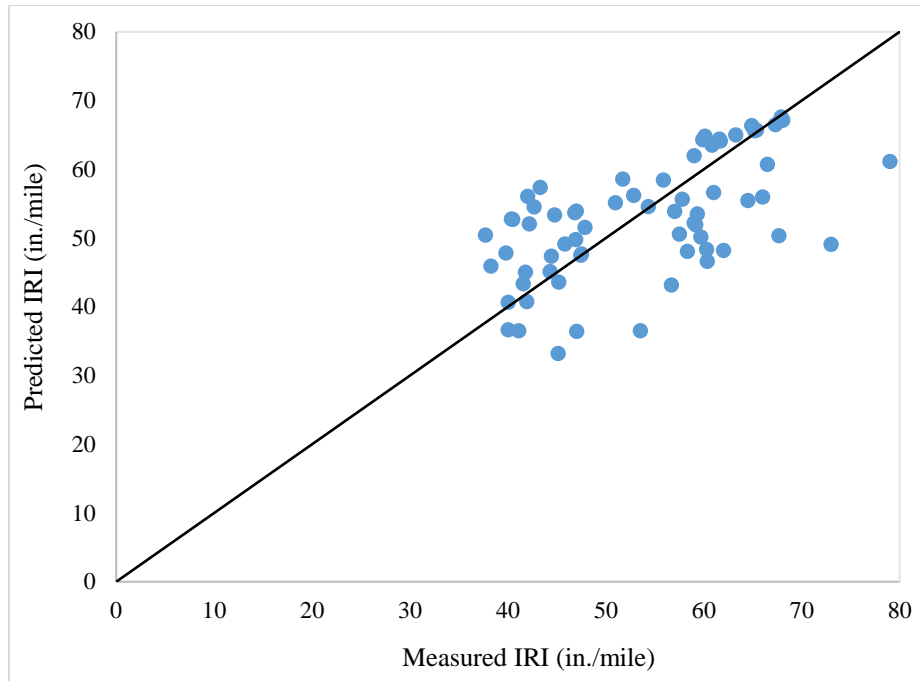


Figure 4-16 Predicted vs measured AC IRI with locally calibrated factors

Statistical analysis results for the rutting model with the validation dataset are shown in Table 4-24. The  $p$ -value from the paired  $t$ -test was less than 0.05, which suggests that there is no evidence that the predicted and measured IRI differ for the validation dataset. However, the  $S_e$  seemed to be extremely high for the validation set with local coefficients.

Table 4-24 Summary statistics for validation set of AC rutting model with local factors

Bias	SSE	$S_e$	$S_e/S_y$	$p$ -value	Hypothesis, $H_0: \sum(Meas.-Pred.) = 0$
267	18,938	30	1.16	0.25	Failed to Reject

## **Chapter 5 - Automated Calibration**

One concern regarding PMED software implementation is the need to recalibrate after distress models update or as new performance data becomes available. This study presents a framework to automate calibration and validation processes of PMED performance models.

### **5.1 Automated Calibration Technique**

State highway agencies have often tried to implement PMED software for routine pavement design, but a recurring implementation challenge has been the need to calibrate the software locally to reflect an agency's design and construction practices, materials, and climate. PMED software improvements also necessitate recalibration of performance models in the software (Tran et al., 2017). Since new performance data and test results are constantly becoming available, performance models in PMED must be continually verified to see if recalibration is needed (Islam, 2019). KDOT has a long-term concern regarding the time, effort, and resources needed to repeat local calibration.

Development of an automatic calibration process for hydrological models has been rigorously investigated, and several automatic global search algorithms have been developed for rainfall-runoff models designed to locate the global optimum on a response surface with numerous local optima (Duan et al., 1992). Madsen et al. (2002) explained that, in automatic calibration, parameters are adjusted automatically according to a specified search scheme and numerical measures of goodness-of-fit. The specified search scheme refers to the minimization of a certain objective function of a dataset using a suitable deterministic algorithm or optimization technique. Fernández (2016) further elaborated that the automated calibration process involves minimizing the objective function of a dataset by adjusting calibration parameters using a deterministic algorithm under a set of constraints. Development challenges,

however, include data availability, availability of a robust and physically meaningful calibrated-model, and computational feasibility.

### 5.1.1 Objective function

The objective function is a mathematical expression that must be minimized or maximized for a given problem. In the PMED performance model calibration process, the objective function refers to the mathematical equation that minimizes the total sum squared error between measured and predicted distresses and IRI. The objective function used in this study is given in Equation 5.1.

$$\text{minimize } F(x) = \sum_{i=1}^n [f(x(\Phi_{Local})) - y_{obs}]^2 \quad (5.1)$$

Where:

$F(x)$  = Objective function that needs to be minimized;

$f(x(\Phi_{Local}))$  = Pavement ME predicted distresses or IRI for  $i^{\text{th}}$  data point;

$\Phi_{Local}$  = Set of locally calibrated coefficients;

$y_{obs}$  = Measured distresses or IRI for  $i^{\text{th}}$  data point; and

$n$  = Total number of data points.

### 5.1.2 Optimization technique

The automated calibration process uses a deterministic algorithm or optimization technique to obtain a set of locally calibrated coefficients that minimize the objective function. Several methods can solve the optimization problem in Equation 5.1. These methods generally iterate on  $x$  in some manner; an initial value of each parameter for  $F(x)$  is chosen, the objective function is computed, and an algorithm is applied to generate a new  $x$  that will reduce the objective function (*Dakota User's Manual*, 2018).

Gradient-based optimization methods are well suited for effective navigation of parameters that minimize the objective function. This study utilized two optimization techniques, Polak and Ribière conjugate gradient (CG) and limited memory Broyden-Fletcher-Goldfarb-Shanno (L-BFGS) method, to calibrate the PMED models.

CG is a nonlinear gradient-based optimization method used to obtain local calibration coefficients. This method minimizes objective function  $F(x)$  by applying an iterative line search strategy (Fernández, 2016). The line search strategy finds a descent direction along which  $F(x)$  will be reduced and then computes a step size that determines how far  $x$  should move in that direction (Shewchuk, 1994). The CG technique is computationally inexpensive and converges quickly.

The L-BFGS optimization technique is an iterative method for solving constrained nonlinear optimization problems. Similar to the CG method, this method also uses a line search strategy, and the algorithm begins with an initial estimate. L-BFGS optimization technique is recommended for bounded problems with large sample sizes, such as 1,000 bootstrap samples. The L-BFGS uses a limited amount of computer memory and is one of the fastest algorithms for parameter estimation in machine learning problems (Mokhtari et al., 2015). In this study, the global default value of PMED models was set as the initial seed values.

## **5.2 Resampling Techniques**

The local calibration guide for the PMED software, developed under the NCHRP 1-40B project, recommended using resampling techniques to improve prediction model accuracy. The local calibration guide listed traditional split sampling and jackknifing resampling approaches for reliable assessment of prediction accuracy. However, the guide recommended using the jackknifing approach for a small sample size of the calibration dataset.

Brink (2015) calibrated and validated PMED performance models for Michigan using five types of sampling techniques: no sampling, traditional split sampling, repeated split sampling, jackknifing, and bootstrapping. The primary objective was to compare calibration results obtained from different resampling techniques. Brink (2015) concluded that PMED models calibrated using the bootstrapping sampling technique consistently showed lower standard error and bias.

The current study incorporated traditional split sampling, jackknifing, and bootstrapping sampling techniques into the automated calibration technique.

### ***5.2.1 Traditional split sampling approach***

Traditional split sampling approach is the most common sampling technique used in PMED model calibration studies. This approach requires that sample projects be randomly split into two subsets (AASHTO, 2010). One set is used to calibrate the performance models, and the other set validates the accuracy of the calibrated models (AASHTO, 2010). Researchers have typically used a 70-30 split or 80-20 split of data to calibrate and validate MEPDG transfer functions. In the traditional split sampling approach, the calibration dataset is used to reduce model bias and standard error and to obtain calibration coefficients. These calibrated coefficients are then used with the validation dataset to verify model accuracy. Goodness-of-fit statistics are reported for both calibration and validation datasets. The local calibration guide for the PMED software asserts that the traditional split sampling approach can produce misleading indications of model accuracy for small sample sizes (AASHTO, 2010).

### ***5.2.2 Jackknifing approach***

The jackknifing method is an iterative process that uses systematic sampling to adjust calibration coefficients of PMED performance models. Samples are selected by taking the



original data vector and systematically deleting one observation from the dataset. One of the  $n$  selected projects is left out one at a time, and calibration is performed for the  $n-1$  samples for each iteration. The prediction and standard errors can then be computed from the omitted sample. Thus, if  $n$  pavement sections are in the dataset, the jackknife sampling technique will consist of  $n$  samples, each with  $n-1$  data points in each sample subset analysis (Nisbet et al., 2018). The process of omitting, calibrating, and predicting is repeated until the total dataset is used for prediction. As a result,  $n$  values of standard error are generated, and jackknife goodness-of-fit statistics can be computed.

The NCHRP 1-40B project recommends the jackknifing method for small sample sizes. According to the report, this technique produces reliable assessments of PMED models in terms of prediction accuracy and goodness-of-fit statistics (AASHTO, 2010).

### ***5.2.3 Bootstrapping approach***

The bootstrapping method is a resampling technique used to compute statistics of a population by sampling a dataset with replacement. For example, for a dataset of  $N$  samples or pavement sections,  $X$  bootstrap samples of size  $N$  are randomly selected with replacement from the original dataset. Each  $X$  bootstrap sample omits several sections and creates multiple copies of other sections, allowing a given observation or pavement section to be included in the given sample size more than once (Brink, 2015). The number of bootstrap repetitions,  $X$ , should be large enough to ensure meaningful statistics can be computed, but the number of samples can only reduce the effects of random sampling errors and not increase the amount of information in the original data.

The purpose of bootstrapping resampling is to gather information economically. This approach can estimate mean, variances, confidence intervals, and other statistical properties by

utilizing the original data as a surrogate population to estimate sampling distribution of a statistic. For AASHTOWare PMED calibration, the bootstrapping method can find a distribution of optimized coefficients of the performance models.

### 5.3 Equivalence Testing

Previous local calibration studies of AASHTOWare PMED software primarily used a traditional equivalence testing or a paired  $t$ -test to determine bias. The local calibration guide of the PMED software also recommends using the paired  $t$ -test to evaluate significant differences between measured and predicted data. A limitation of widespread use of the paired  $t$ -test, however, is that when the null hypothesis states the true effect size is zero, the absence of an effect can be rejected but not statistically supported (Lakens, 2017). In other words, the paired  $t$ -test can successfully conclude if measured and predicted distress data differ, but it cannot confirm measured and predicted distress data are the same irrespective of the statistical  $p$ -value.

#### 5.3.1 Traditional equivalence testing

The null and alternate hypotheses for a traditional equivalence testing are

$$\text{Null hypothesis, } H_0 : \mu_{\text{measured}} = \mu_{\text{predicted}} \quad (5.2)$$

$$\text{Alternate hypothesis, } H_0 : \mu_{\text{measured}} \neq \mu_{\text{predicted}} \quad (5.3)$$

Where:

$\mu_{\text{measured}}$  = Sample mean of measured distress or IRI data; and

$\mu_{\text{predicted}}$  = Sample mean of PMED predicted distress or IRI data.

In a traditional equivalence testing set up, these two means are assumed to be similar if the statistical  $p$ -value is larger than a threshold value, often 0.05, or at a 95% confidence level (i.e., the null hypothesis cannot be accepted). Walker and Nowacki (2011) provided two reasons why use of a traditional comparative test to establish equivalence often leads to incorrect

conclusions. First, the burden of proof for statistical equivalence is on the wrong hypothesis (i.e., that of a difference). In this method, a significant result establishes a difference, whereas a non-significant result implies only that equivalency or equality cannot be ruled out. Consequently, the risk of incorrectly concluding equivalence can be very high. Secondly, since no margin of equivalence is considered in a paired  $t$ -test, the concept of equivalence is not well-defined.

### 5.3.2 Two one-sided $t$ -test

Although the null hypothesis cannot be supported when the true effect size is zero, large effects can be rejected in a frequent hypothesis testing framework in equivalence testing. A two one-sided  $t$ -test (TOST) is a simple equivalence approach that specifies an upper ( $\Delta_U$ ) and lower ( $\Delta_L$ ) equivalence bound based on an equivalence margin,  $\delta$  (Lakens, 2017). In TOST procedure, equivalence is established at the  $\alpha$  significance level if a  $(1-2\alpha) \times 100\%$  confidence interval for the difference in efficacies (new – current) is contained within the interval ( $\Delta_U = \delta, \Delta_L = -\delta$ ).

The null and alternate hypothesis for the TOST equivalence testing is stated below:

$$\text{Null Hypothesis, } H_0 : \mu_{\text{measured}} - \mu_{\text{predicted}} \leq -\delta \quad (5.4)$$

$$\text{Alternate hypothesis, } H_0 : \mu_{\text{measured}} - \mu_{\text{predicted}} > -\delta \quad (5.5)$$

and

$$\text{Null Hypothesis, } H_0 : \mu_{\text{measured}} - \mu_{\text{predicted}} \geq \delta \quad (5.6)$$

$$\text{Alternate hypothesis, } H_0 : \mu_{\text{measured}} - \mu_{\text{predicted}} < \delta \quad (5.7)$$

Determination of equivalence margin  $\delta$  is a critical step in equivalence testing because the value of  $\delta$  directly affects the outcome (Walker and Nowacki, 2011). A small value of  $\delta$  represents a narrow equivalence region and makes it difficult to establish equivalence. In TOST procedure, accuracy of optimized calibration coefficients depends on how well the equivalence margin can be established in terms of relevant evidence and engineering considerations. If the  $p$ -

value is smaller than a threshold (e.g., 0.05), then the difference between the two samples is smaller than the thresholds given by the equivalence margin.

Prior to this study, the TOST procedure had not been used for equivalence testing of AASHTOWare PMED software-predicted data and field measured data, so no established equivalence margin was available for PMED models. Therefore, this study used a heuristic method to set equivalence margin  $\delta$ . First, an initial value of  $\delta$  was assumed to verify PMED models with global coefficients. This initial value of  $\delta$  for a model was assumed to be same as the limiting  $S_e$  recommended by AASHTO (2010). After model calibration, TOST was repeated multiple times to compute the minimum  $\delta$  value for which the equivalence between measured and predicted distresses can be established. This approach of setting the equivalence margin helped determine the narrowest equivalence region for measured and predicted distress data. Table 5-1 lists the initial value of  $\delta$  assumed for PMED model verification.

Table 5-1 Initial value of  $\delta$  for verification of PMED models

PMED Models	$\delta$ value
AC rutting	0.1 in.
Top-down cracking	600 ft/mile
Transverse cracking	250 ft/mile
IRI	17 in./mile

#### 5.4 Automated Calibration Methodology

The primary goal of the automated calibration process is to employ the optimization technique to determine effective calibration parameters to minimize model bias and standard error. This study deployed a systematic method to automatically search for the optimal value of calibration parameters in prediction model transfer functions.

#### ***5.4.1 Programming routine for the automated technique***

The Python 3.7 programming language and Python “xlrd” library was used to read and format information from the Excel files (e.g., PMED outputs and distress data). The Python “NumPy” package was used for scientific computing within the programming routine. PMED model parameters were calibrated using the “SciPy” optimization package. The CG and L-BFGS techniques were used for transfer function parameter optimization.

To calibrate PMED performance models using the automated technique, the user must first successfully run the PMED software. One of the major challenges in automating the PMED software calibration process is to recognize relevant software outputs for a project at a specific time. PMED software generates several Excel, pdf, and text files, so the developed automated calibration technique can search PMED output files and identify mechanistic damages and distresses for a project on a specific date. The user must browse the directory where PMED software outputs are stored.

The automated technique requires inputs such as number of projects, measured distresses, and corresponding distress collection dates. Currently, inputs are provided in a tab-delimited text file. After running the automated technique, the user is prompted to select a model for calibration and choose a sampling technique such as split sampling, jackknifing, or bootstrapping.

After obtaining relevant damage data from the PMED output files, the application predicts distresses with a set of global model calibration coefficients ( $\Phi_{Global}$ ) to verify the prediction model. A paired *t*-test is then conducted to determine initial bias between the actual data and AASHTOWare PMED software-predicted values at 95% confidence level. TOST is also conducted, and the coefficient of determination ( $R^2$ ),  $S_e$ , and SSE are recorded. The CG or L-BFGS optimization technique is applied to the calibration dataset to obtain a set of model

calibration coefficients ( $\Phi_{Local}$ ) that minimizes the SSE between measured and predicted distresses. Bias,  $R^2$ ,  $S_e$ , and SSE are generated for the calibrated model. Equivalence testing is also conducted for the calibrated model, and the application generates graphs for measured versus predicted distress data. Figure 5-1 presents key steps in the automated calibration process.

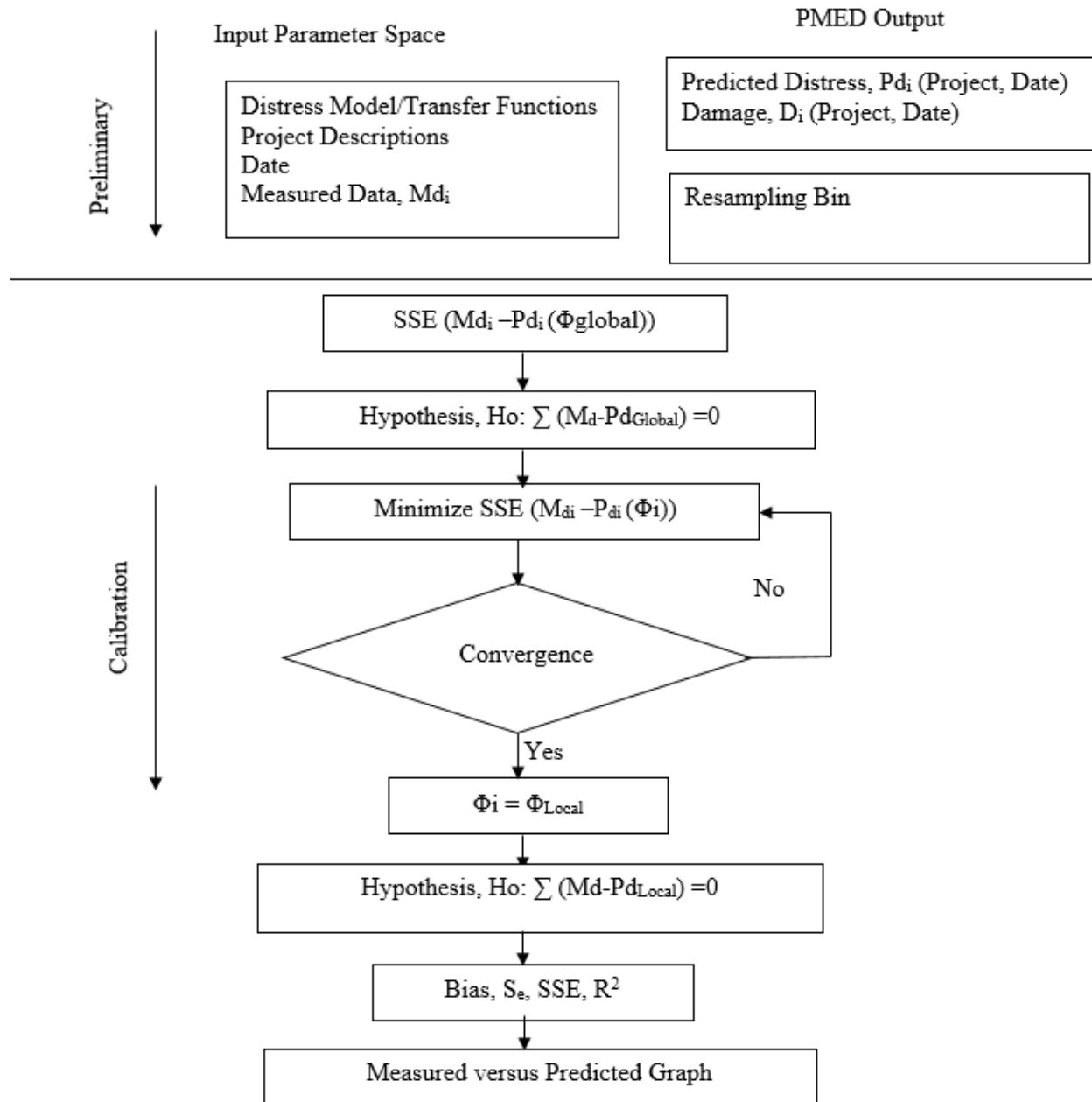


Figure 5-1 Analysis process for automated calibration technique

### ***5.4.2 Incorporating sampling methods into the automated technique***

This study incorporated three types of resampling techniques into the developed automated calibration technique.

#### ***5.4.2.1 Traditional split sampling approach***

Automated calibration requires project information such as the number of projects and project name as inputs. In the split sampling approach, the automated technique randomly divides the projects into calibration and validation sets. In this study, the automated calibration technique considered an 80-20 split of the data for calibration and validation. “Scikit-Learn” machine learning library in the Python programming environment was used to incorporate the traditional split sampling approach, and the CG technique was used for parameter optimization.

#### ***5.4.2.2 Jackknifing sampling approach***

The jackknifing sampling approach was also incorporated to provide users with a distribution of values for the calibration parameter under consideration. To implement the jackknife approach for  $n$  number of projects, the procedure first removes one pavement section from the  $n$  projects, and the model calibration is performed with the remaining  $(n-1)$  set of projects. This process is repeated  $n$  times for all pavement sections in the database, allowing a distribution of calibration parameters to be obtained to help users select appropriate calibration coefficients.

The following example is provided to explain the jack-knife approach used in this study. Six pavement sections, A, B, C, D, E, and F are to be used for calibration. Following the jackknife approach, six calibration datasets can be obtained. Calibration set 1 omits project F, calibration set 2 omits project E, and so on. Model calibration was performed for each calibration set, resulting in a distribution of calibration coefficient. Twenty-five AC over AC sections

generated 25 jackknife samples in this study. Similarly, 18 AC over JPCP sections generated 18 jackknife samples. “Scikit-Learn” library in the Python programming environment was used to incorporate the jackknife sampling approach. The CG technique was used for parameter optimization. Figure 5-2 illustrates the jackknife approach for the given example.

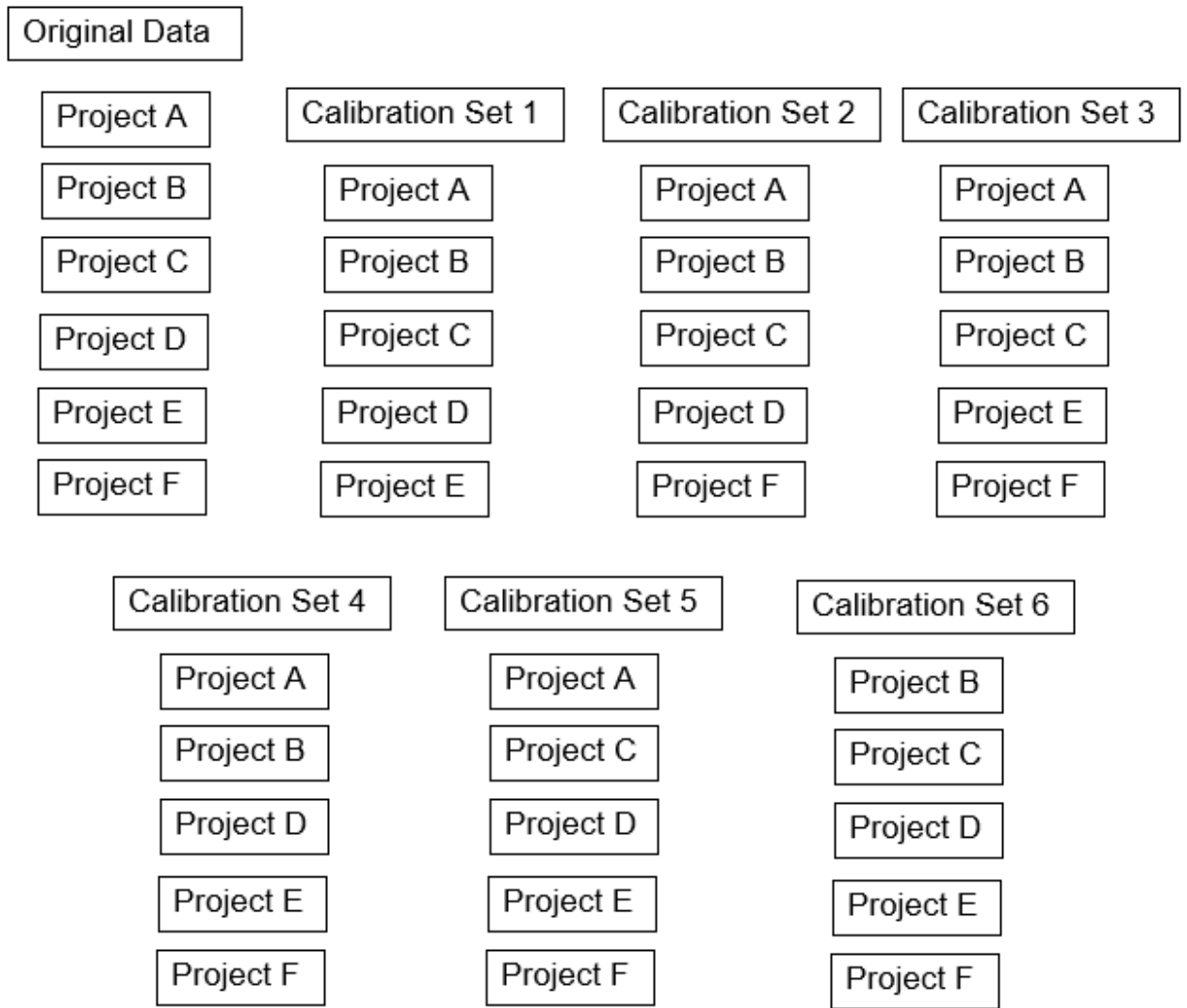


Figure 5-2 Working method of jackknife sampling approach



### 5.4.2.3 Bootstrapping approach

This study incorporated the bootstrap sampling approach into the automated calibration technique. To implement the bootstrap approach for  $N$  number of projects,  $X$  bootstrap samples of size  $N$  are randomly selected with replacement. Each  $B$  sample omits several sections and creates multiple copies of other sections (Brink, 2015). Model calibration is performed for each  $X$  sample, and a parameter distribution can be obtained.

The example used to explain the jackknife approach can be used to describe the bootstrapping approach in this study as well.  $B$  calibration datasets can be obtained using the bootstrapping method. Calibration set 1 omits project F but creates a copy of project A, calibration set 2 omits project F but creates a copy of project B, calibration set 3 omits project B and D but creates copies of project C and E. This process can be repeated  $X$  times (i.e., 1,000 or 10,000 times). For the  $X$  calibration sets, model calibration is performed for each set, and a distribution of calibration coefficients can be obtained. A total of 1,000 bootstrap repetitions can be used in the developed automated calibration method. Figure 5-3 illustrates the bootstrap approach for this example. “Scikits.bootstrap” function was used to incorporate the bootstrap resampling approach. The L-BFGS optimization technique was used for 1,000 bootstrap sample.

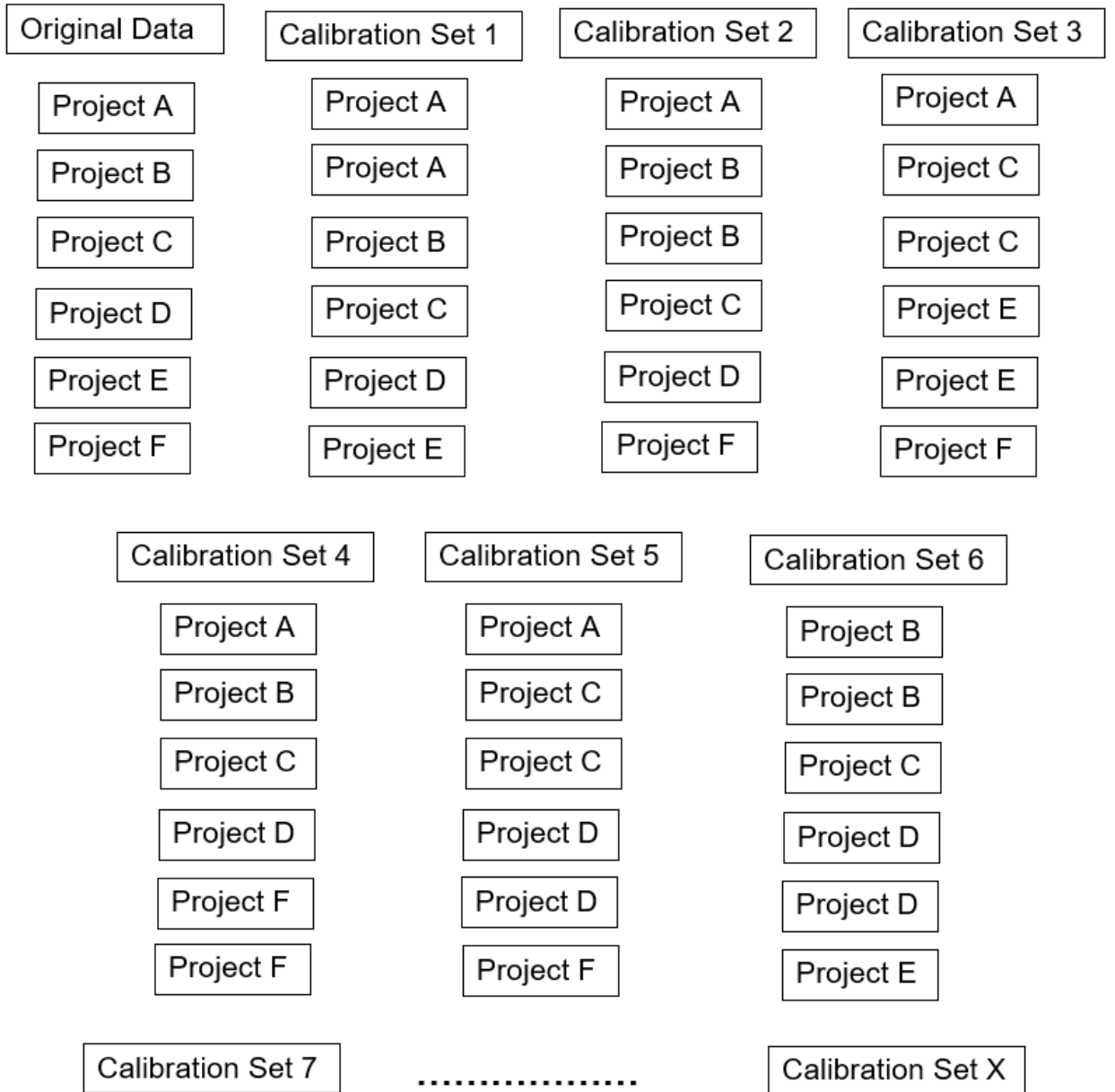


Figure 5-3 Working method of bootstrap sampling approach

## 5.5 Local Calibration of AC over AC sections

The automated calibration technique was used to calibrate PMED performance models for AC over AC sections listed in Table 3-3. Calibrated models include the AC rutting model, transverse cracking model, top-down cracking model, and the IRI model.

### 5.5.1 Permanent deformation model

In PMED model calibration, the first step carried out by the automated technique is to verify the model with global coefficients. The automated calibration technique reported bias, SSE,  $p$ -value from the paired  $t$ -test, and the  $p$ -value from the TOST. Table 5-2 lists verification results of the rutting model for the AC over AC sections, confirming that  $p$ -value from the TOST was less than 0.05 for an equivalence margin of 0.1 in. This result suggests that PMED-predicted rut depth and measured rut depths were equivalent for a margin of 0.1 in. Although the  $S_e$  was 0.06 in., which is within the AASHTO-suggested range, the  $p$ -value from the paired  $t$ -test was less than 0.05, indicating that there is evidence that the predicted and measured rut depths are different.

Table 5-2 Summary statistics for the nationally calibrated rutting model for AC over AC sections

Bias	SSE	$S_e$	$S_e/S_y$	$p$ -value from paired $t$ -test	$p$ -value from TOST
1.26	0.33	0.054	1.28	0.027	<0.001

The automated calibration technique also generated the measured versus predicted total rut depth graph. Figure 5-4 shows measured versus predicted total rut depths with global coefficients. Verification results of the rutting model for the AC over AC sections showed that the bias between predicted and measured rut depths was fairly low. However, the  $\beta_{1r}$  parameter

was optimized using the automated calibration technique. Results were obtained for traditional split sampling, jackknifing, and bootstrapping sampling techniques.

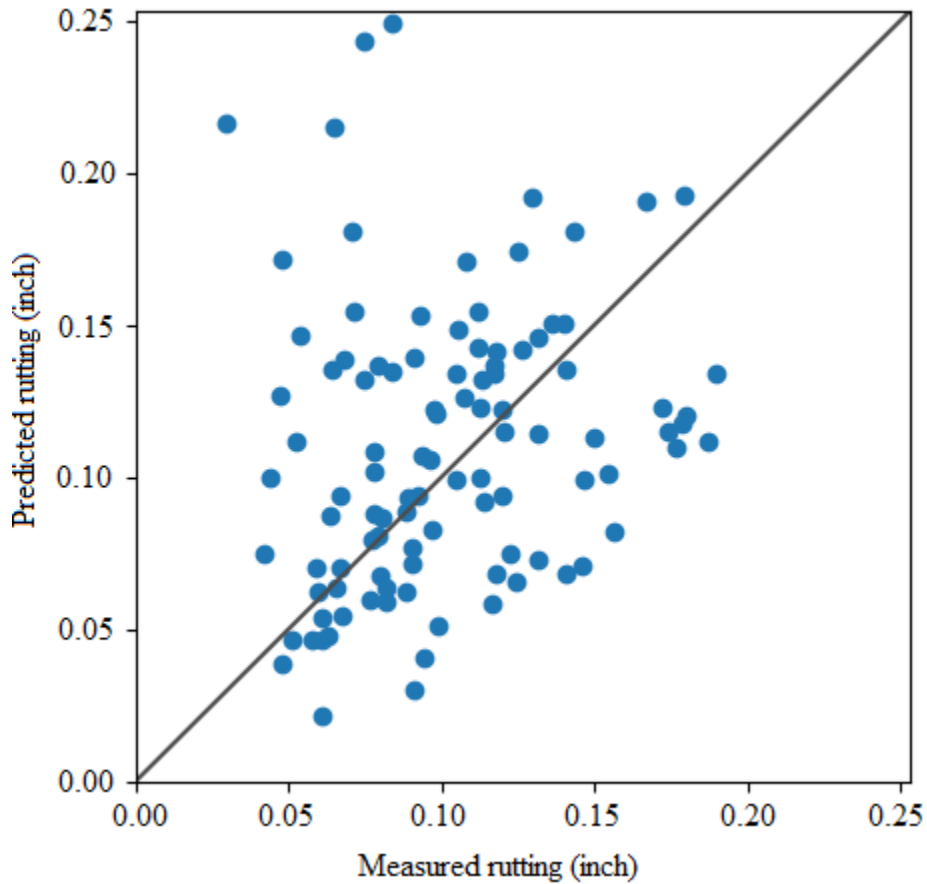


Figure 5-4 Predicted vs measured total rutting with globally calibrated factors

Three types of resampling techniques were incorporated into the developed automated calibration process. The  $\beta_{1r}$  parameter of the rutting model was optimized using those three techniques.

#### 5.5.1.1 Traditional split sampling approach

The permanent deformation model in the AASHTOWare PMED software was calibrated for the AC over AC sections using the automated technique developed in this study. The automated calibration technique considers a random 80-20 split of the data for calibration and validation and employs the CG optimization technique for  $\beta_{1r}$  parameter optimization. Table 5-3

presents summary statistics of the rutting model for the calibration dataset. Results in the table show that the  $p$ -value from the TOST procedure was less than 0.05 for an equivalence margin of 0.1 in., suggesting the calibrated rutting model predictions were equivalent to field rut depths for a margin of 0.1 in. The  $p$ -value from the paired  $t$ -test was higher than 0.05, which suggests that there is no evidence that the predicted and measured rut depths are different.

Table 5-3 Summary statistics for the locally calibrated rutting model for AC over AC sections

Bias	SSE	$S_e$	$S_e/S_y$	$p$ -value from paired $t$ -test	$p$ -value from TOST
-1.73	0.25	0.046	1.07	0.24	<0.001

Section 5.3.1 describes how, after calibrating the permanent deformation model, the TOST procedure was repeated multiple times to determine the narrowest equivalence region for measured and predicted rut depths. Table 5.4 presents a summary of the results of the repeated TOSTs. In all cases, the level of significance ( $\alpha$ ) was 0.05. Results in the table show that the calibrated rutting model predictions for the AC over AC sections were equivalent to measured rut depths for a margin of 0.03 in.

Table 5-4 Calibrated model equivalence margin between measured and predicted rutting

Equivalence margin, $\delta$ (in.)	$p$ -value	Remark
0.1	<0.001	Equivalent
0.075	<0.001	Equivalent
0.05	<0.001	Equivalent
0.03	0.014	Equivalent
0.025	0.068	Not equivalent

Measured versus predicted total rut depths with locally calibrated coefficients are shown in Figure 5-5. A comparison of Figures 5-4 and 5-5 shows that measured versus predicted rut depths with local coefficients demonstrated improved data location relative to the line of equality compared to measured versus predicted rut depth with global coefficients.

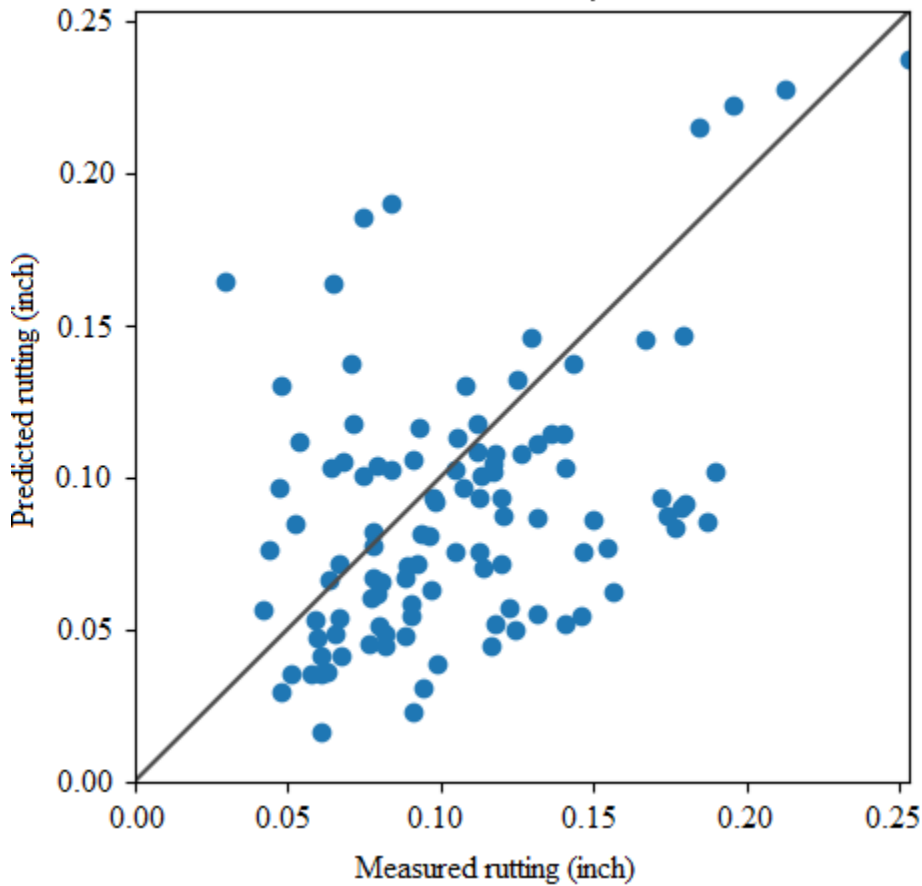


Figure 5-5 Predicted vs measured total rutting with local coefficients for AC over AC sections

Summary statistics for the rutting model after validation are shown in Table 5-5. The bias was slightly high for the rutting model with the validation dataset for locally calibrated coefficients, while rutting model  $S_e$  of the validation projects remained under the AASHTO-suggested 0.1 in. Figure 5-6 illustrates measured versus predicted rutting with local coefficients for the validation dataset.

Table 5-5 Validation results for the calibrated rutting model for AC over AC sections

Bias	SSE	$S_e$	$S_e/S_y$	$p$ -value from paired $t$ -test	$p$ -value from TOST ( $\delta = 0.03$ in.)
0.44	0.17	0.07	1.2	0.28	0.12

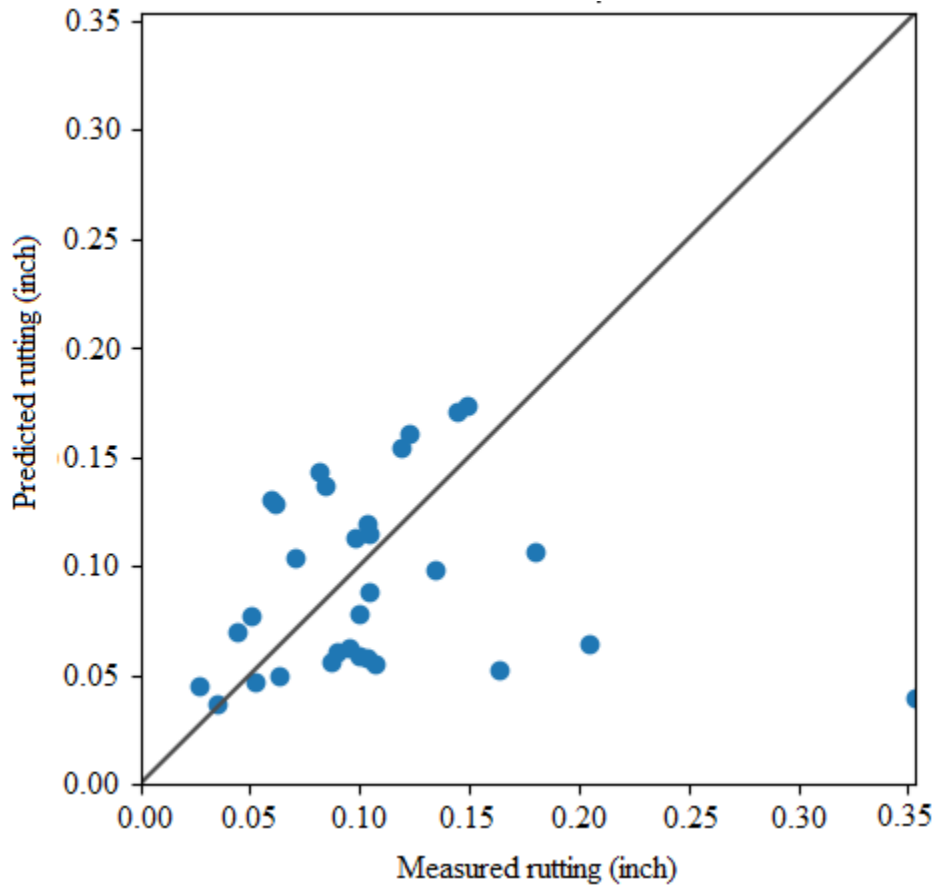


Figure 5-6 Predicted versus measured rutting for the validation dataset for AC over AC sections

### 5.5.1.2 Jackknifing approach

Jackknifing sampling approach was incorporated into the automated calibration technique. Only the  $\beta_{1r}$  parameter of the rutting model was optimized using the CG optimization method. Distribution of the  $\beta_{1r}$  coefficient from 24 jackknife samples for the AC over AC sections is shown in Figure 5-6. The figure shows that the  $\beta_{1r}$  parameter coefficient was in the

range of 0.290–0.325 except for one instance. This range is 0.308–0.312 for 11 of the 24 jackknife samples.

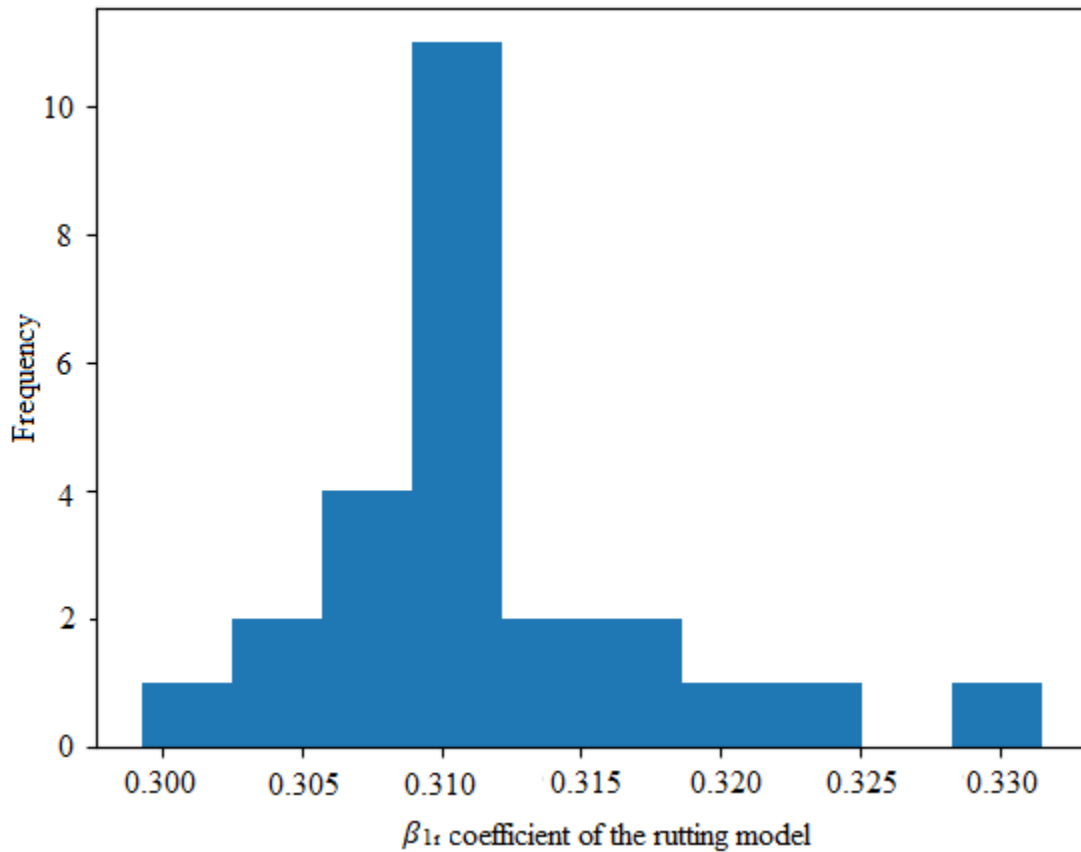


Figure 5-7 Distribution of the  $\beta_{1r}$  parameter using jackknife sampling

The TOST procedure was conducted multiple times for the value of  $\beta_{1r}$  in the range of 0.290–0.325, and the narrowest equivalence margin  $\delta$  was determined in each case. Figure 5-8 illustrates results of the repeated TOST for the above-mentioned range of  $\beta_{1r}$ . For the value of  $\beta_{1r}$  parameter within 0.290–0.325, the PMED-predicted rutting and measured rutting were always equivalent for a margin of 0.03 in. The equivalence margin was lowest (0.02 in.) for a  $\beta_{1r}$  value of 0.325.



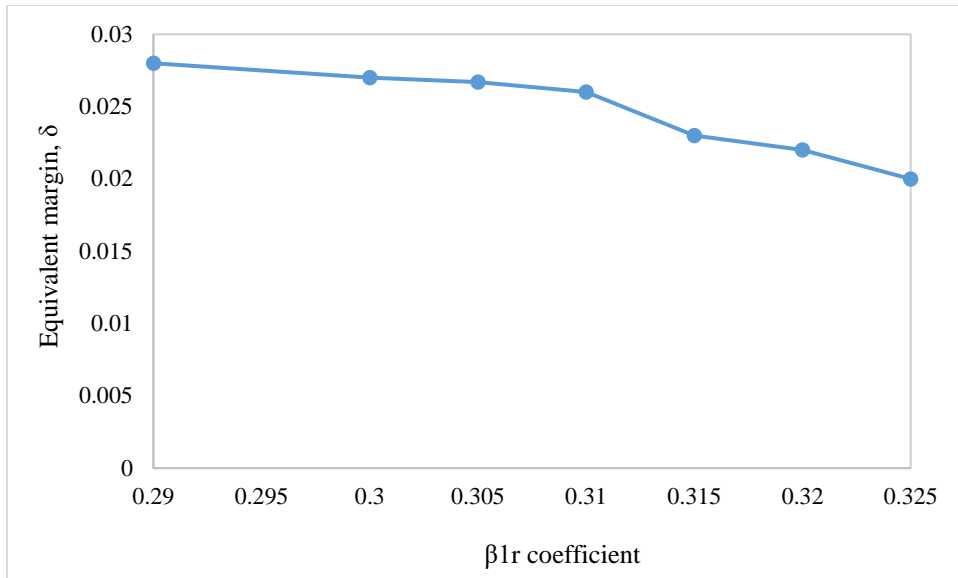


Figure 5-8 Rutting model equivalence margin with respect to  $\beta_{1r}$  parameter

### 5.5.1.3 Bootstrapping approach

The  $\beta_{1r}$  parameter of the rutting model was optimized using the L-BFGS optimization technique for 1,000 bootstrap calibration datasets. Distribution of the  $\beta_{1r}$  coefficient obtained from the 1,000 bootstrap samples for the AC over AC sections is shown in Figure 5-9. The figure demonstrates that, for approximately 460 samples, the value of  $\beta_{1r}$  coefficient was between 0.29 and 0.33. For approximately 990 bootstrap samples, the  $\beta_{1r}$  coefficient was in the range of 0.24–0.41.

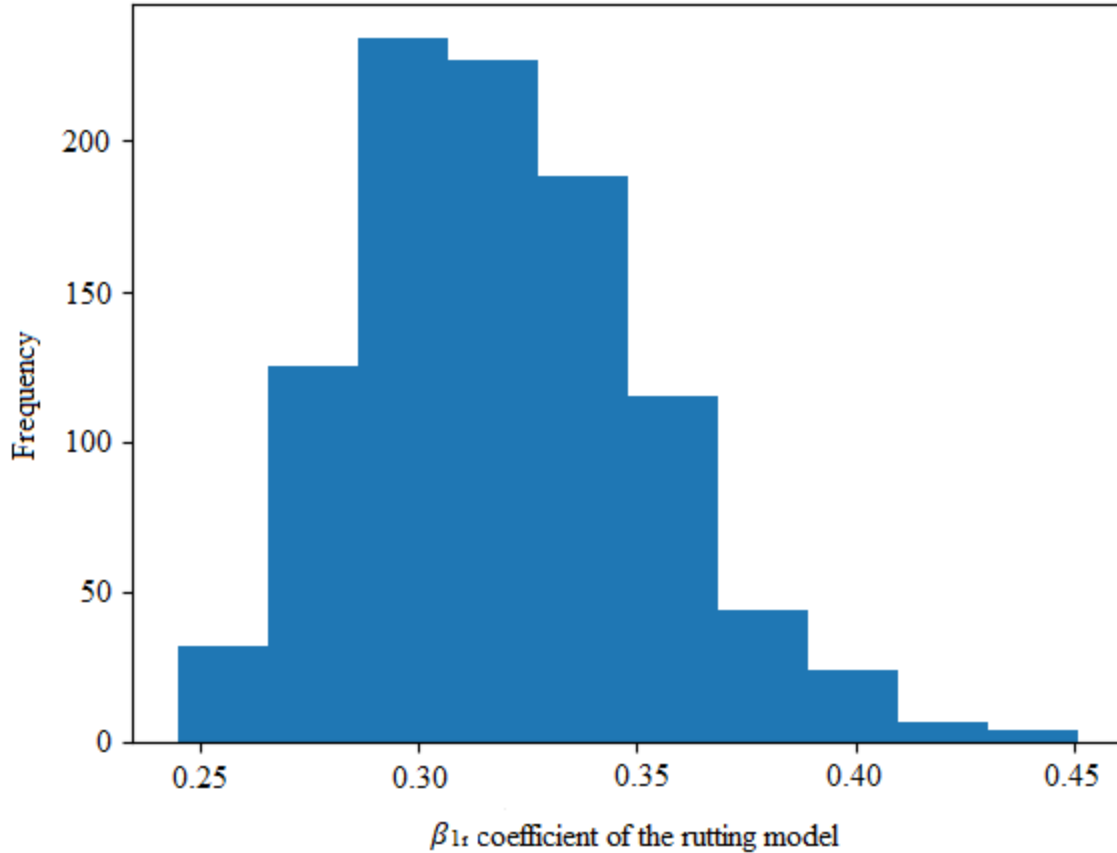


Figure 5-9 Distribution of the  $\beta_{1r}$  parameter using bootstrap resampling approach

Repeated TOST was conducted for the  $\beta_{1r}$  value ranging from 0.24 to 0.41, and the narrowest equivalence margin  $\delta$  was determined in each case. Figure 5-10 presents results of the repeated TOST. For the value of  $\beta_{1r}$  parameter within the 0.24–0.41 range, PMED-predicted rutting and measured rut depths were equivalent for a margin of 0.05 in. The equivalence margin was lowest (0.012 in.) for a  $\beta_{1r}$  value of 0.36. These findings suggest that the equivalence margin for PMED-predicted and measured rut depths was 12 mils when the rutting model coefficient  $\beta_{1r}$  value was 0.36.

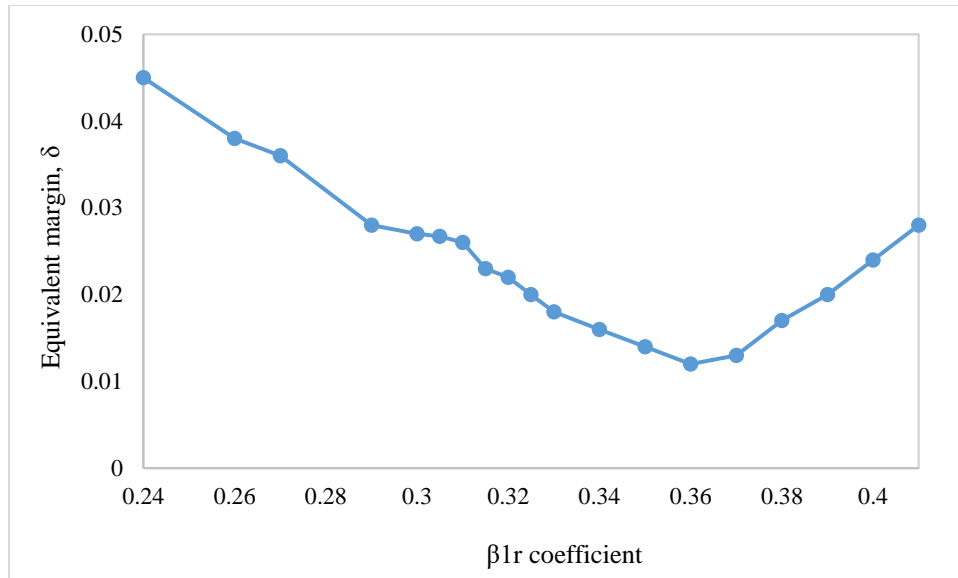


Figure 5-10 Rutting model equivalence margin with respect to  $\beta_{1r}$  parameter

### 5.5.2 Transverse cracking model

The transverse cracking model was calibrated using the automated calibration technique for the AC over AC sections. The first step was to verify the model with global coefficients. Summation of bias, SSE,  $p$ -value from the paired  $t$ -test, and the  $p$ -value from the TOST procedure were reported. Table 5-6 lists summary statistics of the transverse cracking model for the AC over AC sections. Results in the table show that  $p$ -value from the TOST procedure was less than 0.05 for an equivalence margin 250 ft/mile, indicating that the PMED-predicted and measured transverse cracking were equivalent for a margin of 250 ft/mile. The  $S_e$  was 188 ft/mile, which was also within the AASHTO-suggested range. However, the  $p$ -value from the paired  $t$ -test was less than 0.05, indicating that predicted and measured transverse cracking differ.

Table 5-6 Summary statistics for the globally calibrated transverse cracking model

Bias	SSE	$S_e$	$S_e/S_y$	$p$ -value from paired $t$ -test	$p$ -value from TOST
-6508	3995594	188	0.95	<0.001	<0.001

The measured versus predicted transverse cracking plot with global coefficients was also generated using the automated calibration technique. Figure 5-11 shows measured versus predicted transverse cracking with global coefficients. An asymmetrical trend with respect to the line of equality can be observed.

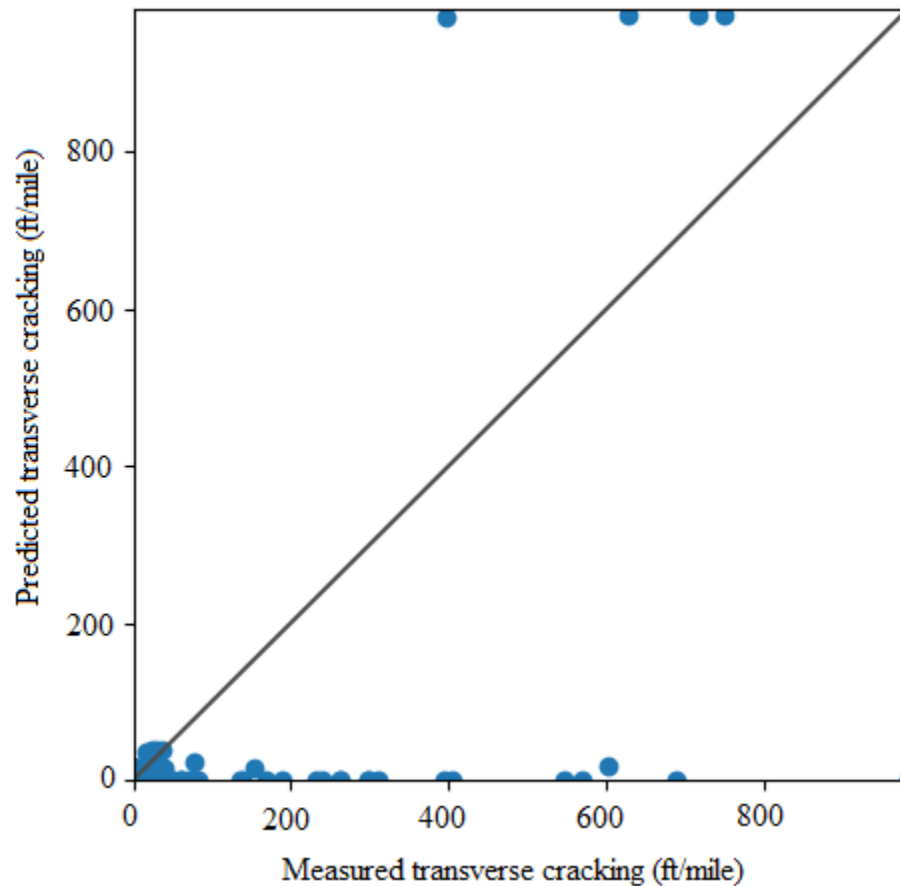


Figure 5-11 Predicted vs measured transverse cracking with globally calibrated factors

#### 5.5.2.1 Traditional split sampling approach

Verification results of the transverse cracking model for the AC over AC sections proved the necessity for model recalibration. Section 4.1.2.2 describes how the PMED transverse cracking model was calibrated by adjusting reflection cracking model coefficients only. The automated calibration technique was used to optimize the reflective cracking model transfer

function calibration coefficients  $C_4$  and  $C_5$ . As discussed, time-series damage ratio ( $D$ ) and percent RCR values must be extracted from the “transverseReflectiveCracking.log” file with respect to the corresponding date to optimize  $C_4$  and  $C_5$ . The automated technique can extract the required time-series  $D$  and RCR values from a particular file for each project. The automated technique then applies the CG optimization technique to determine optimized values of  $C_4$  and  $C_5$ . Results are provided for traditional split sampling, jackknifing, and bootstrapping sampling techniques.

The automated calibration technique uses a random 80-20 split of the data for calibration and validation. Table 5-7 presents summary statistics of the transverse cracking model for the calibration dataset. Results in the table show that  $p$ -value from the TOST procedure was less than 0.05 for an equivalence margin of 250 ft/mile, indicating that the PMED-predicted transverse cracking and measured transverse cracking were equivalent for a margin of 250 ft/mile. The  $p$ -value from the paired  $t$ -test after local calibration was greater than 0.05, which suggests that there is no evidence that the predicted and the measured transverse cracking are different. A comparison of values in Table 5-6 and Table 5-7 shows that transverse cracking model goodness-of-fit statistics improved significantly after local calibration.

Table 5-7 Summary statistics for the locally calibrated transverse cracking model

Bias	SSE	$S_e$	$S_e/S_y$	$p$ -value from paired $t$ -test	$p$ -value from TOST
-798	1,006,772	99	0.50	0.42	<0.001

After calibration, the TOST procedure was done to determine the narrowest equivalence region for measured and predicted transverse cracking. Table 5-8 presents a summary of the repeated TOST procedure. In all cases, the level of significance ( $\alpha$ ) was 0.05. Results in the table

show that the calibrated transverse cracking model predictions for the AC over AC sections were equivalent to measured transverse cracking for a margin of 55 ft/mile.

Table 5-8 Calibrated model equivalence margin between measured and predicted transverse cracking

Equivalence margin, $\delta$ (ft/mile)	<i>p</i> -value	Remark
250	<0.001	Equivalent
150	<0.001	Equivalent
100	0.002	Equivalent
55	0.03	Equivalent
50	0.06	Not equivalent

Measured versus predicted transverse cracking with locally calibrated coefficients is shown in Figure 5-12. A comparison of Figures 5-11 and 5-12 proves that the measured versus predicted transverse cracking with local coefficients showed significant improvement in data location relative to the line of equality compared to measured versus predicted transverse cracking with global coefficients.

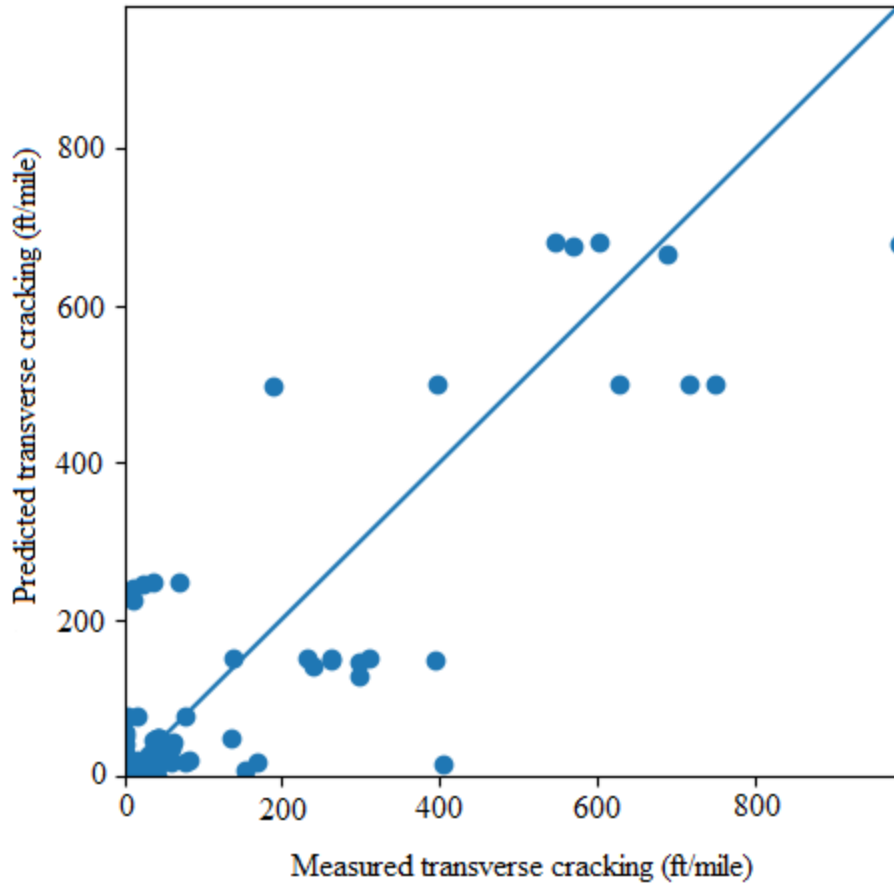


Figure 5-12 Predicted vs measured total rutting with local coefficients for AC over AC sections

Summary statistics for the calibrated transverse cracking model after validation are presented in Table 5-9. The  $p$ -value from the paired  $t$ -test for the validation dataset with local coefficients was greater than 0.05, which suggests that there is no evidence that the predicted and measured transverse cracking differ for projects considered in the validation dataset. However, the  $p$ -value from the TOST procedure was higher than 0.05 for an equivalence margin of 55 ft/mile, which suggests that predicted and measured transverse cracking were not equivalent for a margin of 55 ft/mile for projects in the validation dataset. Repeated TOST procedure was performed again for the validation dataset, and the narrowest equivalence margin was 85 ft/mile.

Figure 5-13 illustrates measured versus predicted transverse cracking with local coefficients for the validation dataset.

Table 5-9 Validation results of the calibrated rutting model for AC over AC sections

Bias	SSE	$S_e$	$S_e/S_y$	$p$ -value from paired $t$ -test	$p$ -value from TOST ( $\delta = 55$ ft/mile)
-887	702322	148	0.89	0.29	0.2

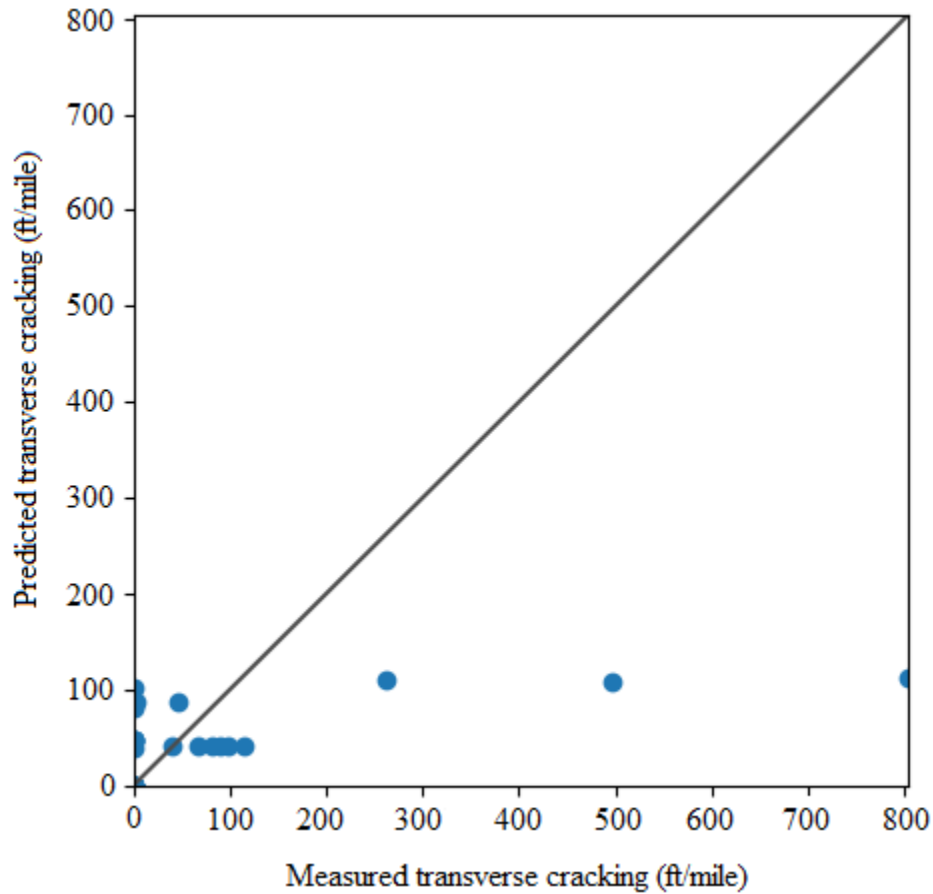


Figure 5-13 Predicted versus measured transverse cracking for the validation dataset

### 5.5.2.2 Jackknifing approach

The CG optimization method was used to optimize the  $C_4$  and  $C_5$  coefficients of the transverse cracking model for all AC over AC sections considered in this study. Figures 5-14 and 5-15 show the distribution of  $C_4$  and  $C_5$  coefficients, respectively, using the jackknife techniques.



Figure 5-14 shows that the range of  $C_4$  was 251–253 for 16 jackknife samples, and Figure 5-15 shows that the value of coefficient  $C_5$  ranged from -2.45 to -2.58 for 18 jackknife samples.

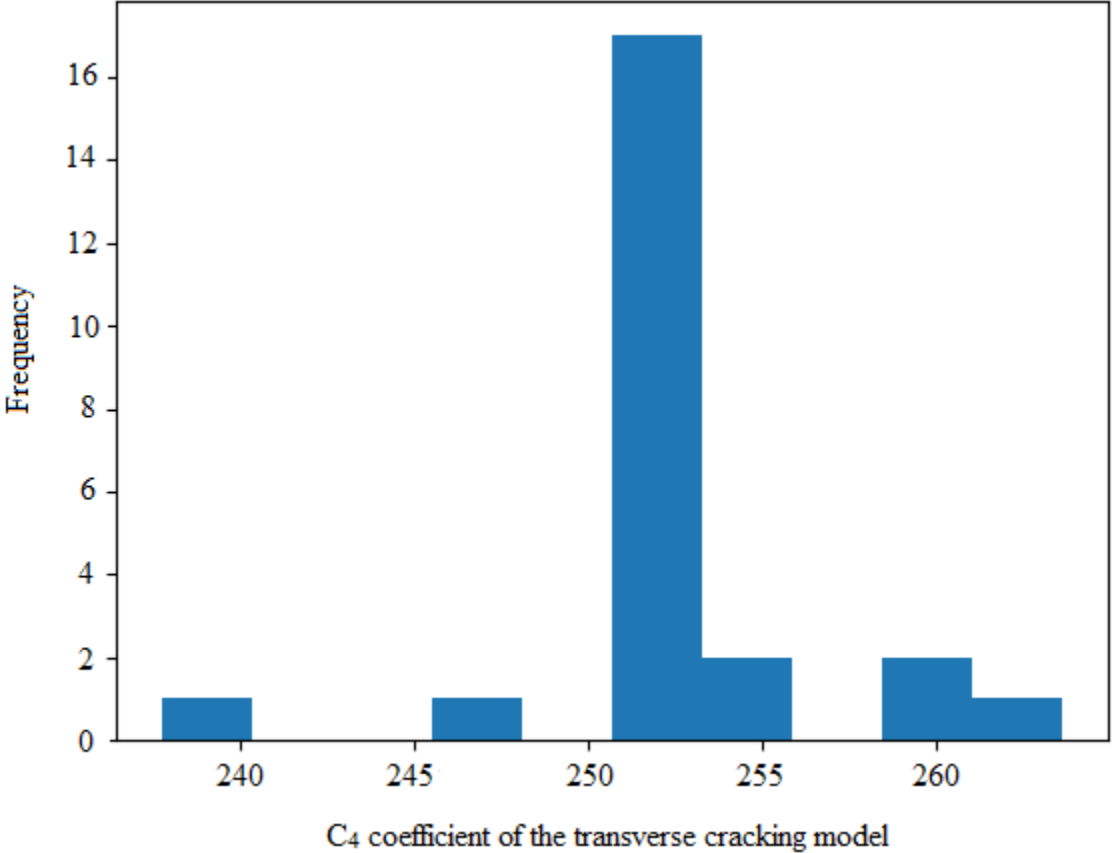


Figure 5-14 Distribution of the  $C_4$  coefficient using jackknife sampling technique

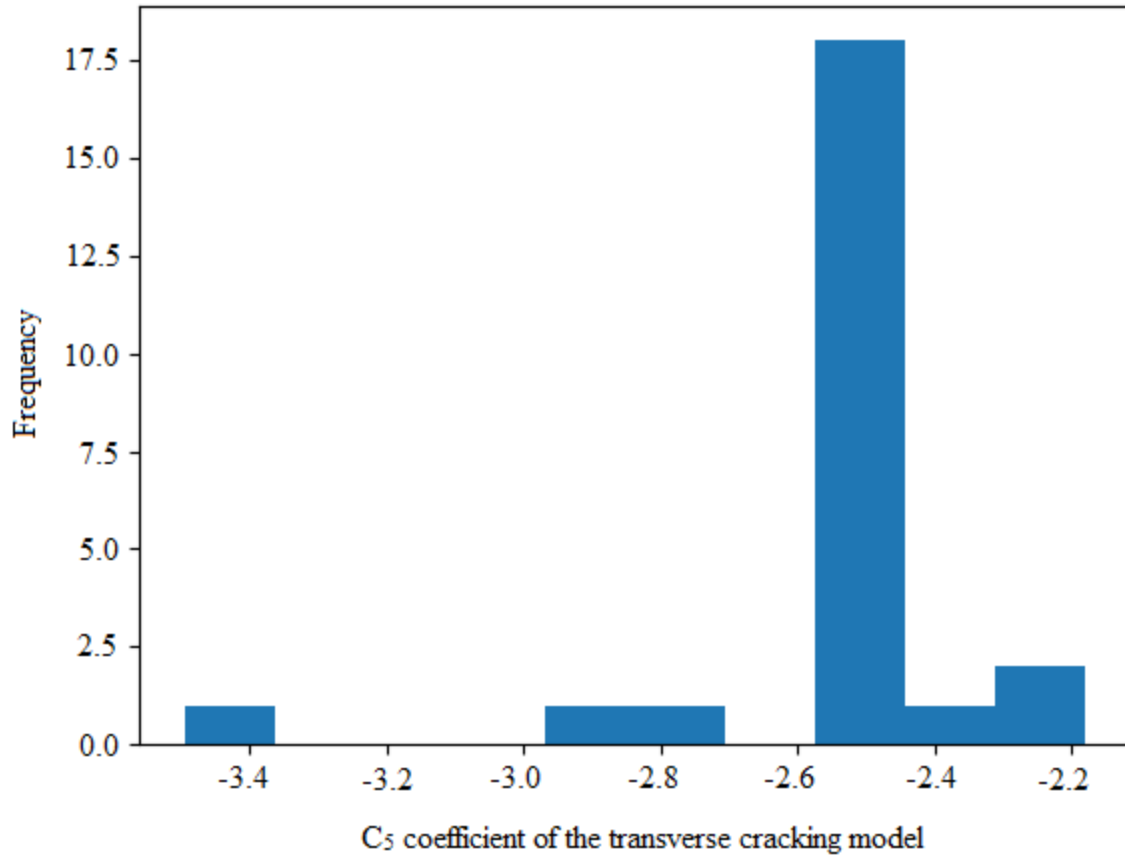


Figure 5-15 Distribution of the  $C_5$  coefficient using jackknife sampling technique

The TOST procedure was repeated for a combination of  $C_4$  and  $C_5$ , with  $C_4$  in the range of 251–253 and  $C_5$  ranging from -2.45 to -2.58. The purpose was to establish the narrowest equivalence margin  $\delta$ . Table 5-10 presents results obtained from the repeated TOST considering the above-mentioned combination of  $C_4$  and  $C_5$ . Results showed that the calibrated transverse cracking predictions for the AC over AC sections were equivalent to measured transverse cracking for a margin of 55 ft/mile for all considered  $C_4$  and  $C_5$  combinations, meaning that the PMED transverse cracking predictions (level of significance,  $\alpha = 0.05$ ) would likely be equivalent to transverse cracking measured in the field for a margin of 55 ft/mile if  $C_4$  and  $C_5$  coefficients range from 251 to 253 and -2.45 to -2.58, respectively.

Table 5-10 Combination of  $C_4$  and  $C_5$  considered for repeated TOST

Calibration Coefficient $C_4$	251	251	253	253
Calibration Coefficient $C_5$	-2.45	-2.58	-2.45	-2.58
Equivalence margin, $\delta$ (ft/mile)	55	55	55	55

### 5.5.2.3 Bootstrapping approach

The  $C_4$  and  $C_5$  coefficients of the transverse cracking model were optimized using the bootstrapping approach. One thousand bootstrap samples were optimized using the L-BFGS optimization technique. Figures 5-16 and 5-17 show the distribution of  $C_4$  and  $C_5$  coefficients using the bootstrap method. Figure 5-16 shows that the range of coefficient  $C_4$  was 266–268 for approximately 600 bootstrap samples. In fact, coefficient  $C_4$  was 260–269 for almost every bootstrap sample. Figure 5-17 shows that coefficient  $C_5$  ranged from -2.75 to -2.15 for all bootstrap samples.

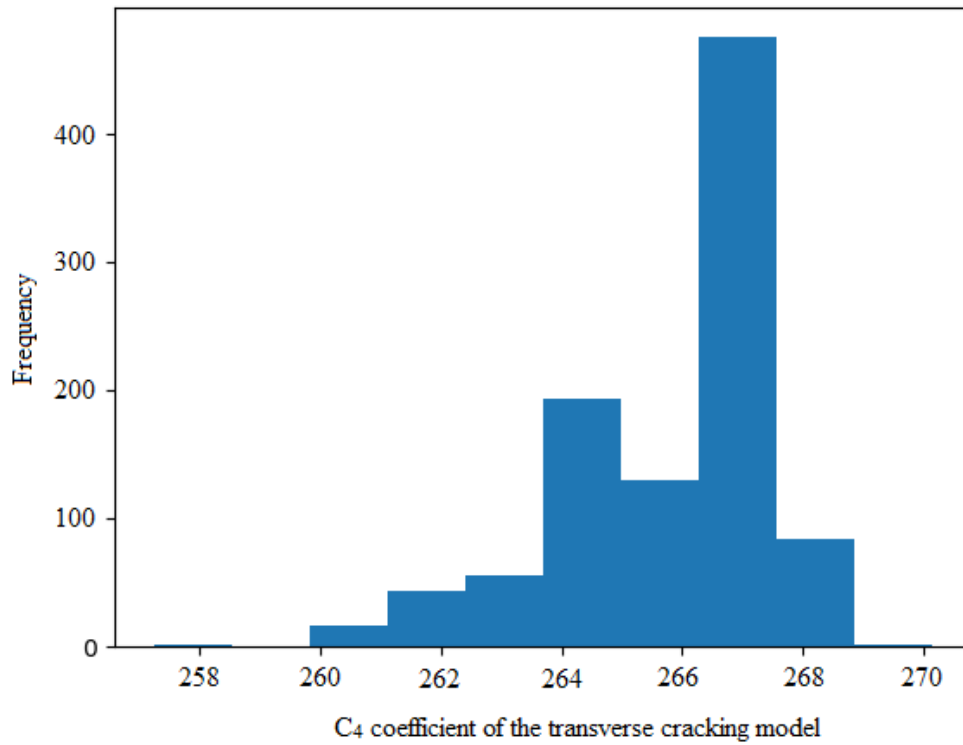


Figure 5-16 Distribution of the  $C_4$  coefficient using bootstrap sampling technique

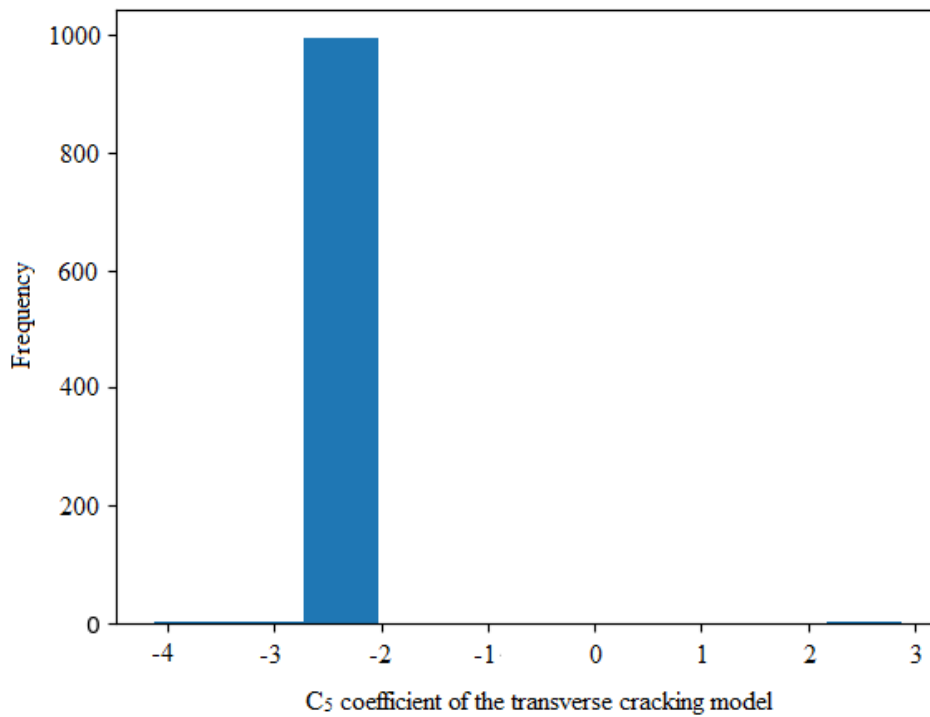


Figure 5-17 Distribution of the  $C_5$  coefficient using bootstrap sampling technique

TOST was repeatedly conducted for a combination of  $C_4$  and  $C_5$ , with  $C_4$  in the range of 260–269 and  $C_5$  ranging from -2.75 to -2.15. Table 5-11 presents results obtained from the repeated TOSTs considering the above-mentioned combination of  $C_4$  and  $C_5$ . Results showed that calibrated transverse cracking predictions for the AC over AC sections were equivalent to the measured transverse cracking for a margin of at least 53 ft/mile for all considered  $C_4$  and  $C_5$  combinations, meaning that PMED transverse cracking predictions (level of significance,  $\alpha = 0.05$ ) would likely be equivalent to transverse cracking measured in the field for a margin of 53 ft/mile if the  $C_4$  and  $C_5$  coefficients range from 260 to 269 and -2.15 to -2.75, respectively.

Table 5-11 Combination of  $C_4$  and  $C_5$  considered for repeated TOST

Calibration Coefficient $C_4$	260	260	269	269
Calibration Coefficient $C_5$	-2.15	-2.75	-2.15	-2.75
Equivalence margin, $\delta$	50	50	50	53

### 5.5.3 Top-down cracking model

The top-down cracking model was calibrated using the automated technique developed in this study. All load-related cracks were longitudinal, top-down fatigue cracking. The first step was to verify the model with global coefficients. Summation of bias, SSE,  $p$ -value from the paired  $t$ -test, and  $p$ -value from the TSOT procedure were reported. Table 5-12 lists summary statistics of verification results of the top-down cracking model. Results in the table show that  $p$ -value from the TOST procedure was higher than 0.05 for an equivalence margin of 250 ft/mile, suggesting that PMED-predicted and measured top-down cracking were not equivalent for a margin of 250 ft/mile. The  $S_e$  was 2,401 ft/mile, which is higher than the AASHTO-suggested value of 250 ft/mile. The  $p$ -value from the paired  $t$ -test was less than 0.05, indicating that predicted and measured top-down cracking are different.

Table 5-12 Summary statistics for the globally calibrated top-down cracking model

Bias	SSE	$S_e$	$S_e/S_y$	$p$ -value from paired $t$ -test	$p$ -value from TOST
-85710	716,010,362	2401	1.39	0.0011	0.9

The measured versus predicted top-down cracking plot with global coefficients was also generated using the automated calibration technique. Figure 5-18 shows measured versus predicted longitudinal cracking with global coefficients, in which the measured versus predicted top-down cracking shows an asymmetrical trend to the line of equality.

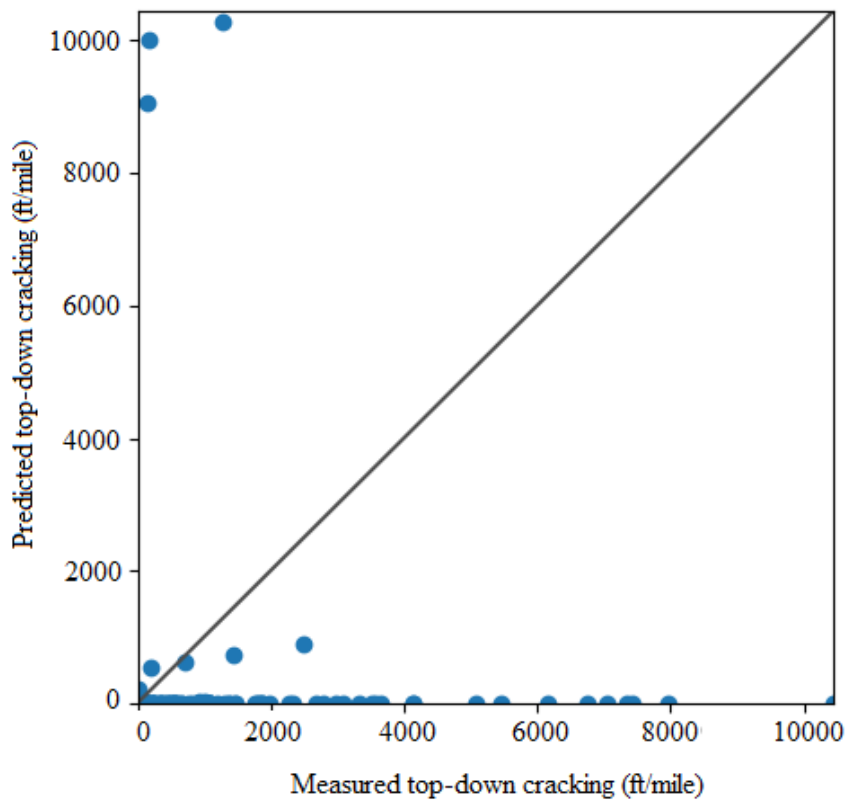


Figure 5-18 Predicted vs measured top-down cracking with globally calibrated factors

### 5.5.3.1 Traditional split sampling approach

Verification results of the longitudinal cracking model for the AC over AC sections affirmed the necessity of model recalibration. Section 4.1.3.2 describes how the PMED top-down cracking model can be calibrated by optimizing calibration parameters  $C_1$  and  $C_2$ . The automated calibration technique was used to extract the values of the time-series cumulative damage index at the top of the surface ( $DI_{top}$ ) from the project-wise Excel output for corresponding dates. The CG optimization technique was applied to determine a combination of  $C_1$  and  $C_2$  parameters that yielded the least SSE between measured and predicted top-down cracking.

The automated technique uses a random 80-20 split for calibration and validation. Table 5-13 presents summary statistics of the top-down cracking model for the calibration dataset. A comparison of values in Tables 5-12 and 5-13 shows that goodness-of-fit statistics of the top-down cracking model significantly improved after local calibration. However, model  $S_e$  remained higher than the AASHTO-suggested value.

Table 5-13 Summary statistics for the locally calibrated top-down cracking model

Bias	SSE	$S_e$	$S_e/S_y$	$p$ -value from paired $t$ -test	$p$ -value from TOST
-1,835	322,233,291	1735	0.98	0.91	0.092

Results in Table 5-13 show that the  $p$ -value from the paired  $t$ -test after local calibration was higher than 0.05, indicating that there is no evidence that the predicted and measured top-down cracking differ. However, the  $p$ -value from the TOST was higher than 0.05 for a  $\delta$  value of 250 ft/mile, indicating that the predicted and measured top-down cracking were not equivalent for a margin of 250 ft/mile. The TOST procedure was then performed multiple times to determine the equivalence margin for measured and predicted top-down cracking. Table 5-14 presents a summary of the results of the repeated TOST procedures. The level of significance ( $\alpha$ )

was 0.05 in all cases. Results in Table 5-14 show that the equivalence margin for predicted and measured top-down cracking was 310 ft/mile. In other words, PMED top-down cracking predictions were not equivalent to measured top-down cracking for any margin less than 310 ft/mile.

Table 5-14 Calibrated model equivalence margin between measured and predicted rutting

Equivalence margin, $\delta$ (ft/mile)	<i>p</i> -value	Remark
250	0.092	Not equivalent
260	0.083	Not equivalent
280	0.067	Not equivalent
300	0.053	Not equivalent
310	0.047	Equivalent

The measured versus predicted plot of longitudinal cracking with local factors is shown in Figure 5-19. An asymmetrical trend with respect to the line of equality can be observed.



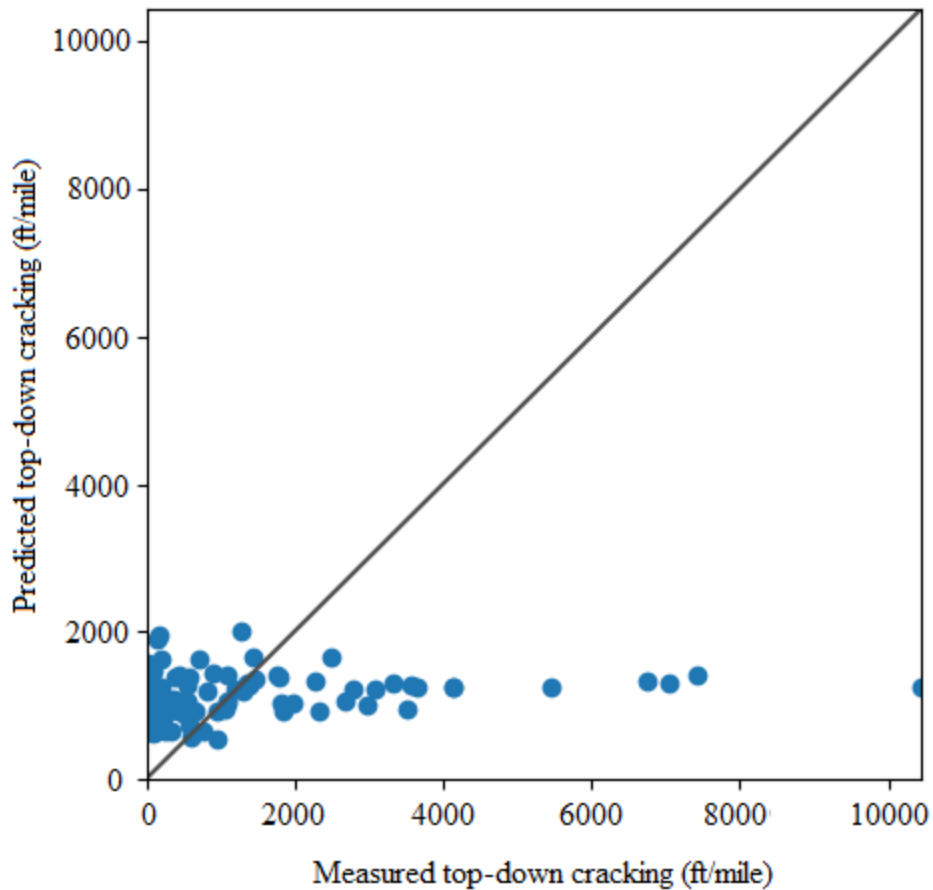


Figure 5-19 Predicted vs measured top-down with local coefficients for AC over AC sections

Table 5-15 tabulates summary statistics for the calibrated top-down cracking model after validation. The  $p$ -value from the paired  $t$ -test for the validation dataset with local coefficients was greater than 0.05, which suggests that there is no evidence that the predicted and measured top-down cracking differ for projects considered in the validation dataset. However, the  $p$ -value from the TOST procedure was higher than 0.05 for an equivalence margin of 310 ft/mile, indicating that the predicted and measured top-down cracking were not equivalent for a margin of 310 ft/mile for projects in the validation dataset. Repeated TOST was performed again for the validation dataset, and the narrowest equivalence margin was 900 ft/mile. Figure 5-20 presents measured versus predicted transverse cracking with local coefficients for the validation dataset.

Table 5-15 Validation results for the calibrated rutting model for AC over AC sections

Bias	SSE	$S_e$	$S_e/S_y$	$p$ -value from paired $t$ -test	$p$ -value from TOST ( $\delta = 310$ ft/mile)
-2959	156,802,349	2212	1.02	0.81	0.29

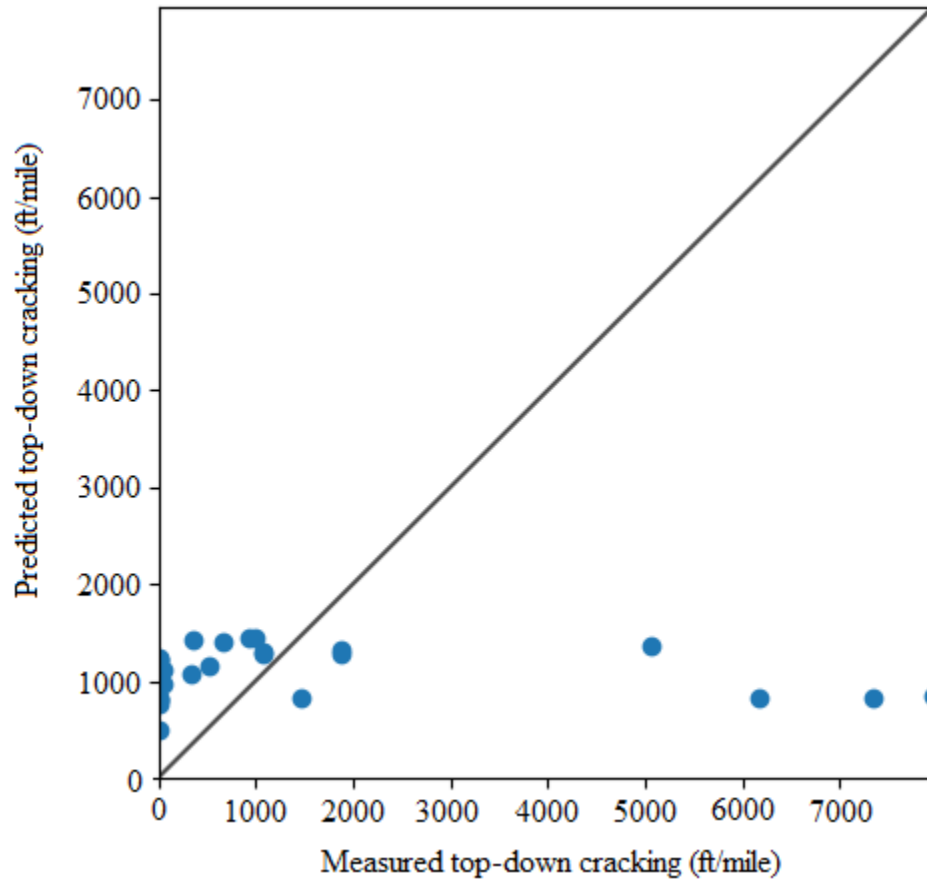


Figure 5-20 Predicted versus measured top-down cracking for the validation dataset

### 5.5.3.2 Jackknifing approach

The jackknifing sampling approach was integrated into the automated technique to calibrate the PMED top-down cracking model. Both  $C_1$  and  $C_2$  coefficients of the top-down cracking model were optimized for 24 AC over AC jackknife samples. The CG optimization technique was used. Figures 5-21 and 5-22 show the distribution of  $C_1$  and  $C_2$  coefficients using

the jackknife technique. Figure 5-21 shows that the range of coefficient  $C_1$  was 1.87–1.93 for 16 jackknife samples, and Figure 5-22 shows that the value of coefficient  $C_2$  ranged from 0.07 to 0.12 for 22 jackknife samples.

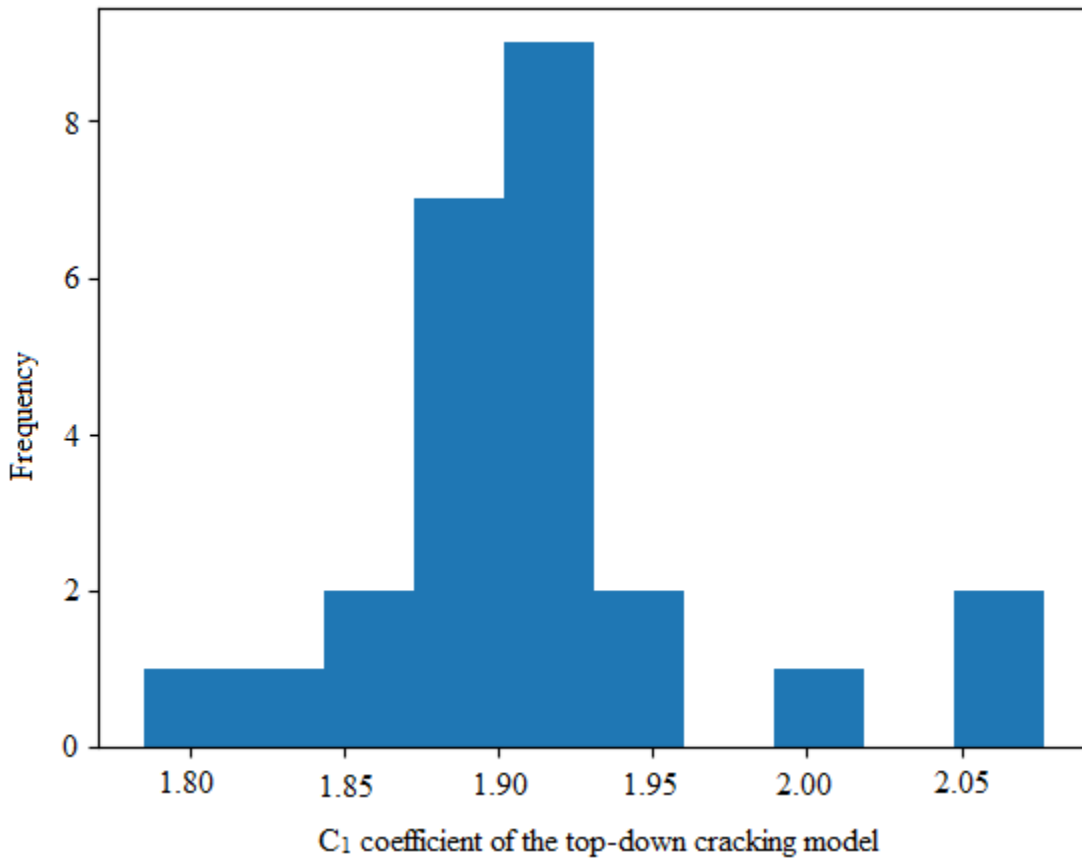


Figure 5-21 Distribution of the  $C_1$  coefficient using jackknife sampling technique

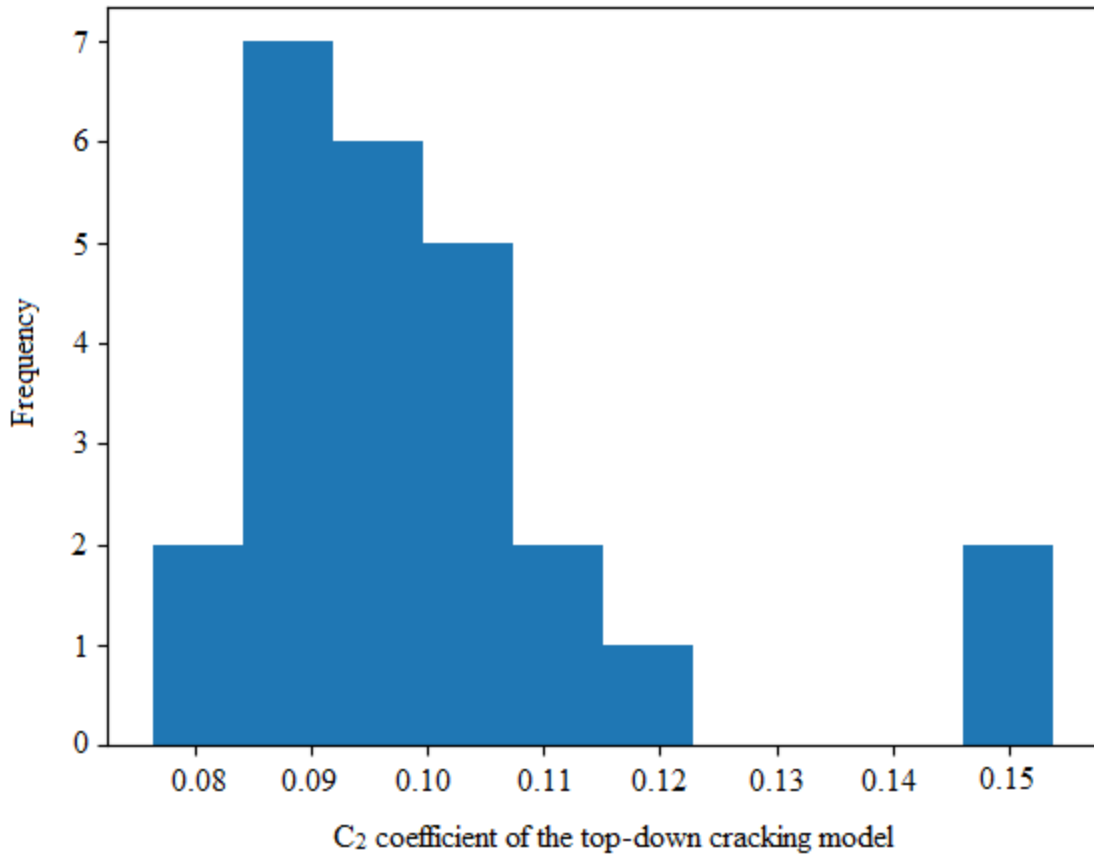


Figure 5-22 Distribution of the  $C_2$  coefficient using jackknife sampling technique

The TOST procedure was repeatedly conducted for a combination of  $C_1$  and  $C_2$ , with  $C_1$  in the range of 1.87–1.93 and  $C_2$  in the range of 0.07–0.12. Table 5-16 presents results obtained from the repeated TOST for the above-mentioned combination of  $C_1$  and  $C_2$ . Results showed that the narrowest equivalence margin for measured and predicted top-down cracking was 300 ft/mile for a  $C_1$  value of 1.87 and a  $C_2$  value of 0.12. These results suggest that PMED top-down cracking predictions (level of significance,  $\alpha = 0.05$ ) would likely be equivalent to top-down cracking measured in the field for a margin of 300 ft/mile if  $C_1$  and  $C_2$  coefficients are 1.87 and 0.12, respectively.

Table 5-16 Combination of  $C_1$  and  $C_2$  considered for repeated TOST for the jackknife technique

Calibration Coefficient $C_1$	1.87	1.87	1.93	1.93
Calibration Coefficient $C_2$	0.07	0.12	0.07	0.12
Equivalence margin, $\delta$ (ft/mile)	400	300	375	350

### 5.5.3.3 Bootstrapping approach

The bootstrap resampling approach was also used to optimize the  $C_1$  and  $C_2$  coefficients of the top-down cracking model. One thousand bootstrap samples were optimized using the L-BFGS optimization technique. Figures 5-23 and 5-24 illustrate the distribution of  $C_1$  and  $C_2$  using the bootstrap technique. Figure 5-23 shows that the range of coefficient  $C_1$  was 1.88–1.93 for 975 bootstrap samples, and Figure 5-24 shows that the value of coefficient  $C_2$  was 0.14–0.18 for each of the 1,000 bootstrap samples.

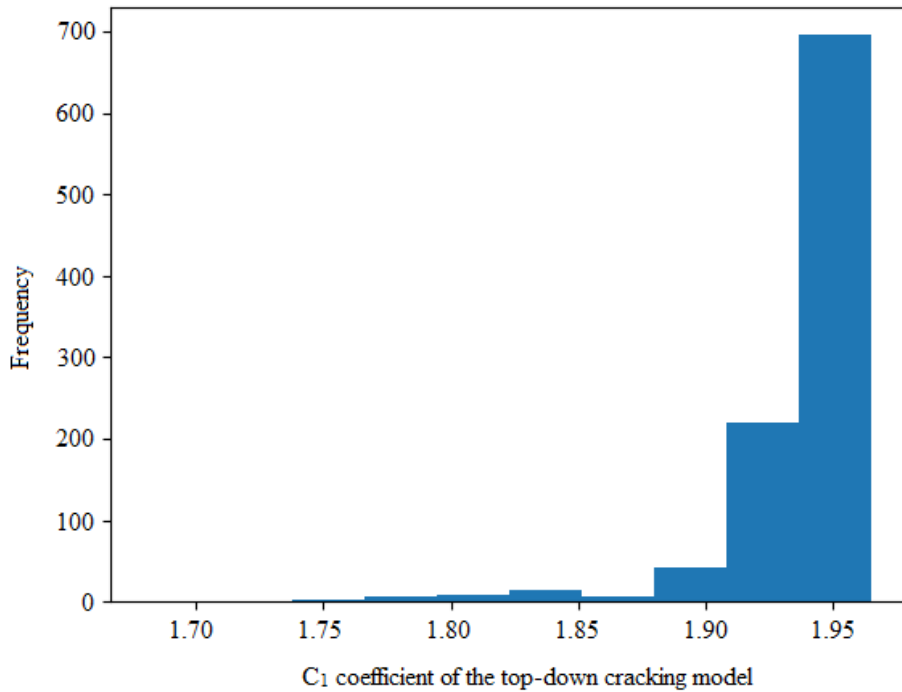


Figure 5-23 Distribution of the  $C_1$  coefficient using bootstrap technique

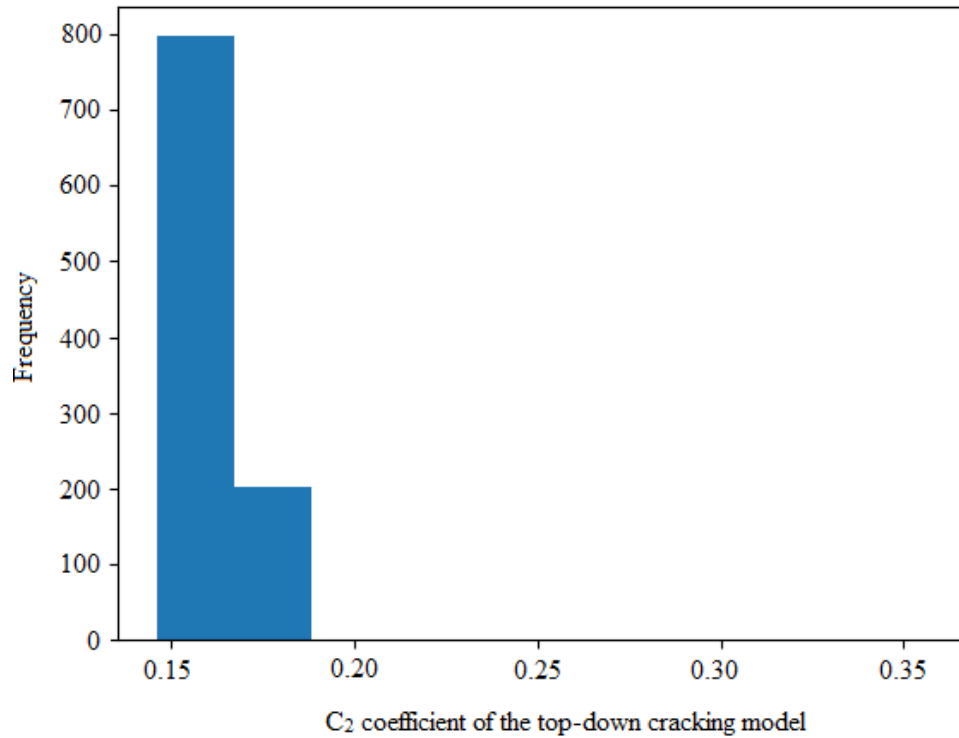


Figure 5-24 Distribution of the  $C_2$  coefficient using bootstrap sampling technique

The TOST procedure was repeatedly conducted for a combination of  $C_1$  and  $C_2$ , with  $C_1$  in the range of 1.88–1.93 and  $C_2$  in the range of 0.14–0.18. Table 5-17 shows that the minimum equivalence margin obtained from the TOST procedures was 300 ft/mile for a  $C_1$  and  $C_2$  combination of 1.88 and 0.14, respectively, while predicted top-down cracking using the PMED software (level of significance,  $\alpha = 0.05$ ) was at least 300 ft/mile off from the measured top-down cracking.

Table 5-17 Combination of  $C_1$  and  $C_2$  considered for repeated TOST for the bootstrap technique

Calibration Coefficient $C_1$	1.88	1.88	1.93	1.93
Calibration Coefficient $C_2$	0.14	0.18	0.14	0.18
Equivalence margin, $\delta$ (ft/mile)	300	325	350	450

#### 5.5.4 IRI model

The IRI model was calibrated using the automated technique developed in this study and verified with global coefficients for the AC over AC pavement sections listed in Table 3-3. Summation of bias, SSE,  $p$ -value from the paired  $t$ -test, and  $p$ -value from the TOST procedure were reported. Table 5-18 lists summary statistics of the IRI model with global coefficients. Results in the table show that  $p$ -value from the TOST procedure was less than 0.05 for an equivalence margin of 17 in./mile, suggesting that PMED-predicted and measured IRI were equivalent for a margin of 17 in./mile. The  $S_e$  was 14 in./mile, which is lower than the AASHTO-suggested value. The  $p$ -value from the paired  $t$ -test was less than 0.05, indicating that the predicted and measured IRI differ.

Table 5-18 Results for the globally calibrated IRI model for AC over AC sections

Bias	SSE	$S_e$	$S_e/S_y$	$p$ -value from paired $t$ -test	$p$ -value from TOST
1,516	41,829	13.8	0.99	<0.001	0.02

The automated calibration technique also generated the measured versus predicted IRI plot with global coefficients. Figure 5-25 shows measured versus predicted IRI with global coefficients, specifically an asymmetrical trend with respect to the line of equality.

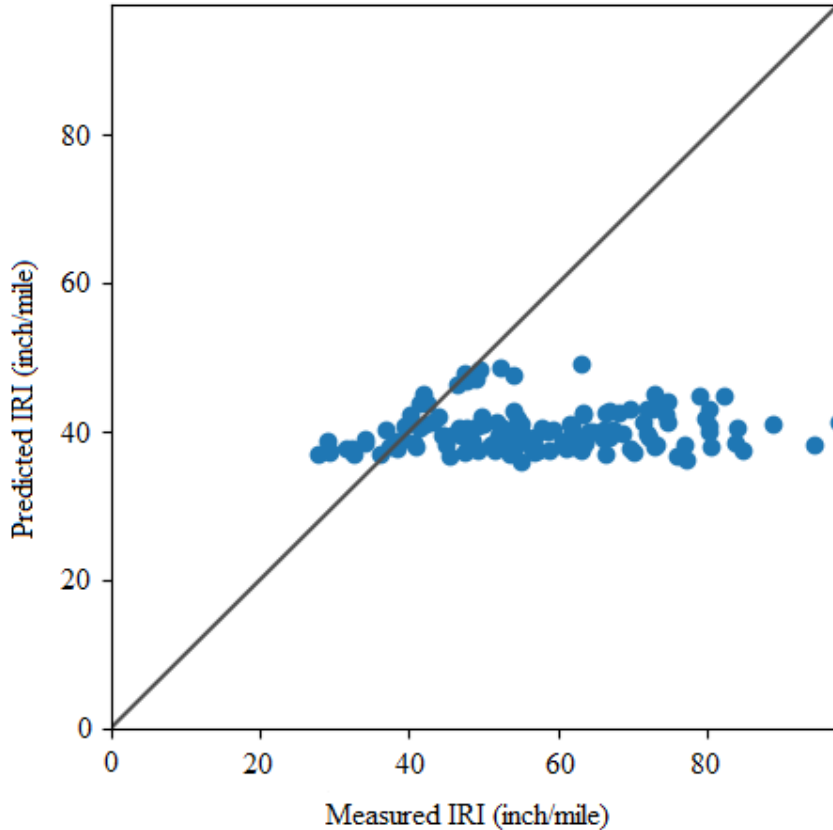


Figure 5-25 Predicted vs measured top-down cracking with globally calibrated factors

Verification results of the IRI model for the AC over AC sections confirmed the necessity of model recalibration. Section 4.1.4 describes how the PMED IRI model can be calibrated by optimizing calibration parameters  $C_1$ ,  $C_2$ ,  $C_3$ , and  $C_4$ .

The automated calibration technique can automatically extract site-specific precipitation and freezing index information from the PMED output file (in Excel spreadsheet). Project-specific soil plasticity index, subgrade soil percent passing through a US No. 4 sieve, and subgrade soil percent passing through a US No. 200 sieve are also automatically extracted from the “FlexibleIRIInput” text file generated by the PMED software for each project. In addition, project-specific rut depth, fatigue cracking, and transverse cracking values are automatically extracted from output Excel files for the corresponding IRI data collection date. Finally, the



optimization technique is applied to determine a combination of  $C_1$ ,  $C_2$ ,  $C_3$ , and  $C_4$  parameters that yields the least SSE between measured and predicted IRI.

#### 5.5.4.1 IRI model constraints

IRI model coefficients were optimized to minimize the SSE, also resulting in improved model goodness-of-fit statistics. However, optimized values of coefficient  $C_2$  and  $C_3$  were negative. Equation 2.15 shows that the IRI model is a function of rut depth, total fatigue cracking, transverse cracking, and site factors, and coefficients  $C_1$ ,  $C_2$ ,  $C_3$ , and  $C_4$  are direct multipliers to  $RD$ ,  $FC_{total}$ ,  $TC$ , and  $SF$ , respectively. None of these coefficients can be negative since all predictor variables contribute positively to the progression of IRI values. Negative values of  $C_2$  and  $C_3$  suggest that fatigue cracking and transverse cracking have regressive effects on IRI and that, if fatigue cracking and transverse cracking increase, IRI will decrease, which is opposite of the common assumption. Brink (2015) optimized PMED IRI models for Michigan and found that the site factor coefficient  $C_4$  could become artificially inflated to compensate for other distresses when minimizing the SSE simultaneously for all four model coefficients. The study optimized IRI model coefficients by setting bounds for model coefficients based on coefficient values obtained by other highway agencies.

This study set bounds for the four calibration parameters of the IRI model (Table 5-19). The L-BFGS optimization technique was used for each of the sampling types since the CG optimization technique is not recommended for bounded problems.

Table 5-19 IRI model coefficients bounds considered for this study

IRI model coefficient	Global value		Lower bound	Upper bound
	AC over AC	AC over JPCP		
$C_1$	40	40.8	10	1000
$C_2$	0.4	0.575	0.01	10
$C_3$	0.008	0.0014	0.0009	10
$C_4$	0.015	0.00825	0.0001	1

#### 5.5.4.2 Split sampling approach

Table 5-20 presents summary statistics for the IRI model calibrated using the traditional split sampling approach. Results in the table show that the  $p$ -value from the paired  $t$ -test after local calibration was less than 0.05, indicating that there is no evidence that the predicted and measured IRI are different. However, the  $p$ -value from the TOST was less than 0.05 for a  $\delta$  value of 17 in./mile, which suggests that the predicted and measured top-down cracking were equivalent for a margin of 17 in./mile.

Table 5-20 Summary statistics for the locally calibrated IRI model

Bias	SSE	$S_e$	$S_e/S_y$	$p$ -value from paired $t$ -test	$p$ -value from TOST
327	24,927	15	1.08	0.04	<0.001

TOST procedure was then performed multiple times to determine the narrowest equivalent region for measured and predicted IRI. Table 5-21 presents a summary of the results of the repeated TOST procedure. The level of significance ( $\alpha$ ) was 0.05 in all cases. Results in the table show that the equivalence margin for predicted and measured IRI was 6 in./mile, and

PMED-predicted IRI values for the AC over AC sections were equivalent to IRI measured in the field for a margin of 6 in./mile.

Table 5-21 Calibrated model equivalence margin between measured and predicted rutting

Equivalence margin, $\delta$ (in./mile)	<i>p</i> -value	Remark
17	<0.001	Equivalent
10	<0.001	Equivalent
7	<0.001	Equivalent
6	0.03	Equivalent
5	0.11	Not equivalent

The measured versus predicted plot of IRI with local factors is shown in Figure 5-26. A comparison of data in Figures 5-25 and 5-26 reveals significantly improved data location after calibration relative to the line of equality.

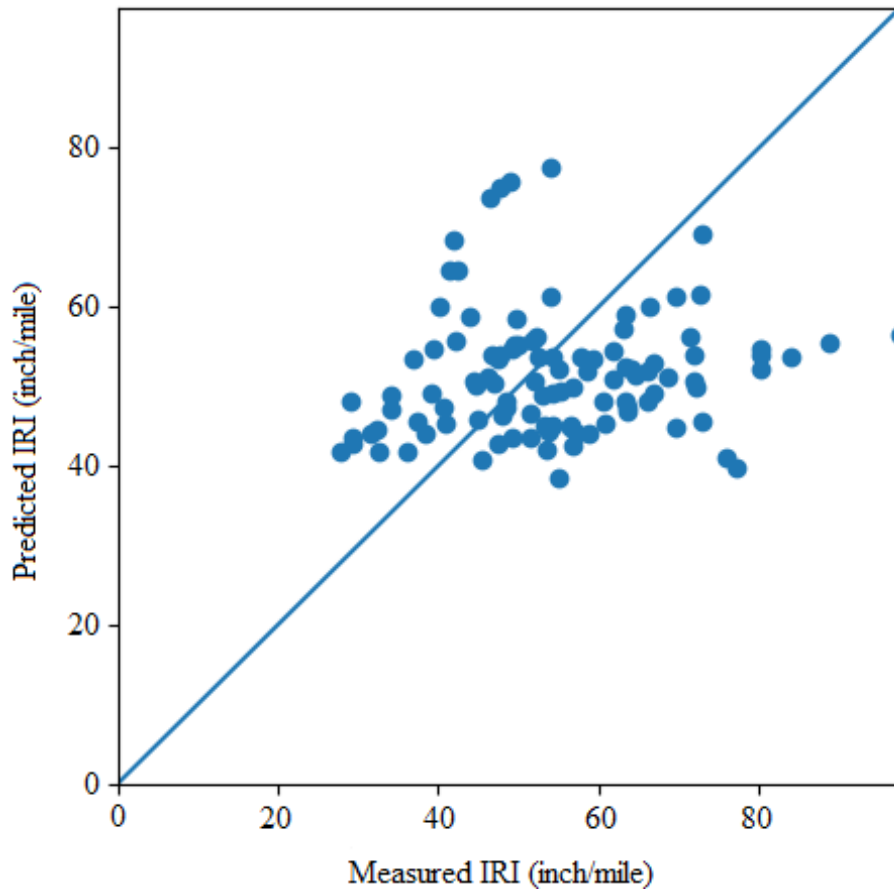


Figure 5-26 Predicted vs measured top-down with local coefficients for AC over AC sections

Summary statistics for the calibrated IRI model after validation are presented in Table 5-22. The  $p$ -value from the paired  $t$ -test for the validation dataset with local coefficients was less than 0.05, indicating that predicted and measured IRI differ for projects in the validation dataset with local coefficients. The  $p$ -value from the TOST was higher than 0.05 for an equivalence margin of 3 in./mile, which suggests that predicted and measured transverse cracking were not equivalent for a margin of 3 in./mile for projects in the validation dataset. TOST was repeatedly performed for the validation dataset, and the narrowest equivalence margin was 20 in./mile. Figure 5-27 presents measured versus predicted transverse cracking with local coefficients for the validation dataset.

Table 5-22 Validation results for the calibrated IRI model for AC over AC sections

Bias	SSE	$S_e$	$S_e/S_y$	$p$ -value from paired $t$ -test	$p$ -value from TOST ( $\delta = 7$ in./mile)
482	13,965	14	1.12	<0.001	0.99

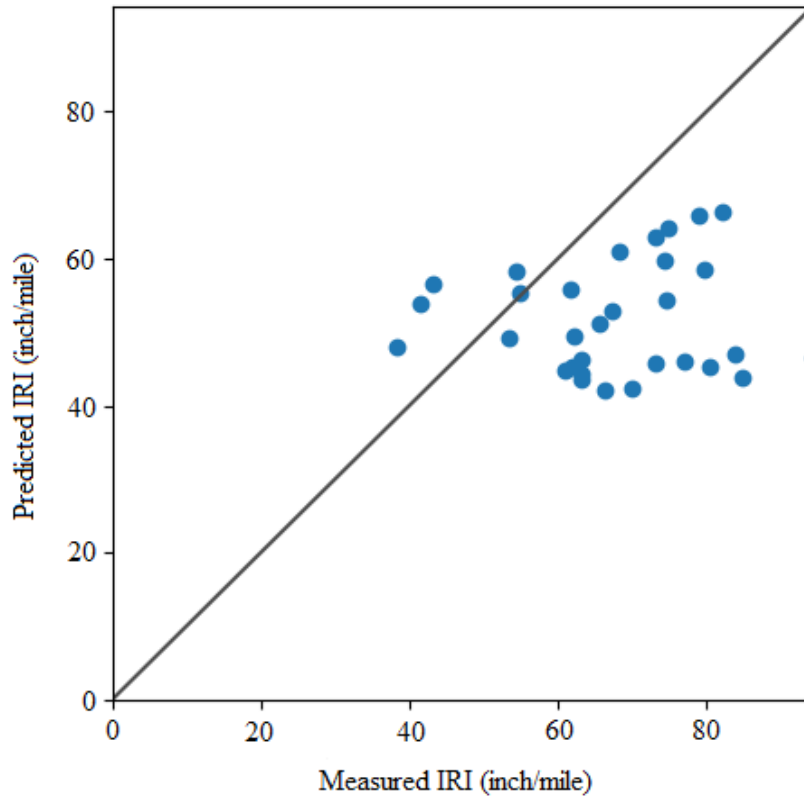


Figure 5-27 Predicted versus measured top-down cracking for the validation dataset

#### 5.5.4.3 Jackknifing approach

The jackknifing sampling approach was also used to calibrate the PMED IRI model. The  $C_1$ ,  $C_2$ ,  $C_3$  and  $C_4$  coefficients of the IRI model were optimized for 24 jackknife samples for the AC over AC sections considered in this study. Figure 5-28 through Figure 5-31 show the distribution of  $C_1$ ,  $C_2$ ,  $C_3$ , and  $C_4$  coefficients using the jackknife technique. These figures demonstrate the following:

- Coefficient  $C_1$  had a range of 145.0–159 for 22 of 24 jackknife samples.
- The value of coefficient  $C_2$  was 0.09–0.098 for all jackknife samples.
- The value of coefficient  $C_3$  was 0.0009–0.0039 for 24 jackknife samples.
- The range of  $C_4$  parameter was 0.008–0.009 for 22 jackknife samples.

TOST was repeatedly conducted for a combination of  $C_1$ ,  $C_2$ ,  $C_3$ , and  $C_4$ , with  $C_1$  in the range of 42.0–42.5,  $C_2$  in the range of 0.10–0.15,  $C_3$  in the range of 0.009–0.0016, and  $C_4$  in the range of 0.26–0.29. Results showed that the narrowest equivalence margin for measured and predicted IRI varied from 7 in./mile to 10 in./mile, suggesting that calibrated IRI predictions (level of significance,  $\alpha = 0.05$ ) would likely be equivalent to IRI measured in the field for a margin of 7–10 in./mile if  $C_1$ ,  $C_2$ ,  $C_3$ , and  $C_4$  coefficients are in the range of 145.0–159, 0.09–0.098, 0.0009–0.0039, and 0.008–0.009, respectively.

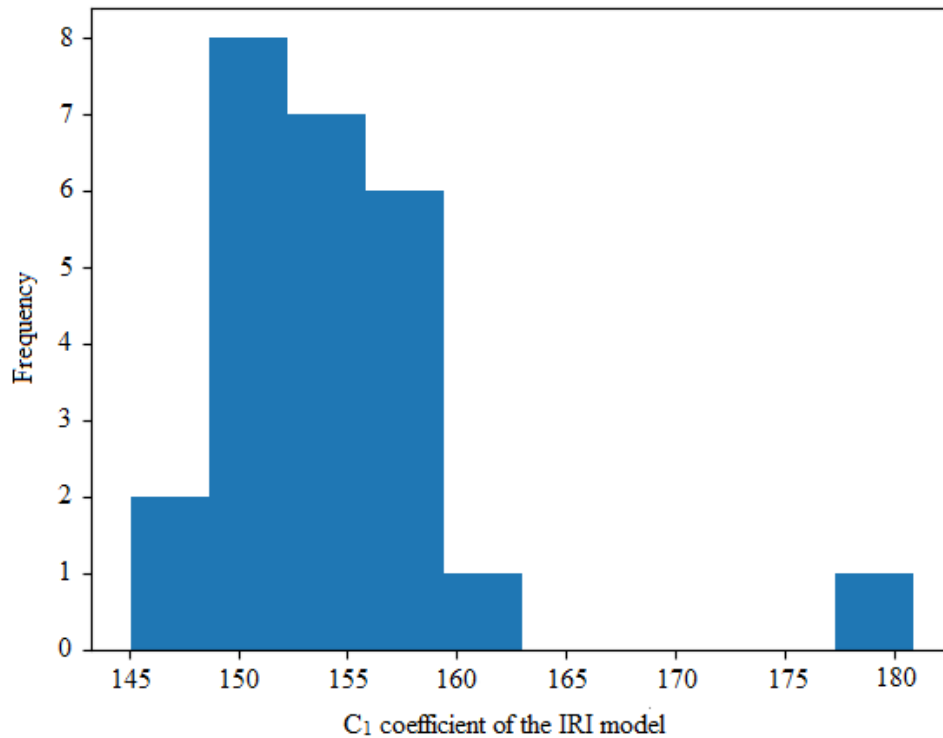


Figure 5-28 Distribution of the  $C_1$  coefficient of IRI model using jackknife technique

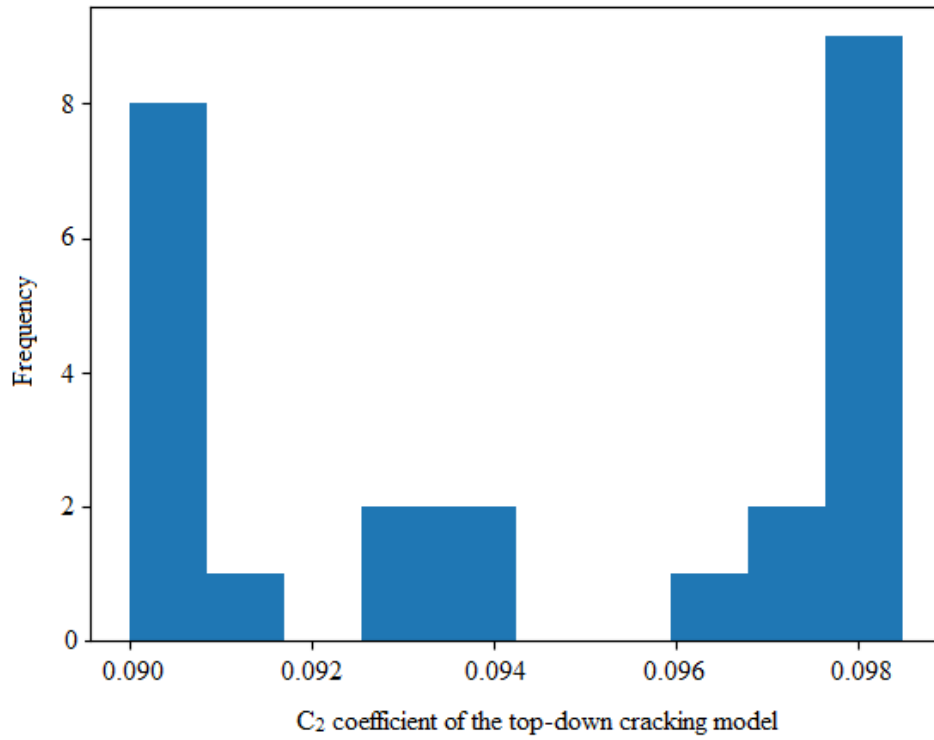


Figure 5-29 Distribution of the  $C_2$  coefficient of IRI model using jackknife technique

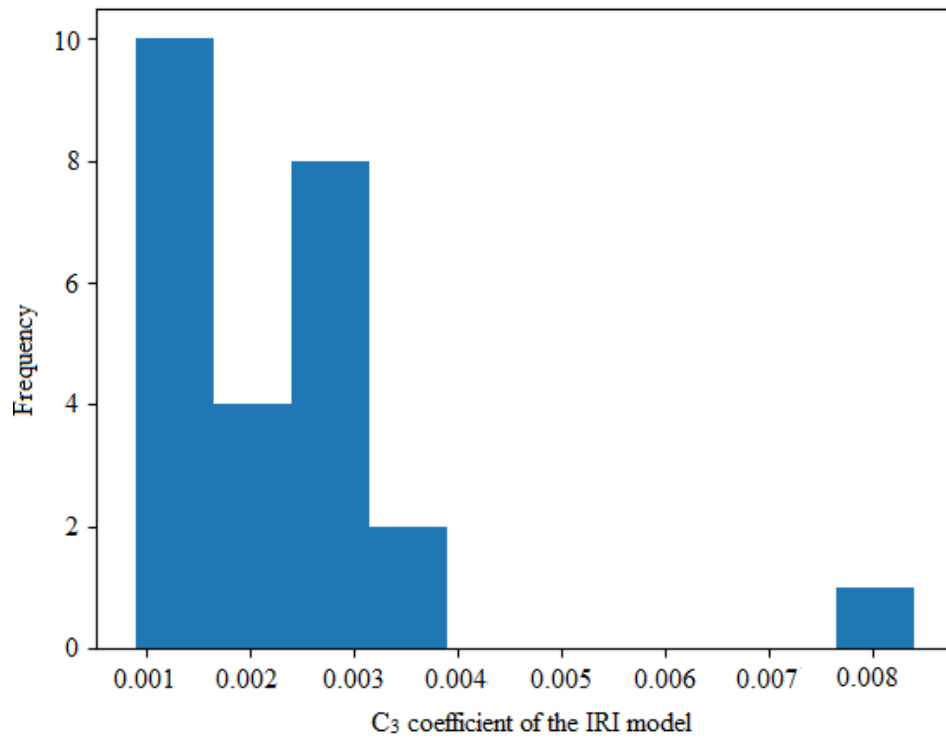


Figure 5-30 Distribution of the  $C_3$  coefficient of IRI model using jackknife technique

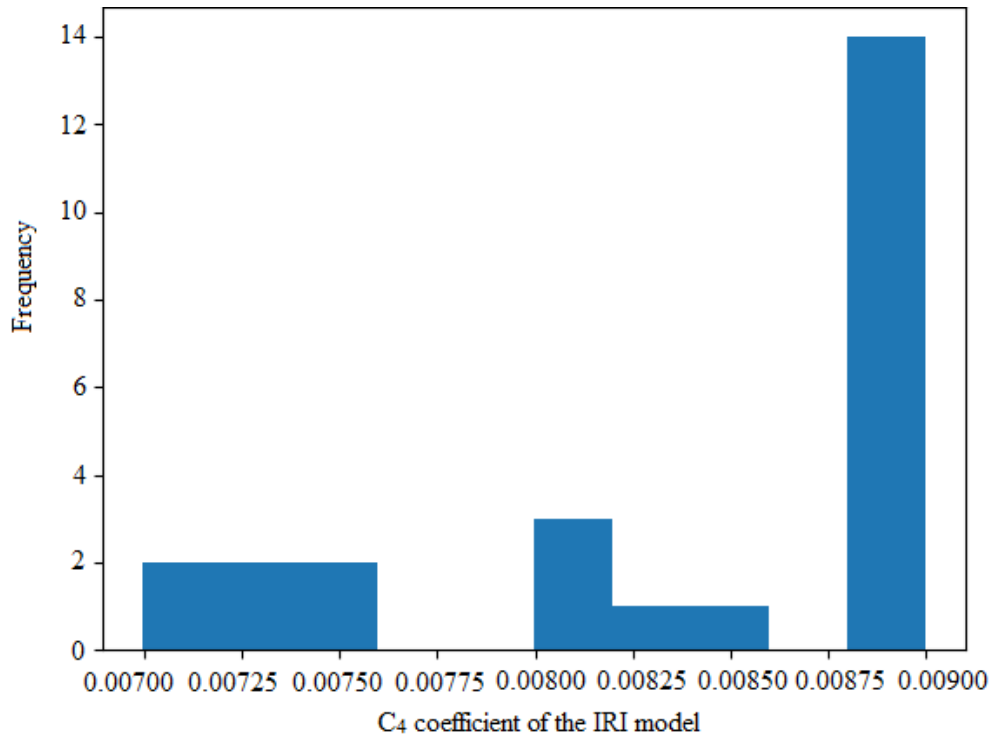


Figure 5-31 Distribution of the  $C_4$  coefficient of IRI model using jackknife technique

#### 5.5.4.4 Bootstrapping approach

The bootstrapping resampling approach was implemented to optimize IRI model coefficients. One thousand bootstrap samples were considered. Figures 5-32 through 5-35 show the distribution of  $C_1$ ,  $C_2$ ,  $C_3$ , and  $C_4$  coefficients using the bootstrap technique. These figures also show the following:

- Coefficient  $C_1$  had a range of 40.5–53.5 for 850 bootstrap samples.
- The value of coefficient  $C_2$  was 0.34–0.41 for more than 950 bootstrap samples.
- The value of coefficient  $C_3$  was 0.0074–0.0082 for more than 950 bootstrap samples.
- The range of  $C_4$  parameter was 0.001–0.002 for more than 900 bootstrap samples.

The TOST was repeatedly conducted for a combination of  $C_1$ ,  $C_2$ ,  $C_3$ , and  $C_4$ , with  $C_1$  in the range of 40.5–53.5,  $C_2$  in the range of 0.34–0.41,  $C_3$  in the range of 0.0074–0.0082, and  $C_4$  in



the range of 0.001–0.002. Results showed that the narrowest equivalence margin for measured and predicted IRI varied between 10 in./mile and 15 in./mile, suggesting that calibrated IRI predictions (level of significance,  $\alpha = 0.05$ ) would likely be equivalent to IRI measured in the field for a margin of 15 in./mile if  $C_1$ ,  $C_2$ ,  $C_3$ , and  $C_4$  coefficients are in the range of 40.5–53.5, 0.34–0.41, 0.0074–0.0082, and 0.001–0.002, respectively.

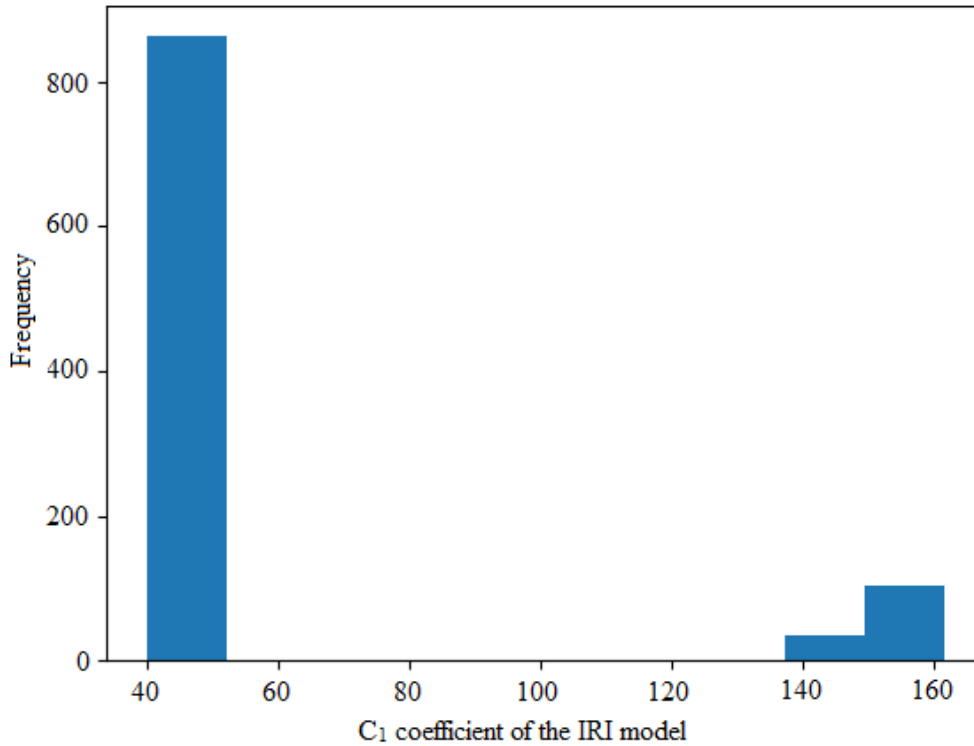


Figure 5-32 Distribution of the  $C_1$  coefficient of IRI model using bootstrap technique

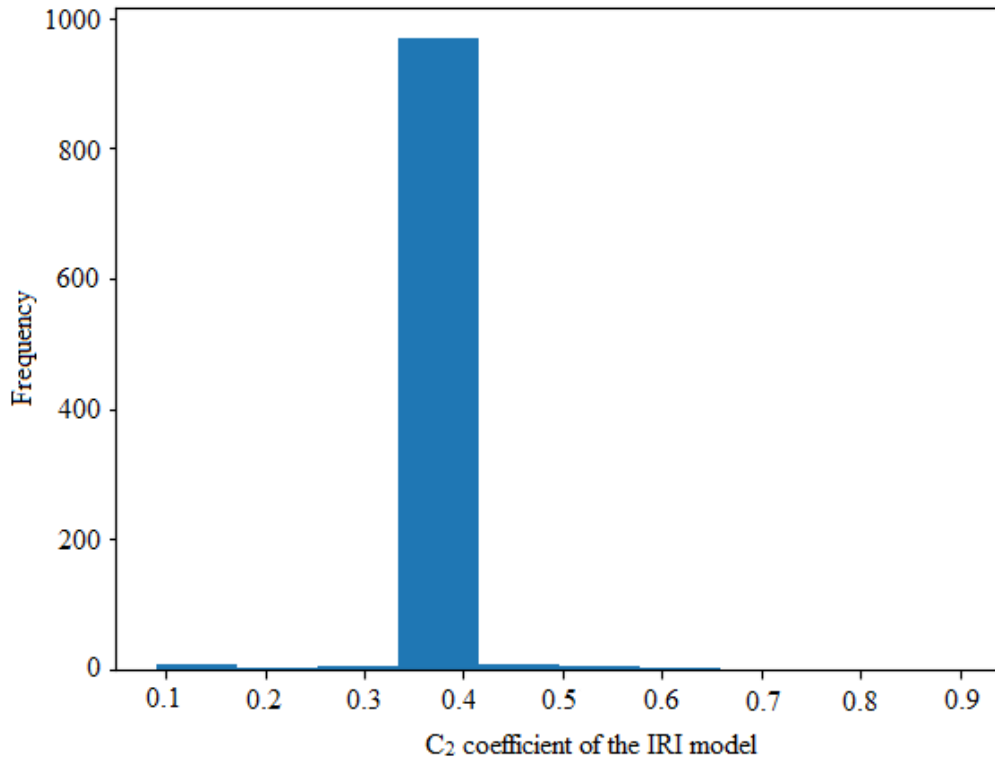


Figure 5-33 Distribution of the  $C_2$  coefficient of IRI model using bootstrap technique

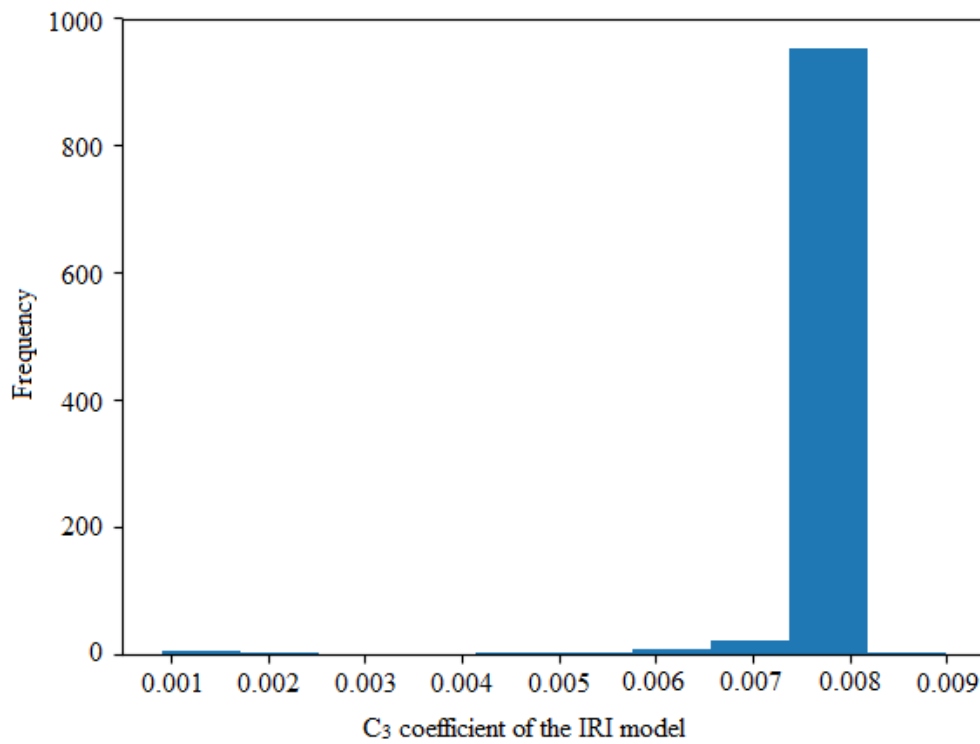


Figure 5-34 Distribution of the  $C_3$  coefficient of IRI model using bootstrap technique

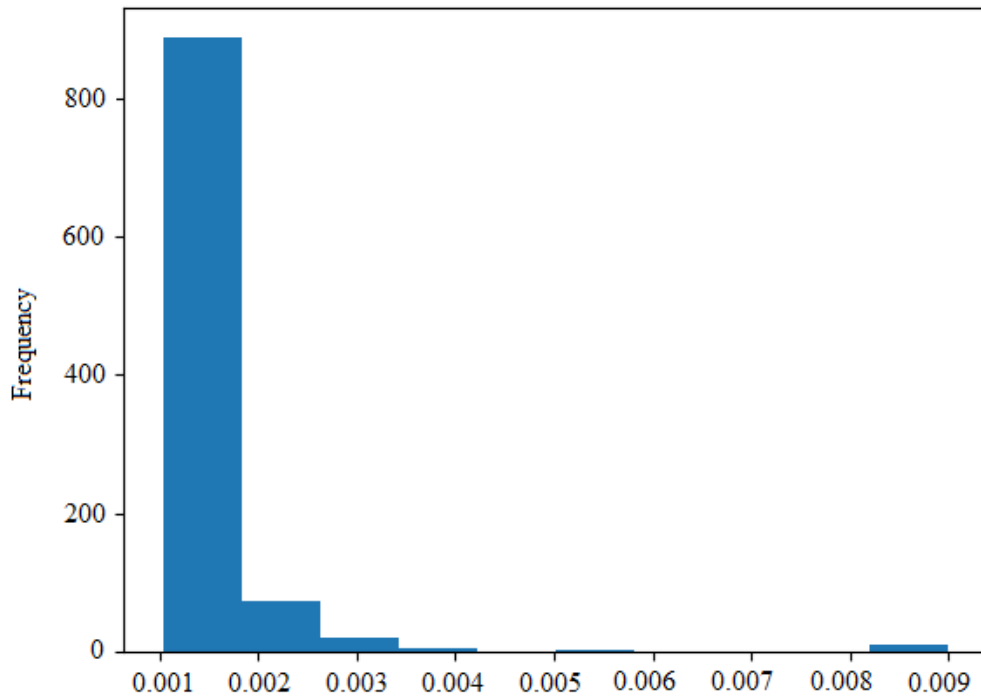


Figure 5-35 Distribution of the  $C_4$  coefficient of IRI model using bootstrap technique

## 5.6 Local Calibration of AC over JPCP sections

The automated calibration technique was used to calibrate PMED performance models for the AC over JPCP sections listed in Table 3-4. The calibrated models were permanent deformation model, transverse cracking model, top-down cracking model, and the IRI model.

### 5.6.1 Permanent deformation model

The permanent deformation model in the AASHTOWare PMED software was calibrated for the AC over JPCP sections using the automated technique developed in this study. The automated technique first verified the globally calibrated rutting model and reported bias, SSE,  $p$ -value from the paired  $t$ -test, and  $p$ -value from the TOST. Table 5-23 lists verification results of the rutting model for the AC over JPCP sections. Results in the table show that  $p$ -value from the TOST was less than 0.05 for an equivalence margin of 0.1 in., suggesting that the globally

calibrated PMED rut depth and measured rut depth were equivalent for a margin of 0.1 in. The  $S_e$  was 0.04 in., which is within the AASHTO-suggested range, and the  $p$ -value from the paired  $t$ -test was less than 0.05, indicating that predicted rut depth and measured rut depth differ.

Table 5-23 Results for the nationally calibrated rutting model for AC over JPCP sections

Bias	SSE	$S_e$	$S_e/S_y$	$p$ -value from paired $t$ -test	$p$ -value from TOST
4.61	0.44	0.04	0.92	<0.001	<0.001

The automated calibration technique also generated the measured versus predicted total rut depth graph. Figure 5-36 shows measured versus predicted total rut depths with global coefficients. The measured versus predicted rutting with global factors shows an unsymmetrical trend to the line of equality.

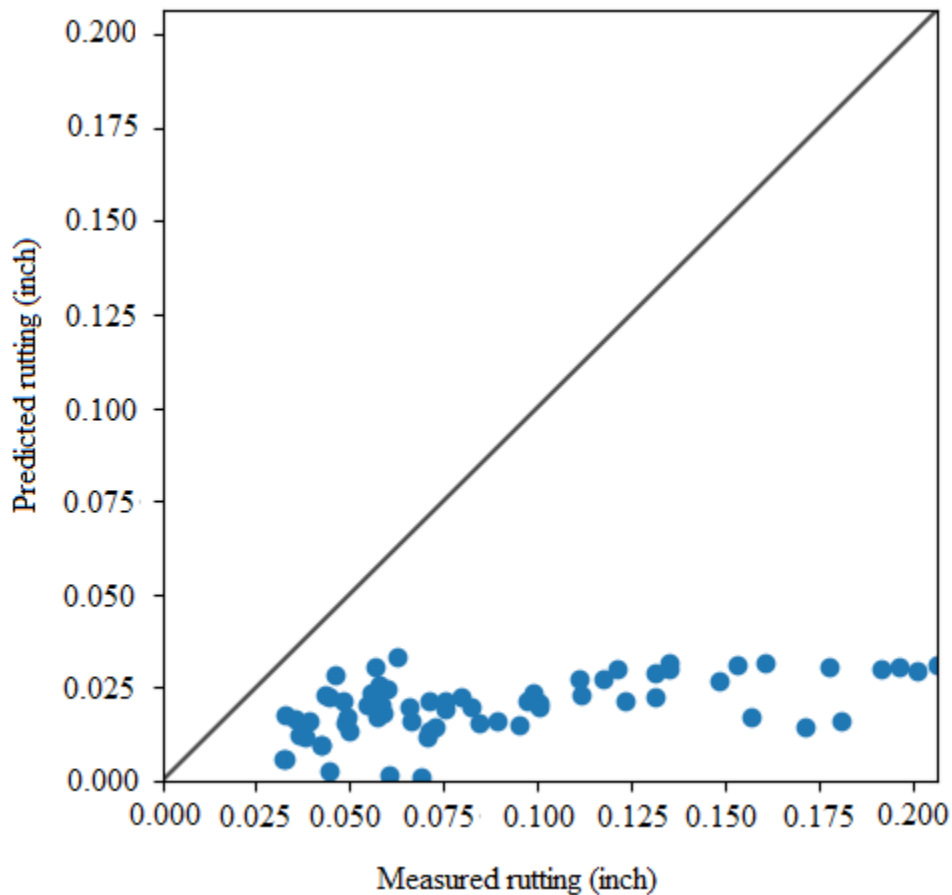


Figure 5-36 Predicted vs measured rutting with global factors for AC over JPCP sections

Verification results of the rutting model for the AC over JPCP sections showed that model calibration of the total rutting model is required for AC over JPCP sections. The  $\beta_{1r}$  parameter was optimized using the automated calibration technique for JPCP rehabilitated sections. Results were obtained for traditional split sampling, jackknifing, and bootstrapping sampling techniques.

5.6.1.1 Traditional split sampling approach

Traditional split sampling was used to calibrate and validate the total permanent deformation model for AC over JPCP sections using the automated technique. The CG optimization technique was used for the split sampling approach. Table 5-24 presents summary statistics of the rutting model for the calibration dataset. Results in the table show that  $p$ -value from the TOST procedure was less than 0.05 for an equivalence margin of 0.1 in., suggesting that calibrated rutting model predictions are equivalent to the field rut depth for a margin of 0.1 in. The  $p$ -value from the paired  $t$ -test was higher than 0.05, which suggests that there is no evidence that the predicted and measured rut depths differ.

Table 5-24 Summary statistics for the locally calibrated rutting model for AC over JPCP sections

Bias	SSE	$S_e$	$S_e/S_y$	$p$ -value from paired $t$ -test	$p$ -value from two one-sided $t$ -test
0.16	0.12	0.04	0.88	0.62	<0.001

The calibrated model was then used to conduct repeated TOST procedures to determine the narrowest equivalence region for measured and predicted rut depth. Table 5-25 presents a summary of results of the repeated TOST. In all cases, the level of significance ( $\alpha$ ) was 0.05. Results in the table show that calibrated rutting model predictions for the AC over JPCP sections were equivalent to measured rut depths for a margin of 0.015 in.

Table 5-25 Calibrated model equivalence margin between measured and predicted rutting

Equivalence margin, $\delta$ (in.)	$p$ -value	Remark
0.100	<0.001	Equivalent
0.075	<0.001	Equivalent
0.05	<0.001	Equivalent
0.025	<0.001	Equivalent
0.015	0.03	Equivalent
0.010	0.15	Not equivalent

Measured versus predicted total rut depths with locally calibrated coefficients is shown in Figure 5-37. A comparison of Figures 5-36 and 5-37 demonstrates improved data location relative to the line of equality for the measured versus predicted rut depths with local coefficients.

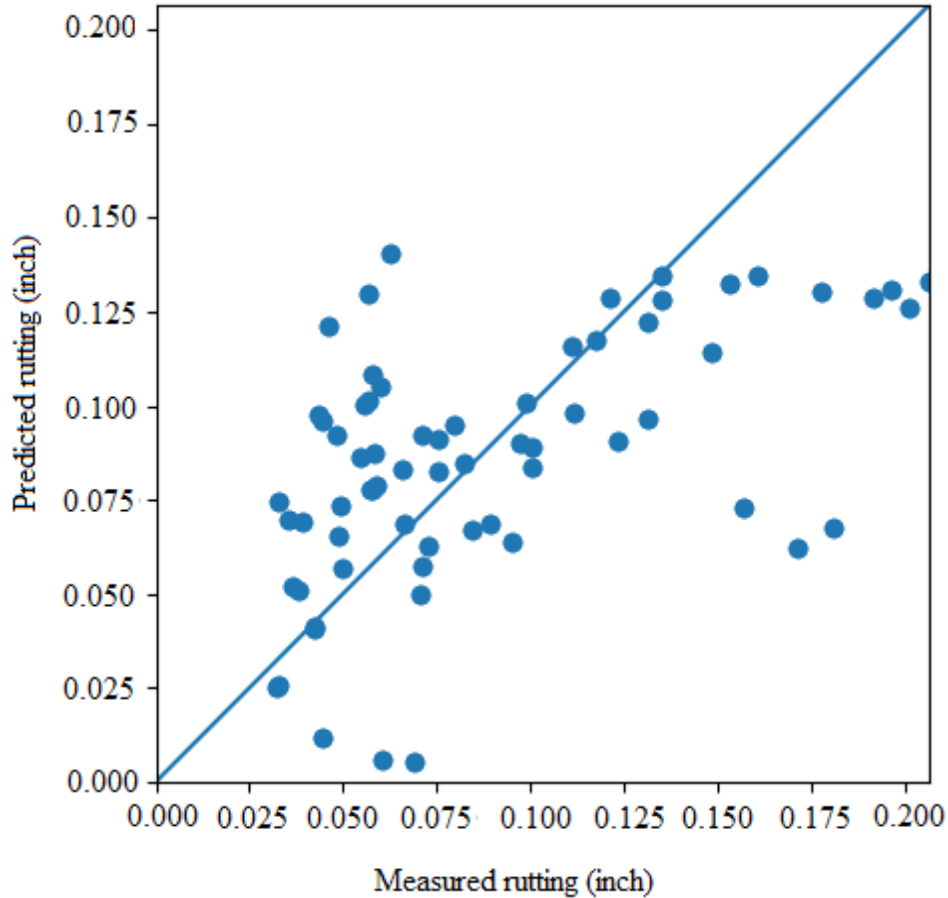


Figure 5-37 Predicted vs measured total rutting with local coefficients for AC over JPCP sections

Summary statistics for the rutting model after validation are shown in Table 5-26. The bias and SSE of the calibrated rutting model with the validation dataset for locally adjusted coefficients were extremely low, and the rutting model  $S_e$  of the validation projects remained under the AASHTO-suggested 0.1 in. Figure 5-38 illustrates measured versus predicted rutting with local coefficients for the validation dataset. The  $p$ -value from the paired  $t$ -test for the validation dataset with local coefficients was greater than 0.05, which suggests that there is no evidence that the predicted and measured rutting differ for projects considered in the validation dataset. However, the  $p$ -value from the TOST was higher than 0.05 for an equivalence margin of 0.01 in, indicating that the predicted and measured total rutting were not equivalent for a margin

of 0.01 in. for projects in the validation dataset. Repeated TOST was performed again for the validation dataset, and the narrowest equivalence margin was 0.025 in.

Table 5-26 Validation results for the calibrated rutting model for AC over JPCP sections

Bias	SSE	$S_e$	$S_e/S_y$	$p$ -value from paired $t$ -test	$p$ -value from TOST ( $\delta = 0.015$ in.)
0.003	0.03	0.04	0.9	0.98	0.24

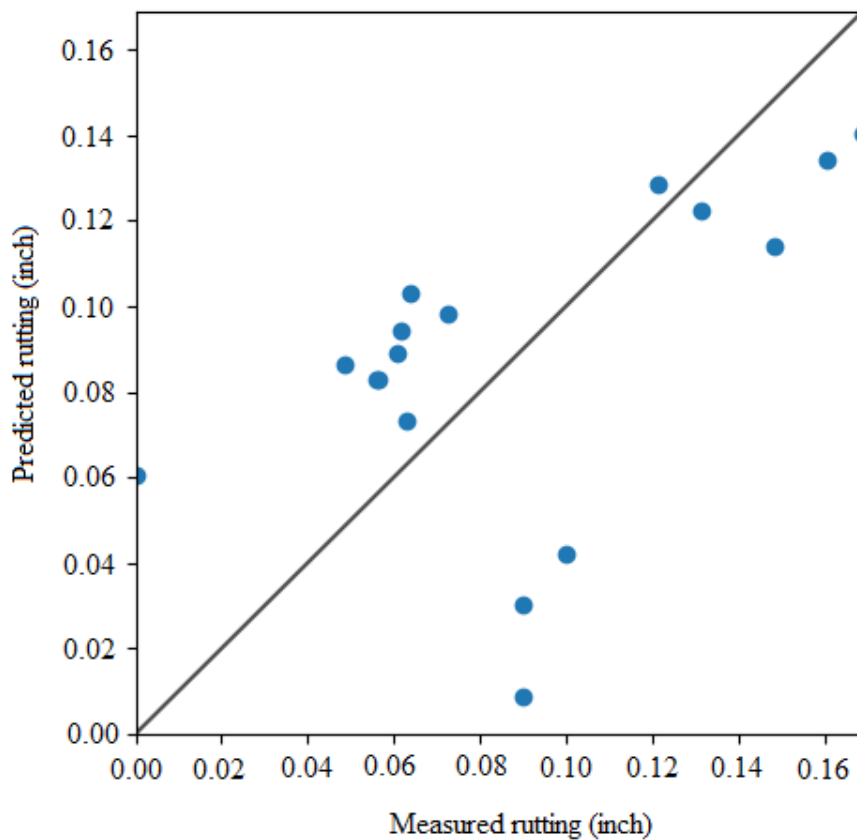


Figure 5-38 Predicted versus measured rutting for validation dataset for AC over JPCP sections

### 5.6.1.2 Jackknifing approach

The jackknifing sampling approach was incorporated into the automated calibration technique to calibrate the total permanent deformation model for AC over JPCP sections. The CG optimization technique was used. Distribution of the  $\beta_{1r}$  coefficient from the 18 jackknife



samples for the AC over JPCP sections is illustrated in Figure 5-39. The figure shows that the  $\beta_{1r}$  parameter coefficient was always in the range of 1.53–1.74, specifically 1.64–1.74 for 14 of the 18 jackknife samples.

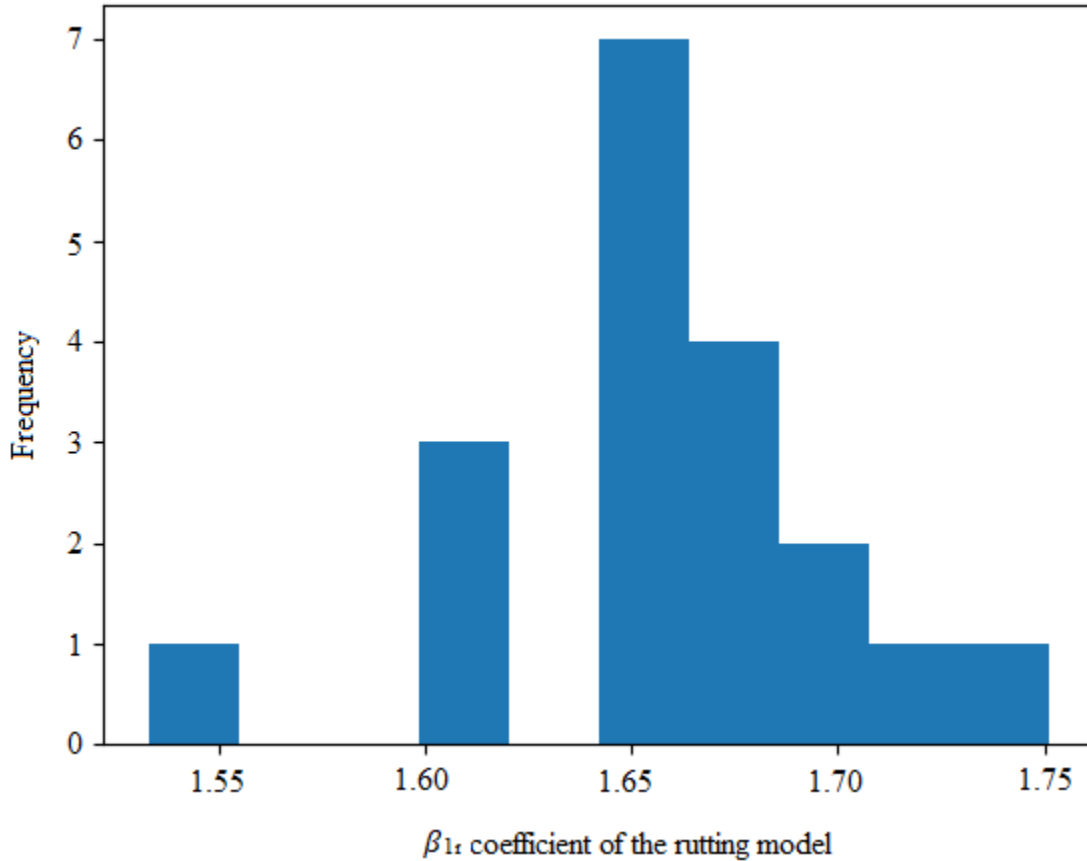


Figure 5-39 Distribution of the  $\beta_{1r}$  parameter using jackknife sampling

The repeated TOST procedure was then conducted for the  $\beta_{1r}$  value ranging from 1.53 to 1.74, and the narrowest equivalence margin  $\delta$  was determined in each case. Figure 5-40 presents results of the repeated TOST for the above-mentioned range of  $\beta_{1r}$ . For the value of  $\beta_{1r}$  parameter within 1.53–1.74, PMED-predicted rutting and measured rutting were always equivalent for a margin of 0.02 in. The equivalence margin was lowest (0.011 in.) for a  $\beta_{1r}$  value of 1.72.

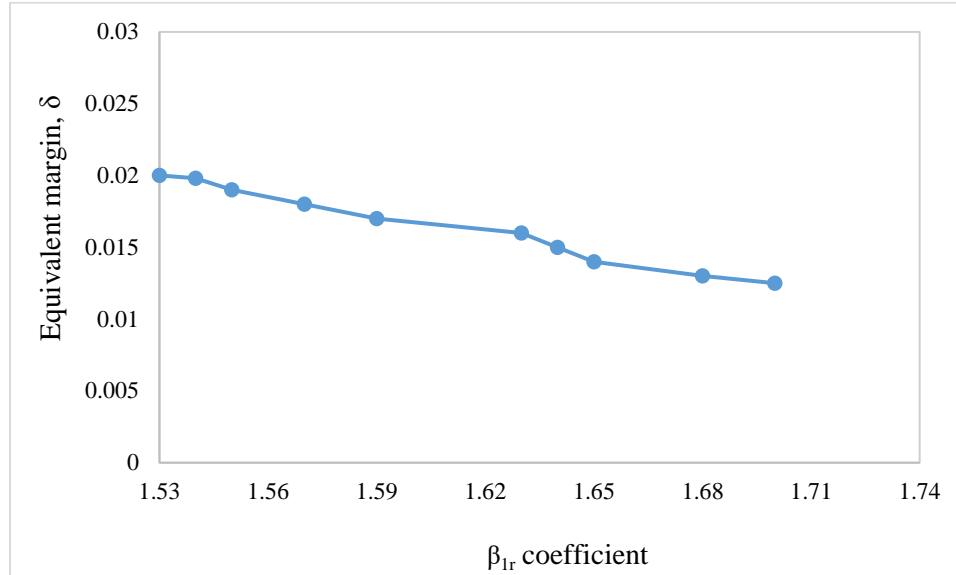


Figure 5-40 Rutting model equivalence margin with respect to  $\beta_{1r}$  parameter

### 5.6.1.3 Bootstrapping approach

The  $\beta_{1r}$  parameter of the rutting model was optimized using 1,000 bootstrap calibration datasets. The L-BFGS optimization technique was used. Distribution of the  $\beta_{1r}$  coefficient obtained using the bootstrap resampling technique for the AC over JPCP sections is illustrated in Figure 5-41. The figure shows that the value of  $\beta_{1r}$  coefficient was 1.59–1.68 for approximately 250 bootstrap samples and 1.69–1.78 for approximately 200 samples. The  $\beta_{1r}$  coefficient was 1.38–1.89 for approximately 850 bootstrap samples.

Repeated TOST was conducted for the  $\beta_{1r}$  value ranging from 1.38 to 1.89, and the narrowest equivalence margin  $\delta$  was determined in each case. Figure 5-42 presents results of the repeated TOST. For the value of the  $\beta_{1r}$  parameter within the 1.38–1.89 range, PMED-predicted and measured rut depths were equivalent for a margin of 0.03 in. The equivalence margin was lowest (0.011 in.) for a  $\beta_{1r}$  value of 1.72.

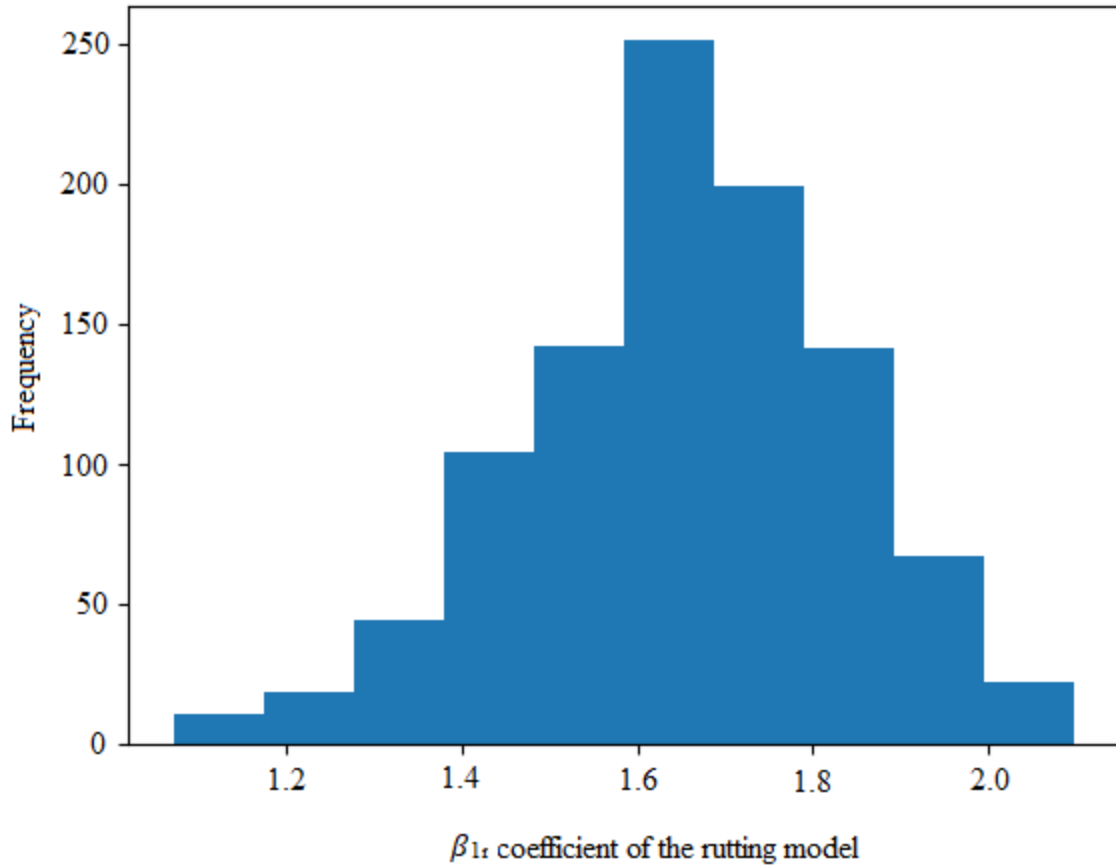


Figure 5-41 Distribution of the  $\beta_{1r}$  parameter using bootstrap resampling approach

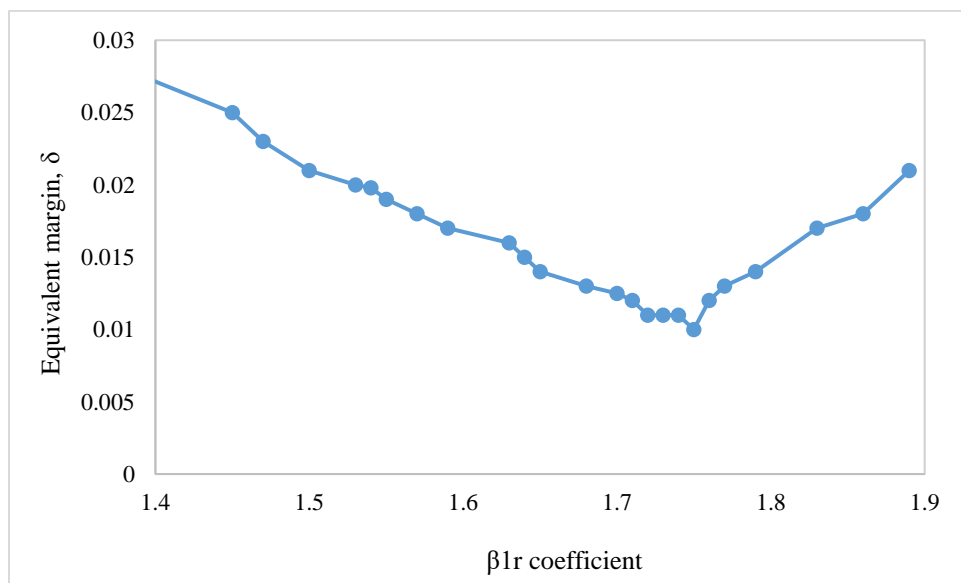


Figure 5-42 Rutting model equivalence margin with respect to  $\beta_{1r}$  parameter

### 5.6.2 Transverse cracking model

The transverse cracking model was calibrated using the automated calibration technique for the AC over JPCP sections. The globally calibrated model was verified, and the summation of bias and SSE,  $p$ -value from the paired  $t$ -test, and  $p$ -value from the TOST procedure were reported by the automated calibration technique. Table 5-27 lists summary statistics of the transverse cracking model for the AC over JPCP sections. Results in the table show that  $p$ -value from the TOST procedure was higher than 0.05 for an equivalence margin of 250 ft/mile, suggesting that PMED-predicted and measured transverse cracking were not equivalent for a margin 250 ft/mile. The  $S_e$  was 619 ft/mile, which is also outside the AASHTO-suggested range. However, the  $p$ -value from the paired  $t$ -test was higher than 0.05, which suggests that predicted and measured transverse cracking do not differ.

Table 5-27 Results for globally calibrated transverse cracking model for AC over JPCP sections

Bias	SSE	$S_e$	$S_e/S_y$	$p$ -value from paired $t$ -test	$p$ -value from TOST
6,778	19,356,533	619	1.28	0.13	0.1

The automated calibration technique generated the measured versus predicted transverse cracking plot with global coefficients. Figure 5-43 shows measured versus predicted transverse cracking with global coefficients. An asymmetrical trend to the line of equality can be observed.

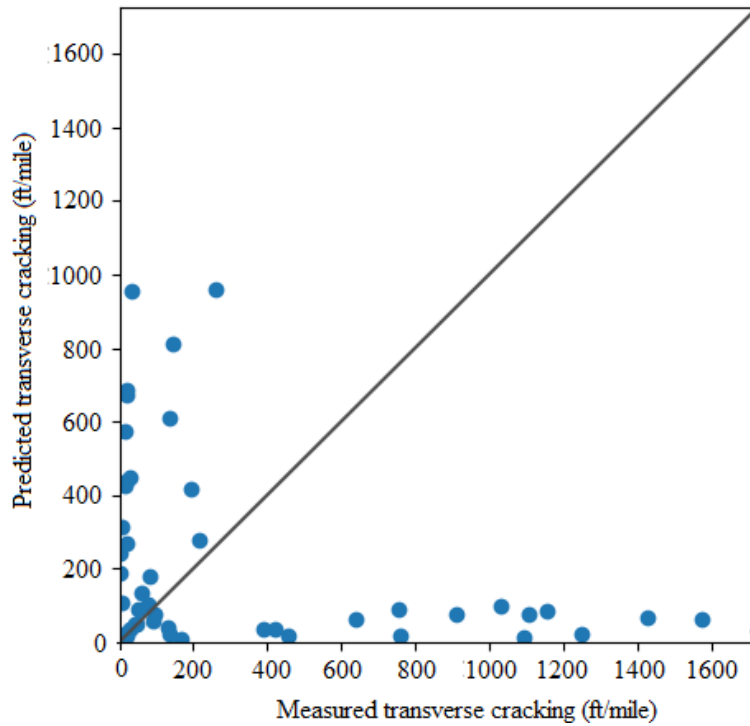


Figure 5-43 Predicted vs measured transverse cracking for AC over JPCP sections (global factors)

Verification results of the transverse cracking model for the AC over JPCP sections confirmed the necessity of model recalibration. This study calibrated the PMED transverse cracking model for JPCP rehabilitated sections by adjusting the reflection cracking model coefficients only. Time-series damage ratio  $D$  and percent RCR values were extracted from the PMED output “transverseReflectiveCracking.log” file for the corresponding dates to optimize coefficients  $C_4$  and  $C_5$ . Traditional split sampling, jackknifing, and bootstrapping sampling techniques were applied.

#### 5.6.2.1 Traditional split sampling approach

The CG optimization technique was used for the split sampling approach. Table 5-28 presents summary statistics of the transverse cracking model for the calibration dataset. Results in the table show that  $p$ -value from the TOST procedure was less than 0.05 for an equivalence

margin of 250 ft/mile, suggesting that PMED-predicted transverse cracking and measured transverse cracking were equivalent after local calibration for a margin of 250 ft/mile. The  $p$ -value from the paired  $t$ -test after local calibration was greater than 0.05, which suggests that there is no evidence that the predicted and measured transverse cracking differ. A comparison of values in Table 5-27 and Table 5-28 shows that transverse cracking model goodness-of-fit statistics improved significantly after local calibration.

Table 5-28 Summary statistics for the locally calibrated transverse cracking model

Bias	SSE	$S_e$	$S_e/S_y$	$p$ -value from paired $t$ -test	$p$ -value from TOST
152	10,986,436	478	0.99	0.96	<0.001

The repeated TOST procedure was done after calibration to determine the narrowest equivalence region for measured and predicted transverse cracking. Table 5-29 presents a summary of results of the repeated TOST procedure. In all cases, the level of significance ( $\alpha$ ) was 0.05. Results in Table 5-29 show that the calibrated transverse cracking model predictions for the AC over JPCP sections were equivalent to measured transverse cracking for a margin of 100 ft/mile.

Table 5-29 Calibrated model equivalence margin for measured and predicted transverse cracking

Equivalence margin, $\delta$ (ft/mile)	$p$ -value	Remark
250	<0.001	Equivalent
225	0.004	Equivalent
200	0.09	Not equivalent

Measured versus predicted transverse cracking with locally calibrated coefficients is shown in Figure 5-44. A comparison of Figures 5-43 and 5-44 shows minimal improvement in

data location relative to the line of equality for measured versus predicted transverse cracking with local coefficients.

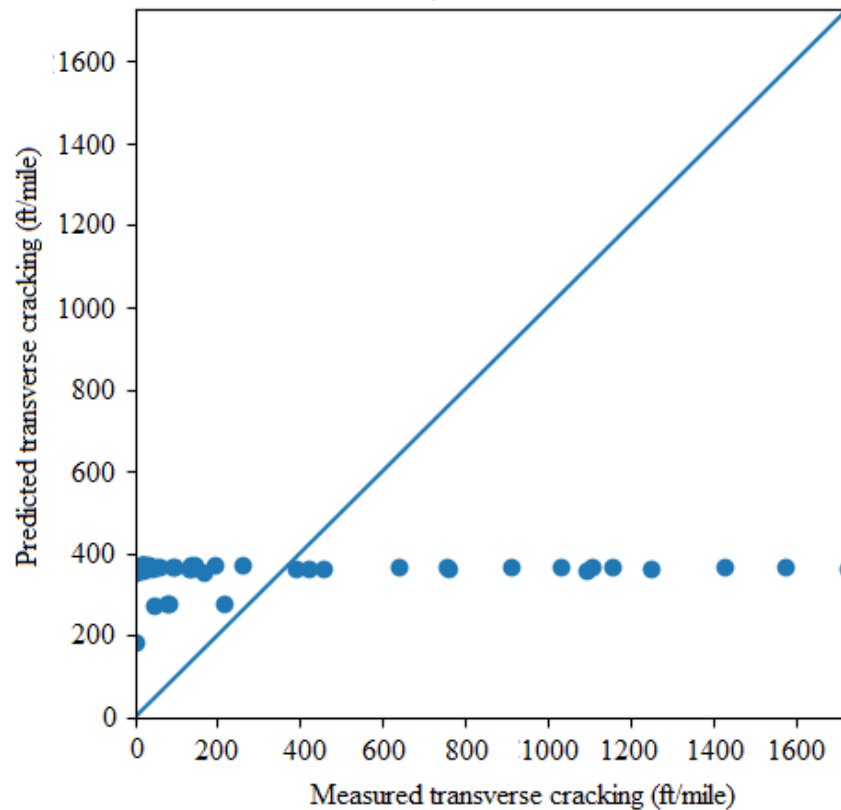


Figure 5-44 Predicted vs measured transverse cracking for AC over JPCP sections (local factors)

Summary statistics for the calibrated transverse cracking model after validation are presented in Table 5-30. The  $p$ -value from the paired  $t$ -test for the validation dataset with local coefficients was greater than 0.05, which suggests that there is no evidence that the predicted and measured transverse cracking differ for projects considered in the validation dataset. However, the  $p$ -value from the TOST procedure was higher than 0.05 for an equivalence margin of 100 ft/mile, indicating that predicted and measured transverse cracking were not equivalent for a margin of 100 ft/mile for projects in the validation dataset. Repeated TOST procedure was performed again for the validation dataset, and the narrowest equivalence margin was 500

ft/mile. Figure 5-45 presents measured versus predicted transverse cracking with local coefficients for the validation dataset.

Table 5-30 Validation results for the calibrated rutting model for AC over JPCP sections

Bias	SSE	$S_e$	$S_e/S_y$	$p$ -value from paired $t$ -test	$p$ -value from TOST ( $\delta = 100$ ft/mile)
3,350	7,976,820	735	1.0	0.22	0.78

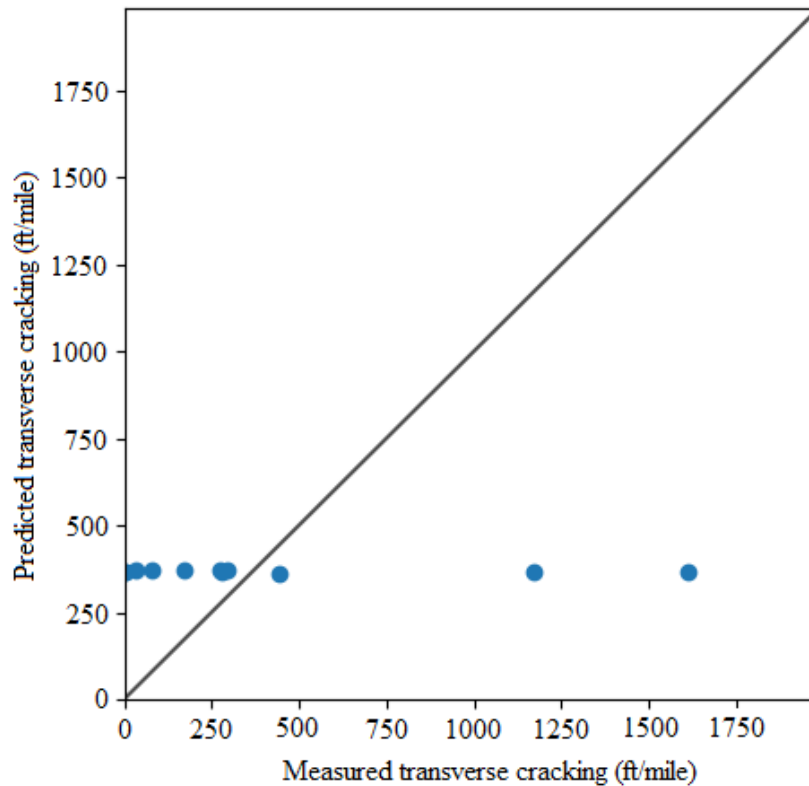


Figure 5-45 Predicted versus measured transverse cracking for the validation dataset

### 5.6.2.2 Jackknifing approach

The  $C_4$  and  $C_5$  coefficients of the transverse cracking model were optimized for the AC over JPCP sections considered in this study. The CG optimization technique was used. Figures 5-46 and 5-47 show the distribution of  $C_4$  and  $C_5$  coefficients, respectively, using the jackknife technique. Figure 5-46 shows that the range of  $C_4$  was 1020–1130 for 16 of 18 jackknife



samples, and Figure 5-47 shows that the value of coefficient  $C_5$  ranged from -0.07 to -0.02 for 17 jackknife samples.

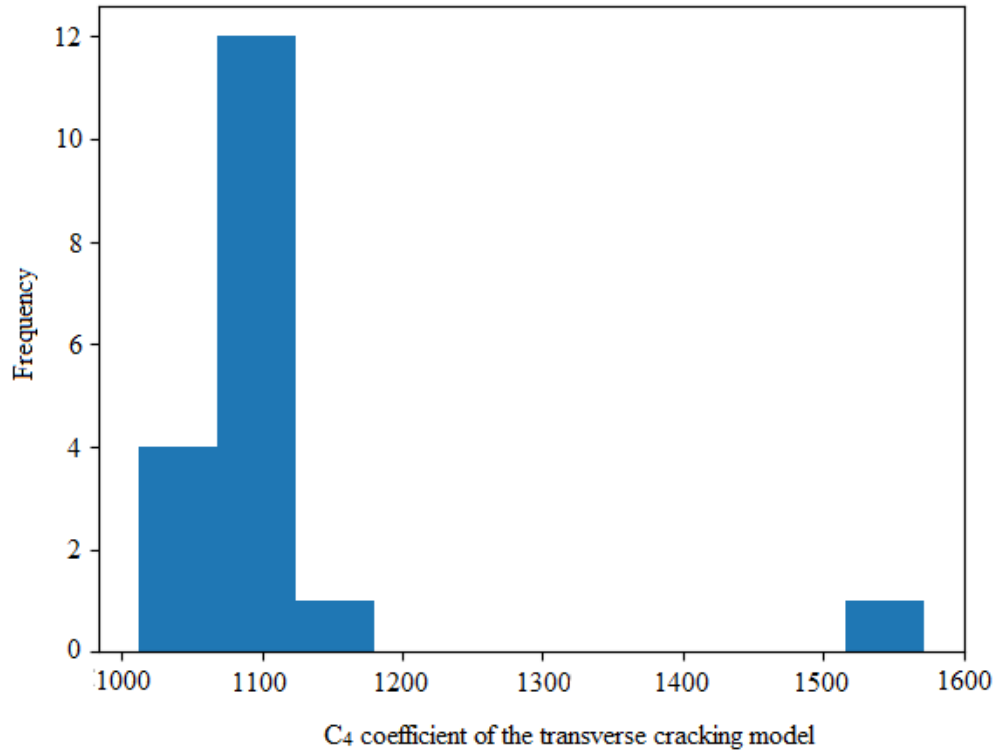


Figure 5-46 Distribution of the  $C_4$  coefficient using jackknife sampling technique

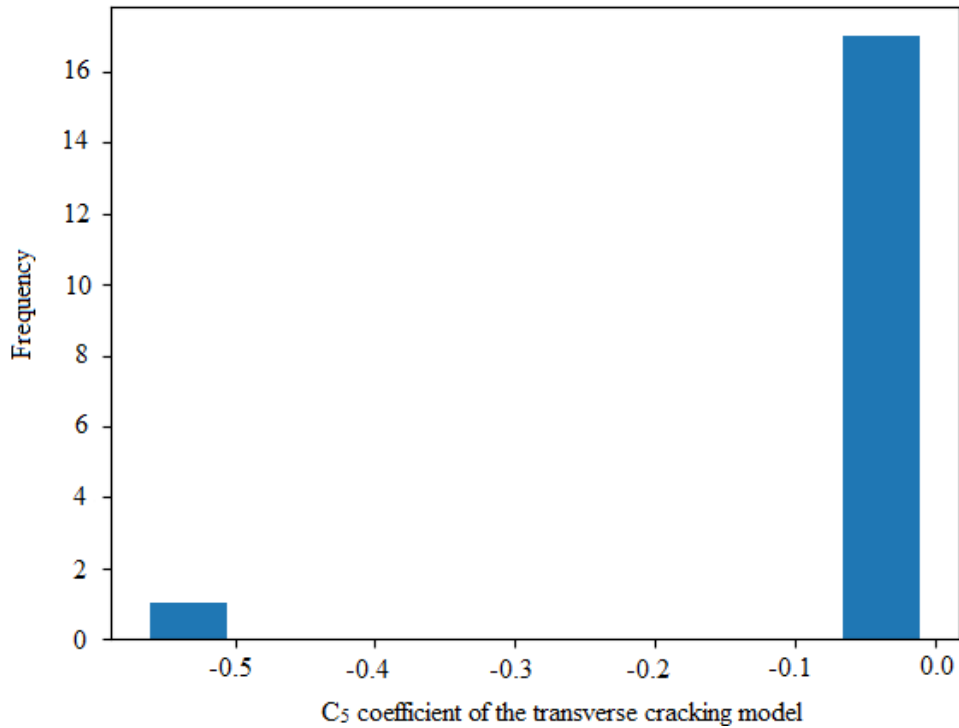


Figure 5-47 Distribution of the  $C_5$  coefficient using jackknife sampling technique

The repeated TOST procedure was conducted with  $C_4$  in the range of 1020–1130 and  $C_5$  ranging from -0.07 to -0.02. Table 5-31 presents results obtained from the repeated TOST considering the above-mentioned combination of  $C_4$  and  $C_5$ . Results showed that calibrated transverse cracking predictions for the AC over JPCP sections were equivalent to measured transverse cracking for a margin of 175 ft/mile for all considered  $C_4$  and  $C_5$  combinations, suggesting that PMED-transverse cracking predictions (level of significance,  $\alpha = 0.05$ ) would likely be equivalent to transverse cracking measured in the field for a margin of 175 ft/mile if the  $C_4$  and  $C_5$  coefficients range from 1020 to 1130 and -0.07 to -0.02, respectively.

Table 5-31 Combination of  $C_4$  and  $C_5$  considered for repeated TOST

Calibration Coefficient $C_4$	1020	1020	1130	1130
Calibration Coefficient $C_5$	-0.02	-0.07	-0.02	-0.07

Equivalence margin, $\delta$ (ft/mile)	125	135	175	175
--	-----	-----	-----	-----

### 5.6.2.3 Bootstrapping approach

The  $C_4$  and  $C_5$  coefficients of transverse cracking model were optimized using the bootstrapping approach for AC over JPCP sections. One thousand bootstrap samples were optimized using the L-BFGS optimization technique. Figures 5-48 and 5-49 show the distribution of  $C_4$  and  $C_5$  coefficients using the bootstrap technique. Figure 5-48 shows that the range of coefficient  $C_4$  was 830–1120 for approximately 800 bootstrap samples and 970–1120 for approximately 600 bootstrap samples. Figure 5-49 shows that the value of coefficient  $C_5$  ranged from -0.09 to -1.50 for approximately 800 bootstrap samples.

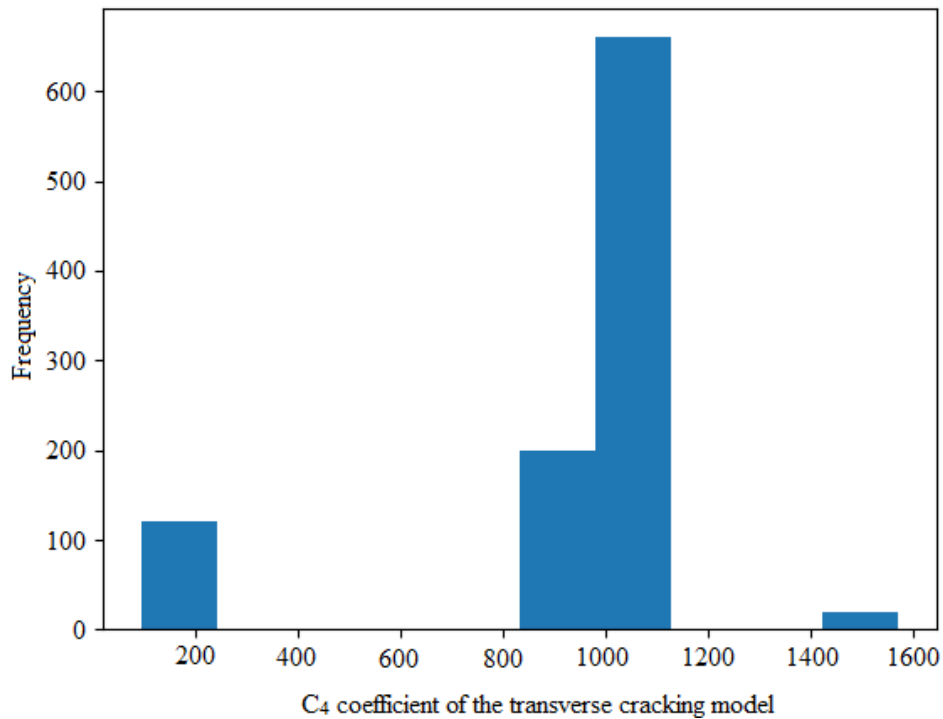


Figure 5-48 Distribution of the  $C_4$  coefficient using bootstrap sampling technique

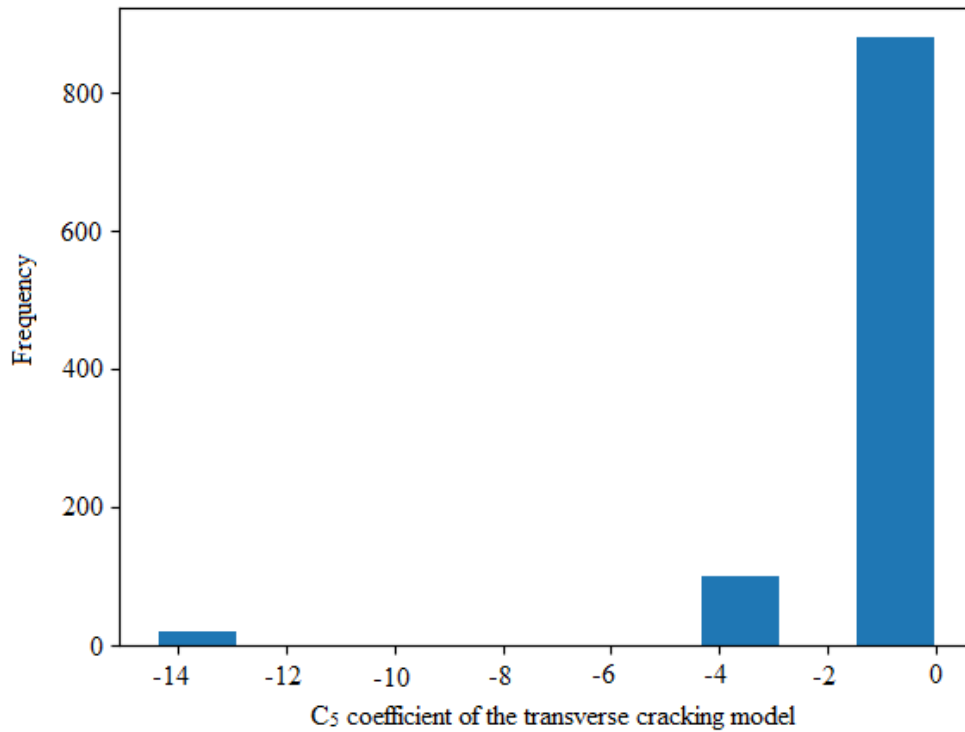


Figure 5-49 Distribution of the  $C_5$  coefficient using bootstrap sampling technique

The TOST procedure was then conducted repeatedly with  $C_4$  in the range of 830–1120 and  $C_5$  ranging from -0.09 to -1.50. Table 5-32 presents results obtained from the repeated TOSTs considering the above-mentioned combination of  $C_4$  and  $C_5$ . Results showed that the PMED transverse cracking predictions (level of significance,  $\alpha = 0.05$ ) would likely be at least 200 ft/mile from the transverse cracking measured in the field.

Table 5-32 Combination of  $C_4$  and  $C_5$  considered for repeated TOST

Calibration Coefficient $C_4$	830	830	1120	1120
Calibration Coefficient $C_5$	-0.09	-1.50	-0.09	-1.50
Equivalence margin, $\delta$	210	215	200	205

### 5.6.3 Top-down cracking model

The top-down cracking model was calibrated for the AC over JPCP sections using the automated technique developed in this study. All load-related cracks were top-down cracking. The first step was to verify the model with global coefficients. Summation of bias, SSE,  $p$ -value from the paired  $t$ -test, and  $p$ -value from the TOST procedure were reported. Table 5-33 lists summary statistics of the top-down cracking model. Results in the table show that the  $p$ -value from the TOST procedure was higher than 0.05 for an equivalence margin of 250 ft/mile, suggesting that PMED-predicted and measured top-down cracking were not equivalent for a margin 250 ft/mile. The  $S_e$  was 862 ft/mile, which is higher than the AASHTO-suggested value of 250 ft/mile. The  $p$ -value from the paired  $t$ -test was less than 0.05, indicating that predicted and measured transverse cracking differ.

Table 5-33 Results for the globally calibrated top-down cracking model for AC over JPCP sections

Bias	SSE	$S_e$	$S_e/S_y$	$p$ -value from paired $t$ -test	$p$ -value from TOST
40639	73,077,300	862	0.99	<0.001	0.99

The automated technique generated the measured versus predicted top-down cracking plot with global coefficients, as shown in Figure 5-50, which shows an asymmetrical trend to the line of equality for the measured versus predicted top-down cracking.

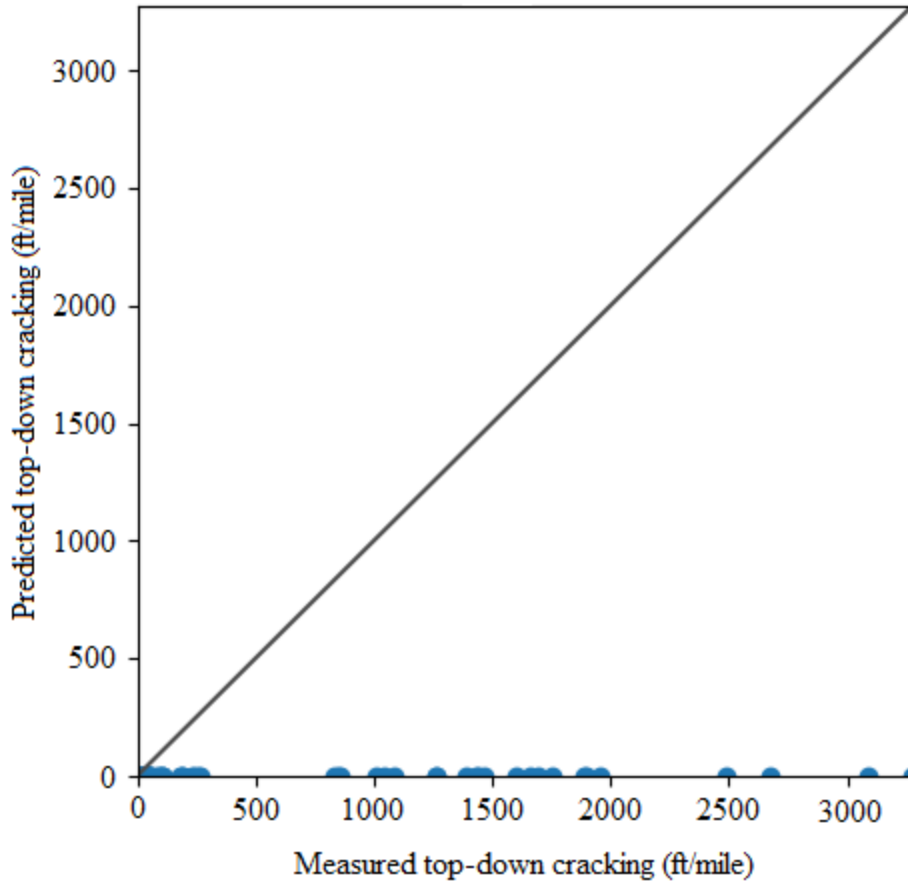


Figure 5-50 Predicted vs measured top-down cracking with globally calibrated factors

Verification results of the longitudinal cracking model for the AC over JPCP sections confirmed the necessity for model recalibration. The PMED top-down cracking model for AC over JPCP sections was calibrated by optimizing calibration parameters  $C_1$  and  $C_2$ . The automated calibration technique was used to extract  $DI_{top}$  values from the PMED output Excel files for each project at the corresponding dates. The optimization technique in the automated technique computed a combination of  $C_1$  and  $C_2$  parameters that yielded the least SSE between measured and predicted top-down cracking.

#### 5.6.3.1 Traditional split sampling approach

The traditional split sampling approach was incorporated into the automated technique to calibrate and validate the top-down cracking model for AC over JPCP sections. Table 5-34

presents summary statistics of the top-down cracking model for the calibration dataset. A comparison of the values in Tables 5-33 and Table 5-34 show that the model bias and SSE decreased significantly and  $S_e$  increased slightly after local calibration. The  $p$ -value from the paired  $t$ -test after local calibration was higher than 0.05, which suggests that there is no evidence that the predicted and measured transverse cracking are different. However, the  $p$ -value from the TOST was higher than 0.05 for a  $\delta$  value of 250 ft/mile, indicating that predicted and measured top-down cracking were not equivalent for a margin of 250 ft/mile.

Table 5-34 Summary statistics for the locally calibrated top-down cracking model

Bias	SSE	$S_e$	$S_e/S_y$	$p$ -value from paired $t$ -test	$p$ -value from TOST
7492	48,740,603	871	1.01	0.29	0.11

The TOST procedure was performed multiple times to determine the equivalence margin for measured and predicted top-down cracking. Table 5-35 presents the summary of results of the repeated TOST procedures. The level of significance ( $\alpha$ ) was 0.05 in all cases. Results in Table 5-35 show that the equivalence margin for predicted and measured top-down cracking was 305 ft/mile; PMED top-down cracking predictions were not equivalent to measured top-down cracking for any margin less than 305 ft/mile.

Table 5-35 Calibrated model equivalence margin between measured and predicted rutting

Equivalence margin, $\delta$ (ft/mile)	$p$ -value	Remark
250	0.113	Not equivalent
275	0.082	Not equivalent
300	0.052	Not equivalent
305	0.047	Equivalent

Measured versus predicted plot of longitudinal cracking with local factors is shown in Figure 5-51. An asymmetrical trend with respect to the line of equality can be observed.

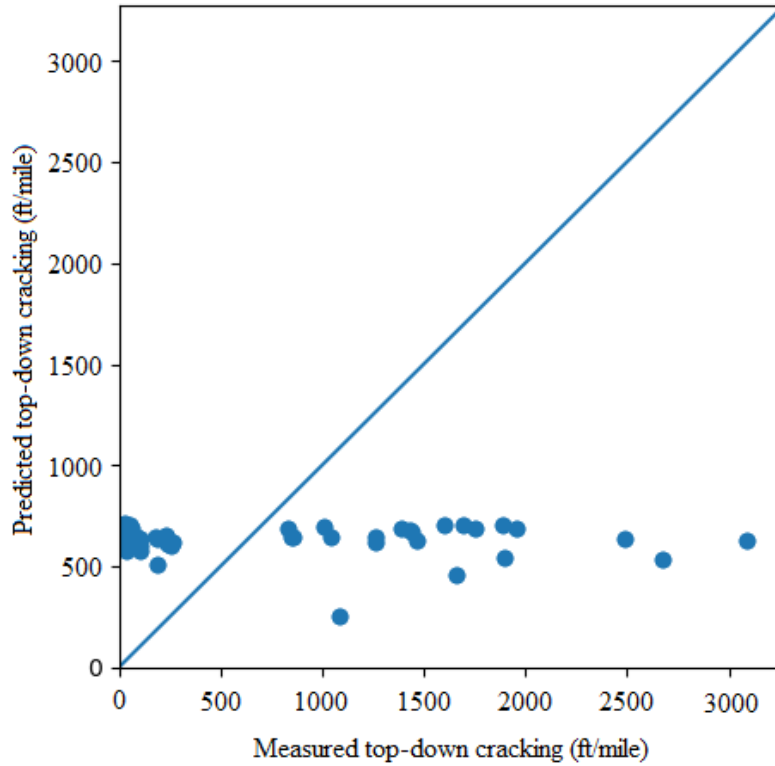


Figure 5-51 Predicted vs measured top-down with local coefficients for AC over JPCP sections

Table 5-36 tabulates summary statistics for the calibrated top-down cracking model after validation. The  $p$ -value from the paired  $t$ -test for the validation dataset with local coefficients was greater than 0.05, which suggests that there is no evidence that the predicted and measured top-down cracking differ for projects considered in the validation dataset. However, the  $p$ -value from the TOST was higher than 0.05 for an equivalence margin of 305 ft/mile, indicating that predicted and measured top-down cracking were not equivalent for a margin of 305 ft/mile for projects in the validation dataset. Repeated TOST was performed again for the validation dataset,



and the narrowest equivalence margin was 850 ft/mile. Figure 5-52 presents measured versus predicted transverse cracking with local coefficients for the validation dataset.

Table 5-36 Validation results for the calibrated top-down cracking model for AC over JPCP sections

Bias	SSE	$S_e$	$S_e/S_y$	$p$ -value from paired $t$ -test	$p$ -value from TOST ( $\delta = 305$ ft/mile)
8228	18,644,157	909	1.02	0.053	0.75

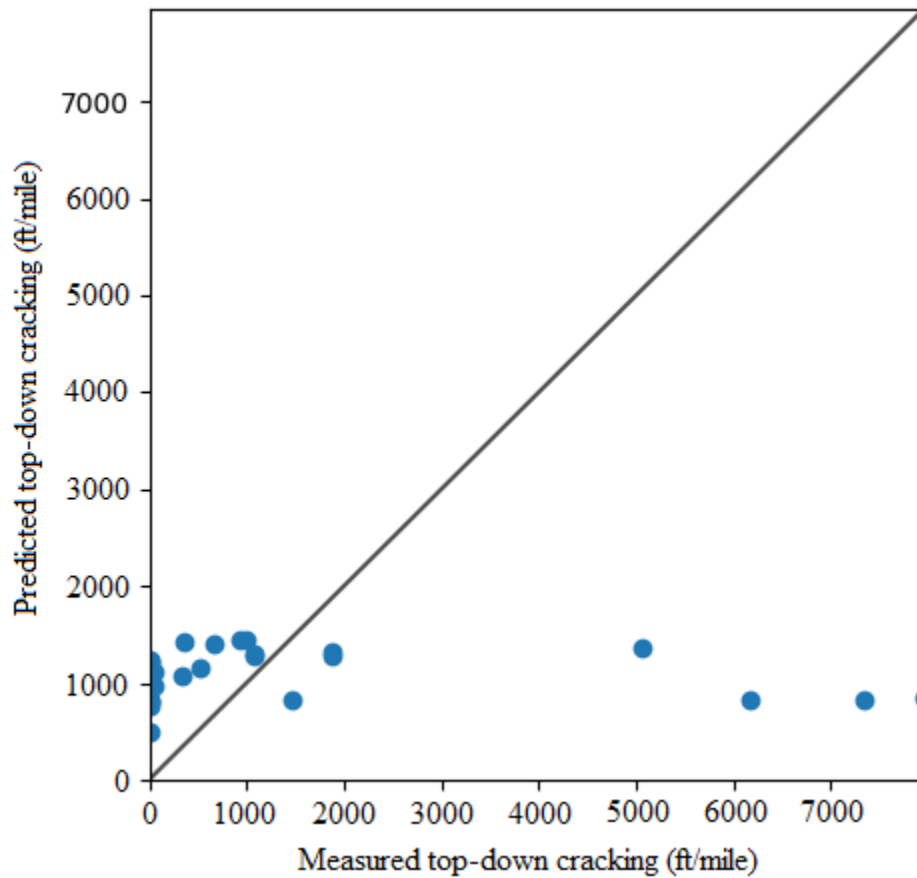


Figure 5-52 Predicted versus measured top-down cracking for the validation dataset

### 5.6.3.2 Jackknifing approach

The jackknifing sampling approach was incorporated into the automated technique to calibrate the PMED top-down cracking model for AC over JPCP sections. Both  $C_1$  and  $C_2$

coefficients of the top-down cracking model were optimized for 18 jackknife samples. Figures 5-53 and 5-54 show the distribution of  $C_1$  and  $C_2$  coefficients using the jackknife technique. Figure 5-53 shows that the range of coefficient  $C_1$  was 2.26–2.61 for 15 jackknife samples, and Figure 5-54 shows that the value of coefficient  $C_2$  was 0.09–0.18 for 16 jackknife samples.

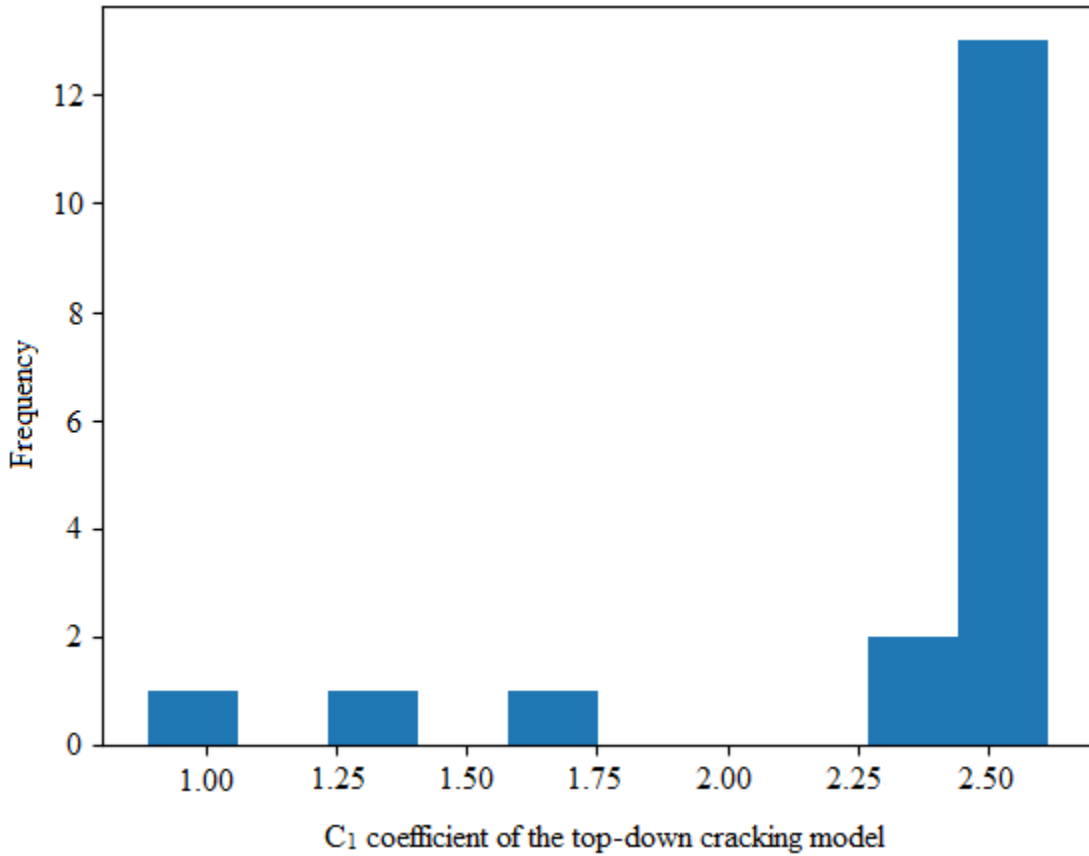


Figure 5-53 Distribution of the  $C_1$  coefficient using jackknife sampling technique

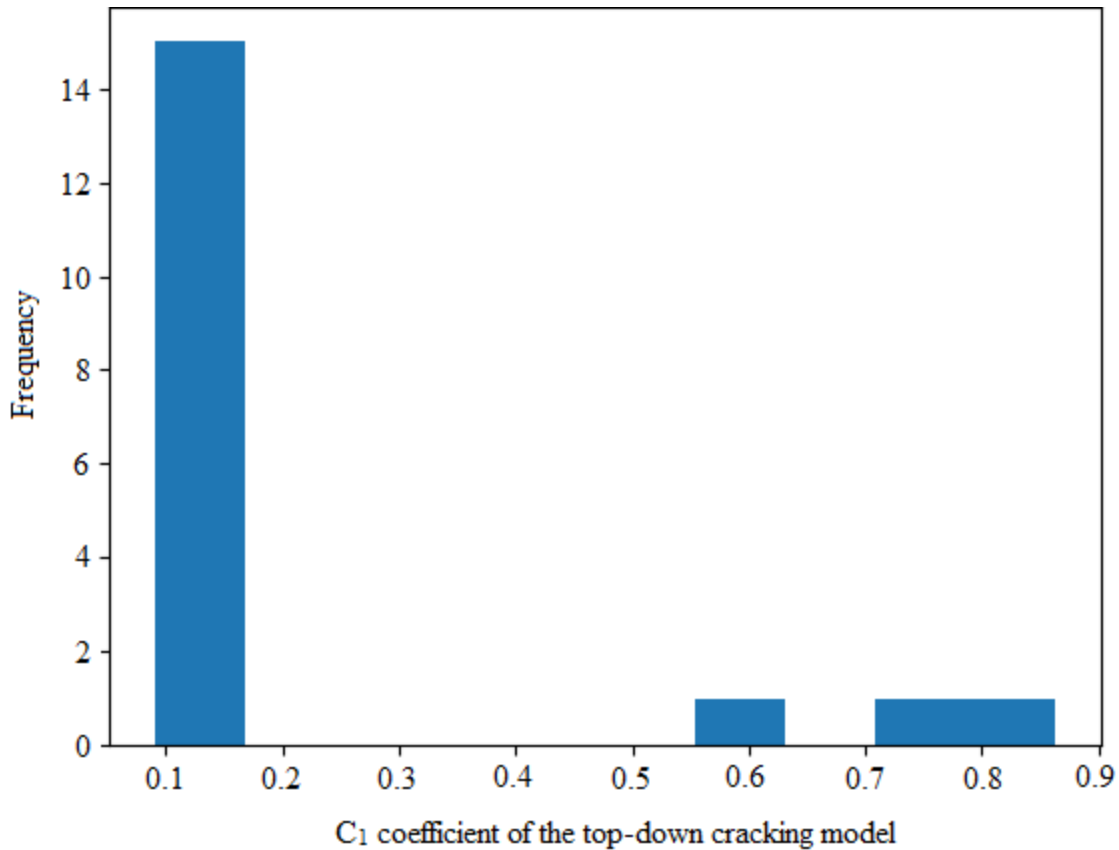


Figure 5-54 Distribution of the  $C_2$  coefficient using jackknife sampling technique

The repeated TOST procedure was conducted for a combination of  $C_1$  and  $C_2$ , with  $C_1$  in the range of 2.26–2.61 and  $C_2$  in the range of 0.09–0.18. Table 5-37 presents results obtained from the repeated TOST for the above-mentioned combination of  $C_1$  and  $C_2$ . Results showed that the narrowest equivalence margin for measured and predicted top-down cracking was 200 ft/mile for a  $C_1$  value of 2.26 and a  $C_2$  value of 0.18. These results suggest that PMED top-down cracking predictions (level of significance,  $\alpha = 0.05$ ) would likely be equivalent to top-down cracking measured in the field for a margin of 200 ft/mile if the  $C_1$  and  $C_2$  coefficients are 2.61 and 0.18, respectively.

Table 5-37 Combination of  $C_1$  and  $C_2$  considered for repeated TOST for the jackknife technique

Calibration Coefficient $C_1$	2.26	2.26	2.61	2.61
Calibration Coefficient $C_2$	0.09	0.18	0.09	0.18
Equivalence margin, $\delta$ (ft/mile)	325	200	250	340

### 5.6.3.3 Bootstrapping approach

The bootstrap resampling approach was used to optimize the  $C_1$  and  $C_2$  coefficients of the top-down cracking model. One thousand bootstrap samples were optimized using the L-BFGS optimization technique. Figures 5-55 and 5-56 show the distribution of  $C_1$  and  $C_2$  using the bootstrap technique. Figure 5-55 shows that the range of coefficient  $C_1$  was 2.35–2.55 for approximately 950 bootstrap samples, and Figure 5-56 shows that the value of coefficient  $C_2$  was in the range of 0.08–0.21 for approximately 925 bootstrap samples.

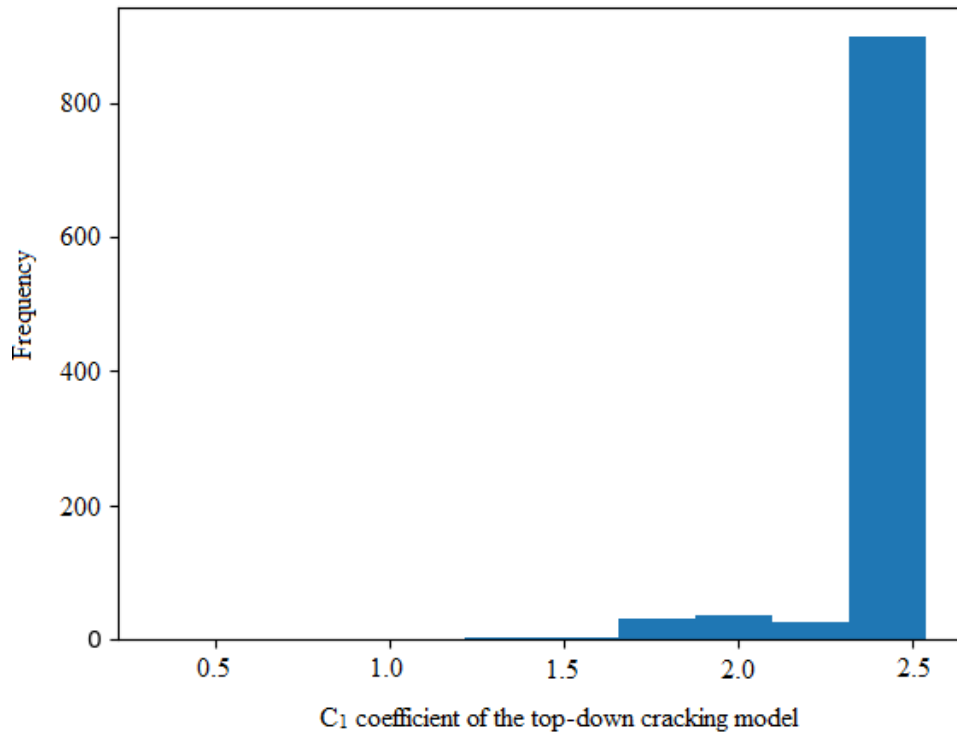


Figure 5-55 Distribution of the  $C_1$  coefficient using bootstrap technique

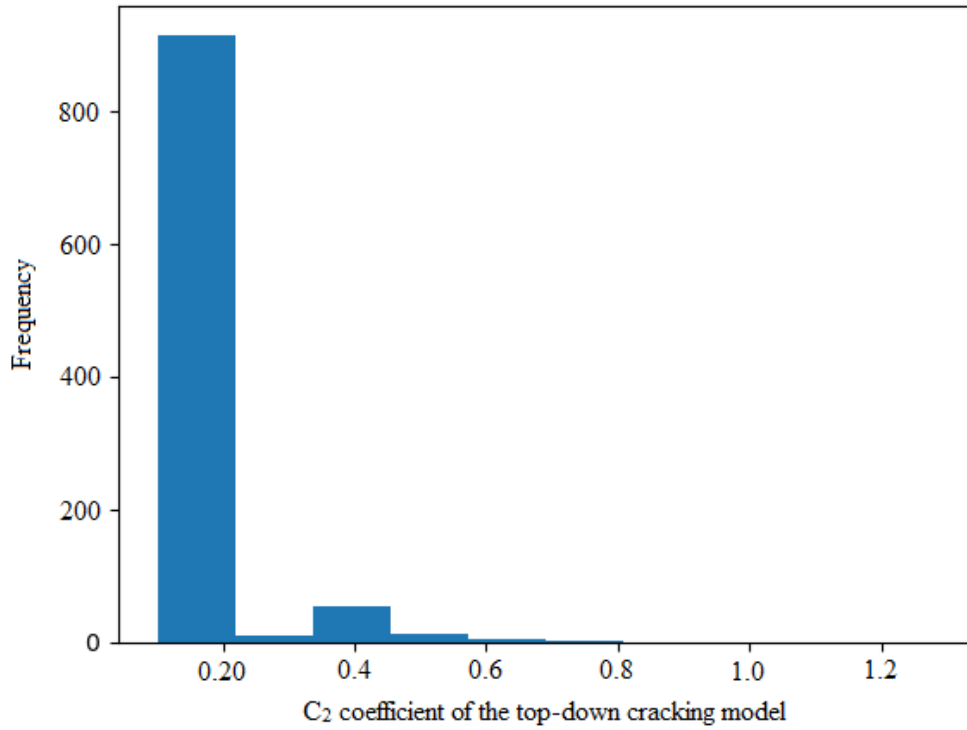


Figure 5-56 Distribution of the  $C_2$  coefficient using bootstrap technique

The TOST procedure was repeatedly conducted for a combination of  $C_1$  and  $C_2$ , with  $C_1$  in the range of 2.35–2.55 and  $C_2$  in the range of 0.08–0.18. Table 5-38 presents the results. The minimum equivalence margin obtained from the TOST procedures was 185 ft/mile for a  $C_1$  and  $C_2$  combination of 2.55 and 0.08, respectively. Predicted top-down cracking (level of significance,  $\alpha = 0.05$ ) using the PMED software was equivalent to measured top-down cracking for a margin of 185 ft/mile.

Table 5-38 Combination of  $C_1$  and  $C_2$  considered for repeated TOST for the bootstrap technique

Calibration Coefficient $C_1$	2.35	2.35	2.55	2.55
Calibration Coefficient $C_2$	0.08	0.21	0.08	0.21
Equivalence margin, $\delta$ (ft/mile)	300	250	185	350

#### 5.6.4 IRI model

The IRI model was calibrated for the AC over JPCP sections using the automated calibration technique and verified with global coefficients. The summation of bias, SSE,  $p$ -value from the paired  $t$ -test, and  $p$ -value from the TOST procedure were reported. Table 5-39 lists summary statistics of the IRI model with global coefficients. Results in the table show that  $p$ -value from the TOST procedure was greater than 0.05 for an equivalence margin of 17 in./mile, suggesting that PMED-predicted IRI with global coefficients and measured IRI were not equivalent for a margin of 17 in./mile. The  $S_e$  was 10 in./mile, which is lower than the AASHTO-suggested value of 17 in./mile. The  $p$ -value from the paired  $t$ -test was less than 0.05, which suggests that measured and predicted IRI are different.

Table 5-39 Results for the globally calibrated IRI model for AC over JPCP sections

Bias	SSE	$S_e$	$S_e/S_y$	$p$ -value from paired $t$ -test	$p$ -value from TOST
1,406	38,586	10	0.98	<0.001	0.99

The automated calibration technique generated the measured versus predicted IRI plot with global coefficients. Figure 5-57 shows measured versus predicted IRI with global coefficients. An asymmetrical trend with respect to the line of equality for the measured versus predicted IRI can be observed.

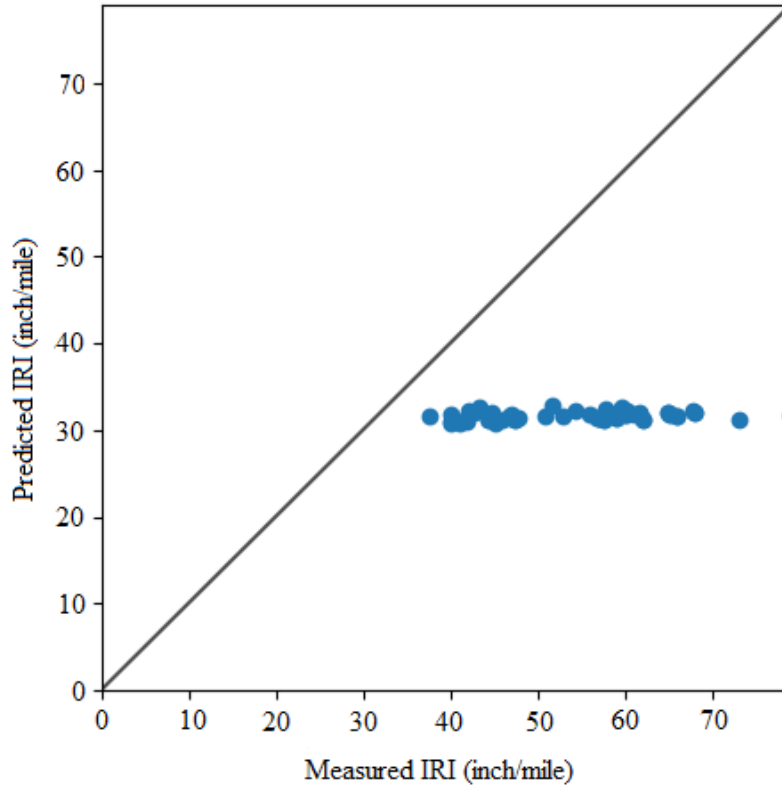


Figure 5-57 Predicted vs measured IRI with global factors for AC over JPCP sections

Verification results of the IRI model for JPCP rehabilitated sections confirmed the necessity of model recalibration. Project-specific precipitation and freezing index, soil plasticity index, subgrade soil percent passing through a US No. 4 sieve, and subgrade soil percent passing through a US No. 200 sieve were automatically extracted using the automated technique. Furthermore, project-specific rut depth, fatigue cracking, and transverse cracking values were extracted from the output Excel files for the corresponding IRI data collection date. Finally, the PMED IRI model for AC over JPCP sections was calibrated by optimizing calibration parameters  $C_1$ ,  $C_2$ ,  $C_3$ , and  $C_4$ . Since none of the IRI model coefficients had negative values, parameter bounds were used as listed in Table 5-17.

#### 5.6.4.1 Split sampling approach

Table 5-40 presents summary statistics for the IRI model calibrated using the traditional split sampling approach. Results in the table show that the model goodness-of-fit statistics significantly improved after local calibration. The  $p$ -value from the paired  $t$ -test after local calibration was higher than 0.05, which suggests that there is no evidence that the predicted and measured IRI are different. The  $p$ -value from the TOST was less than 0.05 for a  $\delta$  value of 17 in./mile, indicating that predicted and measured top-down cracking were equivalent for a margin of 17 in./mile.

Table 5-40 Summary statistics for the locally calibrated IRI model

Bias	SSE	$S_e$	$S_e/S_y$	$p$ -value from paired $t$ -test	$p$ -value from TOST
0.16	3,928	8	0.78	0.99	<0.001

The TOST procedure was then performed multiple times to determine the narrowest equivalence region for measured and predicted IRI. Table 5-41 presents a summary of the results of the repeated TOST procedure. The level of significance ( $\alpha$ ) was 0.05 in all cases. Results in Table 5-41 show that the equivalence margin for predicted and measured IRI was 3 in./mile, while PMED-predicted IRI values for the AC over JPCP sections were equivalent to IRI measured in the field for a margin of 3 in./mile.



Table 5-41 Calibrated model equivalence margin between measured and predicted rutting

Equivalence margin, $\delta$ (in./mile)	$p$ -value	Remark
17	<0.001	Equivalent
10	<0.001	Equivalent
5	<0.001	Equivalent
3	0.03	Equivalent
2	0.10	Not equivalent

The measured versus predicted plot of IRI with local factors is shown in Figure 5-58. A comparison of data in Figures 5-57 and 5-58 shows significant improvement in data location relative to the line of equality after model calibration.

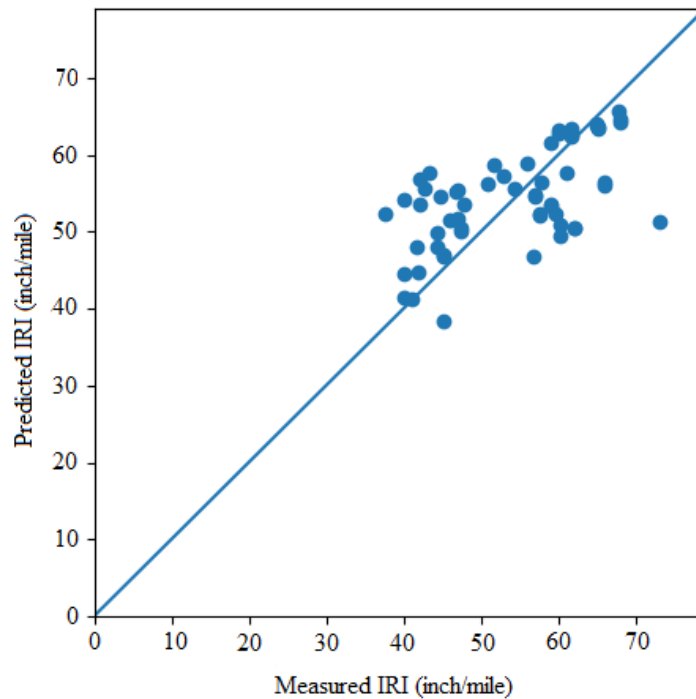


Figure 5-58 Predicted vs measured IRI with local coefficients for AC over JPCP sections

Summary statistics for the calibrated IRI model after validation are presented in Table 5-42. The  $p$ -value from the paired  $t$ -test for the validation dataset with local coefficients was higher than 0.05, which suggests that there is no evidence that the predicted and measured IRI differ for projects in the validation dataset. However, the  $S_e$  was high with local coefficients for the validation dataset, and the  $p$ -value from the TOST was higher than 0.05 for an equivalence margin of 3 in./mile, which suggests that predicted and measured IRI were not equivalent for a margin of 3 in./mile for projects in the validation dataset. The TOST procedure was repeatedly performed for the validation dataset, and the narrowest equivalence margin was 16 in./mile. Figure 5-59 illustrates measured versus predicted transverse cracking with local coefficients for the validation dataset.

Table 5-42 Validation results for the calibrated IRI model for AC over JPCP sections

Bias	SSE	$S_e$	$S_e/S_y$	$p$ -value from paired $t$ -test	$p$ -value from TOST ( $\delta = 3$ in./mile)
114	7,941	22	1.34	0.21	0.87

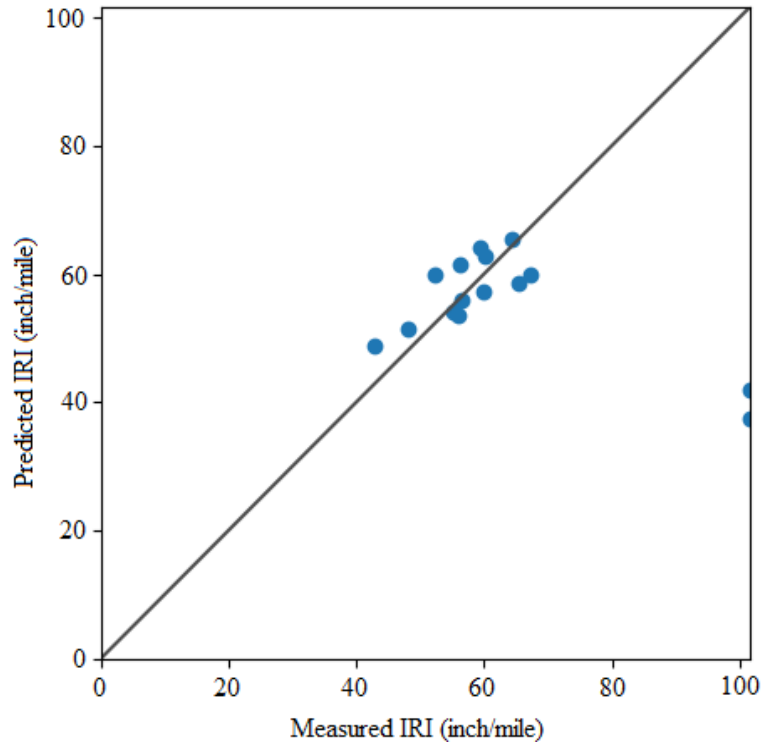


Figure 5-59 Predicted versus measured IRI for the validation dataset with local factors

#### 5.6.4.2 Jackknifing approach

The jackknifing sampling approach was also used to calibrate the PMED IRI model. The  $C_1$ ,  $C_2$ ,  $C_3$  and  $C_4$  coefficients of the IRI model were optimized for 18 jackknife samples for AC over AC sections considered in this study. Figure 5-60 through Figure 5-63 show the distribution of  $C_1$ ,  $C_2$ ,  $C_3$ , and  $C_4$  coefficients using the jackknife technique. The figures present the following results:

- Coefficient  $C_1$  had a range of 847–890 for 15 of 18 jackknife samples.
- The value of coefficient  $C_2$  was 0.615–0.623 for 16 jackknife samples.
- The value of coefficient  $C_3$  was 0.0014–0.0021 for 14 jackknife samples.
- The range of  $C_4$  parameter was 0.0995–0.0999 for 16 jackknife samples.

TOST procedure was repeatedly conducted for a combination of  $C_1$ ,  $C_2$ ,  $C_3$ , and  $C_4$ , with  $C_1$  in the range of 847.0–890.0,  $C_2$  in the range of 0.615–0.623,  $C_3$  in the range of 0.0014–0.0021, and  $C_4$  in the range of 0.095–0.099. Results showed that the narrowest equivalence margin for measured and predicted IRI varied between 3 in./mile and 5 in./mile. These results suggest that calibrated IRI predictions for AC over JPCP sections (level of significance,  $\alpha = 0.05$ ) would likely be equivalent to IRI measured in the field for a margin of 3–5 in./mile if the  $C_1$ ,  $C_2$ ,  $C_3$ , and  $C_4$  coefficients are in the range of 847–890, 0.615–0.623, 0.0014–0.0021, and 0.0995–0.0999, respectively.

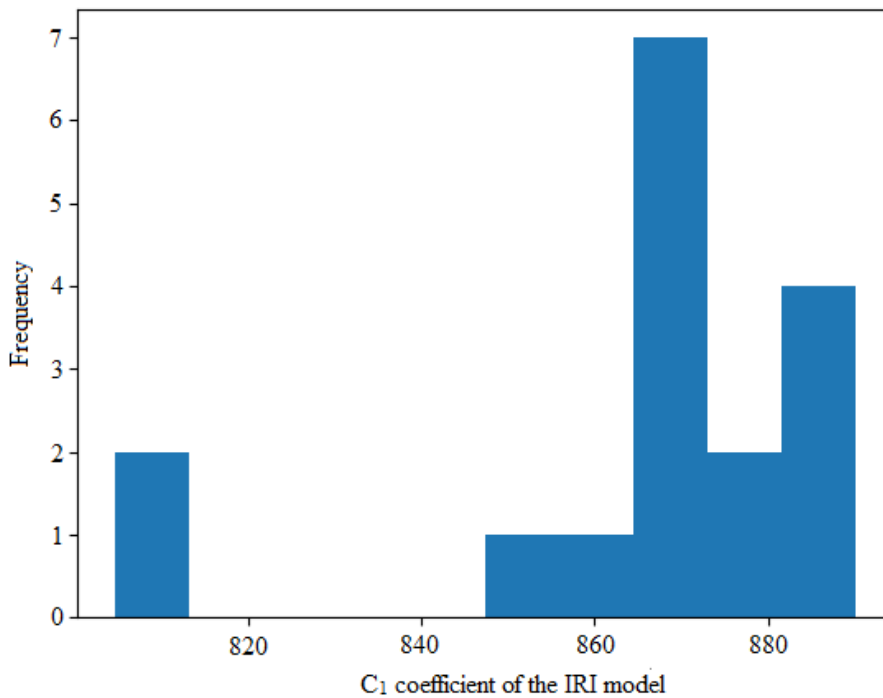


Figure 5-60 Distribution of the  $C_1$  coefficient of IRI model using jackknife technique

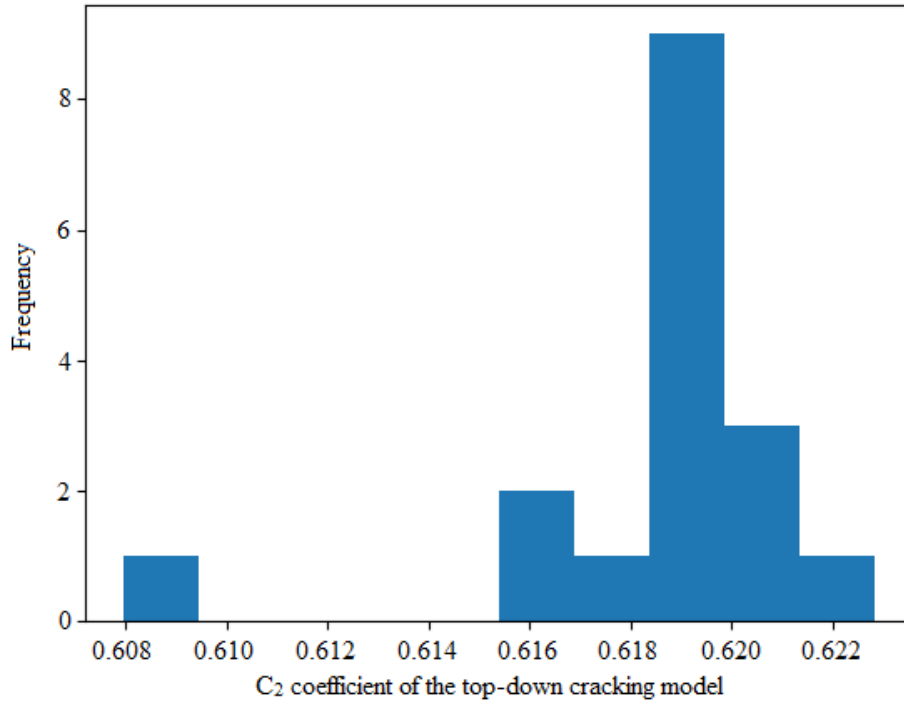


Figure 5-61 Distribution of the  $C_2$  coefficient of IRI model using jackknife technique

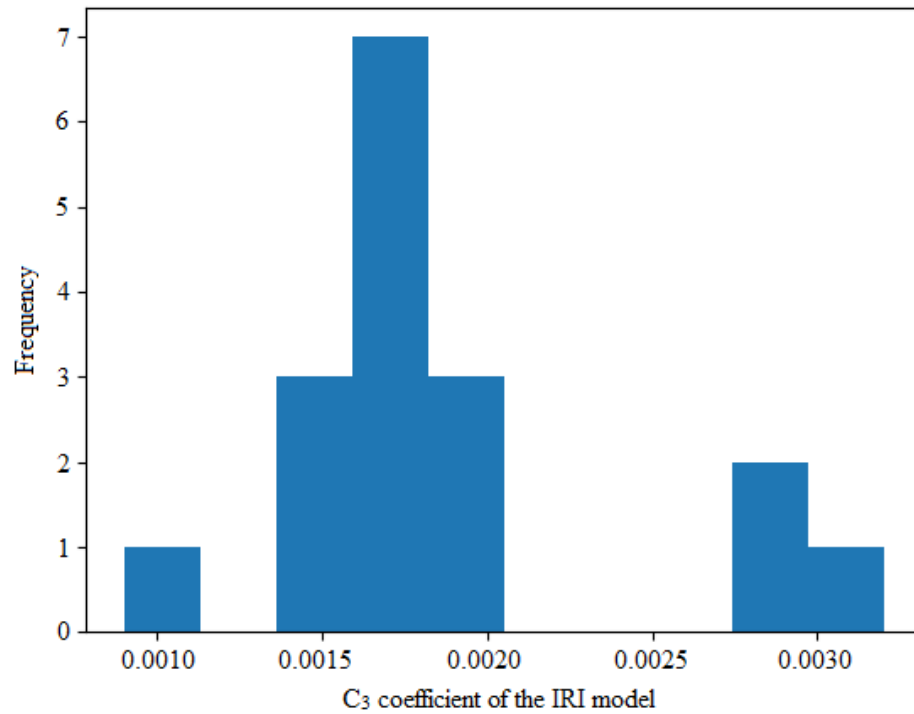


Figure 5-62 Distribution of the  $C_3$  coefficient of IRI model using jackknife technique

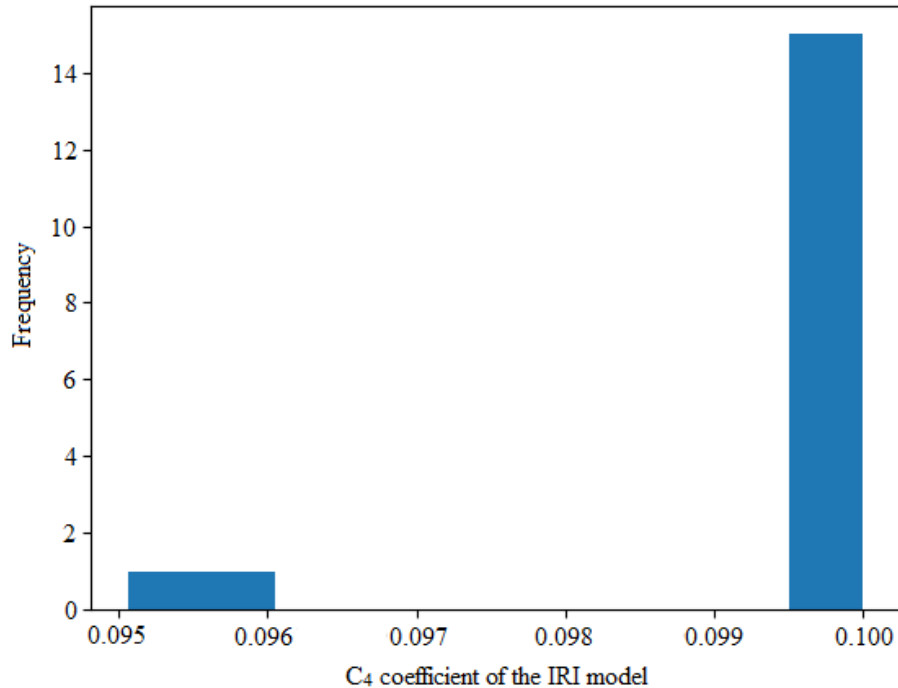


Figure 5-63 Distribution of the  $C_4$  coefficient of IRI model using jackknife technique

#### 5.6.4.3 Bootstrapping approach

The bootstrap resampling approach was implemented to optimize IRI model coefficients. One thousand bootstrap samples were considered. Figures 5-64 through 5-67 show the distribution of  $C_1$ ,  $C_2$ ,  $C_3$ , and  $C_4$  coefficients using the bootstrap technique. These figures also show the following:

- Coefficient  $C_1$  had a range of 880–894 for 700 bootstrap samples.
- The value of coefficient  $C_2$  was in the range of 0.612–0.616 for more than 900 bootstrap samples.
- The value of coefficient  $C_3$  was in the range of 0.0017–0.0021 for approximately 800 bootstrap samples.
- The range of  $C_4$  parameter was 0.0989–0.0999 for approximately 800 bootstrap samples.

The TOST was repeatedly conducted for a combination of  $C_1$ ,  $C_2$ ,  $C_3$ , and  $C_4$ , with  $C_1$  in the range of 880–894,  $C_2$  in the range of 0.612–0.616,  $C_3$  in the range of 0.0017–0.0021, and  $C_4$  in the range of 0.0089–0.0099. Results showed that the narrowest equivalence margin for measured and predicted IRI varied between 5 in./mile and 8 in./mile, suggesting that calibrated IRI predictions (level of significance,  $\alpha = 0.05$ ) would likely be equivalent to IRI measured in the field for a margin of 15 in./mile if the  $C_1$ ,  $C_2$ ,  $C_3$ , and  $C_4$  coefficients were in the range of 40.5–53.5, 0.34–0.41, 0.0074–0.0082, and 0.0989–0.0999, respectively.

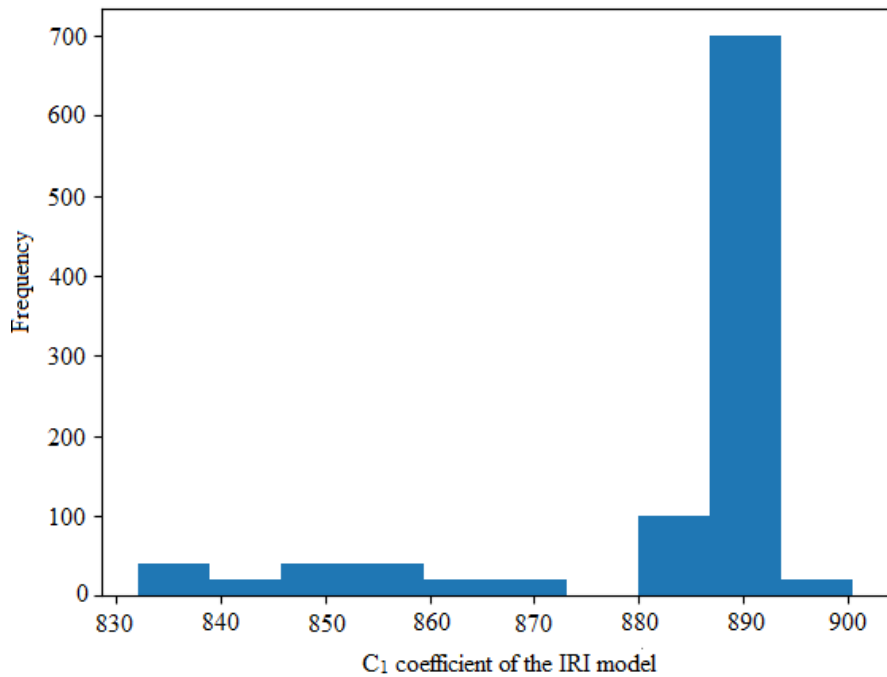


Figure 5-64 Distribution of the  $C_1$  coefficient of IRI model using bootstrap technique

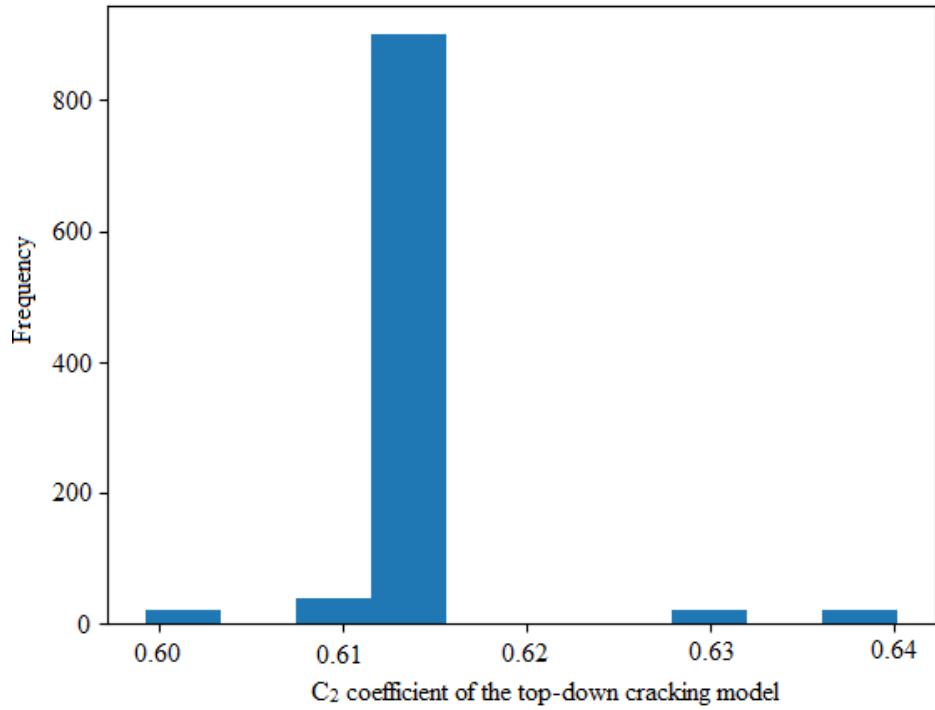


Figure 5-65 Distribution of the  $C_2$  coefficient of IRI model using bootstrap technique

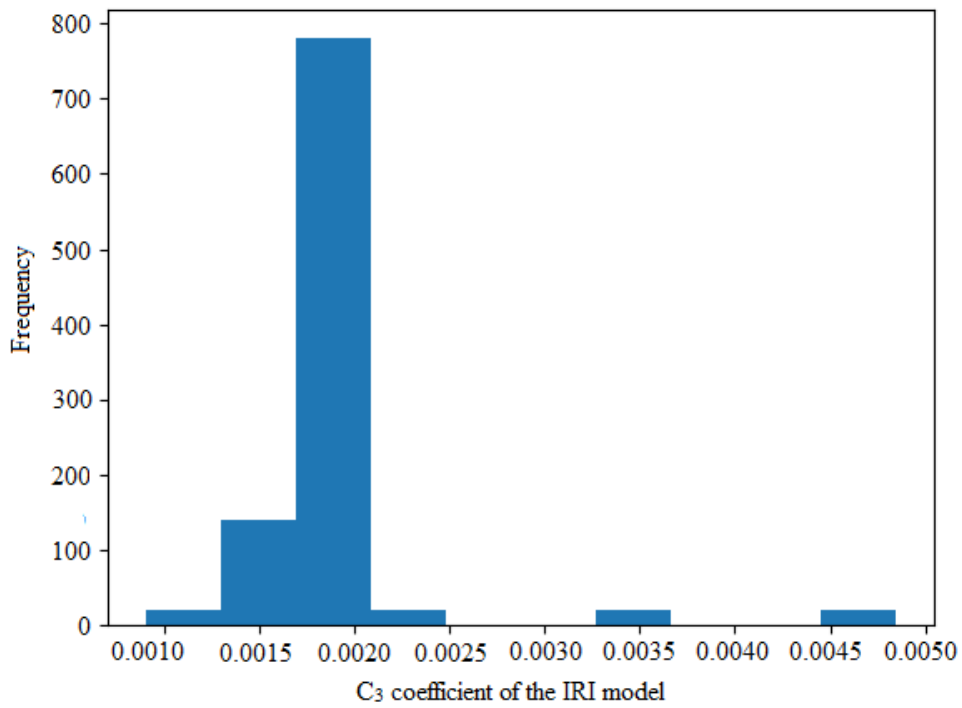


Figure 5-66 Distribution of the  $C_3$  coefficient of IRI model using bootstrap technique



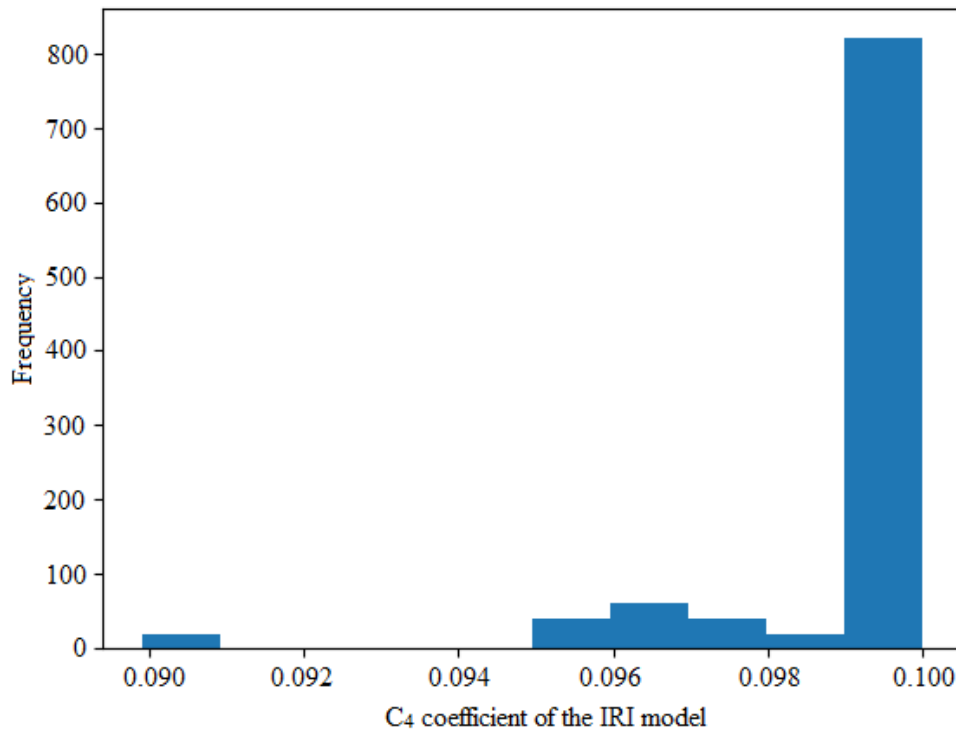


Figure 5-67 Distribution of the  $C_4$  coefficient of IRI model using bootstrap technique

### 5.7 Limitation of the Automated Calibration Technique

Currently, the developed automated technique can only calibrate parameters that do not require multiple simulations of the PMED software. For AC pavements, the permanent deformation, IRI, bottom-up, and top-down fatigue cracking transfer functions can be calibrated. However,  $\beta_{2r}$  and  $\beta_{3r}$  coefficients of the permanent deformation model cannot be calibrated using this approach. Similarly, the thermal cracking model cannot be calibrated using this technique.

One concern regarding application of the automated calibration technique is identifying the bounds of model coefficients. A simple optimization technique typically searches for a local minimum of the objective function (SSE), while the robust optimization techniques have the ability to obtain global minimum where the value of the objective function is smaller than that of the local optima (Yapo et al., 1998). No study has yet been conducted to identify lower and upper bounds of PMED model coefficients beyond realistic predictions. The developed

automated techniques in this study allow users to select lower and upper bounds for the IRI model.

## **Chapter 6 - Conclusion**

The primary objective of this study was to provide KDOT with AC overlay performance models locally calibrated to Kansas conditions in the AASHTOWare PMED software. Twenty-five AC rehabilitated sections and 18 JPCP sections were chosen across the state. Level 2 truck traffic volumetric factors were developed from data collected at 11 AVC stations in Kansas. In addition, traffic load spectra were developed from 10 WIM stations. A database of material input parameters was developed for the chosen pavement sections from the KDOT construction management system, quality control and quality assurance database, and as-build construction plans. Time-series performance data were extracted from the KDOT PMIS database and evaluated for consistencies and potential outliers. The nationally calibrated PMED distress models (e.g., permanent deformation model, transverse cracking model, load-related cracking model, and IRI model) were evaluated for Kansas conditions. The results showed that global models in the PMED

software do not accurately predict pavement performance. Local calibration was carried out for these models, and the results showed significantly improved prediction accuracy. An automated technique was developed to aid in periodic recalibration of PMED prediction models. Robust sampling techniques such as jackknifing and bootstrapping methods were incorporated into the automated technique. In addition, the TOST approach was included to determine an equivalence margin for predicted and measured performance data.

## **6.1 Local Calibration Results**

Verification results of the PMED models with global coefficients confirmed the need to calibrate transfer function coefficients. After a parameter optimization approach, this study conducted local calibration for the permanent deformation model, transverse cracking model, top-down fatigue cracking model, and the IRI model. Key findings from the local calibration effort in this study are summarized below.

### **6.1.1 *Permanent deformation model***

Prediction accuracy of the AC rutting model improved for both asphalt and concrete rehabilitated sections in terms of goodness-of-fit criteria after local calibration; only the  $\beta_{1r}$  parameter of the rutting model was optimized. The calibrated model  $S_e$  was within the AASHTO-suggested range of 0.1 in. for AC over AC and AC over JPCP sections. For both sets of projects, the scattered data points in the measured and predicted rutting (local coefficients) plot appeared to spread symmetrically relative to the line of equality.

### **6.1.2 *Transverse cracking model***

Prediction accuracy of the transverse cracking model improved after local calibration for both AC over AC and AC over JPCP sections. For AC over AC sections, the  $S_e$  of the calibrated model was below the AASHTO-suggested limit of 250 ft/mile. However, for the AC over JPCP

sections, the calibrated model  $S_e$  (570 ft/mile) was outside the AASHTO-suggested range. One reason for such high  $S_e$  for the AC over JPCP sections could be the relatively high variation in the measured data (i.e., a standard deviation of 530 ft/mile for AC over JPCP sections compared to 200 ft/mile for AC over AC sections). Another reason for high  $S_e$  of the transverse cracking model could be use of the globally calibrated AC thermal cracking model. Thermal cracking could be present on the selected JPCP rehabilitated projects as well as on the AC rehabilitated projects, making it difficult to distinguish from reflection cracking. The globally calibrated thermal cracking model did not predict thermal cracks for any of the rehabilitated sections in this study; thus, all transverse cracks measured in the field were regarded as reflective cracks, potentially resulting in a higher  $S_e$  for the transverse cracking model for both AC and JPCP rehabilitated sections.

### ***6.1.3 Load-related cracking model***

The calibrated top-down cracking model provided better predictions with lower bias and  $S_e$  compared to the globally calibrated model. However,  $S_e$  of the top-down cracking model was still very high for AC over AC sections (1900 ft/mile) and AC over JPCP sections and above the AASHTO-suggested range (250 ft/mile). The high  $S_e$  for the top-down cracking model can be explained by three rationales listed below:

- The standard deviation of measured top-down cracking across the AC over AC projects and AC over JPCP projects was 2,000 ft/mile and 1,850 ft/mile, respectively. In this study, a majority of fatigue crack measurements were extracted from LCMS surveyed data. The LCMS measurements included the complete profile of roadway segments. However, manually collected distress data had to be used for measurements prior to 2013, in which three 100-ft samples were selected from 1-mile segments, and an

extrapolated figure was reported as total cracking for each 1-mile segment. For projects that did not any have cracking in the selected three 100-ft sections, cracking for the whole sections was shown as zero in the KDOT PMIS database. Therefore, the actual sections may have cracking that could not be accounted. This discrepancy in data measurement system was reflected by high variability in the measured cracking data, and it potentially generated high  $S_e$  of the calibrated top-down cracking model.

- KDOT does not consider any load-related cracking to initiate from the bottom of the HMA layer. In this study, all load-related cracking was considered to be top-down. However, such variability in top-down cracks, especially across AC over AC projects, suggests a potentially significant amount of bottom-up fatigue cracking that was accounted for as top-down cracking in at least a few sections. Accounting all fatigue cracks as top-down cracks could attribute to the high  $S_e$  for the calibrated longitudinal cracking model.
- The prediction accuracy of top-down cracking has been a long-term concern (Williams et al., 2013). Previous calibration efforts indicated that predictions of longitudinal cracking models were not consistent enough for implementation in pavement design (Von Quintus et al, 2007). Improved AC top-down cracking prediction models are currently being developed for inclusion in the AASHTOWare PMED software under NCHRP 1-52 study. This study assumed all load-related cracking to be top-down cracking.

#### **6.1.4 IRI model**

The bias and SSE of the IRI model decreased after local calibration for both AC over AC and AC over JPCP sections. For AC over AC sections, the  $S_e$  of the calibrated model slightly

increased. However, the calibrated model  $S_e$  for both section types was within the AASHTO-suggested range of 17 in./mile.

## **6.2 Automated Calibration Technique**

One of the primary objectives of this study was to develop an automated technique for highway agencies to perform in-house calibration of PMED performance models. The developed automated technique can search PMED output files and identify damages/distresses for a project on a particular date. After obtaining relevant damage, the developed automated technique conducts model verification with global factors. The traditional paired  $t$ -test and the TOST approach are both conducted, and an optimization technique is used to calibrate PMED model coefficients. The automated technique allows users to select one of three sampling techniques: split sampling, jackknifing, or bootstrapping. Based on the sampling technique choice, calibration coefficient or a suitable range for the coefficient is provided, and a measured versus predicted graph is generated. Model bias, standard error, sum squared error,  $p$ -value from the paired  $t$ -test, and the TOST are also reported.

### **6.2.1 Sampling technique**

Three sampling techniques were incorporated into the automated technique for optimizing PMED transfer function calibration coefficients. These sampling techniques were applied for each of the PMED models calibrated in this study. Both jackknifing and bootstrapping sampling techniques provided a range for the calibration coefficients. The range of adjusted coefficients was wider when the bootstrapping technique was utilized, potentially due to the differences in sample size (e.g., 1000 bootstrap sample versus 25 jackknife sample for AC over AC sections). The width of the range is dependent on variability in the measured distress data across the pavement sections. Since the bootstrapping technique omits several sections and creates multiple copies of others for

each of the 1000 samples, a large variation in distresses from project to project will generate a wide range of calibration coefficients. For example, the range for the transverse cracking model coefficient  $C_4$  using the bootstrapping technique was 260–269 for AC over AC sections and 830–1120 for AC over JPCP sections. The wide range in  $C_4$  for AC over JPCP sections is due to the presence of high variability in measured data (a standard deviation of 200 ft/mile for AC over AC sections and 530 ft/mile for AC over JPCP sections). For such instances, the TOST could be conducted with a factorial of coefficient combinations within the range, and the combination that generates the minimum equivalence margin could be selected.

### **6.2.2 Equivalence testing**

The automated calibration technique conducts a paired  $t$ -test and the TOST. Although the traditional paired  $t$ -test can confirm differences between two datasets, it cannot support agreement among them. The TOST can establish equivalence between two sets of data for a predetermined margin. Since no equivalence margins have been established for any PMED models, this study conducted TOST repeatedly for the calibrated model to identify an equivalence margin. For example, the paired  $t$ -test was conducted for the permanent deformation model for AC over AC sections after local calibration and the null hypothesis could not be rejected. Thus, no evidence showed that the predicted and measured rutting were different after calibration. However, the agreement between measured and predicted rutting could not be established from the paired  $t$ -test. Additionally, no information could be confirmed as to how close or how far off the predictions would be from the field measured rutting. The TOST was then performed multiple times, and an equivalence margin of 30 mils was found to be the narrowest. The conclusion was made that calibrated rutting model predictions and measured rutting in the field were equivalent for a margin of 30 mils.

The repeated TOST was conducted for each of the PMED models calibrated in this study, and the equivalence margin was established in each case. Based on the sampling technique, however, this margin varied slightly. The split sampling and jackknifing method for the transverse cracking model for AC over AC sections resulted in the narrowest  $\delta$  of 55 ft/mile, whereas the bootstrapping technique demonstrated the narrowest  $\delta$  of 53 ft/mile.

### **6.3 Recommendations and Needs for Future Research**

This study calibrated PMED prediction models for AC overlays to Kansas conditions. The following recommendations would improve PMED prediction accuracy:

- The agency must ensure more accurate data for pavement layer material properties (i.e., HMA, concrete, subbase, and soil properties) to improve accuracy of local calibration. Typical HMA overlay mixes should be characterized using the dynamic modulus test and the dynamic shear rheometer (DSR) test. Actual modulus values for stabilized and aggregate bases should be determined from field sampling and laboratory testing.
- In this study, all load-related cracking was considered to be top-down cracking data; however, bottom-up fatigue cracking can be present in AC pavements with high traffic levels, especially in later stages of pavement life (Brink, 2015). For future calibration efforts, full-depth pavement cores should be collected to investigate the origin of crack propagation. Furthermore, the top-down cracking model should be recalibrated once the updated model developed under the NCHRP 1-52 study is added to the PMED software. In addition, the automated technique must be upgraded to accommodate for the updated top-down cracking model.
- Both AC and JPCP rehabilitated pavement sections exhibited significant transverse cracking. Since thermal cracks and reflective cracks could not be distinguished from each



other, the transverse cracking model was calibrated by adjusting reflection cracking model coefficients only for AC and JPCP rehabilitated sections. Global factors were used for the thermal cracking model, and the nationally calibrated model did not predict thermal cracking for any of these sections. The transverse cracking model should be recalibrated once the thermal cracking model for new flexible pavements is conducted. Furthermore, the creep compliance test and the indirect tensile strength test should be conducted for typical AC overlay mixes to characterize low-temperature cracking behavior.

- One of the primary components leading to the standard error of a PMED model is related to measurement errors associated with distress or smoothness measurements in the field (AASHTO, 2010). Prediction accuracy of the calibrated model often decreases due to high variability in the measured data. Distress measurements and data collection systems must be consistent for local calibration of the PMED models. Since use of manual distress survey data yielded high variability across projects, especially in fatigue cracking data, the fatigue cracking model should be periodically recalibrated with updated performance data.
- The automated technique developed in this study cannot calibrate parameters that require multiple simulations of the PMED software. For AC overlays, the  $\beta_{2r}$  and  $\beta_{3r}$  coefficients of the permanent deformation model and the thermal cracking model cannot be calibrated using this application. Wojtkiewicz et al. (2010) used the DAKOTA software and the Cygwin package to run PMED models numerous times outside of the AASHTOWare environment to investigate the effect of variability in HMA mixes on pavement performance prediction. The automated calibrated technique developed in this study could be integrated into the DAKOTA and Cygwin package to automate PMED model calibrations that require multiple PMED simulation.

- This study conducted the TOST to calibrate PMED models with an equivalence margin concept. Prior to this study, the TOST had not been used for equivalence testing between AASHTOWare PMED software-predicted data and field-measured data. This study also utilized a heuristic method to determine the narrowest equivalence margin for the calibrated PMED models. Further research must be conducted to establish a realistic equivalence region for different distress types and models. PMED models then should be calibrated to achieve the equivalence margin.
- The optimization technique employed in this study searches for a global optimum value for the calibration parameter for which the objective function (SSE) value is the smallest. While looking for the optimum model coefficient, unrealistic values for calibration parameters may be obtained, potentially minimizing the SSE but may not make sense from an engineering point of view. Limited study has been conducted until now to identify lower and upper bounds of PMED model coefficients beyond realistic predictions. Further research is needed to establish typical bounds for these calibration parameters.
- This study used the CG and L-BFGS optimization techniques to adjust PMED model parameters. Researchers previously have often used GRG and GA optimization techniques for PMED calibration coefficients (Kim et al., 2011; Ayed et al., 2015). Other robust optimization techniques, such as derivative-free methods and multi-objective and multi-constrained search strategies, may be implemented to determine best possible calibration coefficients for the PMED models



## References

- AASHTO. (1993). "AASHTO Guide for Design of Pavement Structures," American Association of State Highway and Transportation Officials, Vol. 1, AASHTO.
- AASHTO. (2008). "Mechanistic-empirical pavement design guide: A manual of practice," Interim edition, American Association of State Highway and Transportation Officials, Washington, DC.
- AASHTO. (2010). "Guide for the Local Calibration of the Mechanistic-Empirical Pavement Design Guide," American Association of State Highway and Transportation Officials, Washington, D.C.
- AASHTO. (2015). "Mechanistic-Empirical Pavement Design Guide: A Manual of Practice," American Association of State Highway and Transportation Officials, Washington, D.C.
- AASHTO PP 67-16. (2016). "Quantifying Cracks in Asphalt Pavement Surfaces from Collected Images Utilizing Automated Methods," American Association of State Highway and Transportation Officials, Washington, D.C.
- AASHTO PP 68-14. (2016). "Collecting Images of Pavement Surfaces for Distress Detection," American Association of State Highway and Transportation Officials, Washington, D.C.
- AASHTO Pavement ME Nationals Users Group Meetings. (2017). Technical Report: Second Annual Meeting-Denver, Colorado.
- Abdullah, A.Q. (2015). "Development of a Simplified Flexible Pavement Design Protocol for New York State Department of Transportation based on AASHTOWare ME Pavement Design Guide," Ph.D. Dissertation, the University of Texas at Arlington, Arlington, Texas.

- Ahn, S., Kandala, S., Uzan, J., & El-Basyouny, M. M. (2009). "Comparative Analysis of Input Traffic Data and MEPDG Output for Flexible Pavements in State of Arizona," No. 09-2875, Transportation Research Board 88<sup>th</sup> Annual Meeting, Washington, D.C.
- Adams, B. M., Ebidia, S., Eldred, M. S., Geraci, G., Jakeman, J. D., Manupin, K. A.,... and Rushdi, A. (2018). "DAKOTA, a multilevel parallel object-oriented framework for design optimization, parameter estimation, uncertainty quantification, and sensitivity analysis: version 5.0 user's manual," Sandia National Laboratories, Tech. Rep. SAND 2014-4633.
- Ayed, A., & Tighe, S. (2015). "Local Calibration for Mechanistic-Empirical Design Using Genetic Algorithm," Proceedings of the 2015 Conference and Exhibition of the Transportation Association of Canada, Charlottetown PEI, Canada.
- Ayyala, D., Lee, H. S., & Von Quintus, H. (2017). "Damage Characterization in Existing Asphalt Layer Concrete for ME Rehabilitation Design," No. 17-06222, Presented at 97th Annual Meeting of Transportation Research Board, Washington, D.C., 2017.
- Bech, N. (2018). "Use of Falling Weight Deflectometer Testing in the Pavement ME AC/AC Overlay Design Procedure," Doctoral dissertation, University of Pittsburgh, Pittsburgh, Pennsylvania.
- Brink, W. C. (2015). "Use of statistical resampling techniques for the local calibration of the pavement performance prediction models," Doctoral Dissertation, Michigan State University, Lansing, Michigan.
- Buch, N., & Jahangirnejad, S. (2008). "Quantifying coefficient of thermal expansion values of typical hydraulic cement concrete paving mixtures," Report No. RC-1503, Construction and Technology Division, Michigan. Dept. of Transportation, Lansing, Michigan.
- Buch, N., Haider, S. W., Brown, J., & Chatti, K. (2009). "Characterization of truck traffic in Michigan for the new mechanistic empirical pavement design guide," Report No. RC-

1537, Construction and Technology Division, Michigan. Dept. of Transportation, Lansing, Michigan.

Buch, N., Chatti, K., Haider, S. W., Baladi, G., Brink, W., & Harsini, I. (2013). "Preparation for Implementation of the Mechanistic-Empirical Pavement Design Guide in Michigan Part 2: Evaluation of Rehabilitation Fixes," Report No. RC-1594, Michigan. Dept. of Transportation, Lansing, Michigan.

Ceylan, H., Kim, S., Gopalakrishnan, K., and Smadi, O. (2009). "MEPDG Work Plan Task No. 8: Validation of Pavement Performance Curves for the Mechanistic-Empirical Design Guide," CTRE Project 06-274, Center for Transportation Research and Education, Iowa State University, Ames, Iowa.

Ceylan, H., Kim, S., Gopalakrishnan, K., and Ma, D. (2013). "Iowa Calibration of MEPDG Performance Prediction Models," InTrans Project 11-401, Iowa Department of Transportation, Ames, Iowa.

Ceylan, H., Kim, S., Kaya, O., and Gopalakrishnan, K., Ma, D. (2015). "Investigation of AASHTOWare Pavement ME Design/DARWin-ME Performance Prediction Models for Iowa Pavement Analysis and Design," InTrans Project 14-496, Iowa Department of Transportation, Ames, Iowa.

Construction Field Service Division. (2017) "Michigan DOT User Guide for Mechanistic-Empirical Pavement Design," Interim Edition, Michigan. Dept. of Transportation, Lansing, Michigan.

Darter, M. I., Titus-Glover, L., Von Quintus, H., Bhattacharya, B. B., and Mallela, J. (2014). "Calibration and Implementation of the AASHTO Mechanistic-Empirical Pavement Design Guide in Arizona," No. FHWA-AZ-14-606, Arizona Department of Transportation Research Center, Phoenix, Arizona.

- Duan, Q., Sorooshian, S., & Gupta, V. (1992). "Effective and efficient global optimization for conceptual rainfall-runoff models," *Water resources research*, 28(4), pp. 1015-1031
- Federal Highway Administration. (2016). "Traffic Monitoring Guide," U.S. Department of Transportation, Federal Highway Administration, Washington, DC.
- Fernández, B. (2016). "Automated calibration for numerical models of riverflow," Master's thesis, Institute for Modeling Hydraulic and Environmental Systems, University of Stuttgart, Stuttgart, Germany.
- Haas, R., & Hudson, W. R. (2015). "Pavement asset management," John Wiley & Sons, Hoboken, New Jersey.
- Haider, S. W., Buch, N., Chatti, K., & Brown, J. (2011). "Development of Traffic Inputs for Mechanistic–Empirical Pavement Design Guide in Michigan," *Transportation Research Record: Journal of the Transportation Research Board*, Volume 2256, Issue 1, pp. 179-190.
- Haider, S. W., Buch, N., Brink, W., Chatti, K., & Baladi, G. (2014). "Preparation for Implementation of the Mechanistic-Empirical Pavement Design Guide in Michigan Part 3: Local Calibration and Validation of Performance Models," Report No. RC-1595, Michigan. Dept. of Transportation, Lansing, Michigan.
- Huang, Y. H. (1993). "Pavement analysis and design," Englewood Cliffs, New Jersey, Prentice-Hall, Inc.
- Hunter, J. D. (2007). "Matplotlib: A 2D graphics environment," *Computing in Science and Engineering*, 9(3), 90–95.
- Islam, S., Sufian, A., and Hossain, M. (2017). "Effect of Treated Subgrade Layer on Mechanistic-Empirical Pavement Design," *Proceedings of the 10<sup>th</sup> International Conference on the Bearing Capacity of Roads, Railways and Airfields*, Athens, Greece.

- Islam, S., Sufian, A., Hossain, M., Miller, R., and Leibrock, C. (2018). "Mechanistic-Empirical Design of Perpetual Pavement, "Road Materials and Pavement Design, 1-14.
- Islam, S., Hossain, M., Jones, C., Bose, A., Barret, R., and Velasquez, N. (2019). "Implementation of AASHTOWARE Pavement Me Design Software for Asphalt Pavements in Kansas," Transportation Research Record: Journal of the Transportation Research Board, Volume 2673, Issue 4, pp. 490-499.
- Islam, S., Sufian, A., Hossain, M., Velasquez, N., and Barrett, R. (2019). "Practical Issues in Local Calibration and Implementation of AASHTOWare Pavement ME Design Procedure for Concrete Pavements," Journal of Transportation Engineering, Part B: Pavements, volume 145, issue 3, p.04019020.
- Islam, S., Hossain, M., and Jones, C. (2019). "Effect of Concrete Mixture and Strength Properties on Concrete Pavement Design," Proceedings of the International Airfield and Highway Pavements Conference, Chicago, Illinois.
- Jones, E., Oliphant, T., Peterson, P., & others. (2001). "SciPy: Open source scientific tools for Python," Retrieved from "<http://www.scipy.org/>"
- Khazanovich, L., & Gotlif, A. (2003). "Evaluation of joint and crack load transfer final report," No. FHWA-RD-02-088, Office of Infrastructure Research and Development, Federal Highway Administration, McLean, Virginia.
- Khanum, T. (2005). "Kansas Rigid Pavement Analysis Following New Mechanistic-Empirical Design Guide," Master's Thesis, Kansas State University, Manhattan, Kansas.
- Kim, Y. R., Jadoun, F. M., Hou, T., and Muthadi, N. (2011). "Local calibration of the MEPDG for flexible pavement design," No. FHWA\ NC\ 2007-07, NC Department of Transportation Research and Analysis Group, North Carolina Department of Transportation, Raleigh, North Carolina.



- Kutay, M. E., & Jamrah, A. (2013). "Preparation for implementation of the mechanistic-empirical pavement design guide in Michigan: part 1-HMA mixture characterization," Report No. RC-1593, Michigan. Dept. of Transportation, Lansing, Michigan.
- Lakens, D. (2017). "Equivalence tests: a practical primer for t tests, correlations, and meta-analyses," *Social psychological and personality science*, No. 8(4), 355-362, doi: [10.1177/1948550617697177](https://doi.org/10.1177/1948550617697177)
- Laurent, J., Herbert, J. F. and Talbot, M. (2017). "Using full lane 3D road texture data for the automatic detection of sealed Cracks, bleeding and raveling," *Proceedings of the World Conference on Pavement and Asset Management*, Milan, Italy.
- Laurent, J., Lefebvre, D., and Samson, E. (2008). "Development of a New 3D Transverse Profiling System for the Automatic Measurement of Road Cracks," *6th Symposium on Pavement Surface Characteristics*, Portoroz, Slovenia.
- Li, J., Pierce, L., Hallenbeck, M., & Uhlmeyer, J. (2009). "Sensitivity of axle load spectra in the mechanistic-empirical pavement design guide for Washington state," *Transportation Research Record: Journal of the Transportation Research Board*, Issue 2093, pp. 50-56.
- Li, Q., Xiao, D. X., Wang, K. C., Hall, K. D., and Qiu, Y. (2011). "Mechanistic-Empirical Pavement Design Guide (MEPDG): a bird's-eye view," *Journal of Modern Transportation*, 19(2), pp.114-133.
- Lytton, R. L., Tsai, F. L., Lee, S. I., Luo, R., Hu, S., & Zhou, F. (2010). "NCHRP Report 669: Models for Predicting Reflection Cracking of Hot-Mix Asphalt Overlays." *Transportation Research Board of the National Academies*, Washington, DC
- Madsen, H. (2000). "Automatic calibration of a conceptual rainfall-runoff model using multiple objectives," *Journal of hydrology*, 235(3-4), pp. 276-288.

Mallela, J., Titus-Glover, L., Quintus, H. V., Darter, M. I., Stanley, M., Rao, C., and Sadasivam, S. (2009). "Implementing the AASHTO mechanistic-empirical pavement design guide in Missouri volume I: study findings, conclusions, and recommendations," MODOT Study No. RI04-002, Missouri Department of Transportation, Jefferson City, Missouri.

Mallela, J., Titus-Glover, L., Quintus, H. V., Darter, M. I., Stanley, M., and Rao, C. (2009). "Implementing the AASHTO mechanistic-empirical pavement design guide in Missouri volume II: MEPDG model validation and calibration," MODOT Study No. RI04-002, Missouri Department of Transportation, Jefferson City, Missouri.

Mallela, J., Titus-Glover, L., Sadasivam, S., Bhattacharya, B., Darter, M., and Von Quintus, H. (2013). "Implementation of the AASHTO mechanistic-empirical pavement design guide for Colorado," No. CDOT-2013-4, Colorado Department of Transportation – Research, Denver, Colorado.

McKinney, W. (2012). "Python for data analysis: Data wrangling with Pandas, NumPy, and IPython, " O'Reilly Media, Inc.

Mokhtari, A., & Ribeiro, A. (2014). "RES: Regularized stochastic BFGS algorithm," IEEE Transactions on Signal Processing, 62(23), pp. 6089-6104.

Momin, S. A. (2011). "Local Calibration of Mechanistic Empirical Pavement Design Guide for North Eastern United States," Master's Thesis, the University Of Texas at Arlington, Arlington, Texas.

Muthadi, N.R. and Kim, Y. R. (2008). "Local Calibration of Mechanistic Empirical Pavement Design Guide for Flexible Pavement Design," Transportation Research Record: Journal of the Transportation Research Board, Issue 2087, pp.131-141.

Nisbet, R., Elder, J., and Miner, G. (2009). "Handbook of statistical analysis and data mining applications," Academic Press, Canada.

NCHRP. (2004). "Guide for Mechanistic-Empirical Design of New and Rehabilitated Pavement Structures," Final Report for Project 1-37A, National Cooperative Highway Research Program, Transportation Research Board, National Research Council, Washington, D.C.

NCHRP. (2009). "Local Calibration Guidance for the Recommended Guide for Mechanistic-Empirical Design of New and Rehabilitated Pavement Structures," NCHRP 1-40B, Final Report, National Cooperative Highway Research Program, Washington, DC.

NCHRP. (2014). "Implementation of the AASHTO Mechanistic-Empirical Pavement Design Guide and Software," NCHRP Synthesis 457, A Synthesis of Highway Practice, Transportation Research Board of the National Academics, Washington, DC.

Oliphant, T. E. (2006). "A guide to NumPy (Vol. 1)," Trelgol Publishing, USA.

Pavement Interactive. (2012). "What Is Mechanistic-Empirical Design? – The MEPDG and You," Retrieved from <https://www.pavementinteractive.org/what-is-mechanistic-empirical-design-the-mepdg-and-you/>

Pedregosa, F., Varoquaux, G., Gramfort, A., Michel, V., Thirion, B., Grisel, O.,... and Vanderplas, J. (2011). "Scikit-learn: Machine learning in Python," Journal of machine learning research, 12(Oct), 2825-2830.

Rahman, M. M., Uddin, M. M., & Gassman, S. L. (2017). "Pavement performance evaluation models for South Carolina," KSCE Journal of Civil Engineering, No. 21(7), 2695-2706.

Rao, C., Titus-Glover, L., Bhattacharya, B., Darter, M. I., Stanley, M., & Von Quintus, H. L. (2012). "Estimation of key PCC, base, subbase, and pavement engineering properties from routine tests and physical characteristics," Report No. FHWA-HRT-12-030, Office of

- Infrastructure Research and Development, Federal Highway Administration, McLean, Virginia.
- Rao, C., Titus-Glover, L., Bhattacharya, B., and Darter, M. I. (2012). “User’s Guide: Estimation of key PCC, base, subbase, and pavement engineering properties from routine tests and physical characteristics,” Report No. FHWA-HRT-12-031, Office of Infrastructure Research and Development, Federal Highway Administration, McLean, Virginia.
- Rao, C., and Von Quintus, H. L. (2015). “TRB Webinar - Determination of In-Place Elastic Layer Modulus: Backcalculation Methodology and Procedures.” Transportation Research Board Standing Committee on Pavement Structural Modeling and Evaluation, Washington, DC.
- Robbins, M. M., Rodezno, C., Tran, N., and Timm, D. (2017). “Pavement ME Design—A Summary of Local Calibration Efforts for Flexible Pavements,” NCAT Report No.17-07, National Center for Asphalt Technology, Auburn, Alabama.
- Romanoschi, S., Momin, S., Bethu, S., and Bendana, L. (2011). “Development of traffic inputs for new mechanistic-empirical pavement design guide: Case study,” Transportation Research Record: Journal of the Transportation Research Board, Issue 2256, pp. 142-150.
- Shewchuk, J. R. (1994). “An introduction to the conjugate gradient method without the agonizing pain,” School of Computer Science, Carnegie Mellon University, Pittsburgh, Pennsylvania.
- Sufian, A. (2016). “Local Calibration of Mechanistic Empirical Pavement Design Guide for Kansas,” M.S. Thesis, Kansas State University, Manhattan, Kansas.
- Sun, X., Han, J., Parsons, R. L., Misra, A. and Thakur, J. (2015) “Calibrating the Mechanistic-Empirical Pavement Design Guide for Kansas. Report No.: KS-14-17, Kansas Department of Transportation, Topeka, Kansas.

- Tam, W. and Von Quintus, H. (2003). "Use of long-term pavement performance data to develop traffic defaults in support of mechanistic-empirical pavement design procedures," *Transportation Research Record: Journal of the Transportation Research Board*, Issue 1855, pp. 176-182.
- Titus-Glover, L., Bhattacharya, B. B., Raghunathan, D., Mallela, J., & Lytton, R. L. (2016). "Adaptation of NCHRP Project 1-41 Reflection Cracking Models for Semirigid Pavement Design in AASHTOWare Pavement ME Design." *Transportation Research Record, Journal of the Transportation Research Board*, Issue 2590, No. 1, pp. 122-131.
- Tran, N., Robbins, M. M., Rodezno, C., and Timm, D. (2017). "Pavement ME Design—Impact of Local Calibration, Foundation Support, and Design and Reliability Thresholds," NCAT Report No.17-08, National Center for Asphalt Technology, Auburn, Alabama.
- Transportation Works for Kansas. (2011). Retrieved from <http://tworks.ksdot.org/Investments>.
- Von Quintus, H. L., & Moulthrop, J. S. (2007). "Mechanistic-Empirical Pavement Design Guide Flexible Pavement Performance Prediction Models for Montana--Volume I Executive Research Summary," No. FHWA/MT-07-008/8158-1, Helena, Montana.
- Von Quintus, H. L. (2016). "TRB Webinar –Reflective Cracking Integration into Pavement Design." *Transportation Research Board Standing Committee on Pavement Rehabilitation*, Washington, DC.
- Walker, E., & Nowacki, A. S. (2011). "Understanding equivalence and noninferiority testing," *Journal of general internal medicine*, 26(2), pp. 192-196.
- Wargo, A., Islam, S., & Kim, R. (2014). "The Reflective Cracking Tester: A Third-Scale Accelerated Pavement Tester for Reflective Cracking," *Proceedings of the 12<sup>th</sup> conference of International Society on Asphalt Pavements*, Raleigh, North Carolina.

- Williams, R. C., & Shaidur, R. (2013). "Mechanistic-empirical pavement design guide calibration for pavement rehabilitation" Final Report No. SPR 718, Research Section, Oregon. Dept. of Transportation, Salem, Oregon.
- Wojtkiewicz, S. F., Khazanovich, L., Gaurav, G., & Velasquez, R. (2010). "Probabilistic numerical simulation of pavement performance using MEPDG" Road Materials and Pavement Design, No. 11(2), pp. 291-306.
- Wu, Z., and Yang, X. (2012). "Evaluation of current Louisiana flexible pavement structures using PMS data and new mechanistic-empirical pavement design guide," No. FHWA/LA. 11/482, Louisiana Department of Transportation and Development, Baton Rouge, Louisiana.
- Wu, Z., & Xiao, D. X. (2016). "Development of DARWin-ME Design Guideline for Louisiana Pavement Design," No. FHWA/LA. 11/551, Louisiana Department of Transportation and Development, Baton Rouge, Louisiana.
- Yapo, P. O., H. V. Gupta, and S. Sorooshian. (1998). Multi-objective global optimization for hydrologic models. *Journal of hydrology*, 1998. Volume: 204(1-4), pp: 83-97.
- Ziedan, A. (2017). "Comparative analysis between MERRA and updated MEPDG climate database in the state of Tennessee," M.S. Thesis, University of Tennessee at Chattanooga, Chattanooga, Tennessee.

## Appendix A - AASHTOWare Traffic Inputs

Table A-1: Hourly Distribution Factors

Hour	Automatic Vehicle Class Stations										
	CTQ1D1	0DT453	7XRME7	61HLJ3	91TFY5	AW9N83	CV64B3	F10VD5	9LON61	9Q9OK1	7HOM63
0	1.55	2.25	2.03	1.17	1.65	1.69	1.47	1.30	0.79	1.07	1.94
1	1.31	1.97	1.64	0.88	1.25	1.66	1.12	1.13	0.52	0.85	1.60
2	1.19	1.88	1.78	0.81	1.28	1.78	1.06	1.23	0.46	0.80	1.56
3	1.20	1.95	1.83	0.84	1.42	2.17	1.04	1.61	0.57	0.86	1.67
4	1.35	2.09	2.11	1.11	1.58	2.95	1.17	2.19	1.24	1.29	1.83
5	2.08	2.35	2.53	1.69	1.93	3.55	1.46	2.56	2.51	2.25	2.25
6	3.36	2.63	3.17	2.72	2.74	4.27	3.02	3.41	5.29	4.40	2.93
7	4.57	3.37	3.94	4.50	3.91	4.99	4.25	4.78	7.30	7.25	3.82
8	5.68	4.37	5.38	5.32	5.43	6.09	5.48	5.76	5.48	6.65	5.08
9	6.47	4.88	6.43	6.11	6.00	7.05	5.83	6.92	4.84	6.02	6.13
10	7.02	5.08	6.44	6.53	6.26	7.11	6.30	7.35	4.82	6.12	6.39
11	7.08	5.47	6.24	6.41	6.45	6.63	7.23	7.43	5.19	6.40	6.37
12	6.87	5.99	6.36	6.40	6.30	6.31	7.71	7.10	5.53	6.65	6.33
13	6.82	6.29	6.22	6.63	6.52	6.20	7.60	6.96	5.77	6.71	6.30
14	6.71	6.26	6.07	6.97	6.60	5.69	7.27	6.66	6.30	7.10	6.19
15	6.52	6.35	5.87	7.15	6.55	5.15	6.76	6.11	7.71	7.08	6.18
16	6.01	6.38	5.58	7.18	6.40	4.86	7.00	5.68	8.55	6.79	5.98
17	5.29	6.18	5.45	6.81	5.99	4.47	5.77	4.95	8.38	6.33	5.82
18	4.57	5.63	4.91	5.63	5.21	3.89	4.63	4.20	5.69	4.47	5.26
19	3.94	4.85	4.10	4.61	4.52	3.26	3.87	3.53	4.07	3.13	4.40
20	3.24	4.28	3.60	3.69	4.04	3.00	3.35	2.92	3.33	2.56	3.74
21	2.87	3.75	3.08	2.97	3.22	2.79	2.78	2.48	2.66	2.12	3.11
22	2.42	3.06	2.70	2.23	2.63	2.43	2.10	2.00	1.79	1.70	2.73
23	1.88	2.69	2.54	1.66	2.10	2.05	1.72	1.73	1.22	1.39	2.41

Table A-2: Vehicle Class Factors

Class	Automatic Vehicle Class Stations										
	CTQ1D1	0DT453	7XRME7	61ILJ3	91TFY5	AW9N83	CV64B3	F10VD5	9LON61	9Q9OK1	7HOM63
4	0.55	0.84	0.80	52.05	7.40	2.01	9.16	0.75	86.71	0.86	0.84
5	4.27	2.92	5.42	10.85	10.17	3.57	5.31	5.60	2.89	12.12	5.59
6	3.36	1.26	3.26	1.10	1.72	2.63	10.94	4.55	1.87	10.65	3.21
7	0.34	0.81	0.55	2.49	1.16	0.19	0.33	0.48	2.40	1.58	0.78
8	6.64	3.87	5.28	2.34	16.54	5.80	6.02	5.62	1.29	9.17	5.50
9	79.07	77.45	74.90	1.76	57.49	78.41	64.91	77.01	1.82	62.34	72.53
10	4.14	1.00	1.80	7.03	3.08	1.42	1.57	1.37	2.65	1.37	2.21
11	0.49	6.27	5.53	21.19	0.86	5.43	0.25	3.66	0.34	1.35	6.98
12	0.65	3.59	2.22	1.16	0.43	0.27	0.19	0.76	0.03	0.26	2.15
13	0.49	1.99	0.25	0.05	1.15	0.28	1.32	0.20	0.01	0.29	0.21

Table A-3: Monthly Adjustment Factors for AVC Station 0DT453

Month	Class 4	Class 5	Class 6	Class 7	Class 8	Class 9	Class 10	Class 11	Class 12	Class 13
January	0.68	0.57	0.95	0.51	0.57	0.92	0.62	0.95	0.93	0.75
February	0.64	0.58	0.99	0.59	0.61	0.96	0.86	0.93	0.93	0.79
March	0.82	0.76	0.85	0.73	0.72	1.01	0.85	0.99	0.99	0.88
April	0.86	0.86	0.97	0.81	0.91	1.03	1.06	1.07	1.08	0.93
May	0.93	1.13	0.93	1.24	1.14	1.02	0.97	1.00	0.98	1.09
June	1.29	1.50	1.00	1.61	1.38	1.03	1.33	0.99	0.99	1.19
July	1.44	1.60	1.16	1.58	1.41	1.07	1.30	1.08	1.02	1.32
August	1.27	1.28	1.07	1.27	1.30	1.03	1.08	0.93	1.04	1.26
September	1.20	1.09	1.20	1.18	1.24	1.06	1.08	1.02	1.04	1.29
October	1.00	1.07	1.02	1.09	1.02	1.01	0.94	0.99	1.03	1.19
November	0.95	0.83	0.89	0.74	0.80	0.95	1.00	1.03	1.01	0.79
December	0.92	0.71	0.98	0.65	0.90	0.91	0.91	1.02	0.95	0.52



Table A-4: Monthly Adjustment Factors for AVC Station 7XRME7

Month	Class 4	Class 5	Class 6	Class 7	Class 8	Class 9	Class 10	Class 11	Class 12	Class 13
January	0.99	0.88	0.94	0.71	0.81	1.04	0.98	1.05	1.07	0.79
February	1.03	0.82	0.79	0.62	1.05	1.03	0.90	1.06	1.02	0.66
March	1.18	0.95	0.94	0.93	1.04	1.04	1.04	1.11	1.15	0.96
April	1.16	1.15	1.68	0.96	1.29	1.15	1.30	1.11	1.22	1.13
May	1.27	1.16	0.95	1.19	1.22	1.05	1.03	1.07	1.10	1.18
June	1.03	1.29	1.21	1.46	1.39	1.07	1.12	1.05	0.99	1.67
July	1.01	1.19	1.02	1.50	1.07	1.05	0.86	1.11	0.93	1.22
August	0.86	1.11	1.03	1.28	0.99	1.00	0.94	1.01	0.87	0.85
September	0.43	0.53	0.44	0.63	0.45	0.43	0.65	0.28	0.15	0.58
October	1.12	1.13	1.01	1.12	1.09	1.11	1.02	1.19	1.32	1.48
November	0.94	0.92	0.94	0.88	0.83	1.02	1.14	1.01	1.18	0.67
December	0.99	0.88	1.05	0.73	0.77	1.00	1.02	0.94	1.01	0.79

Table A-5: Monthly Adjustment Factors for AVC Station 61ILJ3

Month	Class 4	Class 5	Class 6	Class 7	Class 8	Class 9	Class 10	Class 11	Class 12	Class 13
January	0.89	0.93	0.95	0.79	0.75	0.86	1.05	0.99	1.03	0.65
February	0.84	0.87	0.94	0.78	0.72	0.89	1.04	1.01	0.91	0.60
March	1.03	1.00	1.01	0.96	0.93	1.11	0.98	1.03	1.16	1.62
April	1.06	1.01	1.03	1.04	1.03	1.19	0.92	1.02	1.14	1.25
May	1.06	1.03	1.04	1.08	1.06	0.96	0.88	1.03	1.11	0.78
June	1.06	1.05	1.09	1.11	1.03	0.95	0.93	0.96	0.95	0.98
July	1.10	1.05	1.07	1.19	1.07	0.99	0.99	0.93	0.91	1.01
August	0.99	1.00	1.02	1.09	1.33	1.05	0.97	0.96	0.97	0.81
September	0.96	1.07	1.10	1.14	1.19	1.17	1.25	1.00	0.95	1.21
October	1.00	1.05	1.04	1.08	1.03	1.11	1.07	1.01	1.00	0.79
November	1.00	1.01	0.92	0.94	1.10	0.89	0.96	1.02	0.97	1.28
December	1.02	0.96	0.79	0.82	0.77	0.82	0.95	1.02	0.90	1.02

Table A-6: Monthly Adjustment Factors for AVC Station 91TFY5

Month	Class 4	Class 5	Class 6	Class 7	Class 8	Class 9	Class 10	Class 11	Class 12	Class 13
January	1.06	1.28	1.36	0.36	1.02	1.35	1.16	1.24	1.06	0.82
February	1.18	1.24	1.42	0.39	0.94	1.33	1.05	1.23	0.93	0.77
March	1.58	1.21	1.59	0.45	0.94	1.02	1.87	1.16	1.17	1.04
April	1.70	1.15	1.52	0.45	0.84	0.90	1.92	1.02	1.70	1.31
May	1.25	1.06	0.81	0.43	0.67	0.90	0.73	0.95	0.56	0.89
June	1.22	1.18	0.76	0.45	0.72	0.89	0.59	0.89	0.57	1.04
July	0.84	1.15	0.77	0.44	0.57	0.85	0.68	0.90	0.45	1.09
August	0.43	1.02	0.58	0.37	0.52	0.86	0.65	0.72	0.55	1.42
September	0.66	1.02	0.55	0.40	0.57	0.93	0.64	0.91	0.47	1.27
October	0.87	1.14	0.76	0.48	0.68	0.92	0.67	0.91	0.71	1.35
November	1.10	0.16	0.33	7.49	4.16	0.05	0.32	0.54	2.34	0.26
December	0.12	0.38	1.56	0.30	0.37	2.01	1.74	1.54	1.48	0.74

Table A-7: Monthly Adjustment Factors for AVC Station AW9N83

Month	Class 4	Class 5	Class 6	Class 7	Class 8	Class 9	Class 10	Class 11	Class 12	Class 13
January	1.68	0.77	0.56	0.95	0.57	0.60	0.52	0.71	0.82	0.40
February	2.03	0.86	0.66	0.32	0.70	0.72	0.57	0.98	1.88	0.53
March	2.51	1.44	0.67	0.76	0.67	1.05	0.72	1.13	1.37	0.00
April	0.87	2.71	1.73	3.03	2.07	1.83	1.65	1.38	2.19	2.13
May	1.46	2.02	1.49	1.14	2.02	1.34	1.83	1.35	1.64	1.46
June	0.93	0.90	1.15	0.30	0.98	1.27	1.14	1.32	0.77	1.81
July	0.67	0.90	1.31	1.26	1.31	1.38	1.46	1.30	0.91	2.04
August	0.51	0.79	1.75	1.19	1.15	1.31	1.66	1.34	0.75	1.61
September	0.15	0.41	0.82	0.63	0.70	0.66	0.60	0.66	0.62	0.37
October	0.23	0.48	0.68	0.91	0.92	0.71	0.73	0.69	0.36	0.37
November	0.36	0.36	0.70	0.76	0.67	0.64	0.70	0.64	0.48	0.13
December	0.61	0.36	0.48	0.76	0.24	0.49	0.41	0.50	0.22	1.17

Table A-8: Monthly Adjustment Factors for AVC Station CTQ1D1

Month	Class 4	Class 5	Class 6	Class 7	Class 8	Class 9	Class 10	Class 11	Class 12	Class 13
January	0.54	0.91	0.68	0.97	0.66	0.91	1.05	1.23	0.88	0.58
February	0.68	0.92	0.75	0.72	0.58	0.99	1.16	1.22	0.91	0.56
March	0.93	0.98	1.01	1.11	0.76	1.07	1.42	1.26	1.05	0.80
April	0.67	0.95	0.88	1.18	0.86	1.00	1.14	0.74	0.91	0.64
May	0.64	1.05	1.12	1.03	0.85	1.00	1.39	0.60	1.03	0.77
June	0.83	1.01	1.35	1.59	0.98	1.06	1.15	0.91	1.00	1.26
July	0.78	0.99	1.07	1.47	0.97	1.05	0.96	0.99	0.95	1.26
August	0.54	0.90	0.92	1.54	0.84	1.02	1.02	1.27	1.05	1.60
September	1.67	1.07	1.09	1.13	1.45	0.99	0.72	0.82	1.18	1.29
October	2.13	1.21	1.14	0.37	1.51	1.02	0.61	1.15	1.03	1.09
November	1.38	0.99	1.06	0.53	1.35	0.96	0.68	0.99	1.00	1.04
December	1.22	1.03	0.93	0.37	1.18	0.93	0.71	0.82	1.00	1.12

Table A-9: Monthly Adjustment Factors for AVC Station CV64B3

Month	Class 4	Class 5	Class 6	Class 7	Class 8	Class 9	Class 10	Class 11	Class 12	Class 13
January	2.17	1.02	0.70	0.34	0.79	0.97	2.30	1.81	2.92	1.96
February	2.13	0.90	0.84	0.59	0.83	0.90	0.86	1.75	1.67	1.91
March	1.33	0.95	1.00	1.10	1.01	1.08	0.97	1.46	0.75	1.41
April	0.83	1.32	1.05	1.13	1.02	1.19	1.27	1.25	0.56	1.55
May	0.74	1.28	1.09	0.85	0.91	1.12	1.44	0.68	1.46	1.02
June	0.56	1.00	1.05	1.31	0.77	1.10	0.61	0.16	0.61	0.06
July	0.51	0.86	1.05	0.96	1.11	0.99	0.65	0.18	0.31	0.08
August	0.85	1.02	1.17	0.88	1.37	1.04	0.72	0.29	0.30	0.07
September	0.84	1.12	1.17	1.89	1.09	0.92	1.02	0.62	0.00	0.11
October	0.75	1.00	1.21	1.14	1.39	1.04	0.94	0.79	0.16	0.58
November	0.86	0.84	0.89	0.64	0.97	0.85	0.77	1.51	1.48	1.93
December	0.43	0.71	0.77	1.18	0.74	0.80	0.44	1.50	1.77	1.32

Table A-10: Monthly Adjustment Factors for AVC Station F10VD5

Month	Class 4	Class 5	Class 6	Class 7	Class 8	Class 9	Class 10	Class 11	Class 12	Class 13
January	0.55	0.86	1.02	0.56	0.89	0.88	1.81	0.91	1.15	0.93
February	0.63	0.88	0.84	0.36	0.87	0.92	1.14	0.94	1.03	0.98
March	1.06	0.97	0.92	0.85	0.93	0.97	1.14	1.00	0.91	0.56
April	1.05	1.11	0.92	0.91	1.16	1.06	0.85	1.19	0.98	1.00
May	0.99	1.05	1.09	0.62	1.11	1.04	0.94	1.07	0.90	1.42
June	1.06	0.98	1.11	0.71	1.15	1.07	1.04	1.03	1.06	1.49
July	1.22	0.98	1.01	1.08	1.11	1.04	0.76	1.05	1.14	0.88
August	1.19	0.97	1.07	0.94	1.04	1.00	1.07	0.96	0.96	1.47
September	1.07	1.07	1.20	1.08	1.05	1.02	0.88	1.00	1.04	1.11
October	1.24	1.17	1.17	0.99	0.99	1.10	0.99	1.05	1.04	0.92
November	1.11	0.99	0.91	3.32	0.84	0.93	0.72	0.88	0.85	0.77
December	0.84	0.96	0.75	0.58	0.87	0.97	0.66	0.93	0.95	0.47

Table A-11: Monthly Adjustment Factors for AVC Station 9LON61

Month	Class 4	Class 5	Class 6	Class 7	Class 8	Class 9	Class 10	Class 11	Class 12	Class 13
January	0.96	0.97	0.84	0.77	0.80	0.95	1.01	0.94	0.71	0.70
February	0.96	0.93	0.84	0.76	0.80	0.92	1.00	0.96	0.72	0.80
March	0.97	0.95	0.86	0.82	0.84	0.94	0.99	0.98	0.92	0.83
April	1.03	0.99	1.01	1.04	1.06	0.98	0.99	0.90	1.05	1.11
May	0.97	0.97	0.91	0.88	0.90	0.94	0.98	0.97	0.94	0.87
June	1.03	1.02	1.10	1.18	1.22	1.06	1.02	1.07	1.13	1.03
July	1.02	1.03	1.10	1.17	1.18	1.06	1.02	1.09	1.11	1.00
August	1.02	1.04	1.10	1.16	1.14	1.04	1.01	1.07	1.11	0.99
September	1.01	1.05	1.10	1.15	1.12	1.06	1.02	1.08	1.14	1.00
October	1.01	1.05	1.10	1.14	1.11	1.05	1.01	1.08	1.13	1.09
November	1.01	1.04	1.09	1.11	1.08	1.04	1.00	1.04	1.11	1.13
December	1.01	0.94	0.94	0.81	0.75	0.95	0.96	0.80	0.93	1.45

Table A-12: Monthly Adjustment Factors for AVC Station 9Q9OK1

Month	Class 4	Class 5	Class 6	Class 7	Class 8	Class 9	Class 10	Class 11	Class 12	Class 13
January	0.99	1.18	1.01	0.83	0.91	1.06	0.92	0.94	1.02	1.18
February	1.23	1.39	1.18	1.03	1.14	1.32	1.09	1.21	1.21	1.22
March	1.41	1.47	1.41	1.64	1.35	1.43	1.33	1.37	1.40	1.36
April	1.50	1.75	1.45	1.41	1.47	1.43	1.32	1.42	1.43	1.54
May	1.38	1.68	1.63	1.55	1.54	1.44	1.46	1.58	1.32	1.33
June	1.63	1.42	1.76	1.64	1.75	1.56	1.72	1.59	1.66	1.31
July	1.31	1.08	1.24	1.25	1.31	1.21	1.26	1.25	1.39	0.93
August	0.60	0.43	0.51	0.49	0.57	0.56	0.70	0.64	0.56	0.40
September	0.49	0.46	0.52	0.57	0.59	0.57	0.67	0.59	0.67	0.38
October	0.54	0.45	0.55	0.60	0.55	0.57	0.59	0.60	0.48	0.36
November	0.48	0.37	0.42	0.61	0.46	0.46	0.51	0.47	0.47	0.70
December	0.42	0.33	0.31	0.37	0.37	0.39	0.42	0.34	0.40	1.27

Table A-13: Monthly Adjustment Factors for AVC Station 7HOM63

Month	Class 4	Class 5	Class 6	Class 7	Class 8	Class 9	Class 10	Class 11	Class 12	Class 13
January	0.89	0.77	0.91	0.80	0.74	0.97	1.14	1.04	1.08	0.83
February	1.08	0.83	0.80	1.50	1.00	0.96	1.65	1.61	1.12	0.59
March	1.11	0.85	0.92	1.54	1.01	0.97	1.46	1.37	1.23	0.95
April	1.09	1.01	1.52	1.78	1.21	1.05	1.68	1.41	1.24	1.10
May	1.11	1.01	0.88	0.74	1.07	0.98	0.76	0.76	1.03	1.28
June	0.97	1.22	1.20	1.56	1.31	1.02	1.19	1.08	1.01	1.80
July	0.87	1.05	0.94	0.97	0.94	0.99	0.64	0.80	0.87	1.32
August	0.79	1.04	1.06	0.77	0.91	0.97	0.71	0.75	0.84	1.03
September	0.96	1.29	1.09	0.82	1.04	1.12	0.92	0.83	0.96	0.79
October	1.04	1.11	0.93	0.64	0.97	1.02	0.69	0.81	0.92	1.00
November	1.07	0.93	0.97	0.44	1.01	0.98	0.60	0.75	0.86	0.67
December	1.04	0.88	0.78	0.44	0.79	0.96	0.56	0.80	0.83	0.63

Table A-14: Axle group per vehicle for WIM station 2WOA86

Axle Type	Class 4	Class 5	Class 6	Class 7	Class 8	Class 9	Class 10	Class 11	Class 12	Class 13
Single	2.00	2.08	1.57	0.00	2.35	1.75	2.34	5.00	4.00	5.63
Tandem	0.00	0.46	1.43	0.00	1.47	3.24	2.47	0.00	2.00	2.75
Tridem	0.00	0.04	0.00	0.00	0.00	0.01	1.28	0.00	0.00	2.25
Quad	0.00	0.00	0.00	0.00	0.00	0.00	0.00	0.00	0.00	0.00

Table A-15: Axle group per vehicle for WIM station 3MXC22

Axle Type	Class 4	Class 5	Class 6	Class 7	Class 8	Class 9	Class 10	Class 11	Class 12	Class 13
Single	1.10	2.20	1.15	2.00	2.26	1.46	2.17	5.00	4.04	0.00
Tandem	0.57	0.44	1.85	2.00	1.57	3.54	2.34	0.00	1.96	0.00
Tridem	0.00	0.23	0.00	0.00	0.00	0.00	1.54	0.00	0.00	0.00
Quad	0.00	0.00	0.00	0.00	0.00	0.00	0.00	0.00	0.00	0.00

Table A-16: Axle group per vehicle for WIM station 4LGSU3

Axle Type	Class 4	Class 5	Class 6	Class 7	Class 8	Class 9	Class 10	Class 11	Class 12	Class 13
Single	1.10	2.20	1.15	2.00	2.26	1.46	2.17	5.00	4.04	0.00
Tandem	0.57	0.44	1.85	2.00	1.57	3.54	2.34	0.00	1.96	0.00
Tridem	0.00	0.23	0.00	0.00	0.00	0.00	1.54	0.00	0.00	0.00
Quad	0.00	0.00	0.00	0.00	0.00	0.00	0.00	0.00	0.00	0.00

Table A-17: Axle group per vehicle for WIM station 9M4PS3

Axle Type	Class 4	Class 5	Class 6	Class 7	Class 8	Class 9	Class 10	Class 11	Class 12	Class 13
Single	1.76	2.21	1.16	1.67	2.00	1.36	2.06	5.00	4.06	0.00
Tandem	0.49	0.52	1.84	1.33	1.01	3.63	2.72	0.00	1.94	0.00
Tridem	0.00	0.08	0.00	0.50	0.00	0.00	1.33	0.00	0.00	0.00
Quad	0.00	0.00	0.00	0.67	0.00	0.00	0.00	0.00	0.00	0.00

Table A-18: Axle group per vehicle for WIM station 20PUF5

Axle Type	Class 4	Class 5	Class 6	Class 7	Class 8	Class 9	Class 10	Class 11	Class 12	Class 13
Single	4.64	2.05	1.25	4.00	2.13	1.56	3.58	0.00	4.00	7.00
Tandem	0.36	1.01	1.75	0.00	1.83	3.44	2.22	0.00	2.00	1.33
Tridem	0.00	0.00	0.00	0.00	0.00	0.00	0.36	0.00	0.00	0.50
Quad	0.00	0.00	0.00	0.00	0.00	0.00	0.04	0.00	0.00	0.00

Table A-19: Axle group per vehicle for WIM station 9ORQP1

Axle Type	Class 4	Class 5	Class 6	Class 7	Class 8	Class 9	Class 10	Class 11	Class 12	Class 13
Single	2.075	2.11	1.289	1.789	2.294	1.875	2.33	5	4	0
Tandem	0.402	0.345	1.715	0.684	1.507	3.089	1.961	0	2	0
Tridem	0	0.282	0	0.632	0	0.036	1.589	0	0	0
Quad	0	0	0	1.263	0	0	0.235	0	0	0

Table A-20: Axle group per vehicle for WIM station 9Q9OK1

Axle Type	Class 4	Class 5	Class 6	Class 7	Class 8	Class 9	Class 10	Class 11	Class 12	Class 13
Single	4.607	2.019	1.301	1.634	2.327	1.358	1.7	5	6	7
Tandem	1.607	0.345	1.699	0.295	1.436	3.661	2	0	0	0
Tridem	0	0.01	0	1.524	0	0.003	1.9	0	0	0
Quad	0	0	0	0.984	0	0	0.4	0	0	0

Table A-21: Axle group per vehicle for WIM station BWGAA6

Axle Type	Class 4	Class 5	Class 6	Class 7	Class 8	Class 9	Class 10	Class 11	Class 12	Class 13
Single	2.494	2.146	1.455	2	2.297	1.708	2.857	5	1.588	0.772
Tandem	0.501	0.659	1.545	2	1.576	3.269	2	0	4.412	0.913
Tridem	0	0.016	0	0	0	0.023	1	0	0	0
Quad	0	0	0	0	0	0	0.571	0	0	0

Table A-22: Axle group per vehicle for WIM station DVMSP3

Axle Type	Class 4	Class 5	Class 6	Class 7	Class 8	Class 9	Class 10	Class 11	Class 12	Class 13
Single	1.877	2.179	1.45	2.182	2.275	1.529	2.264	5	4.378	4.412
Tandem	0.359	0.582	1.549	1.454	1.543	3.465	2.189	0	1.623	3.422
Tridem	0.01	0.013	0	0.545	0	0.006	1.415	0	0	0
Quad	0	0	0	0	0	0	0.226	0	0	0

Table A-23: Axle group per vehicle for WIM station F07WC7

Axle Type	Class 4	Class 5	Class 6	Class 7	Class 8	Class 9	Class 10	Class 11	Class 12	Class 13
Single	0	1.943	1.273	1.727	2.33	1.185	1.92	5	4	6.3
Tandem	0	0.582	1.727	0.363	1.4	3.801	2.16	0	2	1
Tridem	0	0	0	1.909	0	0.014	2.04	0	0	0
Quad	0	0	0	0	0	0	0	0	0	0



## Appendix B - Site Specific Material Properties

Table B-1: Site-specific asphalt properties for AC over JPCP sections

Project Name	Pavement Layer	Thickness (in)	Binder Grade	Binder Content (By Volume)	Gradation (% Passing)			
					3/4"	3/8"	#4	#200
K-7823-01	Overlay-Surface Course	1.5	PG 70-22	10.70	100	77	60	6
	Overlay-Binder Course	2.5	PG 70-22	9.60	100	82	69	5
KA-2835-01	Overlay- Surface Course	1.5	PG 70-22	14.40	100	99	82	5
	Overlay - Binder Course	2.5	PG 70-22	9.90	98	83	63	5
KA-2836-01	Surface Course	1.5	PG 70-22	14.00	100	99	82	5
	Binder Course	2.5	PG 70-22	11.60	98	83	63	5
KA-3282-01	UBAS	0.625	PG 70-28	11.95	100	75	37	4
	Overlay Course	3.0	PG 76-22	10.67	100	83	62	4
KA-2669-01	Overlay Course	3.0	PG 70-22	11.30	100	88	76	5
KA-4136-01	UBAS	0.625	PG 70-28	11.70	100	97	51	5
	Overlay	3.0	PG 70-22	10.30	100	89	78	4
KA-1950-01	Overlay Course	3.0	PG 70-28	12.70	100	88	77	5
KA-1951-01	Overlay Course	3.0	PG 70-28	12.70	100	88	77	5
KA-1931-01	Overlay Course	3.0	PG 70-28	11.90	100	88	77	5
KA-2681-01	Overlay Course	3.0	PG 70-28	10.20	100	88	66	4
KA-2682-01	Overlay Course	3.0	PG 70-28	10.20	100	88	66	4
KA-4036-01	Surface Course	1.5	PG 70-22	12.70	100	86	72	5
	Binder Course	1.5	PG 70-28	10.80	100	85	62	5
KA-3848-01	UBAS	0.625	PG 70-28	13.20	100	99	52	4
	Overlay course	2.5	PG 70-28	11.10	100	84	59	4
	RCI course	1.0	PG 70-28	15.0	100	100	98	5

KA-0378-01(2)	UBAS	0.58	PG 70-28	10.70	100	98	45	5
	Overlay course	2.0	PG 70-28	9.90	100	83	63	4
	RCI course	1.0	PG 70-28	16.90	100	100	97	2
KA-0378-01(1)	UBAS	0.58	PG 70-28	10.70	100	98	45	5
	Overlay course	2.0	PG 70-28	9.90	100	83	63	4
	RCI course	1.0	PG 70-28	16.90	100	100	97	2
KA-4236-01	Overlay course	3.5	PG 70-22	10.70	100	85	65	5
	RCI course	1.0	PG 70-28	14.80	100	100	94	4
KA-2001-01	UBAS	0.625	PG 64-28	10.80	100	98	47	4
	Overlay course	2.0	PG 70-28	11.50	100	86	65	4
	RCI course	1.0	PG 70-28	15.80	100	100	99	5
KA-3006-01	Overlay course	2.0	PG 70-28	10.10	100	85	37	5

Table B-2: Site-specific asphalt properties for AC over AC sections

Project Name	Pavement Layer	Thickness (in)	Binder Grade	Binder Content (By Volume)	Gradation (% Passing)			
					3/4"	3/8"	#4	#200
KA-2628-01	Existing AC-surface course	2.0	PG 76-28	9.35	100	70	61	4.6
	Existing AC-base course	8.2	PG 70-28	7.45	98	59	32	2
	Overlay course	3.0	PG 70-28	10.33	100	87	72	4.6
	UBAS	0.625	PG 70-28	11.00	100	88	34	4.1
KA-9466-01	Existing AC surface course milled off							
	Existing AC-binder course	7	AC 10	8.85	100	71	63	7
	Existing AC-base course	9	AC 10	8.43	98	92	80	11
	Overlay- surface course	1.5	PG 76-28	10.85	100	96	62	4.2
	Overlay - binder course	1.5	PG 76-28	9.35	100	70	61	4.6
KA-4013-01	Existing AC-surface course	1.5	PG 64-28	11.2	100	91	55	4.1
	Existing AC-binder course	2.5	PG 64-28	9.13	98	80	54	4.6
	Existing AC-base course	5.5	PG 64-22	9.53	97	82	70	4.6
	Overlay course	1.5	PG 58-28	12.96	100	87	69	3.4
KA-1436-01	Existing AC-surface course	1.5	AC 10	9.76	100	93	51	5.4
	Existing AC-base course	8.5	AC 10	10.22	100	67	43	6
	Overlay Course	1.5	PG 58-28	11.89	100	88	73	5.1
KA-2188-01	Existing AC-surface course	2.5	PG 64-28	8.26	100	87	67	6
	Existing AC-base course	11.5	PG 58-28	9.00	100	68	41	3.4
	Overlay- surface course	4	PG 64-28	11.62	100	87	74	3.1
	Overlay - binder course	2	PG 58-28	11.70	100	86	72	3.4
KA-0813-01	Existing AC-surface course	1.5	PG 58-28	11.24	100	98	60	2.8
	Existing AC-base course	7.1	PG 58-28	11.60	99	79	53	3
	Overlay Course	1.5	PG 64-28	11.50	100	87	76	4.3

K-0657-01	Existing AC-surface course	1.0	AC 10	11.19	100	95	53	5
	Existing AC-base course	10.5	AC 10	6.71	99	71	39	6
	Overlay Course	1.5	PG 76-22	13.66	100	76	31	4
KA-0811-01	Existing AC-surface course	1.0	PG 70-28	8.52	100	95	54	6
	Existing AC-binder course	3.0	PG 58-28	7.99	100	68	42	5.2
	Existing AC-base course	2.5	PG 52-28	7.98	100	68	42	5.2
	Overlay course	1.0	PG 64-22	10.98	100	97	72	4
KA-0310-01	Existing AC-surface course	1.0	PG 58-28	12.20	100	100	68	4
	Existing AC-binder course	4.0	PG 58-28	10.30	100	74	42	3
	Existing AC-base course	6.0	PG 52-28	9.80	100	73	39	4
	Overlay course	2.0	PG 70-28	11.19	100	85	67	2.1
KA-4192-01	UBAS	0.5	PG 70-28	11.90	100	99	55	4.7
	Existing AC-surface course	1.5	PG 64-28	11.11	100	98	70	4.6
	Existing AC-binder course	2.5	PG 64-28	9.99	97	83	64	5.3
	Existing AC-base course	4	PG 64-22	10.01	98	84	63	3.5
	Overlay course	1.5	PG 64-28	11.58	100	86	73	4.9
KA-2941-01	Existing AC-surface course	1.5	PG 64-28	11.61	100	97	77	4
	Existing AC-binder course	2.5	PG 64-28	10.24	97	83	64	5.3
	Existing AC-base course	8.0	PG 64-22	9.24	98	83	63	2.6
	Overlay course	1.5	PG 58-28	11.75	100	87	75	5
KA-2923-01	Existing AC-surface course	2.0	PG 64-28	11.41	100	98	64	3.2
	Existing AC-base course	5.5	PG 58-28	11.44	100	67	45	3
	Overlay Course	1.5	PG 70-28	11.63	100	86	67	4.3
KA-8431-01	Existing AC-surface course	1.0	AC 20	9.42	100	85	71	5
	Existing AC-base course	1.0	AC 10	9.86	99	69	42	3.7

	Overlay Course	13.0	PG 76-22	10.71	100	95	67	4.6
KA-1480-01	Existing AC-surface course	1.5	AC 10	10.29	100	91	53	5
	Existing AC-base course	8.5	AC 20	8.95	100	72	40	3
	Overlay course	1.5	PG 58-28	11.07	100	88	74	5.1
K-7756-01	Existing AC-surface course	1.0	AC 10	11.32	100	98	55	4.5
	Existing AC-base course	7.0	AC 10	9.3	100	81	64	5.8
	Overlay course	2.0	PG 64-28	9.89	100	87	57	3.1
KA-1460-01	Existing AC-surface course	1.5	AC 10	11.66	100	95	54	5.8
	Existing AC- base course	7.0	AC 10	10.67	98	84	63	3.5
	First overlay action	2.0	PG 64-28	10.43	100	84	50	3
	Second overlay action	1.5	PG 58-28	11.81	100	89	78	5
KA-2200-01	Existing UBAS	Existing UBAS milled off						
	Existing AC-surface course	Existing AC surface course milled off						
	Existing AC-binder course	3.0	PG 64-28	9.7	99	64	39	3.4
	Existing AC-base course	6.0	PG 58-28	9.8	99	64	39	3.4
	Overlay- surface course	3.0	PG 58-28	10.36	100	88	71	4.9
	Overlay - base course	4.0	PG 58-28	10.08	97	80	65	4.1
KA-2204-01	Existing AC-surface course	Existing AC surface course milled off						
	Existing AC-binder course	Existing AC binder course milled off						
	Existing AC-base course	4.0	PG 58-28	9.8	99	64	39	3.4
	Overlay course	7.0	PG 58-28	10.36	100	88	71	4.9
KA-2966-01	Existing AC-surface course	1.0	AC 10	9.84	100	99	54	7
	Existing AC-base course	9.0	AC 10	9.98	100	84	39	2.7
	Overlay course	1.5	PG 70-28	11.43	100	89	77	3.4
KA-2505-01	Existing AC-surface course	Existing AC surface course milled off						

	Existing AC-base course	6.3	PG 64-22	8.28	100	67	40	3.8
	Overlay course	2.0	PG 58-28	11.20	100	83	68	4.9
KA-1444-01(1)	Existing AC-surface course	Existing AC surface course milled off						
	Existing AC-base course	5.0	AC 10	10.1	100	67	43	6
	First overlay action	1.5	AC 10	9.8	100	93	51	5.4
	Second overlay action	1.5	PG 58-28	11.0	100	88	76	4.7
KA-1444-01(2)	Existing AC-surface course	Existing AC surface course milled off						
	Existing AC-base course	5.0	AC 10	10.1	100	67	43	6
	First overlay action	1.5	AC 10	9.8	100	93	51	5.4
	Second overlay action	1.5	PG 58-28	11.0	100	88	76	4.7
KA-3674-01	Existing AC-surface course	1.5	PG 64-28	11.71	100	96	64	5.4
	Existing AC-binder course	2.5	PG 64-28	10.01	100	80	63	5.9
	Existing AC-base course	8.0	PG 64-22	8.91	100	80	63	5.9
	Overlay course	1.5	PG 58-28	16.78	100	89	73	4.7
K-9364-01	Existing AC-surface course	1.5	PG 58-28	8.92	100	85	71	6
	Existing AC-base course	3.5	PG 52-28	7.73	100	70	39	5.5
	Overlay- surface course	1.0	PG 64-22	9.42	100	87	68	4
	Overlay - binder course	1.0	PG 64-22	9.97	100	85	70	3.9
KA-3496-01	Existing AC-surface course	1.0	PG 70-28	10.47	100	97	59	3.5
	Existing AC-binder course	1.0	PG 70-28	9.1	98	82	53	3.6
	Existing AC-base course	5.5	PG 58-28	9.6	98	82	53	3.6
	Overlay course	1.5	PG 70-28	9.95	100	87	63	4

Table B-3: Site-specific PCC properties for AC over JPCP sections

Project Name	PCC thickness (inch)	Cementitious content (lb./yd <sup>3</sup> )	Water-cement ratio	JPCP joint spacing (feet)	JPCP dowel diameter (inch)
K-7823-01	9	623	0.46	15	1.5
KA-2669-01	11	521	0.44	15	1.375
KA-2835-01	12	521	0.44	15	1.5
KA-2836-01	12	521	0.43	15	1.5
KA-3282-01	10	620	0.49	20	1.25
KA-4136-01	10.5	620	0.49	30	1.375
KA-1931-01	9	620	0.46	15	1.25
KA-1950-01	10	620	0.43	15	1.25
KA-1951-01	10	620	0.42	15	1.25
KA-2681-01	12	545	0.45	15	1.25
KA-2682-01	9.5	545	0.45	15	1.25
KA-4036-01	10	565	0.45	15	1.25
KA-3848-01	9	592	0.46	15	1.125
KA-0378-01(1)	9	639	0.44	15	1.125
KA-0378-01(2)	10	620	0.43	15	1.125
KA-2001-01	9	620	0.44	15	1.125
KA-4236-01	11	545	0.44	15	1.375
KA-3006-01	9	620	0.49	15	1.125

Table B-4: Site-specific subgrade soil inputs for AC over AC sections

Project Name	County	Soil Texture	Soil Type (Unified)	Resilient Modulus (psi)	Gradation (% Passing)				Atterberg Limits	
					#4 Sieve	#10 Sieve	#40 Sieve	#200 Sieve	Liquid Limit	Plastic Limit
KA-0310-01	Osage	Silty clay loam	-		75-95	55-95	55-85	50-80	35-50	15-25
K-9364-01	Jefferson	Silty clay loam	-		85-100	85-100	85-100	80-95	25-45	11-23
KA-2188-01	Republic	Silty clay, silty clay loam; silt & clay	CH and CL		100	100	-	75-90	63	39
KA-0813-01	Washington	Silty clay loam, clay loam, silt, silty clay, sandy clay loam, sandy clay & loam	Mostly CL and CH; Some CL-ML & SC		85-100	70-100	70-95	70-95	40-60	20-35
KA-9466-01	Saline	Silty clay loam, clay loam, sandy clay loam; silty clay, silt, clay and loam	Mostly CL; some CH; CL-ML & SC-SM	3100	95-100	90-100	85-100	60-90	20-35	5-15
KA-2628-01	Saline	Silty clay loam, clay loam, sandy clay loam	Mostly CL; some CH	3100	100	100	95-100	85-100	50-75	30-45
KA-2923-01	McPherson	Silty clay, Silty clay loam; silt & clay	CH and CL		100	100	90-100	85-95	45-70	20-40
KA-4013-01	Osborne	Silt, silty clay loam, silty clay, silt loam.	Mostly CL and CH; Some CL-ML & SC		100	95-100	85-100	75-95	52	29
KA-1436-01	Cheyenne	Loam, clay loam, sandy clay loam, silt loam, fine silt loam & fine sand	CL-ML, CL, SC, SC-SM; some ML, SC, SM, GC		80-100	75-100	50-95	35-85	20-40	5-15
KA-1444-01(1)	Phillips	Silt, silty clay loam; loam and clay loam	CL, CL-ML, CH		100	100	90-100	65-90	20-35	4-19
KA-1444-01(2)	Phillips	Silt, silty clay loam; loam and clay loam	CL, CL-ML, CH		100	100	90-100	65-90	20-35	4-19
KA-2505-01	Rooks	Silt, silty clay loam; fine silt	CL-ML, CL	3500	100	95-100	80-100	55-90	20-40	3-20
KA-2966-01	Ellis	Silt, silty clay loam, silty clay;	CL, ML, CH; some CL-ML, ML, SC		70-100	75-95	65-95	60-90	39	21



		gravelly clay loam & fine silt								
KA-3674-01	Norton	Silt, silty clay loam	CL and CH	3600	100	100	95-100	90-100	40-55	20-30
K-0657-01	Bourbon	Silty clay loam & silty clay	CH, CL; some GC & MH		100	96-100	96-100	80-99	37-70	15-40
KA-0811-01	Montgomery	Loam, silt & silty clay loam	CL, CH, and some SC	3500	95-100	95-100	90-100	80-98	37-65	15-35
K-7756-01	Chautauqua	Silty clay loam, silt & silty clay	CL, CH; some CL-ML		100	100	95-100	90-100	56	30
KA-2200-01	Allen	Silt, silty clay loam, silty clay	CH, CL; some GC & CL-ML		100	95-100	95-100	90-100	50-65	30-45
KA-2204-01	Anderson	Silt, silty clay loam, some silty clay	CL, CH; some SC, GC & CL-ML		100	100	90-100	85-98	37-65	15-33
KA-2941-01	Butler	Silty clay loam, silt; isolated gravelly silty clay & channery silty clay	CH & CL; some ML and isolated MH & CL-ML	2600	100	100	95-100	95-100	56	33
KA-4192-01	Butler	Mostly silt, some clay, silty clay loam and silty clay	Mostly CL & CH; some CL-ML, ML & SC, GC, SP-SC & GP-GC	2600	20-80	16-76	16-70	16-66	46	25
KA-1460-01	Cowley	Silty clay loam, silty clay, silt; isolated gravelly & channery silty clay, clay loam and clay	Mostly CL & CH with isolated MH, ML, CL-ML, SC, GC, SP-SC & GP-GC	2600	95-100	95-100	65-100	45-80	32-52	11-25
KA-3496-01	Sedgwick	Silty clay loam, silty clay, silt, isolated loam; parachannery silty clay & parachannery silty silty clay loam	CL & CH		100	100	95-100	90-100	50-65	25-40
K-8431-01	Seward	Clay loam, silty clay loam, silty clay; some clay, loam, fine silt and silt loam	Mostly CL, SC & CH; some SC-SM, CL-ML, SM & ML	4700	100	100	100	90-100	30-45	10-25
KA-1480-01	Clark	Clay loam, silt, silty clay loam;	CL, CL-ML, ML & SC; some		75-100	55-100	50-95	36-85	20-40	4-20

gravelly loam,  
fine silt loam,  
sandy clay loam

CH & SC-SM;  
isolated SM &  
MH

Table B-5: Site-specific subgrade soil inputs for AC over JPCP sections

Project Name	County	Soil Type	Resilient Modulus (psi)	Gradation (% Passing)				Atterberg Limits	
				#4 Sieve	#10 Sieve	#40 Sieve	#200 Sieve	Liquid Limit	Plastic Limit
K-7823-01	Johnson	A-7-6	2600	100	100	98.5	97.5	60	37.5
KA-2669-01	Shawnee	A-6	3100	100	99	69	18	33	16
KA-2835-01	Wabaunsee	A-7-6	2600	100	100	97.5	90	55	33
KA-2836-01	Shawnee	A-7-6	3100	100	100	99	35	45	22
KA-3282-01	Wyandotte	A-7-6	3300	100	100	95	80	51	30
KA-4136-01	Shawnee	A-7-6	3100	100	100	99	35	45	22
KA-1931-01	Cloud	A-7-6	3000	100	100	-	35	46	24
KA-1950-01	Marion	A-7-6	2600	88	85	83	80	50	28
KA-1951-01	Chase	A-7-6	2700	100	100	100	95	38	16
KA-2681-01	Marion	A-7-6	2600	100	100	97.5	90	60	40
KA-2682-01	Chase	A-7-6	2700	100	100	100	96	38	16
KA-4036-01	Sherman	A-6	4100	100	100	100	92.5	38	18
KA-3848-01	Labette	A-7-6	2700	99	98	98	81.5	50	29
KA-0378-01(1)	Harvey	A-6	2700	100	100	97.5	92	39	18
KA-0378-01(2)	Harvey	A-6	2700	100	100	97.5	92	39	18
KA-2001-01	Butler	A-6	4000	100	100	97.5	92	39	18
KA-4236-01	Harvey	A-7-6	3500	100	100	97.5	95	50	30
KA-3006-01	Finney	A-6	3200	100	100	100	95	40	21

## Appendix C - Backcalculated Modulus

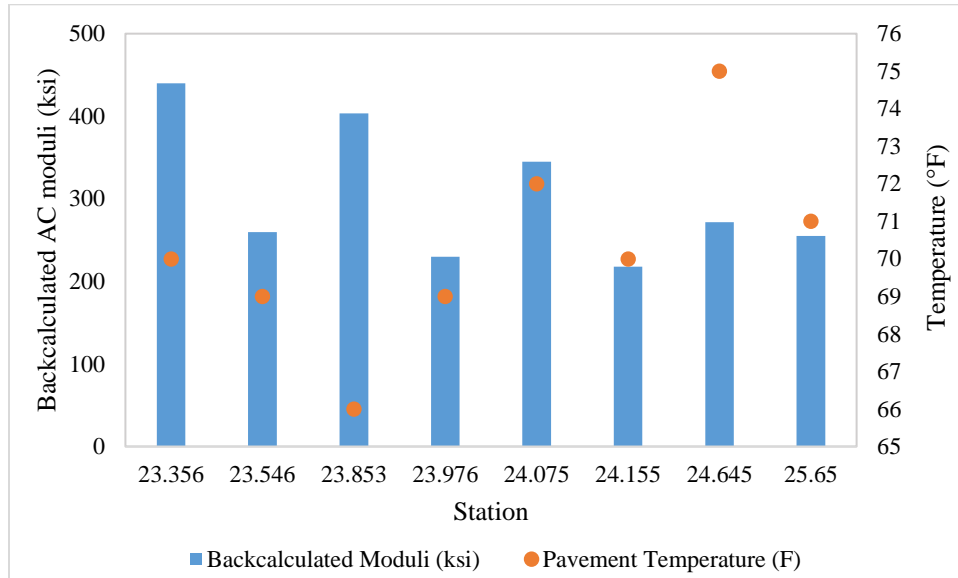


Figure C-1 Backcalculated moduli for the pavement section KA-4013-01

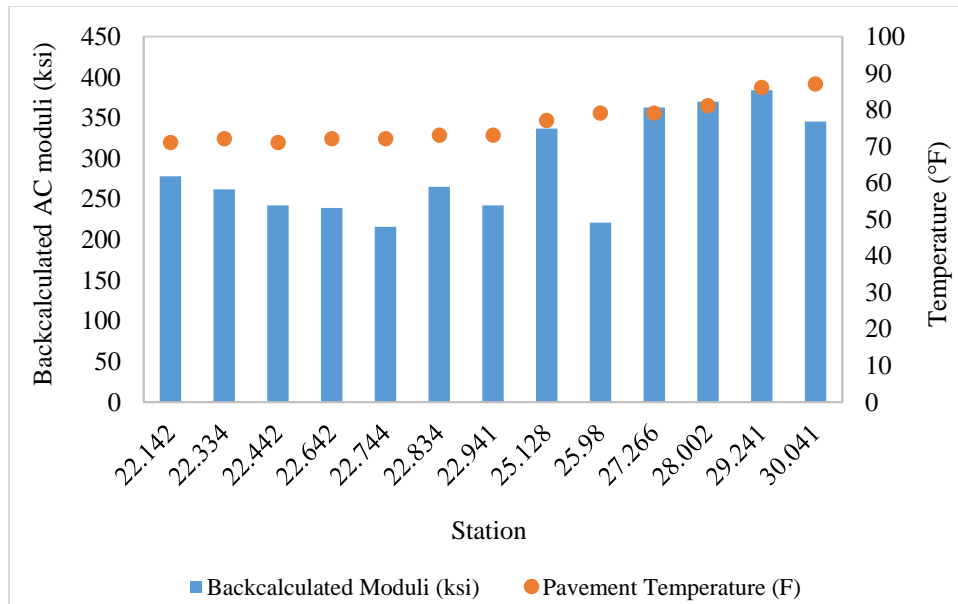


Figure C-2 Backcalculated moduli for the pavement section KA-3674-01

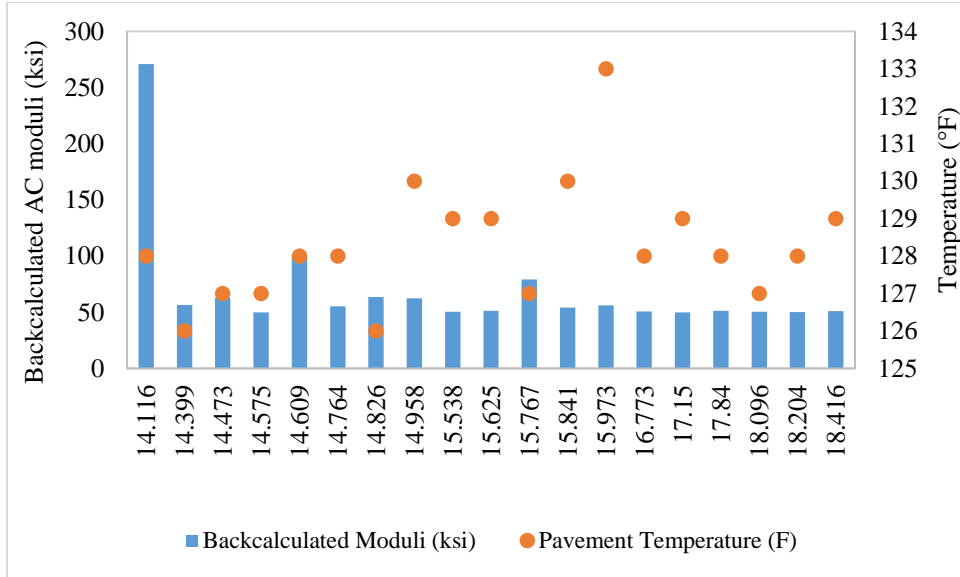


Figure C-3 Backcalculated moduli for the pavement section KA-1436-01

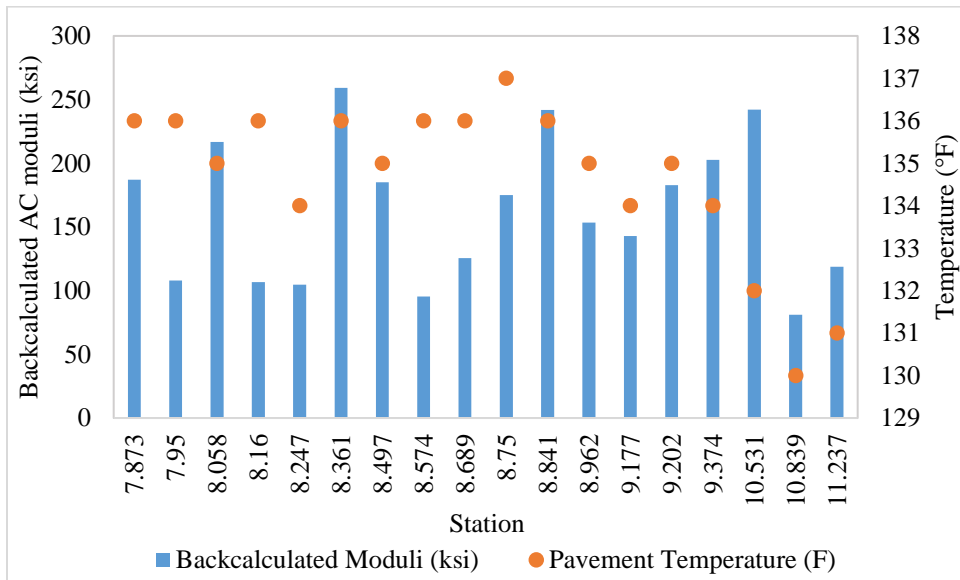


Figure C-4 Backcalculated moduli for the pavement section KA-0310-01

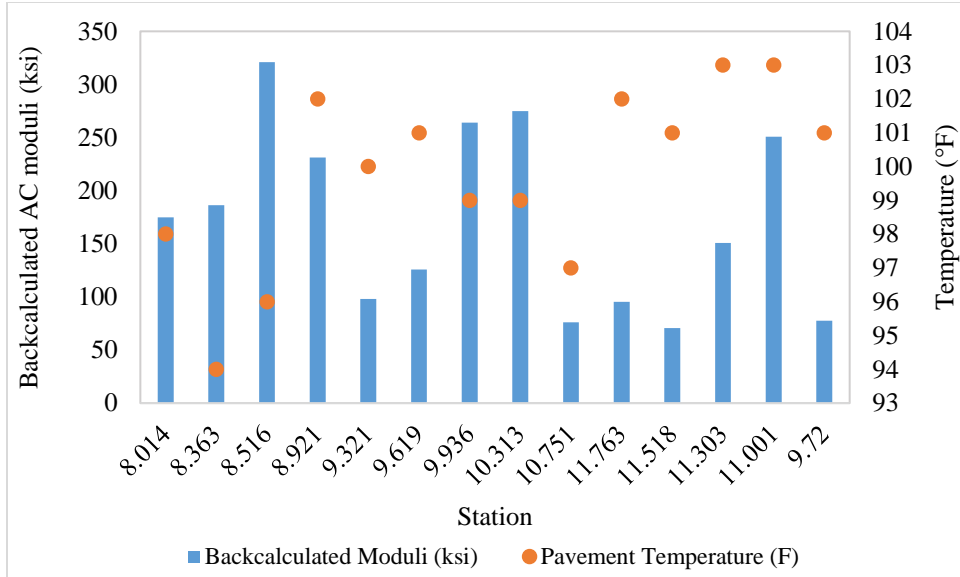


Figure C-5 Backcalculated moduli for the pavement section KA-9364-01

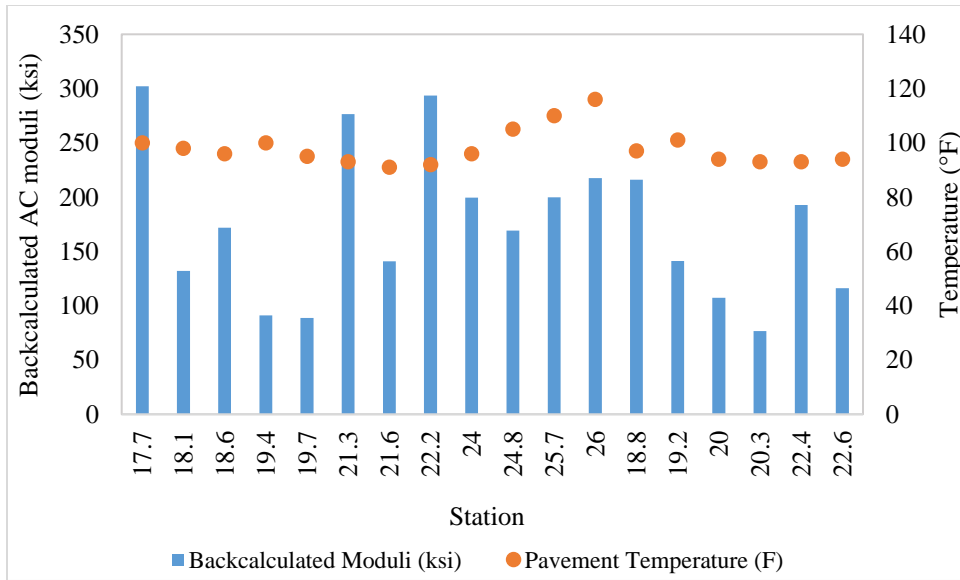


Figure C-6 Backcalculated moduli for the pavement section KA-0813-01

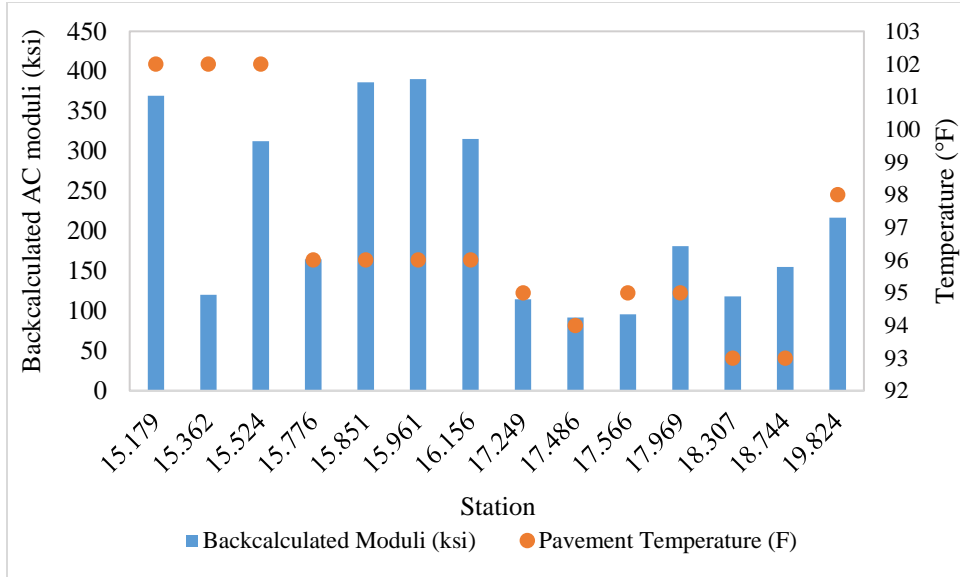


Figure C-7 Backcalculated moduli for the pavement section KA-1444-01(1)

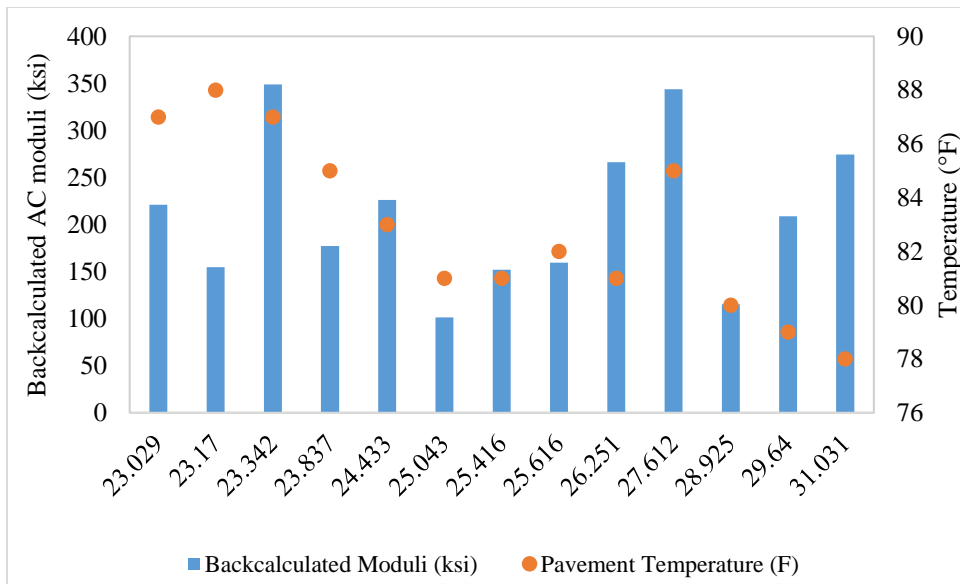


Figure C-8 Backcalculated moduli for the pavement section KA-1444-01(2)

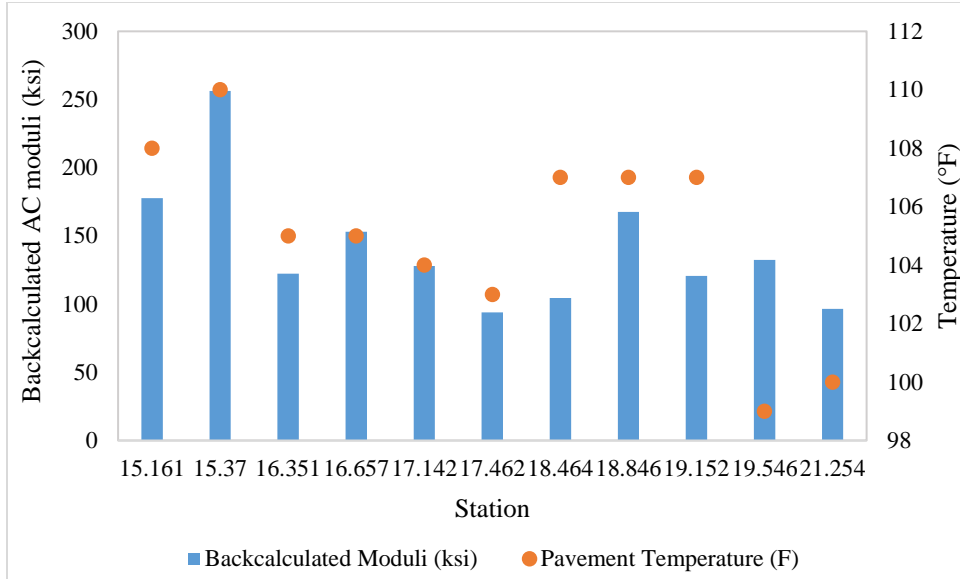


Figure C-9 Backcalculated moduli for the pavement section KA-2200-01

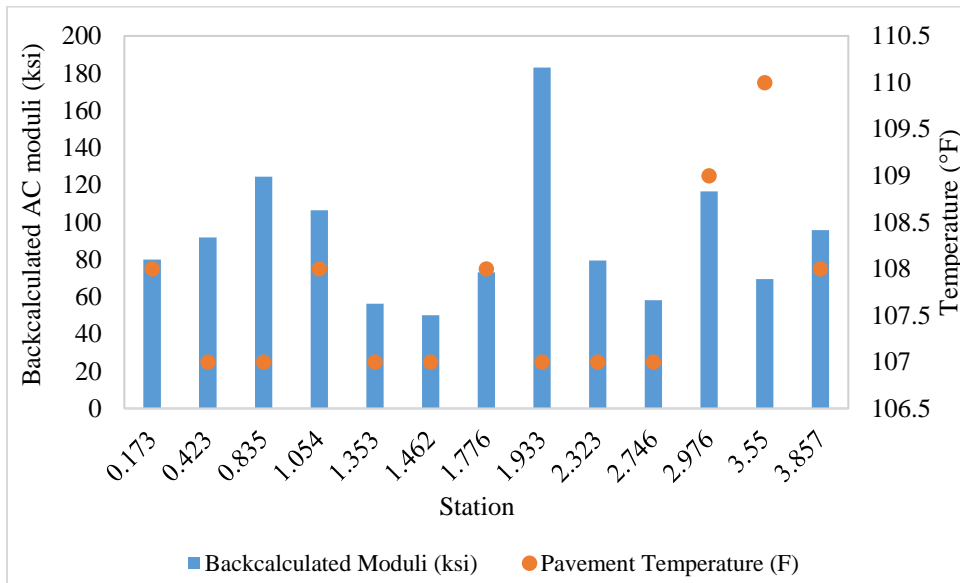


Figure C-10 Backcalculated moduli for the pavement section KA-2204-01

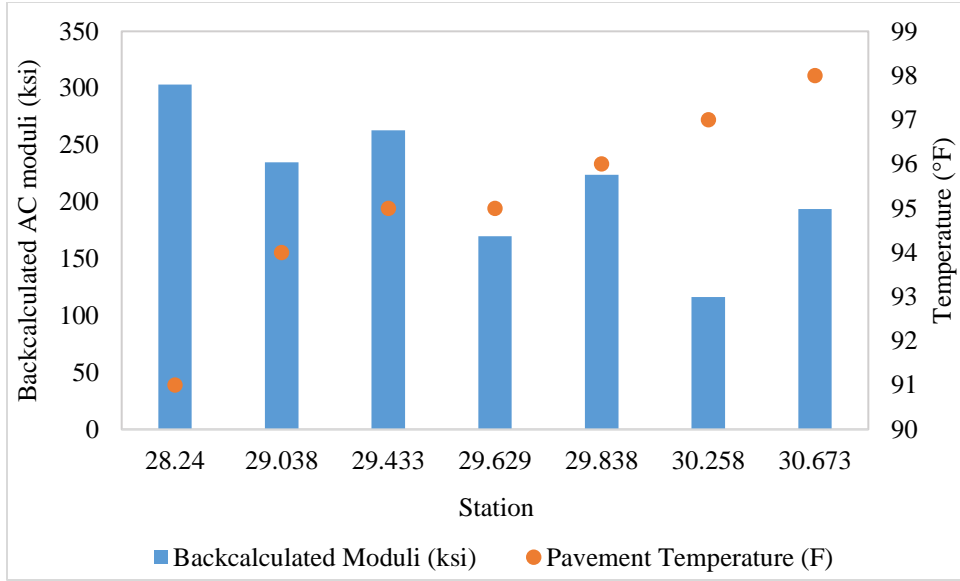


Figure C-11 Backcalculated moduli for the pavement section KA-0811-01

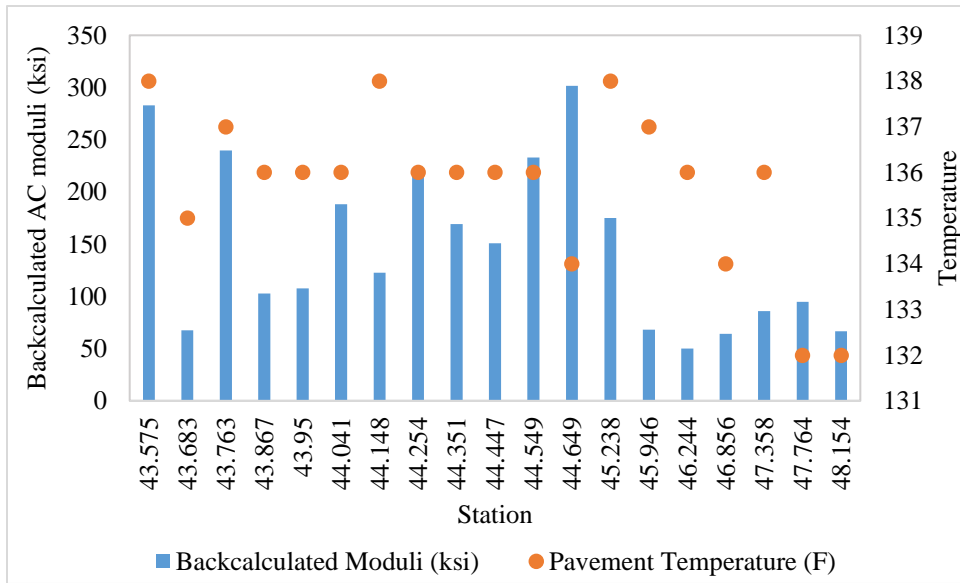


Figure C-12 Backcalculated moduli for the pavement section KA-2941-01



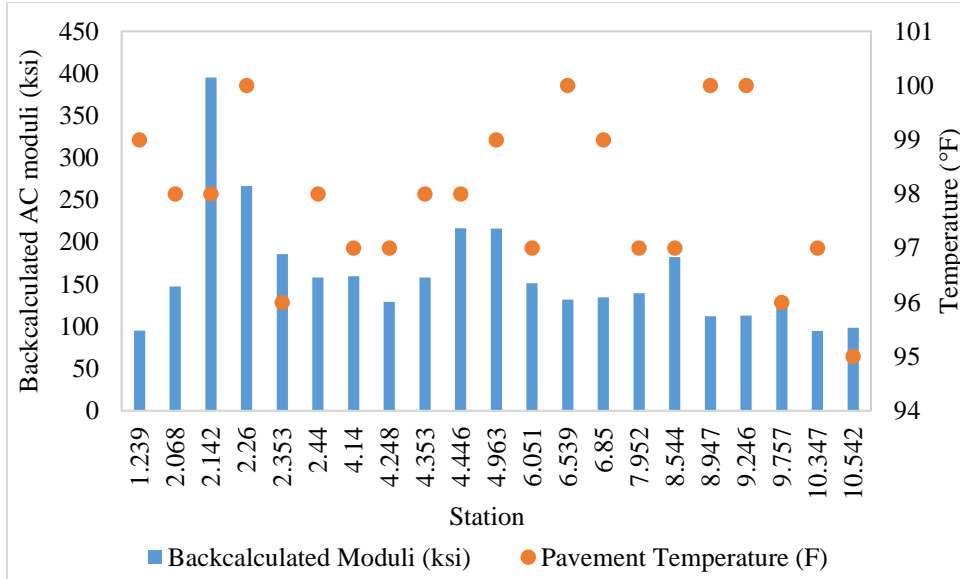


Figure C-13 Backcalculated moduli for the pavement section KA-4192-01

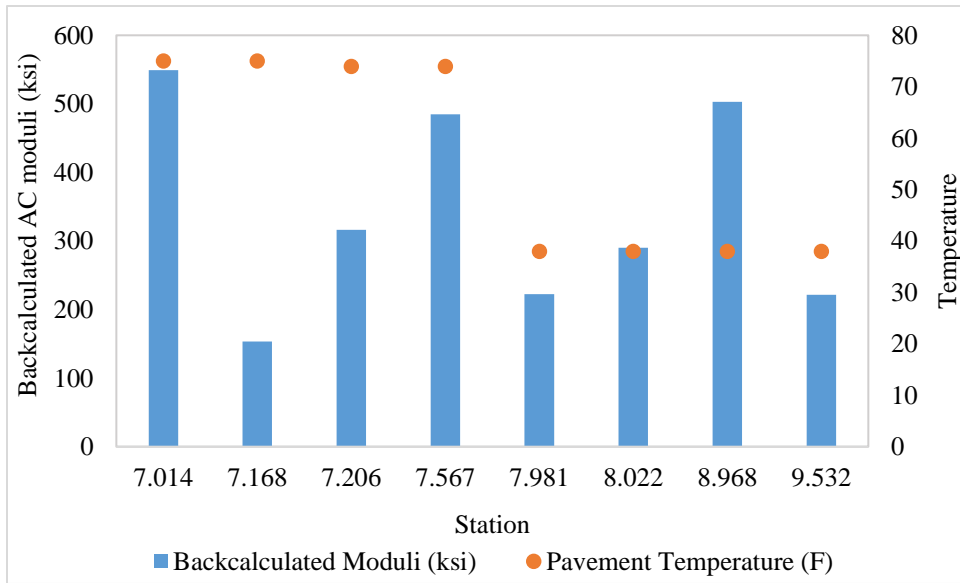


Figure C-14 Backcalculated moduli for the pavement section KA-3496-01

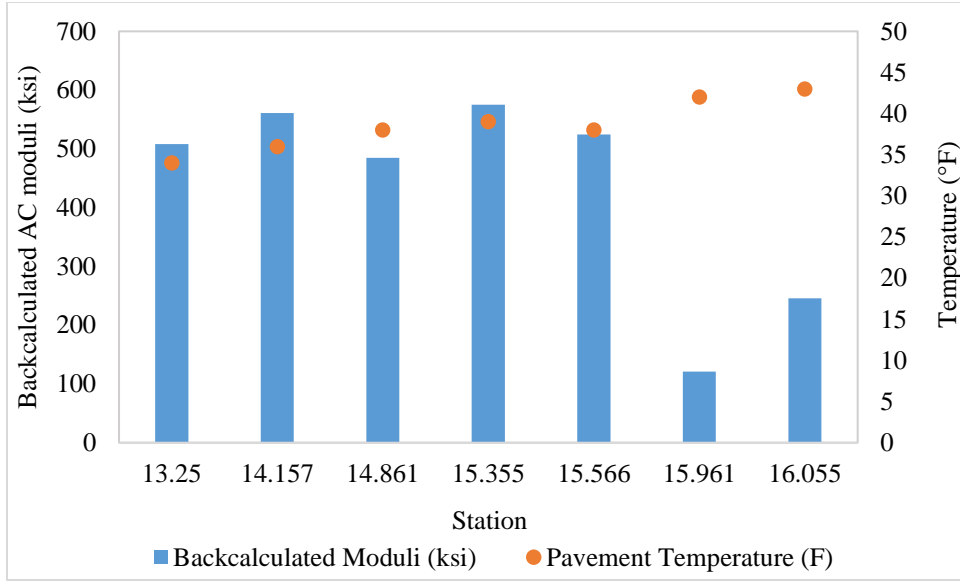


Figure C-15 Backcalculated moduli for the pavement section KA-1460-01

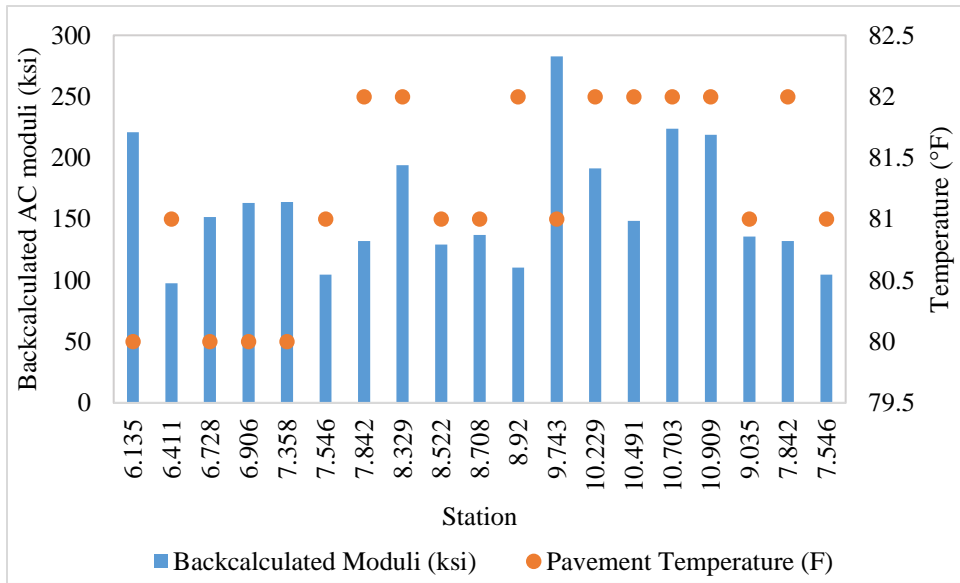


Figure C-16 Backcalculated moduli for the pavement section KA-1480-01